A.A. 2006/2007

Università degli studi di Roma
"Tor Vergata"

Radiative properties of complex magnetic elements in the solar photosphere.

Thesis Author:
Dr. Serena Criscuoli

Thesis Advisors:
Prof. Mark Rast, Prof. Francesco Berrilli

Thesis Coordinator:
Prof. Roberto Buonanno

A thesis submitted to
The University of Rome "Tor Vergata"
in partial fulfillment of the requirements for the degree
of
Doctor of Philosophy in Astronomy.

Soles,
soles solerum,
mea verba dicata sunt.

To the Sun,
Star among the Stars,
these words are dedicated

Contents

List of Figures

List of Tables

Acknowledgements

I am grateful to University of Rome "Tor Vergata" and to the High Altitude Observatory, which gave me the possibility of completing my studies and achieving the title of Doctor Philosophiae.
I would like to particularly thank Prof. Roberto Buonanno, the PhD students coordinator at University of Rome, for all the help provided. I would also like to thank Dr. Michael Knölker, the director of HAO, and the visitor committee, for giving me the possibility of developing most of the research presented in this thesis. Special thanks go of course to my advisor, Dr. Mark Rast, who will always be for me an example to follow.
I am also in debt with the people of the Solar Group of Rome Observatory and the Solar Group at University of Rome "Tor Vergata", for the fruitful collaborations and for the support they always provided.

Abstract

In this thesis I investigate the photometric and geometric properties of bright magnetic features in the lower solar atmosphere. The contribution of these features to Total Solar Irradiance (TSI here after) variations observed at different temporal scales has been broadly showed during the last years. Nevertheless, measurements and theoretical investigations of their properties, on which reconstructions of TSI variations are based, have produced discrepant results.

In order to interpret discrepancies presented in the literature and to improve our understanding of physical properties of magnetic elements, both experimental and theoretical aspects have been investigated.

In the first part of the thesis I show results obtained by the analysis of full disk PSPT broad band images from Rome and Hawaii. Geometric properties and the possible connection with photometric properties have been investigated through the measurement of fractal dimension of features observed in chromosphere. Results I obtain agree very well with the ones presented in the literature carried out on similar data and with the same fractal dimension estimator. The fractal dimension increases in fact with features area and reaches a plateau at areas larger than about 1000-2000 Mm^2. Nevertheless, by the analyses of images of fractals whose dimension is known by the theory, I show that fractal dimension estimation is critically effected by pixelization, technique employed to select magnetic structures on images and resolution. In particular the increase of fractal dimension with object size is an effect of pixelization and thus some conclusions previously drawn in the literature should be revisited.

Photometric properties are investigated by the analyses of contrast of identified features in two photospheric bands and in the chromosphere. In particular the variation of the contrast with position on the solar disk and with object size is investigated. I show that the contrast in the chromosphere is not dependent on disk position and that in the photosphere monotonically increases from the center toward the limb. A comparison with previously published results shows a better agreement with authors that employed an identification methods similar to the ones I employed to select magnetic features on images. The contrast, especially at the limb, is also critically affected by seeing. Comparison of the scaling of average and maximum contrast with object size suggests that the smaller magnetic elements, whose clustering forms the features analyzed, are characterized by different photometric properties. The increase of average contrast with object size, very similar to the increase observed for the fractal dimension, is instead an effect of filling factor.

In order to investigate the physical origin of the results and validate some of the conclusions drawn, 2D numerical codes based on the magnetic flux tube model have been developed. Plane parallel gray atmosphere in LTE is supposed and radiative and convective energy transport mechanisms have been taken into account. In particular two classes of models are investigated. In the first one convection is modelled by the Mixing length theory and radiation by the radiative diffusion approximation. In the second one only radiation is taken into account, but radiative diffusion approximation is dropped and radiative equilibrium is imposed by an iterative scheme. The presence of the magnetic field is mimicked by imposing a lower pressure and density in the magnetic region.

In order to evaluate the radiation field a numerical code, based on the short characteristic technique, was developed. A detailed description of the code, as well as results obtained by tests aimed to investigate and compare different numerical techniques and spurious effects, are presented. The radiative flux is finally evaluated by a quadrature scheme. At this aim two schemes have been developed and compared. The software developed has allowed to investigate radiation field through the flux tube models studied. I show that the presence of a magnetic structure generates areas of different shapes and contrast around it. These features vary with the position of the structures on the solar disk (the sight angle) and have spatial scales smaller than the typical scale of a flux tube (about 100 km), so resolution better than 0.1 arcsec is required to observe them. The contrast of magnetic features varies also in function of the optical depth, so that for the same model different center to limb variations of the contrast can be observed. This indicates that when observing magnetic structures at different wavelengths the contrast can be very different, thus partially explaining the discrepant results obtained in the literature. Investigation of the results also shows that the center to limb variation of the contrast reflects the temperature stratification inside and outside the tube. Measurements carried out at different wavelengths are thus fundamental for the determination of temperature of magnetic structures and for the investigation of their physical properties.

Chapter 1

Introduction: The Solar Magnetic Field

The Sun is a very complex and active object on which many phenomena, characterized by different spatial, temporal and energetic scales, take place. These phenomena have also been observed on other stars. Their investigation on our star provides more observational details and is thus an incredible test for theoretical and numerical models developed to explain the physical processes that regulate them.

What makes the Sun such a complex and active object is its magnetic field. The study of physical and observational properties of particular magnetic structures is the purpose of this thesis. In this chapter I will thus describe some characteristic of the magnetic field of the Sun and in particular will illustrate the features of magnetic origin observed on the photosphere. Moreover, some of the phenomena observed on our star have deep influence on the earth. One of these is the variation, on different time scales, of the solar energy output, that is thought to have a role in climate changes. These variations are related, in the manner I will explain in the following, to properties of magnetic features observed in photosphere and chromosphere. The investigation of total solar energy output is for this reason the motivation that drives most of the studies, as well as part of this work, of photometric properties of magnetic features. A brief description of solar energy output variations measurements and reconstructions is thus given.

The content of this chapter is introductory. Its purpose is to present to the reader some vocabulary, physical aspects and open questions that concern the studying of the Sun and its Magnetic field. The reader familiar with these problematic will want to read only the last paragraph, in which I describe the main purpose of this thesis and its structure.

1.1 The Sun

The Sun is G2 type star. It is 5 billions years old, its average distance from the Earth is about 1.5×10^{11} meters, has a mass of about 2×10^{30}Kg and its Luminosity is 3.8×10^{26} W. In the core, the central area of thickness 0.3 solar radii, energy is generated by nuclear reactions, mainly p-p chains through

which Hydrogen is burnt into Helium. Also CNO reactions take place, but they produce only 1.2% of the total energy. Here the temperature is about 10 millions degrees and the matter density is about 10^5 kg/m^3. The energy propagates from the center to the outer layers through radiative processes, electron conduction and convection. The first two processes dominate up to a distance of 0.7 solar radii so that the zone between 0.3 and 0.7 solar radii is referred as Radiative. In this layer the temperature drops from about 8×10^6 to 5×10^5 degrees and the density from about 10^4 to about 10 kg/m^3. At a distance larger than 0.7 solar radii the opacity of the gas increases because the temperature and density are such that Hydrogen and Helium are partially ionized. As a consequence the radiative flux is not enough to carry the total energy flux and convection sets in. Convective instability ceases at the base of the photosphere, the lower layer of the solar external atmosphere. At this level matter becomes transparent and radiation can escape. Technically we define the surface of the Sun as the surface at which the optical depth is equal to unity. Convection overshoots into the photosphere for about 200 km. Structures of convective nature are thus observed in these layers. Namely with the term granulation we refer to cellular patterns of hexagonally shaped structures (the granules) of typical size of about 1000 km, surrounded by dark lanes. The center of granules is about 30% brighter than the surrounding atmosphere and have associated upflow motion. Downflow motion is associated to the dark lanes. Granulation typical lifetime is about 10 minutes. It is organized in larger structures (5000-10000 km), characterized by longer lifetime but lower vertical velocity respect to the granulation. These motions are referred as Mesogranulation. The term Supergranulation refers finally to structures of typical spatial scale of 35000 km, that evolve on temporal scales of several days and that have associated horizontal velocities of about 4000 km/sec and vertical motions of 50-200 m/sec.

The thickness of the photosphere is about 500 km. Above it we find the Chromosphere (about 2000 km) and the Corona. While the gas density continues to decreases with height (it is about 10^{-4} kg/m^3 at the base of the photosphere and decreases to about 10^{-13} kg/m^3 in the Corona), the temperature decreases from about 6000 degrees at the base of the photosphere to about 4000 degrees at a height of about 300 km. It then rapidly increases in the chromosphere to reach again the value of some million degrees in the Corona. These upper layers are dominated by the magnetic field, whose evolution gives rise to several phenomena.

A sketch of the interior of the Sun and its atmosphere is given in fig.1.1.

The interior of the Sun is investigated through helioseismological techniques. The outer atmosphere is instead investigated through spectroscopic and/or imaging techniques. In particular, because of the different physical conditions, different layers of the atmosphere emit at different wavelengths and can therefore be observed through different filters. The base of the photosphere is for instance observed in the IR and visible, while UV and X-rays allow to explore the chromosphere and the Corona, as shown in fig.1.2.

1.2 The Solar Magnetic Field

The Solar magnetic at the largest scales is roughly approximated by a dipole, but structures of all spatial scales are present. Phenomena associated with the

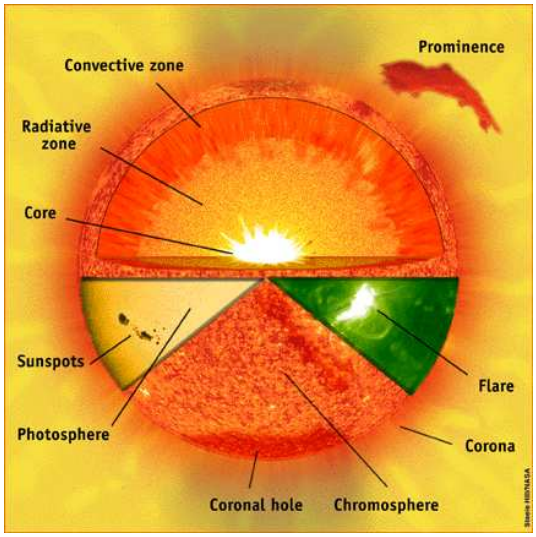

Figure 1.1: The interior and the atmosphere of the Sun are ideally separated into layers. In the core energy is produced by nuclear reactions. The Radiative and the Convective zones are named after the predominant energy mechanism transport in these layers. The photosphere is the lowest layer of the atmosphere that can be observed. Above it the chromosphere and the corona host several phenomena of magnetic origin (in the picture: flares and prominences). The flare, sunspots and photosphere, chromosphere, and the prominence are all clipped from actual images of the Sun taken by instruments onboard on SOHO spacecraft.

evolution of the magnetic field vary on a wide range of time scales (from minutes to centuries). The most well known is the 11 years activity cycle during which the magnetic field changes gradually its polarity. This modification is accompanied by a gradual increase in the complexity of the magnetic field lines, that loose their bipolar shape to assume less organized pattern. This complexity is accompanied to the increase in the appearance of phenomena of magnetic origin, like the number of sunspots and active regions, flares and Coronal Mass Ejections (CME's hereafter). Roughly the maximum is reached at the middle of the cycle. Afterwards a gradual decrease of the number and intensity of these events is observed. The activity is at the minimum when the bipolar, reversed polarity configuration is established again. The most used indicators to describe the solar activity cycle are: the sunspot number, the Ca II K plage Index (derived from the area and brightness of plages, bright features of magnetic origin observed in CaIIK), and the Radio Flux at 10.7 cm. The solar magnetic field is not the remnant of the interstellar medium magnetic field, since this would have been dispersed by diffusion processes a long time ago (Durrant, 1988). It is instead most likely generated in the interior of the Sun by the interaction of magnetic field and plasma motion. This process is called the *solar dynamo*. Several models have been proposed and many details are still debated (for a review see Carbonneau (2005)). The *Kinematic models* prescribe velocity fields and ask how the magnetic field respond. According to these models the original

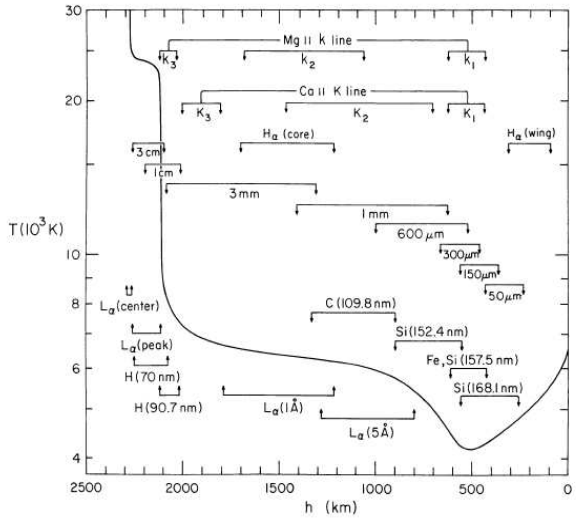

Figure 1.2: Temperature as a function of height in the Solar atmosphere. The layers at which lines and bands have stronger emissivity are also shown. Observations at different wavelengths thus allow to investigate different portions of the atmosphere. From Vernazza et al. (1981).

poloidal field (fig.1.3(a)) is slowly converted into toroidal field by the differential rotation (the Sun rotates faster at the equator), as shown in fig.1.3(b). This is call the Ω *effect*. Both theory and helioseismological data suggest that this happens in a region between the convective and radiative regions of the interior of the Sun, at a distance of 0.7 solar radii, called *tachocline*. In the convective region the field is transported outward or downward by convective plasma motions. This motion couples with the rotation of the star, so that, by the Coriolis effect., in the Northern hemisphere the upflow motions are rotated clockwise and downward motions are rotated in the opposite sense. As a result magnetic field emerges in Ω shaped loops twisted in opposite directions in the two hemispheres (fig.1.3(c,d)). The emergence and the twisting of the field are called α *effect*. The emerged ropes appear on the surface of the Sun as bipolar active regions. As the active regions evolve, the area of polarity opposite to the one of the pole migrates toward the pole (where it cancels), while the other migrates toward the equator, where it will be eventually cancelled by a region of opposite polarity (fig.1.3(f)). The migration of the two opposite polarity regions toward different directions was ascribed by Leighton (1969) to diffusion by convective motions.

This mechanism provides an explanation to the periodic reversal of polarity as well as to some observed properties of active regions observed in the photosphere and chromosphere. Nevertheless, not all the structures of magnetic origin can be associated with active regions. In particular first observations revealed that the magnetic field manifests in discrete structures of intense associated field, surrounded by a substantially field free medium (Zwaan, 1987). More recent studies have revealed that a low intensity magnetic field permeates even the so called Quiet Sun (Trujillo Bueno et al., 2004), so that now it is

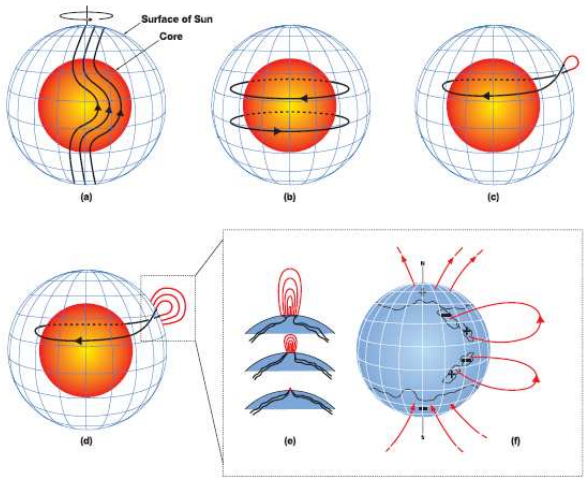

Figure 1.3: Solar dynamo sketch. (a) At the minimum of activity the magnetic field is bipolar. (b) Because of the differential rotation a stronger and stronger toroidal component is created as the time passes. (c) Magnetic ropes eventually emerge forming loops whose foot points, because of the Coriolis force, are twisted.(d) and (e) More magnetic field emerges and spread. These loops form bipolar regions, with the polarities oriented as shown in (f). The migration toward the equator and the poles finally causes flux cancellation and reversal of the polarity of the field. The red sphere represents the radiative region and the blue net is the base of the photosphere. These two regions are separated by a convective unstable layer. Adapted from Dikpati and Gillman (2006).

better to address magnetic features as regions of low gas to magnetic pressure ratio, and the Quiet Sun as regions of high gas to magnetic pressure ratio. *Local dynamo* processes, generated by turbulent motions at granular scales, have also been suggested (Cattaneo, 1999; Lin, 1995; Meneguzzi and Pouquet, 1989).

At photospheric levels the magnetic field is essentially vertical, but, because of the high pressure stratification, it gradually expands to fill the whole space in the outer layers of the solar atmosphere. In the chromosphere and corona magnetic structures are very complex. Arches of different sizes, whose foot points lie in the photosphere and maybe beneath, connect regions of opposite polarities. Reconnection events give rise to flares, transitory phenomena that have associated releases of energy and particles. Some flares have associated CME's, that is expulsion of matter from the Corona.

All these events are manifestations of the evolution of the magnetic field and its interaction with convective plasma. Nevertheless, a complete detailed description of these phenomena through a unique model or numerical simulation is not possible, because of the large differences of the physical scales characteristic of these events. The models and simulations nowadays employed to describe features and phenomena that take place in the corona, are thus very different from the ones used to describe photospheric features or processes that take place in the deeper convective layers.

This thesis mainly concerns the studying of features observed at photospheric

Hierarchy of photospheric magnetic features

Property[a]	Sunspot with penumbra: Large	Sunspot with penumbra: Small	Pore	Magnetic knot (micropore)	Faculae, network clusters	Flux fiber
Φ (10^{18} Mx = 10^{10} Wb)	3×10^4	500	250–50	≈10	≲20	≲0.5?
R (Mm)	28	4	—	—	—	—
R_u (Mm)	11.5	2.0	1.8–0.7	≈0.5	—	≲0.01
B (in G = 10^{-4} T)	2900±400	2400±200	2200±200	≈1500–2000	—	≈1500
Overall contrast:	dark					bright
Cohesion:	single compact structure				cluster of	
Behavior in time:	remain sharp during decay, shrinking				—	modulated by granulation
Occurrence:	exclusively in active regions				both inside and outside active regions	

[a] Φ is magnetic flux, R is the average radius of a sunspot, R_u is the radius of sunspot umbrae and of smaller elements, and B is the magnetic field strength (at the axis of the element).

Figure 1.4: Classification of Solar Magnetic Features observed in the Photosphere. From Zwaan (1987).

level. In the following I will briefly describe these features and their characteristics.

1.3 Photospheric magnetic features

In photospheric layers the magnetic field manifests itself thorough several different features. These structures are essentially discrete, although, as mentioned in previous paragraph, a low intensity magnetic field permeates the whole surface. Most of these features are classified according to the magnetic flux intensity they have associated (fig.1.4).

Sunspots appear as dark structures (the *umbra*) surrounded by a filamentary and less dark annular region called *penumbra*. They can appear isolated or in groups and their size and shape can vary considerably. The typical average magnetic field strength associated with sunspots is 1000-1500 G, but it is higher in the umbra (1800-3700G) and lower in the penumbra (700-1000G). The associated strong magnetic pressure and tension inhibit convection making the structure colder and therefore darker than the surrounding photosphere. The temperature deficit estimated is about $2000°K$ (see for instance Maltby et al. (1986)). The contrast of sunspots umbra is a function of wavelength, disk position and size, even though different authors have reported contradictory results about these dependences (e.g. Albregtsen et al., 1984; Steinegger et al., 1996; Walton and Preminger, 2003a). Albregtsen et al. (1984) also measured a variation of the contrast with solar cycle, but their results have not been confirmed,

so far, by similar studies.

Magnetic field in sunspots is still the subject of numerous investigations (see Solanki (2003) for a review). Nevertheless most of the proposed models and observations suggest the magnetic field to be vertical in the center and more and more inclined in the penumbra. The bright and dark features observed in the penumbra are a manifestation of the azimuthal variation of the field. High resolution observations reveal higher contrast structures in the umbra, the *umbral dots*, that have been suggested to be the manifestation of not totally suppressed convective motion. Radial plasma motion (the *Evershed Effect*) at typical velocities of 1-2 km is observed in the penumbra.

Pores have been classified in the past as distinct structures from sunspots, since they appear smaller, without a penumbra and have associated a less intense magnetic field. Nevertheless, higher resolution observations have revealed penumbral structures also in pores (usually for pores whose size is larger than 3.5 Mm), thus making the distinction between the two features looser. The fact that sunspots are formed by the coalescence of pores (Zwaan, 1985) then suggests they are the same phenomenon observed at different scales.

Magnetic knots, or micropores, have typical sizes comparable to the ones of granules (1000 km) and appear darker than the surrounding photosphere. They are abundant in young magnetic active regions, where they contain most of the flux.

The term faculae is used to address the brightening that surrounds sunspots and that usually precedes their appearance. The contrast of these features varies with disk position and wavelength. In white light, for instance, they are almost invisible at disk center, but the contrast increases of 5%-10% toward the limb (see for instance Foukal et al. (2004); Ahern and Chapman (2000a); Lawrence and Chapman (1988)). On the contrary they are visible at disk center when observed in lines. Faculae are also called plages when observed in chromospheric strong Fraunhofer lines. In these lines the contrast is usually higher (30 %) and less dependent (or independent) on disk position (see for instance Ermolli et al. (2007); Walton and Preminger (2003a)). Negative contrast has instead been reported by measurements in the Infrared (Sànchez et al., 2005; Wang et al., 1998). Photometric properties also depend on associated magnetic field intensity (Ortiz et al., 2002) and structure size (Ermolli et al., 2007; Walton and Preminger, 2003a). Low resolution images show faculae as compact bright patches. High resolution observations have revealed they are made up of smaller bright elements, as shown by fig.1.5. Comparisons of images of faculae with contemporary magnetograms have shown that they have associated intense magnetic field. Nevertheless this correspondence is not that clear at higher resolution (better than about 1 arcsec), due most probably to the interaction of the structures with the granular motions. Results shown in this thesis also indicate that radiative processes might be responsible for this discrepancy.

Network and filigree are technically classified as distinct structures from faculae, but they are essentially the same phenomenon, that is the aggregation of smaller magnetic bright elements. Network is located even outside of active regions (see below) and defines the border of supergranular cells. Its photometric properties are similar to the ones described for faculae. Photometric properties of faculae do not change with solar cycle (Ermolli et al., 2007) while controversial results have been obtained for network (Ortiz et al., 2006; Ermolli et al., 2003).

As stated above, in the photosphere the magnetic field is essentially vertical,

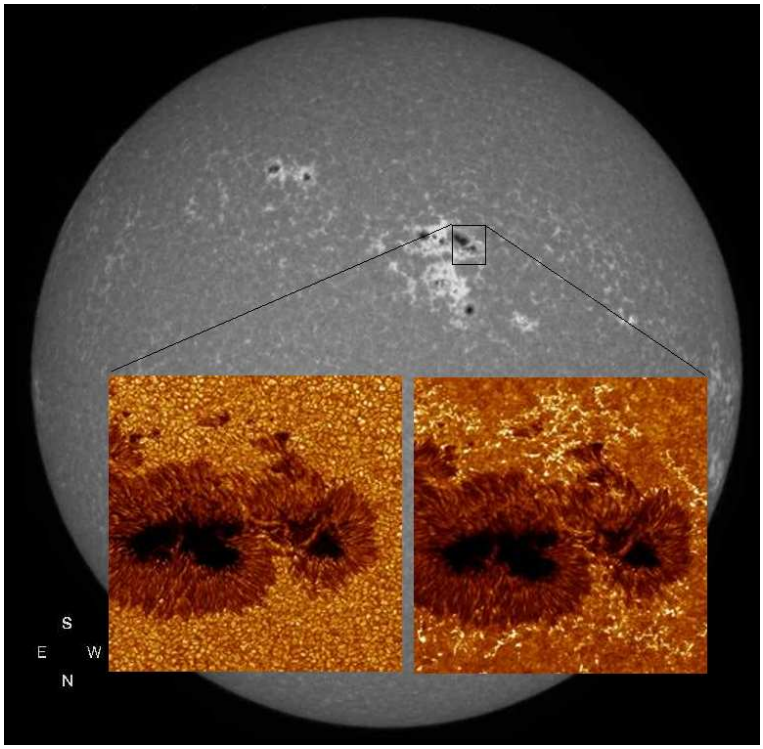

Figure 1.5: Active region (AR 424, 8 August 2003) observed at different resolution and at different spatial scale. The high resolution images show that both faculae and sunspots are made up of smaller substructures. Faculae are in particular made up of smaller brilliant elements. Full disk image: CaII K image from Rome-PSPT archive (2 arcsec/pixel). Inset on the left: 436.4 continuum, from Swedish Solar Telescope (0.04 arcsec/pixel). Inset on the right: CA II H, from Swedish Solar Telescope. The two high resolution images were acquired by G. Scharmer and K. Langhans. The SST is operated on the island of La Palma by the Institute for Solar Physics of the Royal Swedish Academy of Sciences.

with the exception of penumbrae, where strong horizontal components are measured. Pores and faculae field lines fan in the outer parts of the atmosphere, at chromospheric level. High resolution observations have also shown that smaller magnetic elements are inclined of tens of degrees, most probably because of the interaction with granular motions. Photometric properties of spots, faculae and network are investigated through the concept of flux tube, described in detail in chapter 4. Basically the strong magnetic field associated with the structure inhibits convection (as already explained for the sunspots) thus lowering the temperature. The presence of the magnetic field also evacuates the tube by providing forces that resist the collapse even in a region of low gas pressure. The reduction of temperature makes the tube more transparent to radiation so that, for structures whose size is comparable with the mean free path of photon in the atmosphere, channelling of radiation from the hotter surrounding atmosphere through the tube flanks can occur. As a consequence the structure heats up. This effect is expected to be larger at higher levels, where the opacity is

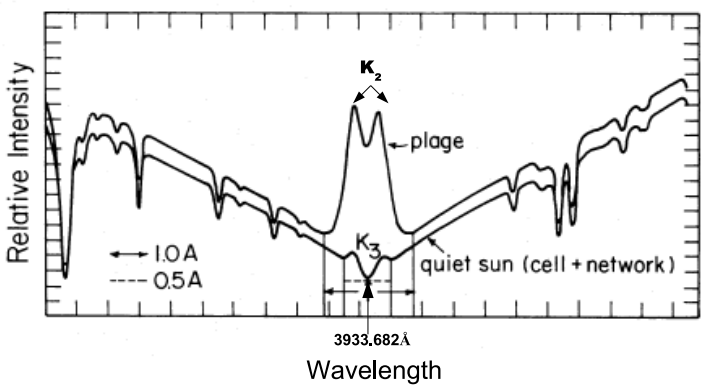

Figure 1.6: Solar calcium K line in quiet and plage regions. Adapted from Skumanich et al. (1984).

lower because of the density and the temperature stratification. Therefore the structure results hotter or cooler respect to the external atmosphere at different heights, thus making faculae to appear darker or brighter than the quiet Sun when observed at different wavelengths. Heating is not observed in sunspots, that are too large for the radiative channelling to be effective. The flux tube model also explains the center to limb variation of the contrast of bright features. When observing the tube at disk center, we are observing radiation that escapes from deeper layers, the tube being evacuated and more transparent than the 'quiet sun'. Depending on the temperature stratification and on the wavelength of observation, the contrast is negative, zero or slightly positive (this last happens if radiative channelling is efficient). When the same structure is observed off disk center, the 'hotter' flank of the tube is visible and consequently the contrast increases.

Brightening at chromospheric layers of magnetic features is not solely ascribed to the channelling heating described above, since other effects like molecular dissociations and atomic transitions take place. Contrast enhancement due to emission are observed for instance in the lines of Hydrogen, both neutral and ionized Helium, the bands of CN. In particular, due to the high opacity of cores of $H\alpha$, $H\beta$, Ca H and Ca K, observations in these lines show faculae with a contrast ten times higher than in the photosphere (fig.1.6).

The studying of photometric properties of facular regions is the subject of this thesis. Both observational and theoretical aspects of this topic are discussed in more detail in following chapters.

1.3.1 Active regions: formation and evolution

The features described above usually appear together on the solar disk, in structures that are named Active Regions, at latitudes between + and -45 deg. Active regions are usually bipolar with the axis that connects the two regions slightly inclined (up to 15 deg) respect to the east-west direction (fig.1.3). They are characterized by a wide range of spatial and temporal scales. Larger active regions usually have associated sunspots and last for months. Smaller active

regions, with less or no sunspots at all, last for some weeks. As a general rule, the lifetime is proportional to the magnetic flux at the maximum development of the region. Regions of the chromosphere and corona that are cospatial with active regions in the photosphere usually host other features and phenomena like prominences, flares and CMEs.

Active regions are preceded by magnetic flux emergence which has associated bright compact faculae. The facular feet move apart and new flux emerges. If it is enough, pores start forming and then sunspots by their merging. After 10 days most of the flux is emerged and the whole hierarchy of structures (faculae, knots, pores and spots) is present. The active region is at the maximum. In the following days sunspots gradually disappear, mainly by fragmentation, and facular features slowly expand and dissolve into *enhanced network*.

It has been proposed that the individual small elements that form larger structures by coalescence, are part of a larger flux tube, that is anchored in the lower part of the convective zone. The large flux tube fragments when emerges on the photosphere, but then the small flux tubes tend to come together. Garcia de La Rosa (1987) proposed for instance that sunspots maintain a memory of the original elements and that when they fragment (during the decaying phase) they split into the original flux tubes. On the contrary, Parker (1992) proposed the coalescence to be generated by the attraction between vortices that surround each magnetic element.

The dispersal of the field is regulated by the turbulent plasma motions, that tend to dissolve the field by diffusion. Active regions dissolve at a rate that is slower than the one would expected for a random walk, but faster compared to supergranular time scales. Flux cancellation also contributes to determine the properties of active regions.

1.4 Solar Variability and Irradiance Variations

The Total Solar Irradiance (TSI here after) or *Solar Constant*, is the energy integrated over the spectrum per second and square meter at the distance of 1 AU from the Sun. In spite of its name, its value varies on different time scales. In particular, it shows cyclic variations in phase with the solar activity cycle. Measurements carried out by bolometers on board of spacecrafts, like ERB/Nimbus-7 (Hickey et al., 1988), ACRIM/SMM (Willson, 1981), SOLSTICE/UARS Rottman et al. (1981), SARR/ATLAS 2 (Crommelynck et al., 1995), VIRGO/SOHO (Frohlich et al., 1995), have revealed that these variations are very small, of about 0.05-0.1% (Frohlich, 2000). Larger variations (about 0.2%) occur at other time scales and are associated with the presence on the solar disk of active regions (Hudson et al., 1982). In particular the presence of sunspots reduces the total irradiance received on Earth, while the presence of plages increases it. At the maximum of the cycle the negative energy contribution associated to spots is overcompensated by the positive energy contribution associated to brilliant regions so that the TSI signal is maximum as well. The physical reasons of the long term variations are not well understood yet. Because of the correlation of TSI variations with magnetic features on the solar disk, some authors completely ascribe the variations to the magnetic cycle (Spruit, 1982; Fligge and Solanki, 2000; Krivova et al., 2003; Wenzler et al., 2005). This view is corroborated by the fact that this correlation is also observed for other

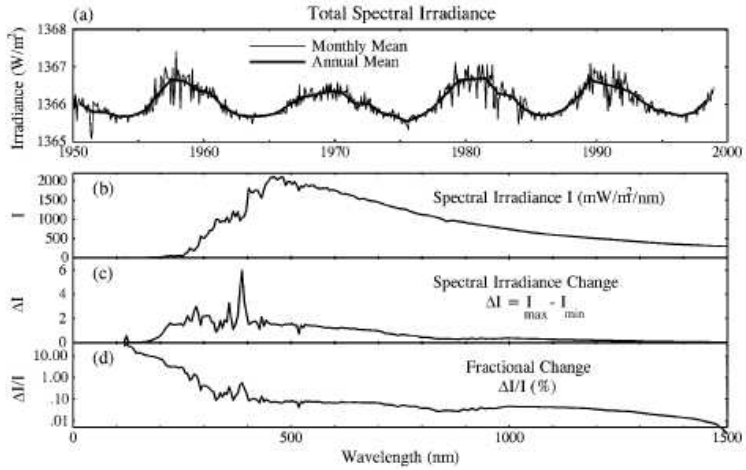

Figure 1.7: a): TSI over the period 1950-1998. b): Spectral Irradiance. c): Spectral Irradiance changes between 1989 (solar maximum) and 1996 (solar minimum). d): Fractional Irradiance change for the period as in panel c). At shorter wavelengths of the spectrum, Irradiance relative variations are higher (up to two orders) respect to longer wavelengths. From Hansen et al. (2002).

Sun-like stars (Radick et al., 1998). Other mechanisms have been suggested, like temporal changes in the latitude dependent surface temperature of the Sun (Kuhn et al., 1988), structural changes in the convection zone (Balmforth et al., 1996) or the internal magnetic field (Li and Sofia, 2001), with possible changes in the solar radius (Sofia, 1998). Nevertheless, none of these latter mechanisms is supported by strong observational evidence (Foukal et al., 2006).

Quite larger variations respect to the ones listed above are measured when the analyses is restricted to spectral bands or particular lines, as shown in fig.1.7. In UV the variations on the solar cycle are of some percents, in EUV of more than 200% and in X-ray spectral region the flux is 500-1000 times larger at maximum than at minimum. The TSI and Spectral Solar Irradiance (SSI in the following) variations have been the subject of numerous studies during the last twenty years because of their possible relevance for Earth climate and global warming. A connection between solar variability and Earth climate is suggested by the striking correlation with solar activity of the temporal variation of several observables, like the temperatures of the oceans (White et al., 2003), the Earth stratosphere (Labitzke, 2004) and troposphere (Coughlin and Tung, 2004). The UV variations are responsible for more than 40% of ozone variations in the last 120 years and appear to be correlated with cloud coverage (e.g. Lean et al., 2005). In particular, the fact that to the small ice age that occurred in Europe in the 18th century corresponded a period of very low solar magnetic activity, has induced many authors to try to reconstruct past temperature global variations using magnetic activity proxies (like sunspot numbers). By contrast, the most recent studies do not reproduce such a clear correlation. Global circulation models, for instance, show that TSI variations are insufficient to explain the global temperature increases registered over the last 120 years and indicate other forcing mechanisms (like greenhouse gases concentration) as

more important (Lean et al., 2005; Foukal et al., 2006). Effects of SSI, especially UV and IR variations, on global weather are instead still under investigation. Such a discrepancy between modelling and observations has to be ascribed to the poor understanding that we have, so far, of the physical mechanisms that connect TSI and SSI variations to global circulation. Moreover, precise measurements of solar energy output are available only since early 1980's and past TSI and SSI variation reconstructions are made under some assumptions. Reconstructions performed with sunspot number only, for instance, estimate facular contribution assuming a constant facular brighting-sunspot dimming ratio over the time. Reconstructions based on other proxies like radio-isotopes (^{10}Be or ^{14}C concentrations) suffer from other uncertainties, since they are not a direct measurement of solar magnetic activity, but are generated by the interaction of energetic cosmic rays (whose transport in the heliosphere is effected by the complexity of the solar magnetic field and strength of the solar wind) with Earth atmosphere molecules.

These topics thus require further investigation. By contrast, reconstructions of present TSI variations are rather accurate, since more than 90% of the measured signal is reproduced. Different models and methods have been proposed, but they are all basically performed by a 'linear combination of two or more quantities which are taken to represent some portion of the TSI variation' (Walton, 2005). These quantities are usually derived from photometric (contrast) and geometric (area and disk position) properties of magnetic features. In particular, sunspot area and location are estimated through analyses of full-disk white light (Lean et al., 1998) or other continua (e.g. Penza et al., 2003) images, or through magnetograms (Krivova et al., 2003). Because of their lower contrast in the photosphere, 'bright regions' contribution is of more difficult estimation. Usually faculae are identified in the chromosphere, where their contrast is more pronounced and less dependent on disk position. CaIIK full-disk images (Penza et al., 2003; Walton and Preminger, 2003b), as well as CaII and MgII emission lines flux (Frohlich and Lean, 2004) are employed for this purpose. The Irradiance is then reconstructed either by making use of the feature contrast measured on the images analyzed (e.g. Walton and Preminger, 2003b) or by the use of semi empirical atmosphere models (Fontenla et al., 1999; Krivova et al., 2003; Penza et al., 2003). Note that while first reconstructions were basically two-component models (bright or dark features), more recent reconstructions take into account of a variety of structures separately (for instance, Fontenla et al. (1999) distinguishes among umbra, penumbra, network, enhanced network, faculae, bright faculae, quiet sun). The contribution of faint bright magnetic features is the source of the largest error in these reconstructions. According to Walton and Preminger (2003b), for instance, the coverage and photometric properties of network remain constant over the solar cycle, so that this component need not to be considered. On the contrary, other authors (e.g. Fontenla et al., 1999; Penza et al., 2003; Fontenla and Harder, 2005; Wenzler et al., 2005) include this component in their models. Similar methods are employed to reconstruct the SSI at different wavelengths. In this case the agreement of models with observation is not always good. Accurate measurements of photometric and geometric properties are thus needed, as well as an improvement of semi empirical models, which are also based on some measurements of magnetic features contrast.

1.5 Aim of the thesis

The aim of this thesis is to improve the understanding of bright magnetic features observed in the photosphere. In particular I investigate the relation between photometric and geometric properties of these features. This is accomplished by the analyses of full disk images and comparison with results obtained by numerical simulations. In particular, in the first part of the thesis I describe measurements of bright features contrast carried out through the Precision Solar Photometric Telescope (PSPT) located in Rome, Italy, at Osservatorio Astronomico di Roma, and the one located in Hawaii, USA, at Mauna Loa Solar Observatory. I investigate the Center to Limb variation of the contrast observed in two continua (409.4 and 607.1 nm) and its variation as a function of structures size. I also investigate geometric properties of these features through the analyses of their fractal dimension. Finally, a comparison of the measured contrast and measured complexity is presented. I will show that these kind of measurements are critically affected by resolution of data employed and that some results recently presented in the literature should be revisited.

In a second part of the thesis I present the theoretical and numerical investigation of the problem. In chapter 4 I introduce the concept of flux tube. The physics and equations that describe the interaction of magnetic field with convective plasma and the assumptions of different models of flux tubes are illustrated. I will also show the necessity of models and numerical techniques for the evaluation of both Convective and Radiative flux, that appear in the energy equation. A brief review of recent 2D and 3D simulations is presented. In the fifth chapter I describe the radiative transfer equation and some analytical solutions presented in the literature. I also describe the Short Characteristic technique, the numerical method on which the software I developed to solve the Radiative Transfer equation is based. Since the energy equation requires the estimate of the Radiative flux, quadrature techniques for the estimate of this quantity are illustrated. The development of a software for both the solution of the Radiative Transfer Equation and the Radiative Flux in a 2D plane parallel atmosphere, have been fundamental steps in the development of this thesis. The Short characteristic, in particular, allows to estimate the intensity field at the desired optical depth and for a given view angle. It is thus fundamental for the investigation of photometric properties of simulated structures. For this reason, great care was dedicated to the investigation of several numerical aspects that might introduce spurious effects. The results of this investigation, as well as the problems related to quadrature techniques, are illustrated in chapter 6. In chapter 7 I describe the models developed, based on the magnetic flux tube concept, and in chapter 8 I show the results obtained. In particular the variations of contrast caused by the presence of the magnetic structures in the photosphere are investigated. Conclusions and future works are drawn in chapter 9.

Chapter 2

Fractal dimension estimation of facular regions

In this chapter I show the results obtained by a study of geometric properties of magnetic features identified in the chromosphere on CaIIK PSPT images. At this aim, the fractal dimension variations with features size and with solar activity was investigated. I show that variations with size are critically affected by spurious effects like pixelization and that variations with time are not clearly correlated with solar cycle. Part of the work here presented has been developed in collaboration with Solar Group at Osservatorio Astronomico di Roma and is also described in Criscuoli et al. (2007).

2.1 Fractals: introduction

The term fractal, coined in 1975 by the mathematician Benoît Mandelbrot, comes from the Latin *fractus* that means "broken" or "fractured." The author addressed with this term some particular curves and geometrical shapes, like the Peano curve, the Von Koch snowflake or the Sierpinski carpet, that do not fit the patterns of Euclidean geometry and were thus regarded at that time as 'monsters'. Mandelbrot developed a new kind of geometry in order to interpret these 'anomalies' and showed, in *The fractal Geometry of Nature* (Mandelbrot, 1982), that they are instead the 'normality' since many shapes and phenomena (from the structure of a cauliflower to the stock prices temporal variations) can be described by this new formalism. Formally he defined fractals as those objects whose *Hausdorff-Besicovitch* dimension exceeds the topological dimension (Mandelbrot, 1975b). I will expand later on this point, when talking about the fractal dimension. Here is important to notice that this definition is related to the concept of *self-similarity*. An object is self-similar if, when observed at different scales, it has similar appearance. A cauliflower or the decimal metric system are common life examples. In fig.2.1 is shown the von Koch curve, that is a fractal curve constructed according to some particular mathematical rules (Peitgen and Jurgen, 1992). If we take a portion of the curve and enlarge it, the new portion will appear as the original one, in the same way in which if we split a cauliflower in smaller and smaller parts, the new pieces will resemble the whole one. According to self-similarity properties, fractals are classified in the

following categories:

- *Exact self-similarity*: this is the strongest type of self-similarity; the fractal appears identical at different scales. Fractals defined by iterated function systems, like the vonKoch curve, the Sierpinsky gasket or the Menger sponge, often display exact self-similarity.

- *Quasi self-similarity*: the fractal appears approximately (but not exactly) identical at different scales. Quasi-self-similar fractals contain small copies of the entire fractal in distorted and degenerate forms. Fractals defined by recurrence relations, like the Mandelbrot or the Julia sets, usually belong to this category.

- *Statistical self-similarity*: the fractal has numerical or statistical measures which are preserved across scales (an obvious measure might be the fractal dimension, discussed further). Random fractals, like 1/f noise, fractal landscapes Brownian trees and Diffusion Limited Aggregations, are good examples of fractals belonging to this category.

In fig.2.1 are shown fractals belonging to these categories. Some fractals can also present self-similar properties up to a certain scale. This is referred to as *Self similarity at a point*. In general, 'real life' fractals belong to this category. A cauliflower, for instance, can't be split infinitely and has instead a minimum size beyond which its approximate self-similarity is broken, in the same way in which, while the metric system is self-similar at each scale, a ruler cannot be.

Self similarity is not enough to describe fractal properties. According to previous definitions, for instance, a line would a be fractal, since smaller and smaller segments always resemble the original one. But a line is not a fractal, since, as mentioned before, its Hausdorff dimension equals the topological dimension. Mandelbrot expands on this point in his famous article *How long is the coast of Britain?* (Mandelbrot, 1967). As was known by geographers, the length of coast-lines or nation borders L are related to the map resolution G by the formula:

$$L(G) = F \cdot G^{1-D} \tag{2.1}$$

where F is a positive constant and D is also a constant at least equal to unity. The relation means that, when measured with different rulers, Britain's coast results of different lengths, the smaller the ruler the longer the coast. This relation is illustrated in fig.2.2. Here the coast and the ruler lengths are plotted in logarithmic scales and are fitted by a straight line whose slope is ≈ -0.26. From relation 2.1 D ≈ 1.26. The same measurement for a circle or a line would have lead to $D = 1$. Topologically speaking, this implies that coast lines, as well as other types of curves, are not "rectifiable" and the higher is D the more 'fragmented' the curve appears.
Mandelbrot referred to D as *similarity dimension* and generalized the discussion to n-dimension structures. He introduced the term 'fractal' in a subsequent work. For fractal objects the similarity dimension, or fractal dimension, is greater than the topological dimension (for instance 1 for a line) and lower than the topological dimension +1.
Such definition of fractal dimension is operative and very used in the literature.

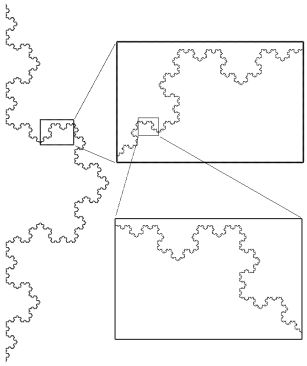

Von Koch curve. An enlargement of a portion of the curve has the same appearance as the original one. By construction, the self-similarity holds for infinite enlargements, so that this curve has *Exact self-similarity* properties.

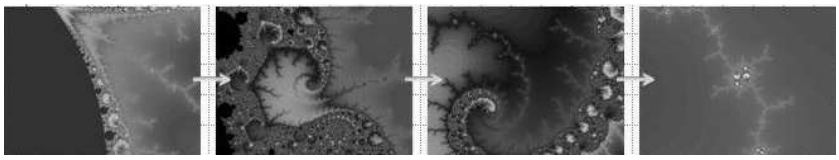

Mandelbrot set example. When zooming the picture (from left-to right) images appear approximately the same, but are not identical. This is thus an example of *Quasi self-similarity*.

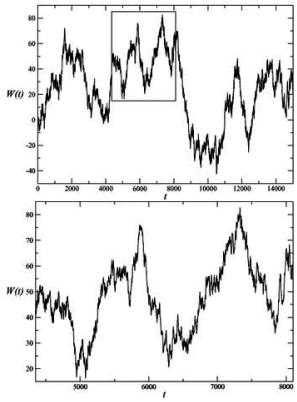

Fractional brownian motion. The curve in the bottom is a blow-up of a the section delimited by a rectangle in the curve on the top. The two curves look the same statistically and are thus an example of *Statistical self-similarity*. From Vasconcelos (2004).

Figure 2.1: Fractals are classified according to their self-similarity properties. Here examples from the three categories described in the text are shown.

Nevertheless there exist many others, as well as different techniques or *estimators*, to evaluate it. The *Box Counting dimension* and the already mentioned *Hausdorff-Besicovitch dimension* are the most common. To define the first one, let us consider a closed set X, that we cover with a minimum number N(r) of square boxes of size r. As we reduce the size r the minimum number of boxes N(r) scales as $1/r^{d_B}$. d_B is by definition the Box-Counting dimension. More formally

$$d_B := -\lim_{r\to 0} \frac{\log N(r)}{\log r}. \tag{2.2}$$

For fractals d_B, if the limit exists, is greater than the topological dimension and in general is not a natural number. For instance the von Koch curve has dimension $d_H = \frac{2\ln 2}{\ln 3} \approx 1.26$, while its topological dimension is 1. Box Counting definition is of very simple implementation and is one of the most employed to evaluate structures complexity. If the set is covered by small sets of varying sizes, instead of boxes of fixed size, than the limit gives the Hausdorff-Besicovitch dimension. It can be proved that for self similar sets the self similar, box counting and Hausdorff-Besicovitch dimensions coincide.

The estimator adopted in this thesis, thoroughly explained in 2.4, is the perimeter-area relation, that also allows a measurement of the similarity dimension.

2.2 Fractal dimension estimation of solar magnetic features

In 1975 Mandelbrot (1975a) pointed out that turbulent motions generated patterns have a fractal nature. On the Sun the generation of magnetic structures, as well as their evolution and decay, is determined by the two main processes through which magnetic field interacts with convective plasma: concentration and fragmentation as noticed by (e.g. Abramenko and Longcope, 2005). On one hand, magnetic structures are generated by concentration of field lines induced by advection of magnetic field by turbulent diffusion. On the other hand, turbulent motions cause cancellations (of different polarities structures)

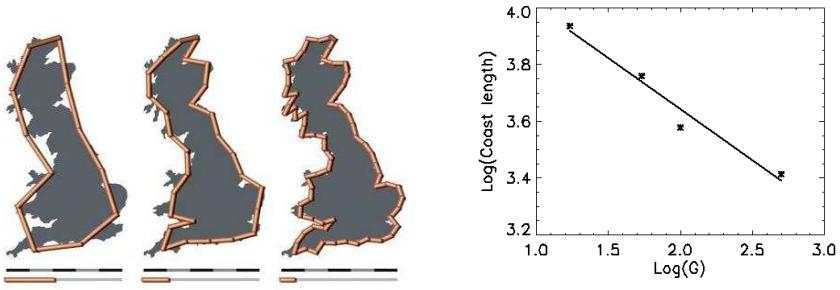

Figure 2.2: When measured with smaller and smaller size rulers, the length of coast of Britain increases. Scatter plots in log scale of coast length and ruler precision, are fitted by a straight line whose slope is ≈ -0.26. The fractal dimension is thus $D \approx 1.26$.

Study	Data[a]	Method	FD[b]
Roudier & Muller (1987)	WL granules	D_{PA}	1.25 for $d < 1''.37$
Hirzberger et al. (1997)	WL granules	D_{PA}	1.30 for $d < 1''.39$
	WL granular cells	D_{PA}	1.16
Bovelet & Wiehr (2001)	Wl granules	D_{PA}	1.09
Janssen et al. (2003)	B small scale	D_{PA}	1.41 ± 0.05, $d < 1''.8$
	S magnetoconvection	D_{PA}	1.38 ± 0.07, $d < 1''.8$
Tarbell et al. (1990)	B plage	D_{LA}	1.45–1.60
Lawrence (1991)	B active region	D_{LA}	1.56 ± 0.08
Schrijver et al. (1992)	S percolation theory	D_{LA}	1.56
Lawrence & Schrijver (1993)	B active region	D_{LA}	1.56 ± 0.08
Balke et al. (1993)	B plage	D_{LA}	1.54 ± 0.05, $l < 3''$
Meunier (1999)	B active regions	D_{PA}	1.48–1.68
		D_{LA}	1.78–1.94
Meunier (2004)	B active regions	D_{PA}	1.35–1.70
Gallagher et al. (1998)	EUV quiet-Sun	D_{BC}	1.30–1.70
Georgoulis et al. (2002)	Hα Ellerman bombs	D_{BC}	1.4
Fragos et al. (2004)	S cell automation	D_{BC}	1.5 ± 0.1
Vlahos et al. (2002)	S cell automation	D_{BC}	1.42 ± 0.12
Lawrence et al. (1993)	B	D_{BC}	Multifractal
Cadavid et al. (1994)	B	D_{BC}	Multifractal
Lawrence et al. (1996)	B	D_{BC}	Multifractal

[a] WL: White light; B: magnetic field; S: simulation; EUV: extreme ultraviolet.
[b] d: Diameter; l: length.

Figure 2.3: Summary of papers concerning fractal analyses of solar magnetic features. Studies have been carried out on different kind of data and with different estimators (PA:Perimeter-Area; BC: Box Counting; LA: minimum external box size-Area), so that fractal dimension estimates (right column) are often discrepant. From McAteer et al. (2005).

and fragmentation. These competitive processes generate magnetic structures of several sizes that present self similar (in the statistical meaning) properties (Stenflo and Holzreuter, 2002). Fractal analyses of magnetic structures is thus a powerful tool to study the interaction of magnetic field with convective surrounding plasma. Investigations carried out during the last 15 years, generally on solar vector magnetograms, revealed the complexity and self-similar properties of active regions, but results obtained are widely different depending on the resolution of the observation and on the technique used for the investigation. The lack of a unique definition of fractal dimension makes the comparison of results also very confusing.

Lawrence (1991) studied the "random walk" of 170 magnetic elements detected on 220 BBSO magnetograms of an active region. He showed that the motion occurs on a 'fractal' rather than a 2D geometry and that in the bulk of the region both fractal dimension D and diffusion coefficient K are lower (respectively 1.3 and 150 km^2) respect to the surrounding area (for which they found D=1.7 and K=310 km^2).

Balke et al. (1993) analyzed a few high resolution magnetograms (0.3 arcsec). They determined the fractal dimension of small structures (areas between 4 and 20 pixels only) by using the relation between the area and the linear size of the structures. They did not detect any systematic variation of the fractal dimension with the magnetic threshold between 200 and 900 G and obtained and average fractal dimension of 1.54. These results were interpreted in terms of percolation theory, according to which if the concentration of magnetic field is below a certain threshold, the fractal dimension of the observed clusters of

elements is 1.56 (Schrijver et al., 1992; Lawrence and Schrijver, 1993).

Nesmes-Ribes et al. (1996) estimated the fractal dimension of facular regions determined from Meudon spectroheliograms (with a pixel size of 1.8 arcsec/pixel) obtained in the K_{1v}. Applying three different fractal dimension estimators to structures of sizes larger than the supergranular scales, they obtained the values 1.60, 1.64 and 1.72. For smaller size features they measured a smaller dimension, with a minimum of 1.2. Their results were not in good agreement with the ones obtained by Balke et al. (1993). However, as I will explain in the following paragraphs, different samples and spatial resolutions can explain these differences.

The analysis of a very large dataset, based on ≈ 8000 full-disk and ≈ 800 high resolution megnetograms obtained from April 1996 to June 2002 with SOHO-MDI instrument, was carried out by Meunier (2004). The geometry of facular structures of different spatial scales in relation to magnetic field intensity, flare activity, and solar cycle phase, was investigated in this work. The author found that while a region complexity generally increases with magnetic field intensity, there is no clear correlation with flare activity or the solar cycle. Moreover, the measured fractal dimension was found to increase with structure size (in agreement with Meunier (1999) and Nesmes-Ribes et al. (1996)), showing a peculiar change in behaviour near structures of area 550-800 Mm^2.

The correlation between active regions fractal dimension and flare activity was investigated by several other authors. McAteer et al. (2005), by a comparison analysis of MDI full disk magnetograms and GOES X-ray data, found a correlation between active regions fractal dimension and flare number and intensity production. Gergoulis (2005) and Abramenko (2005) investigated the correlation of magnetic active region complexity and associated flare activity via multifractal analyses of few MDI high resolution magnetograms. Particularly, Gergoulis (2005) employed several complexity definitions and techniques (fractals and multifractals) in order to determine the most suitable to investigate the correlation. He suggested multifractal analyses as the most suitable, and, as well as reported by Abramenko (2005), found an increase of multifractality of active regions during pre-flare phases. Because of the small number of active regions analyzed, these topics deserve more investigation.

Self similarity was also observed in structures generated by Magneto Hydro Dynamic numerical simulations. Jansen et al. (2003) compared by means of fractal analyses the shapes of observed small-scale magnetic structures on very high resolution observation of the Sun with those of magnetic regions from simulations. Both real and simulated data gave a fractal dimension of about 1.4. The authors also reported an increase of fractal dimension with the structure size, similar to the one observed by Nesmes-Ribes et al. (1996), Meunier (1999) and Meunier (2004). Bushby and Houghton (2005) used fractal dimension estimate of simulated structures to determine the magnetic flux that best reproduced results of Balke et al. (1993). They also observed an increase of fractal dimension with object size.

Table 2.3 summarizes some of the main results obtained in the literature. Investigations have been carried out on several kind of data sets, for different solar features and with different techniques. The resulting discrepancies are not surprising. Other authors already pointed out that several spurious effects can influence fractal dimension estimations. Both image resolution and projection affect the correlation, mass function and perimeter-area estimators in studies

of interstellar molecular clouds (Sànchez et al. (2005), Vogelaar and Wakker (1994)), and resolution and thresholding effects are important in fractal dimension estimation of flow patterns in field soil by box-counting methods (Baveye et al. (1998)). Lawrence et al. (1996) has studied similar effects in multifractal and fractal measures (box-counting, cluster dimension, threshold set) of solar magnetic active regions.

In order to investigate the complexity of magnetic features using observations representative of chromospheric heights, I have analyzed the fractal dimension of bright features identified in full-disk CaIIK images acquired by the Precision Solar Photometric Telescopes (PSPTs) at Osservatorio Astronomico di Roma (OAR) and Mauna Loa Solar Observatory (MLSO). The data analyzed span the last 6 years and thus allow considerations of variation with the solar cycle. Among the ones analyzed in literature, because of the image resolution and the long time span, the dataset of Meunier (2004, 1999) and Nesmes-Ribes et al. (1996) are the most similar to the one I analyzed. In order to compare the results with the ones presented by these authors, I thus employed the same fractal dimension estimator, that is the perimeter-area relation. In order to validate and discuss the results I have also investigate the sensitivity of the deduced fractal dimension to the pixelization, the resolution of the image and the perimeter measure algorithm employed. In particular, I have determined how these influence the geometric properties deduced for objects of different sizes, and try to answer the question whether the perimeter-area relation can be used to study the fractal and multifractal nature of solar magnetic features as a function of solar cycle. The analyses, the results and their interpretations are shown in following paragraphs and in Criscuoli et al. (2007).

2.3 Observations, processing and definitions

2.3.1 PSPT data

The bulk of the data I analyzed is from the archive of daily full-disk observations carried out with the PSPT at Osservatorio Astronomico di Roma (OAR here after). This was supplemented with data from the PSPT at Mauna Loa Solar Observatory (MLSO) for consistency and resolution tests. The images were taken with "twin" telescopes at the two sites, through interference filters centered at three wavelength bands (CaIIK line center 393.4nm, fwhm 0.27nm, blue continuum 409.4nm, fwhm 0.27nm, and red continuum 607.1nm, fwhm 0.46nm for OAR), with a 2048 $\times$ 2048 16 bit/pixel CCD camera, yielding a spatial scale of $\sim$ 1arcsec per pixel. Images from OAR are binned to half resolution, yielding a final spatial scale of $\sim$ 2arcsec per pixel. Images from the two telescopes were independently dark and flat-field corrected and had the mean center-to-limb variation removed. These pre-processing procedures are slightly different for the two sets of images. Details are given in Ermolli et al. (2003) and Meisner and Rast (2002). The images of anyone triplet were resized and aligned to allow pixel by pixel comparison between filters.

For this study I selected OAR daily image triplets (CaIIK, blue continuum and red continuum), obtained on 238 different observing days during the summers (July to September) of 2000 through 2005. I chose images acquired during

the summer months because these are generally of higher quality. The largest sample of the images was obtained by co-adding frames acquired with very short exposure time (usually less than 50 ms). This procedure allows to increase the photometric accuracy up to 0.5% per pixel. In order to compare results obtained with the two instruments, I also selected 44 triplets (the best in the CaIIK band of the day, according to quality criteria described in 2.3.2.) from the MLSO and OAR archive taken during the summer of 2005. For comparison, MLSO images were rescaled to match OAR spatial scale images (~ 2 arcsec per pixel).

Finally I was able to quantify the effects of atmospheric seeing by using MLSO images acquired at 10 minutes intervals throughout the day, weather permitting. According to quality criteria explained in next paragraph, I selected two groups of 27 high and low quality images (one for each day) throughout the year 2005 (February to October). For this analysis, the full resolution (~ 1 arcsec per pixel) MLSO data were employed.

2.3.2 Data quality

The geometric properties of solar features extracted from the images are likely sensitive to the spatial resolution of the image being analyzed. This in turn depends on atmospheric and instrumental operation conditions during the observation. To estimate the inherent quality of any given data image I measured (in pixel units) the width of a Gaussian fit to the limb profile. Small values of the solar limb width indicate lower instrumental or atmospheric smearing and thus better quality images. The limb width distributions of our datasets are asymmetrically shaped with a long tail toward higher values, so that the mean is not the most probable value. The mean limb profile width of the OAR CaIIK (binned to half resolution) images analyzed is 2.5 ± 4.0 with a median value of 1.42. That of the MLSO CaIIK images from the summer 2005 is 4.1 ± 0.8 for the mean and 3.9 for the median (measured on full resolution images), while that for the OAR images acquired in the same period are 4.0 ± 6.5 and 2.2 respectively (measured on binned half resolution images). Considering the different pixel scale of MLSO and OAR images, the two 2005 dataset quality are peaked near the same value (about 4 arcsec), but OAR dataset contains a higher number of low quality images.

The MLSO limb width distribution for year 2005 has its maximum at a value of 3.7 pixels (measure on full resolution images). To study dependence on seeing condition, images from each day were grouped in two sets: those whose limb width lied below 0.1σ from the peak, and those whose limb width lied between 0.8σ and 3.0σ above the peak. From each group, the best and the worst image were selected, so that I had, for each observing day, two different quality images. This restricted the analyses to 27 observing days. The mean limb width obtained are 3.5 ± 0.2 and 4.9 ± 0.3 for *high* and *low* quality images respectively.

2.3.3 Feature identification

Bright features were identified in the CaIIK images using two methods based on a combination of pixel intensity and connectivity. As explained in previous chapter, because of the link between CaIIK brightness and magnetic flux intensity, these features are assumed to represent small magnetic structures, but this

assumption plays no role in their identification.

The first identification method is analogous to that used by Meunier (2004), taking into account intensity alone and based on fixed thresholding values. While Meunier (2004) employed thresholding on magnetograms, I select pixels whose intensity contrast [1] in the CaIIK images exceeds a given value. Similarly, sunspots and pores were identified in the blue continuum images by selecting those pixels whose intensity was below a given threshold. These thresholds were set to exclude network while keeping active regions, including umbral and penumbral pixels.

The second identification method employed takes into account both pixel intensity and connectivity. It is described in chapter 3 and I will refer to it as *Ktr*.

For the subsequent fractal analysis, I produced binary images from each triplet processed, in each of which pixels satisfying the identification criterion above have a value of one, with all other pixels set to zero. To reduce distortion due to projection effects, analysis was restricted to structures near disk center, $\mu > 0.8$, where μ is the cosine of the heliocentric position angle. Additionally, isolated bright points were removed from consideration by discarding all structures of area less than 10 pixel^2.

2.3.4 Perimeter and area evaluation

There are several ways to define and evaluate the perimeters and areas of features in a binary image (Gonzalez and Woods, 2002), and thus characterize the independent structures. The goal is to define, detect, and count the pixels which constitute the feature edges. For this study I considered three methods, and evaluate the errors associated with them.

In the first method, I defined border pixels by row and column, identifying for each the pixel for which the binary value changes. The perimeter was then evaluated summing the external sides of the border pixels, so that for example an object made up of 1 pixel has an area of 1 and a perimeter of 4, while one made up of two pixels has an area of 2 and a perimeter of 6 or 8 depending on the pixels' relative positions.

In the second method, I applied the Roberts operator (Turner et al., 1998) to the image in order to identify border pixels and defined the perimeter as the sum of the all pixels whose value is not zero. Using this method, an object of 1 pixel has a perimeter of 4 and an object of two pixels has always perimeter 6, independent of the relative positions.

In the third method, pixels are identified as border pixels if they are connected from between 1 and 7 of the neighbouring 8 contiguous pixels. The perimeter is the sum of the selected pixels, so that an object 1 pixel in area has a perimeter of 1 and an object of area 2 has a perimeter of 2, independent of the pixels relative positions.

I refer to these three methods as *Sides*, *Roberts* and *8-cont* respectively. Nevertheless, only the results obtained using the first method are included in the body of this thesis. The reasons for this are discussed in 2.7.1 and in the Appendix to this chapter.

[1] $I_c = \frac{I - I_0}{I_0}$, where I is the intensity measured at each pixel and I_0 is that representative of the quiet sun and obtained by a fit to its center to limb intensity variation.

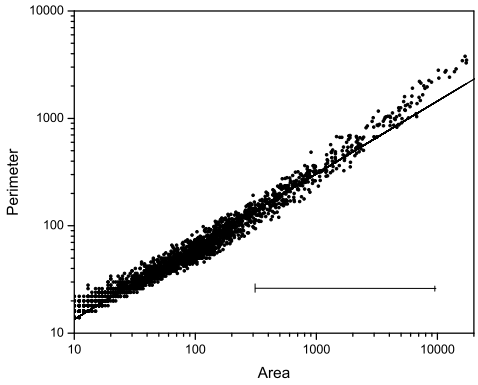

Figure 2.4: Perimeter (in units of pixel) and Area (in units of pixels square) in logarithmic scale of detected structures on OAR PSPT data taken during summer 2002. Continuous line is the fit to the whole set of data ($D = 1.354 \pm 0.005$). Points at area greater than about 1000 pixels square are better approximated by a higher slope line. Horizontal line is the area window width over which $d1$ is estimated.

2.4 Fractal Dimension Estimator: The Perimeter Area relation

Several definitions of the fractal dimension of two-dimensional structures and corresponding techniques for its estimation exist (Turner et al. (1998); section 2.1 this thesis).

If a structure is self-similar, its perimeter L and area A display a power-law relation:

$$L \propto A^{d/2} \ , \tag{2.3}$$

where d is the fractal dimension. With this definition, $1 \leq d \leq 2$ and d=*1* for non-fractal structures.

I estimated d using two methods. In the first I performed a simple linear fit to the logarithm of the perimeters and areas measured for structures of different sizes; I indicate the fractal dimension so obtained as D. In order to investigate the size dependence of the fractal dimension estimated in this way, the fit is performed over the entire data set or, when specified, imposing a minimum threshold area. In the second I adopted a method first proposed by Nesmes-Ribes et al. (1996) and later employed by Meunier (1999, 2004), in which perimeter and area values are averaged over bins in area, each of width $\Delta \log A = 0.05$ and the fitting is done on these averages for a series of overlapping windows of constant width $\Delta \log A = 1.5$, producing a measure of d which is a function of A. I indicate the fractal dimension estimated in this way as *d1*. For both methods linear fits were performed by a chi square minimization, and the associated error is the standard deviation of the fit (Press et al., 1994). The relation between the two estimators and their meaning is illustrated in fig. 2.4, that shows the perimeter-area relation for structures selected in OAR-PSPT images. The straight line is a linear fit to the points. It is evident that points

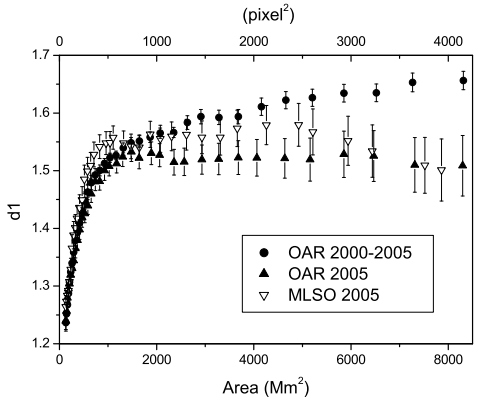

Figure 2.5: Fractal dimension $d1$ versus area of bright features identified on calcium images ($\sim 2arcsec/pixel$). Full circles: summers 2000-2005 OAR-PSPT. Open triangles: summer 2005 MLSO-PSPT. Full triangles: summer 2005 OAR-PSPT. $d1$ increases fast with object size at area smaller than 2000 Mm^2. For larger areas, a plateau is observed for summer 2005 OAR and MLOA data, and a slow rise on the 2000-2005 OAR dataset.

$OAR2000-2005$	$OAR2005$	$MLSO2005$
1.337 ± 0.002	1.307 ± 0.003	1.307 ± 0.004
1.64 ± 0.02	1.53 ± 0.07	1.54 ± 0.09

Table 2.1: Fractal dimension D estimated for features selected on OAR-PSPT and MLSO-PSPT CAIIK images. First row: fractal dimension D considering the entire area range structures. Second row: fractal dimension D considering only structures larger than 2000 Mm^2.

do not lay on a single line, but rather on a curve. One is thus tempted to measure the tangent to the curve as a 'local' measure of the fractal dimension. This is what the measure in *d1* employed in the text does. The measured *d1*, as well as the area at which it becomes constant, are functions of the window size.

When using this estimator, is important to keep in mind that any fractal estimate requires the autosimilarity to be valid on some orders of magnitude (Baveye et al., 1998) (the area range $\Delta \log$ A =1.5 adopted for *d1* in this and in other works is therefore in principle too small). If this requirement is not satisfied, as I will show in the following for solar faculae, structures cannot be classified as fractals and the perimeter area relation should be regarded as an indicator of the geometric properties but not of self similarity.

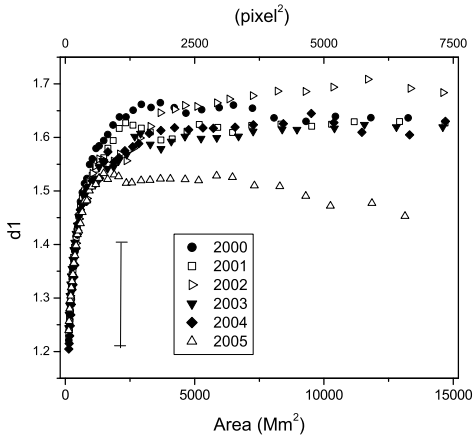

Figure 2.6: Temporal variation of the fractal dimension $d1$ versus area for features identified on OAR-PSPT calcium images. The bar on the left represents the largest error bar, obtained for the largest areas for year 2004. At area smaller than about 1000 Mm^2 all the curves overlap, while differences (not clearly correlated with solar cycle) are observed at the largest areas.

2.5 Results

2.5.1 Fractal dimension and feature size

Figure 2.5 shows the variation in fractal dimension *d1* of the identified chromospheric features as a function of their size, as derived from the OAR and MLSO PSPT CaIIK rebinned data using the second identification method (Ktr) described in 2.3.3. The results obtained from three data sets are shown: the full 2000-2005 OAR period, the single 2005 year OAR data, and the single year 2005 MLSO data. For all data sets, $d1$ increases with object size, increasing faster for structures of smallest areas and becoming almost constant at the largest scales. The three curves overlap for structures of area less than about 1000 Mm^2, corresponding to about 500 pixel^2. For objects of size greater than about 1000-1500 Mm^2 the 2005 OAR and MLSO data both show a plateau in the measured fractal dimension. Somewhat surprisingly, this plateau is less evident when analyzing structures from the full 2000-2005 OAR data set. The fractal dimension deduced over this longer period continues to slowly increase even at the largest scales.

Table 2.1 shows the value of D obtained from the different data sets when a single fit to the perimeter area relation made over structures of all sizes (top row) or only those of area greater than 2000 Mm^2 (bottom row), the threshold being suggested by trends observed in fig.2.5. In agreement with *d1* estimates, the fractal dimension D is reduced by the inclusion of the small and apparently less complex regions.

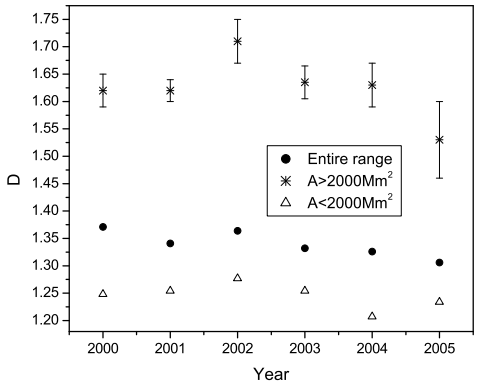

Figure 2.7: Temporal variation of the fractal dimension D versus area for selected OAR-PSPT calcium images and for different area range. Error bars in the case of fits performed on the whole dataset (circles) or at smallest objects (triangles) are smaller then the symbol size. Results obtained for the largest area are in good agreement with results obtained by $d1$ estimator (fig.2.6).

2.5.2 Temporal variation

Figure 2.6 shows the variation of fractal dimension *d1* with both feature size and time for the six year OAR period analyzed. For sake of clarity, only the largest error bar (belonging to the largest area objects of year 2004) is shown on the plot. The fluctuations in the other values shown are generally smaller than the largest differences observed among the years. I find that the variation in fractal dimension does not show a clear correlation with solar cycle over the period analyzed (the descending phase of Solar Cycle 23). The values show large year to year variations for large structures, with the maximum and the minimum values measured for 2002 and 2005 respectively. The reliability of the 2005 values are supported by the nearly identical results obtained from the independent OAR and MLSO measurements (Tab. 2.1, Fig.2.5). The other years show a plateau value at about 1.6, although in the area range 2500-7000 Mm^2 year 2000 has a mean value of about 1.65. Note that if we restrict the analyses to the area range 2500-7000 Mm^2 then a weak trend with the last cycle, that showed a double activity peak in 2000 and 2002, is observed. Figure 2.7 shows the temporal variation in D for three different area ranges. In this measure a small trend with solar cycle is observed when the entire structure size range is included in the fit. When fit is performed on the largest objects, the highest fractal dimension is measured for year 2002, and the lowest for year 2005, and similar values are measured for the other years, in agreement with results obtained for $d1$. For smaller magnetic regions, again the maximum is observed in 2002, but a minimum is found for year 2004 data.

2.6 Comparison to previous results

2.6.1 Fractal dimension and structure size

Since the work of Roudier and Muller (1987) the fractal geometry of structures found in images of the outer layers of the solar atmosphere has been investigated by a number of authors. Both magnetic features, at moderate to high spatial resolution, and non-magnetic features associated with plasma motions have been studied. In order to ensure a meaningful comparison, I will only compare the results I have found here to previously published results for active regions investigated by the perimeter-area estimator.

In agreement with previous results, I find a fractal dimension that increases with feature size, from a minimum value of about 1.2, to an approximately constant value of $1.5-1.7$ for structure areas greater than $\sim 1000-2000$ Mm^2. This range in $d1$ agrees well with measurements by Nesmes-Ribes et al. (1996), but not with those reported by Meunier (1999, 2004), who found generally a higher minimum value (around 1.4). From the analysis of both real and simulated data I know that the minimum value measured is somewhat dependent on both the identification method employed and the image resolution. The higher minimum value reported by Meunier (1999, 2004) may be a consequence of image resolution (see 2.7.2), as the full-disk MDI data she analyzed are unaffected by atmospheric degradation. The plateau in $d1$ beyond object sizes of 2000 Mm^2 also agrees with previous results, but this time more so with those of Meunier (2004) and less so with Nesmes-Ribes et al. (1996), who found the plateau to occur already for structures of size > 300 square-pixels (corresponding to about 500 Mm^2). Tests with both real and simulated data suggest that this difference may lie in the area range over which the fit for $d1$ at each point was made, a value not quoted by Nesmes-Ribes et al. (1996), but taken in our study to be $\Delta \log A = 1.5$ in agreement with that used by Meunier (2004).

An increase of fractal dimension with magnetic feature size was also observed by Jansen et al. (2003). They studied fractal dimension of magnetic features analyzing high resolution (approximately 0.4 arcsec) magnetograms acquired with the Vacuum Tower Telescope and synthetic images obtained through MHD numerical simulations. They found $D = 1.38 \pm 0.07$ on synthetic data, and $D = 1.21 \pm 0.05$ on real data, corrected to $D = 1.41 \pm 0.05$ when taking in to account resolution effects. Note that my estimates, $D \cong 1.3$ (fit on entire area range), are in between these last two values. Their scatter plots showed a deviation from these fits at log(A/pixel^2)>2.5 (corresponding to 315 pixel^2) for both real and simulated data, despite the differing pixel scale of the two data sets ($\sim$ 72 km for real data and $\sim$ 21 km for simulated ones), suggesting that this change is not related to the physical scale of the object but rather to the image scale. Fits to objects whose areas was larger then this threshold gave $D = 1.47$ (value not corrected for resolution effects) and $D = 1.9$ for real and simulated objects respectively.

2.6.2 Temporal variation

Meunier (2004) performed a time-dependent analysis, evaluating the fractal dimension *d1* variation with object size for three different periods: minimum,

ascending and maximum phase of the current solar cycle. A correlation with solar activity for structures of size ~ 1000 Mm^2 was reported, with the highest fractal dimension being measured during the cycle maximum period. Larger structures (2000-7000 Mm^2) were found to have a higher fractal dimension during the ascending phase of the cycle rather than at cycle maximum. Variations were of the order of few per cent. The same trends were found for estimates of D, but with larger amplitude variations. If I restrict my analyses to the area range 2000-7000 Mm^2, I instead find a little correlation of *d1* with solar cycle, the highest values being measured for years 2000 and 2002, and the smallest for 2005. The amplitude of the variations in my data is slightly higher, the largest yearly variation measured over the six year period being of order 10%. The trend at moderate sizes (1000 Mm^2) is not observed.

2.7 Discussion of fractal dimension estimation

Assessment of the fractal dimension of features in digitalized images requires a series of operations:

- Image segmentation to isolate regions of interest,
- Edge identification in the resulting bi-level images,
- Perimeter and area measurement of structures so identified,
- Fractal dimension evaluation using these measures.

Each of these steps introduces a certain degree of arbitrariness which influences the result. Moreover, the results are sensitive to intrinsic differences between image sets, unrelated to the geometric properties of the features they capture. In this section I focus on the effects of edge identification technique, pixelization and resolution by the analyses of synthetic images of objects whose fractality is known: non-fractal objects, the von Koch curve, and objects obtained by fractional Brownian motion. Seeing effects are further investigated by the analyses of MLSO PSPT data. For clarity's sake, in the following I present the main results obtained by the tests, while a further description is given in the appendix.

2.7.1 Perimeter definition and pixelization effects

To study the influence of the perimeter finding algorithm, I examined the empirical dimension of non-fractal objects as a function of their size. The three different perimeter-area identification techniques (described in 2.3.4) were applied to three geometric shapes (squares, right triangles, and circles). In the absence of error, all three methods should yield a value of one since the objects are non-fractal, but because of image pixelization, fractal dimensions greater or lower than one were measured.

I found that errors in fractal dimension evaluation of regular structure are greatest for objects of small size but persist to surprisingly large scales for both D and *d1*. In *d1* estimations, errors of less than 5% are achievable for object sizes greater than some hundreds-1000 pixel^2, but for circular objects, which can not be grid aligned, the error never drops below 1%, independent of the

	D_{th}	D	ϵ
fBm	1.8	1.516 ± 0.001	16%
fBm	1.6	1.413 ± 0.001	12%
vonKnoch	1.26	1.310 ± 0.002	-3%

Table 2.2: Theoretical fractal dimension D_{th} and measured fractal dimension D for the studied objects and the relative error $\epsilon = (D_{th} - D)/D_{th}$. Pixelization errors increase with increasing structure complexity.

perimeter measure employed. This is true even for object sizes exceeding 5000 pixel^2. For any given size object D is significantly closer to its expected value of 1 than is *d1*. This is because the evaluation of D in the perimeter-area fit is performed over all points above a minimum size. This includes the large objects not included at small scales in the the evaluation of *d1*. Therefore, the object size threshold above which the error is lower then 5% occurs at lower scales, but is not usually less then some hundred square pixels.

The origin of these errors is in the impossibility of representing on a rectangular grid curves or non-grid aligned lines. This causes the area and the perimeter to scale differently respect to what is expected for non fractal objects. For instance, in the case of a right triangle whose two sides are grid aligned, the overestimation of the hypotenuse leads to the overestimation of both perimeter and area. It can be shown (see appendix) that, because the relative error in the perimeter estimation is not size dependent, while the relative error in area estimation decreases with increasing object size, the estimated fractal dimension of right triangles is always overestimated.

No error was measured when estimating fractal dimension of grid aligned squares with the first method explained in par.2.3.4, so that in the following I present results obtained only with this technique.

The analysis described above was also applied to fractal structures: the von Koch snowflakes (Peitgen and Jurgen, 1992) and fractional Browian motion (fBm) images (Turner et al., 1998). For the first object, whose fractal dimension is ~ 1.26, I produced snowflakes up to level 6 of different sizes (see Appendix) and studied their perimeter and area scaling. For fBms (see Appendix) I created two sets of 150 images of expected fractal dimensions 1.8 and 1.6 respectively. Each fBm image was segmented with seven different thresholds (Turner et al., 1998) and perimeter and area of the structures selected by the different thresholds were combined to study the fractal dimension.

In fig.2.8 the measured dimension $d1$ is plotted as a function of object size for von Koch snowflakes of level 6. The fractal dimension increases with object size from a minimum value, in this case 1.15, to an almost constant value approximating the theoretical one, over the size range 1000 to 5000 pixel^2. Note that the plateau value, about 1.34, exceeds the one expected theoretically. This reflects the overestimation of the snowflake perimeter inherent in the perimeter measure algorithm employed, as discussed previously for simple non fractal triangle. A rise of fractal dimension with object size was also observed for fBm images, and is surprisingly reminiscent of that found for real solar structures. The estimated fractal dimension of fBm synthetic structures at the largest areas was lower than the expected theoretical one (see appendix to this chapter).

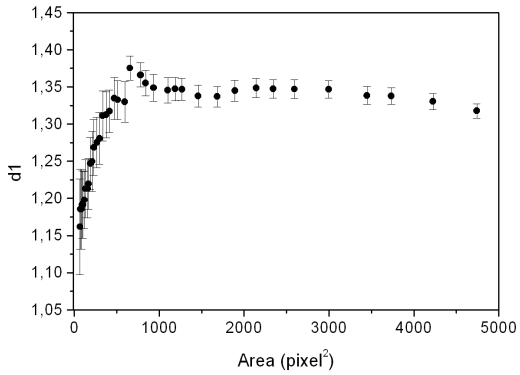

Figure 2.8: $d1$ evaluated for von Koch snowflakes of level 6. Likewise non fractal objects and real data, $d1$ increases with object size and reaches a plateau at areas $\geq$ 1000 pixel^2. The plateau value, about 1.34, is an overestimate of the snowflake fractal dimension (see text).

Measurements of D are similarly affected by pixelization at small scales, with more complex structures harder to resolve and thus showing greater measurement error in the deduced fractal dimension, as shown in table 2.2.

Both regular and fractal objects show similar pixelization induced errors in the fractal dimension estimation. These effects are greater at smaller areas, where the lack of resolution causes the objects to appear round, thus both *d1* and D increase rapidly with object size for object areas less than $\sim 500 - 1000$ pixel^2 and some hundred pixels square respectively. For objects of larger area D and *d1* increase more slowly, but show deviations from the expected theoretical value reflecting how the structures map onto the pixel grid.

I thus suggest that the minimum object size thresholds (usually about some tens of pixel^2) applied in previous works (e.g. Vogelaar and Wakker (1994)) are insufficiently conservative, with residual pixelization effects significantly influencing the final results even for objects of $\sim$ 1000 pixel^2.

2.7.2 Resolution and seeing effects

The fractal dimension estimate of solar features depends on the resolution of the images analyzed. Resolution is determined not only by the detector pixel size (image scale), but also by the aperture of the telescope, any instrumental aberration, and, for ground based instrumentation, the distortion introduced by atmospheric turbulence (seeing). Thus the pixel scale and the resolution are not the same. To evaluate the effects of resolution on the estimation of fractal dimension, I analyzed the scaling of *d1* and D with area after convolving von Koch snowflake and fBm images with Gaussian functions of different widths. I obtained, as one might have expected, a decrease in both *d1* and D accompanying the increase of smoothing. Table 2.3 of D (fit over the entire perimeter area range) shows also that the smoothing effects become more important as the structure complexity increases.

A Gaussian function is a rough approximation to seeing and instrumental aberration Point Spread Function in real images. Moreover, seeing is a time

	D_{th}	D	D_{sm}	ϵ
fBm	1.80	1.516 ± 0.001	1.366 ± 0.001	9.9%
fBm	1.60	1.413 ± 0.001	1.303 ± 0.001	7.8%
von Koch	1.26	1.310 ± 0.002	1.273 ± 0.002	2.8%

Table 2.3: Fractal dimension measure for different fractals, before D and after D_{sm} smoothing by convolution with a Gaussian of fwhm=2, and the relative error $\epsilon = (D - D_{sm})/D$. Note that to distinguish resolution from pixelization induced effects, the error is evaluated respect to D and not to D_{th}.

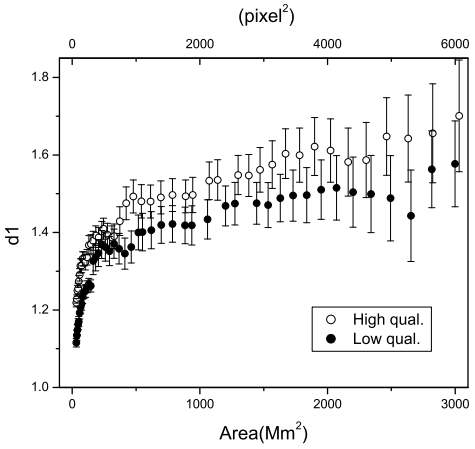

Figure 2.9: Facular fractal dimension estimated on the two different full resolution MLSO quality sets described in the text. When the estimation is carried out on images less affected by seeing degradation, the measured fractal dimension is higher.

dependent phenomenon, so that images acquired at different times are affected by different degradation. In order to investigate directly the effect of variable seeing on the computed fractal dimension of structures in real data, I examined full resolution PSPT images from MLSO after selection based on the quality criteria described in 2.3.2. Images were segmented with the first technique explained in 2.3.3. In agreement with results obtained with synthetic data, fig. 2.9 shows that a real decrease in resolution resulting from degraded observing conditions leads to an underestimation of feature's complexity at all scales.

2.8 Results interpretation

I have shown that pixelization and resolution affect the fractal dimension determined by the two estimators *d1* and *D*. Understanding these effects is essential to the interpretation of the results obtained from OAR and MLSO PSPT images as well as those previously reported from studies carried out with similar techniques on full-disk observations. Pixelization errors occur at all scales, but are generally more important for smallest area objects. This causes the estimated fractal dimension to increase rapidly with object size and become almost constant at areas larger than a certain threshold, that I estimated to be $\sim 500-1000$ pixel^2 for *d1* and some hundred pixel^2 for *D*. Seeing induced image degradation smooths edges making structures appear rounder, resulting in a reduced fractal dimension. This effect is expected, on the basis of synthetic fractal data, to be more important for more complex objects.

I thus suggest that the rise of *d1* with object size observed in PSPT data, as well as for example in Meudon spectroheliograms (Nesmes-Ribes et al., 1996) and MDI magnetograms (Meunier, 1999, 2004), is most likely an effect of image pixelization, rather than a signature of an intrinsic multifractality of active regions. Pixelization may also likely be the cause of the 'break of similarity' observed by Jansen et al. (2003), the break occurring at the same scale (measured in pixel^2) for both real and simulated images, in spite of the different physical scale magnetic structures they studied. The break also occurred at the same pixel area suggested by my simulations.

For larger objects, fractal dimension estimate is most affected by seeing. The values measured for large scale structures in the PSPT observations (1.5 to 1.7) are therefore likely an underestimate of the real value. Note that MDI magnetograms, while not affected by seeing, are slightly defocused, so that the resolution is twice that of the pixel scale (Scherrer, 1995). One thus expects results obtained with these data sets to be also an underestimate of the real value.

A study of the fractal geometry of solar active regions and its variation with the magnetic activity cycle is thus feasible if it focuses only on large features, employs a constant segmentation technique throughout, and utilizes data of consistent high quality. The OAR PSPT images analyzed over a period of six years marginally meet these requirements, and so the observed variations in time (fig.2.6) may be significant. They do not show, however, a clear correlation with the solar cycle. The variations appear to be dominated by size distribution of the features examined, which in turn weights the perimeter-area fit (this is true especially for *D* evaluated on the entire area range).

It is important to notice that, as demonstrated by Baveye et al. (1998)

for the box counting method, pixelization effects can influence other fractal dimension estimators as well, and careful quantitative measure of the effects for each measure employed is essential to the interpretation of the results. I have not addressed this problem in this work and leave also this issue for future research.

Chapter 3

A study of faculae photometric properties

In this chapter I show the results obtained by a study of photometric properties of magnetic features identified in the photosphere and chromosphere on Blue, Red and CaIIK PSPT images and on MDI magnetograms. I investigate the variations of contrast measured in the three wavelengths respect to disk position and features size. The effects of segmentation technique employed to identify features on images and the seeing induced degradation are also investigated. Results are compared with the ones presented in the literature. Most of this work has been developed in collaboration with Solar Group at Osservatorio Astronomico di Roma and is also described in Ermolli et al. (2007).

3.1 On the importance of magnetic features contrast measurements

The study of the photometric properties of faculae, the positive contrast features observed in the solar photosphere that have associated high magnetic flux (see chapter 1) is important for several reasons.

The measurements of the contrast of these features at different disk positions, observed at different wavelengths, has been successfully employed to reproduce space based measurements of Solar Irradiance variations (Foukal and Lean, 1988; Chapman et al., 1996; Lean et al., 1998; Walton and Preminger, 2003b; Penza et al., 2003; Fontenla et al., 2004; Wenzler et al., 2005). These reconstructions differ from author to author for the number of structures considered, the models assumed and the kind of data and techniques employed to measure features properties. They can reproduce more than 90% of the Irradiance variations observed. The residual variations have been variously ascribed, among other hypotheses, to internal structural changes of the sun (Balmforth et al., 1996; Sofia, 1998; Rozelot et al., 2004), to variations of properties of features not usually taken into account like the network (Caccin et al., 1997; Fligge and Solanki, 2000; Wenzler et al., 2002), or to inaccurate measurements of bright features photometric properties (Fligge and Solanki, 2000; Ortiz et al., 2002).

Measurements of photometric properties of bright magnetic features are also

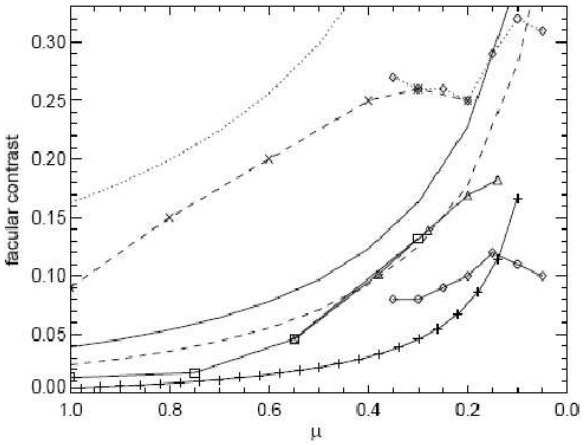

Figure 3.1: Center to Limb variation of facular contrast measured at different wavelengths by different authors. Squares: 5250Åfrom Frazier (1971). Crosses: 5750$\AA$ from Auffret and Muller (1991). Diamonds: 3860$\AA$ and 5250$\AA$ from Wang and Zirin (1987). Triangle: 5250$\AA$ from Taylor et al. (1998). Plus: 6264$\AA$ from Lawrence and Chapman (1988). The thick curves without symbols represent semi empirical models evaluated at 386nm (dotted line), 525nm (solid line) and 575 (dashed line). From Unruh et al. (2000).

essential to the validation and improvement of semi empirical atmosphere models (Fontenla et al., 2004; Penza et al., 2004), flux tube models and MHD simulations (Fligge and Solanki, 2000; Keller et al., 2004; Steiner, 2005a). These latter are discussed in detail in chapter 4.

In spite of the fact that measurements of the contrast of faculae and its variation on disk position started more than 60 years ago (as discussed in Solanki (1993)), results obtained in the literature are wide and controversial. Fig. 3.1 shows for instance some center to limb variation measurements of facular contrast obtained by different authors (see also fig. 3.8 in this chapter). At disk center, negative, zero or positive contrast has been reported. It increases toward the limb. In some cases a maximum has been observed at positions between $\mu = 0.4$ and $\mu = 0.2$, where μ is the cosine of the heliocentric angle. In other cases, a monotonic rise is observed. Discrepancies in the results are partially due to physical reasons, the contrast being a function of wavelength at which the structures are observed, their size and the associated magnetic field (e.g. Ortiz et al., 2002; Walton and Preminger, 2003a). But other factors like instrumental resolution, variable seeing and image reduction and analyses techniques can also play an important role (Fligge and Solanki, 2000; Ermolli et al., 2007).

In order to contribute on this topic, in collaboration with the Solar Group of Rome Observatory, I analyzed a long temporal dataset of full-disk images and magnetograms. We investigated the dependence of Center to Limb Variation (CLV) of magnetic selected regions on several observational constrains, like spectral range, spatial resolution and activity level, as well as the method employed to select structures on images. Results obtained by this analisys are summarized in the following. More details are given in Ermolli et al. (2007).

3.2 Observations and data reduction

3.2.1 PSPT data

The bulk of the data we analyzed is from the archive of daily full-disk observations carried out with the Precision Solar Photometric Telescope (PSPT) at Osservatorio Astronomico di Roma (OAR). This was supplemented with data from the PSPT at Mauna Loa Solar Observatory (MLSO) for consistency and resolution tests. Images characteristics and data reduction procedures have been already described in previous chapter.

For this study we selected OAR daily image triplets (CaIIK, blue continuum and red continuum), obtained on 291 different observing days during the summers (July to September) of 1998 through 2005. The largest sample of the images was obtained by co-adding short exposure frames, as explained in paragraph 2.3.1. In order to evaluate resolution degradation effects induced by atmospheric seeing, single frame images were also analyzed.

In order to take investigate seeing, instrumental and image calibration effects, a sample of 42 images taken during summer 2005 (July to September) at MLSO, was also analyzed. For each observation day, the best quality image, according to criteria explained in chapter 2, were selected.

Finally, we analyzed MDI full-disk magnetograms (Scherrer, 1995), selected from those available in the SoHO archive (http://soi.stanford.edu/data/) during the months between July and September from 1999 to 2005. There are no MDI observations for the same months in 1998, due to SoHO spacecraft problems. Among all the data available, we had to search for the full-disk magnetograms acquired almost simultaneously to the Rome PSPT images. The analyzed data set consists of 237 magnetograms, recorded during 112 days spread over the period described above. We tried to maximize the number of usable MDI data, but we found difficulties in obtaining magnetograms close in time to the PSPT observations. In all the analyzed images, MDI and PSPT data were recorded within 10 min from each other.

The MDI data provide a measure of the line-of-sight component of the magnetic field averaged over a 2 $\times$2 arcsec resolution element. We mainly used single magnetograms acquired with 30 s integration time, on which center to limb variation of noise level was estimated by computing the standard deviation on 40$\times$ 40 pixels running box. We have also analyzed two samples of magnetograms acquired during the year 2000, with 30 s and 300 s integration times, as well as averages of single magnetograms, so as to evaluate how much the results are affected by the reduction of the data-noise level. Results obtained by this last analysis are presented in (Ermolli et al., 2007).

3.2.2 Magnetic regions identification technique

Five different magnetic regions identification techniques were employed in order to study the dependence of results on this issue. In brief, the methods are the following: 1) a thresholding of CaII K contrast images, with the threshold value evaluated by an iterative technique, as suggested in Nesmes-Ribes et al. (1996) (*NR*, hereafter);2) thresholding of CaII K contrast images, with the threshold value being a function of heliocentric angle, as suggested by Ahern and Chapman (2000b) (*CH*, hereafter); 3) structures are singled out on CaII K images by

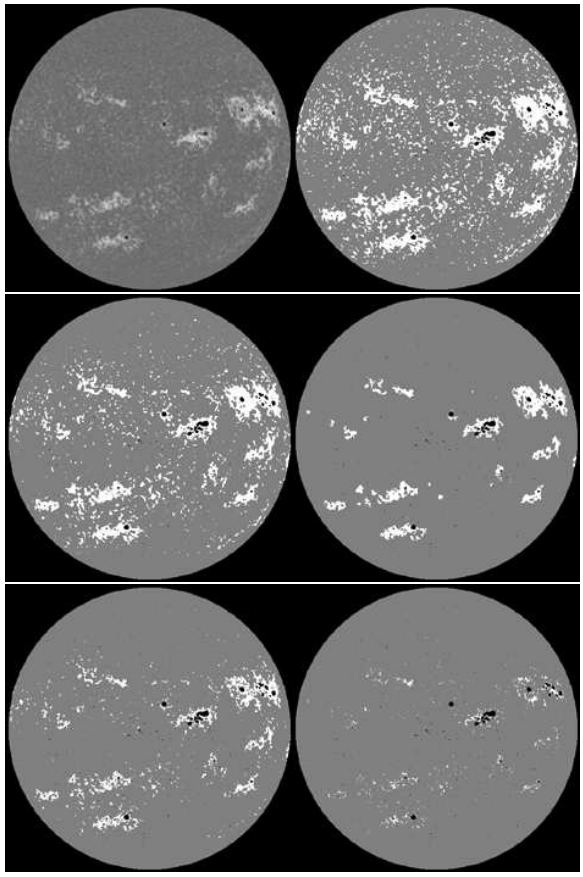

Figure 3.2: Examples of the results obtained by the processing of images acquired on June 26 2000. From the left, top: Rome PSPT CaII K image and mask image obtained by the *NR* method; middle: mask images obtained by the *CH* and the *Ktr* methods; bottom: mask images obtained by the the *B-R* and the *Mag* methods. Gray pixels represent quiet sun, black pixels spots and pores, white pixels the bright magnetic regions selected for the analysis.

thresholding, size and connectivity criteria (*Ktr*); 4) thresholding of color image obtained by the difference of blue and red bands images (*B-R*); 5) thresholding of magnetic signal measured on MDI magnetograms (*Mag*).

Through the different methods applied, we obtained five binary images with masks of the identified facular regions for each day. We excluded from these masks all the pixels whose contrast on the corresponding PSPT red continuum images was below the 3σ of the average contrast of each image. In this way, possible isolated dark pixels were also removed from the identified features. An example of the regions selected with the different methods is given in fig. 3.2. Each region is then labelled and the heliocentric angle of its barycentre evaluated in order to study the dependence of the contrast on the position on the disk and the region size.

For each PSPT band, we took into consideration the maximum contrast and the mean contrast of each region. In order to reduce quiet sun center to limb variation effects, the contrast is defined as the ratio between the pixel intensity (or the mean intensity of pixels belonging to the region) and the mean intensity of quiet sun (as determined from a global center to limb fit) at the same heliocentric angle minus one. In formula

$$C_\lambda(\mu) = \frac{I^f_\lambda(\mu)}{I^q_\lambda(\mu)} - 1 \tag{3.1}$$

where $C_\lambda(\mu)$ is the contrast at a certain wavelength and disk position, I is the measured intensity and the superscripts f and q indicate *facula* and *quiet sun* respectively.

Finally, in order to exclude enhanced network and bright points, structures whose size was lower than 10 pixels squares were rejected from the analyses.

3.3 Results

3.3.1 Center to Limb variation

The physical mechanisms that determine the photometric properties of magnetic regions in the photosphere are different from those in chromosphere (see chapter 1). Results obtained on CaII K images (that sample the chromosphere) and on Blue and Red images (that sample the photosphere) are thus quite different.

The five methods single out chromospheric regions that are characterized by different average contrast values, as shown in fig.3.3. The relative difference between maximum and minimum values obtained, which are achieved with *Mag* and *NR*, respectively, is about 15% in the PSPT CaII K band. The contrast values of CaII K features identified by *NR, CH*, and *Ktr*, as well as the deviation in measured values, do not show a disk position dependence. The contrast values are ≈ 1.24, 1.24, 1.34, for the three methods. The deviation of measured values is roughly the same for all the three methods, specifically ± 0.02. By contrast, the results obtained with *B-R* and *Mag* show a monotonic increase in the average contrast of features from the disk center to $\mu = 0.2$. This increase is about 1% and 5%, for the two methods. The standard deviation of measured values also slightly increases toward the limb. The mean contrast at the disk center is $\approx 1.31 \pm 0.02$ and 1.35 ± 0.04 in the two methods respectively.

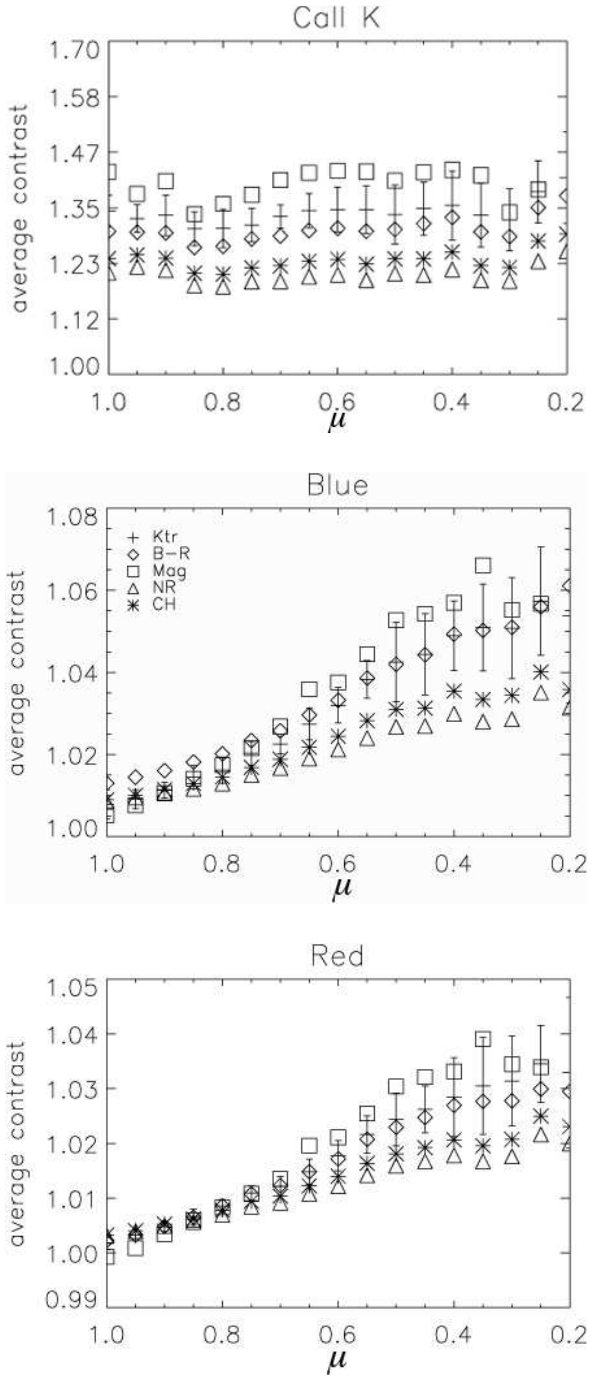

Figure 3.3: Center to limb variation CLV of facular contrast in CaIIK and two PSPT continuum bands computed for the year 2000, using the five methods described in the text. Error bars represent the standard deviation over the position bin; for clarity, they have been superimposed only over the results obtained with the *Ktr* method. Details about the deviation of contrast results obtained with the other methods are given in the text.

Figure 3.3 shows also the average contrast CLV in the PSPT blue and red bands. In both cases, the contrast CLV increases almost monotonically toward the limb, with no maximum up to $\mu = 0.2$. Actually, the CLV obtained with *Mag* shows nearly a plateau for disk position corresponding to $\mu < 0.4$, but this is likely due to the applied compensation of the noise pattern (see Ermolli et al. (2007) for more details).

Notice that the contrast CLV obtained depends largely on the identification method used. In particular, the results differ for up to a factor 3% and 2% at $\mu = 0.2$ on PSPT blue and red bands, respectively.

The contrast of features selected with *Ktr* is slightly larger than that computed by all the other methods, save the one of the magnetic signal. Actually, *Ktr* selects larger size features that mainly occur on activity belts. *Mag* identifies much smaller size features than do the other methods, features that are also not strictly distributed along activity belts, but mostly occur there. We find that the average contrast of these features is slightly larger than the one obtained by *Ktr* ($> 1\%$ at $\mu < 0.5$). On the other hand, the contrast values obtained for the features identified at the disk center by *Mag* is lower than the values measured with the other selection criteria ($\approx 0.5\%$). Average contrast values lower than unity, i.e. features that show a negative contrast relative to the quiet sun, are found strictly at the disk center of the red band observations. Negative contrast measurements are found up to $\mu = 0.9$, but the average value is positive.

The vertical bars in Fig. 3.3 show the standard deviation of measured values with *Ktr* method. Deviations obtained with *B-R* are very similar. The ones obtained by *CH* and *NR* are smaller, up to half the value at disk positions $\mu > 0.6$. The deviations of values obtained by *Mag* are up to 1.5 - 2 larger than the one obtained by the *Ktr* at each disk position.

The maximum contrast and its deviation vary in a similar fashion to the average values, though its dependence on disk position is twice as large. The average value of the maximum contrast obtained at each disk position does not depend on the method. In fact, the absolute difference among the obtained values is smaller than the deviation of the contrast measurements at each disk position. On the contrary, the average of the minimum contrast value depends slightly on the method applied for disk position $\mu < 0.8$. Nevertheless, the absolute difference among the obtained values lies in the largest deviation computed. The average of the minimum value obtained is negative at each disk position for both the continuum bands analyzed.

3.3.2 Black body approximation

The comparison of the contrast of magnetic features is an important tool for the investigation of the temperature stratification. According to Allen (2000), the contrast $C_\lambda(\mu)$ is related to the contrast measured at $5300\mathring{A}$ by the formula:

$$C_\lambda(\mu) = C_{5300}(\mu) 0.5 \lambda^{-1} \tag{3.2}$$

The ratio of contrasts measured at two different wavelengths λ_1 and λ_2 is thus

$$\frac{C_{\lambda_1}(\mu)}{C_{\lambda_2}(\mu)} = \frac{\lambda_2}{\lambda_1} \tag{3.3}$$

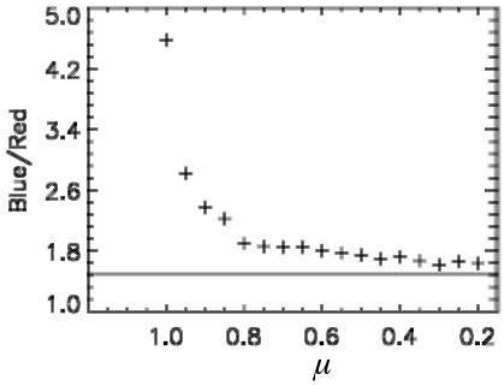

Figure 3.4: Ratio between the mean contrasts measured in the Blue and Red bands as a function of disk position. If faculae and quite sun were emitting like Black Bodies, points would lie on the straight horizontal line shown, whose value is $\lambda_R/\lambda_B = 1.48$. Results obtained with *Ktr* method are shown.

that is a constant and is not expected to change with position on the solar disk. Figure 3.4 shows instead that the ratio of the contrast in the two PSPT continua is constant toward the limb, at $\mu < 0.8$, while at the center it decreases rapidly with the decrease of μ. This is most likely due to the fact that relation 3.2 is derived under the assumption that both the magnetic structure and the 'quiet sun' emit radiation as black bodies of a certain temperature. In next chapters it will be shown that atmospheres in both magnetic and non magnetic regions are stratified and that observations at different heliocentric angles sample different layers of the atmosphere. The discrepancy of results shown in fig.3.4 from relation 3.2 is thus not surprising. The approximation is instead expected to hold when comparing measurements obtained at the same disk position for different wavelengths, although deviations are expected due to the dependence of H^- opacity on wavelength (Lawrence, 1988). In particular, wavelengths were the opacity is higher sample upper regions of the photosphere, while wavelengths were the opacity is lower sample deeper regions. Due to the temperature stratification in the magnetic features and in the quiet sun (see chapters 4, 7 and 8 for more details), the black body approximation is therefore expected to hold for structures located at the same (or close) heliocentric angle and observed at wavelengths that sample close layers of the solar atmosphere.

In chapter 8 I will describe in more details the derivation of formula 3.2 and explain, by numerical simulations, why the deviation of the curve from a straight line is larger at disk center and smaller at the limb.

3.3.3 Size and Activity Cycle dependence

As will be explained in detail in chapter 4, according to flux tube models the observed contrast depends on the structure size. Tubes whose size (diameter) is lower than the optical depth (about 100 km in the solar photosphere) of the atmosphere are expected to be brighter, because of the radiative channelling

from the flanks. Tubes whose size is larger are expected to have a negative contrast, because the radiative heating is not enough to counterbalance the temperature decrease due to the convection inhibition by the magnetic field. The structures we investigated are clusters of flux tubes. Nevertheless, as will be shown below, their photometric and geometric properties reflect properties of single magnetic elements.

In order to study this topic, we have investigated the scaling of the maximum and average contrasts of the regions with their area. Figure 3.5 shows results obtained in the three bands for the average and maximum values for structures identified with the *Ktr* method. In order to reduce projection effects, analyses was restricted to structures whose baricenter was at disk center ($\mu \geq 0.9$). Contrasts were averaged in bins of areas of width $\Delta \log A = 0.05$.

The average contrast of chromospheric faculae (CaII K band) increases with feature size for area values of about 2000 square pixels, corresponding to about 4000 Mm^2. At larger values, the contrast oscillates around the value 0.3. At photospheric level, that is in the blue and red continua, the contrast decreases from the smallest to the largest areas and oscillates around the values 0.007 and 0.002 respectively at areas larger than 2000 square pixels. On the contrary, the maximum contrast increases at areas smaller than 2000 square pixels and is constant at larger areas in all the three wavelengths. It is important to notice that these variations are smaller than the error bars (not shown in fig.3.5). Nevertheless the large scale trends reflect some physical properties of identified features.

The rise of both the mean and maximum contrast at the smallest areas is an effect of filling factor and resolution. The detector has in fact a finite pixel size, much larger than the mean size of a single magnetic element (2000 km against about 200 km estimated for the diameter of flux tubes). Each pixel can then contain several elements. If each element has associated the same brightness, the pixels that contain more elements (higher filling factors) will have higher contrast than pixels that contain less elements. This is in agreement with the fact that the scatter plots (not shown) showed a large scatter at small areas, with some small regions being characterized by large contrast. Nevertheless, at these smallest sizes the effect of seeing, that spreads energy over an apparent area that is larger than the physical one, is also expected to be larger, thus reducing both mean and maximum contrasts. The decrease of mean contrast in Blue and Red images has to be ascribed to the negative contrast associated to flux tubes whose size is larger than the mean free path of photons. This view is corroborated by the fact that the scatter plots (not shown) also showed that a small number of structures have a mean negative contrast at disk center. The fact that the largest structures also have associated the highest maximum contrast is an observational evidence of the fact that active regions are populated by flux tubes of different sizes, as suggested by Walton and Preminger (2003a) and as observed by Spruit and Zwaan (1981) by the analyses of high resolution data.

Temporal variations of measured contrast were also investigated. Figure 3.6 shows the average and the maximum contrasts of features identified at disk center ($\mu \geq 0.9$) and separated by their size for each year of the period analyzed. The reference area value considered is 2000 $pixel^2$. The choice of this area value lies in the contrast dependence on size shown above. The identification method is the *Ktr*. Figure 3.6 shows that, independently from size and wavelength,

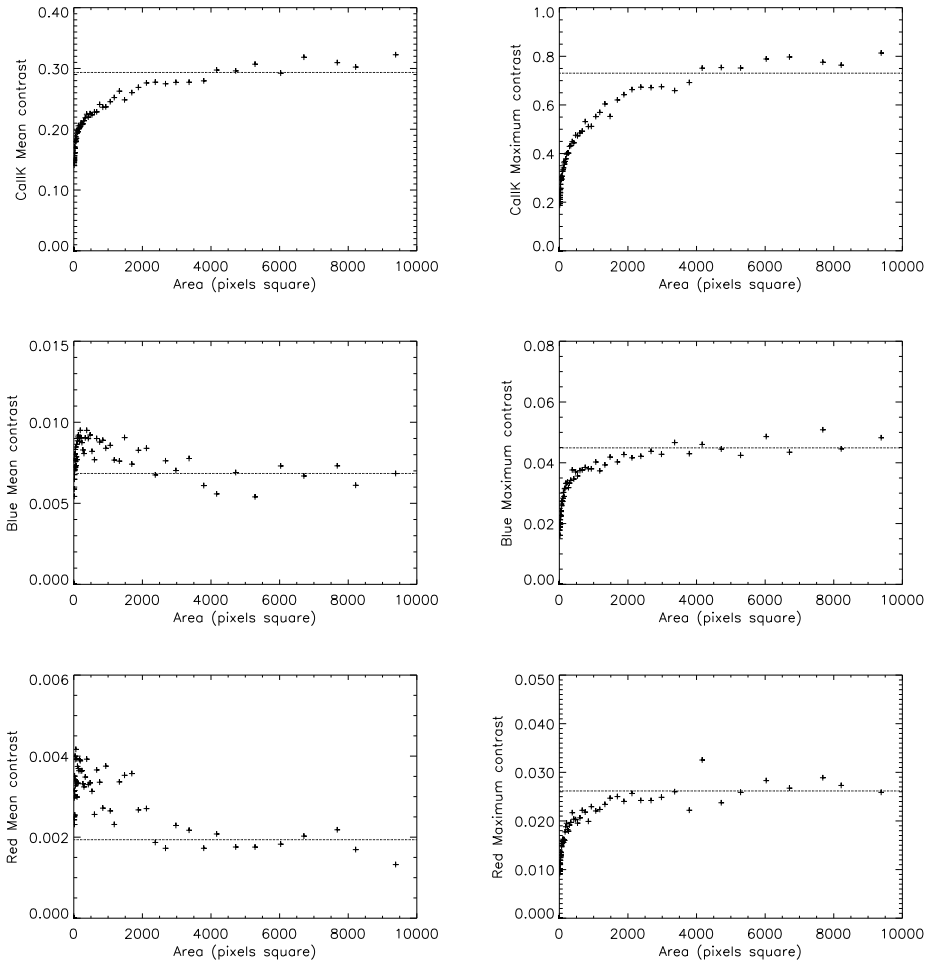

Figure 3.5: Dependence of mean (left column) and maximum (right column) contrast on area of features identified with *Ktr* method in the three OAR-PSPT wavelengths.

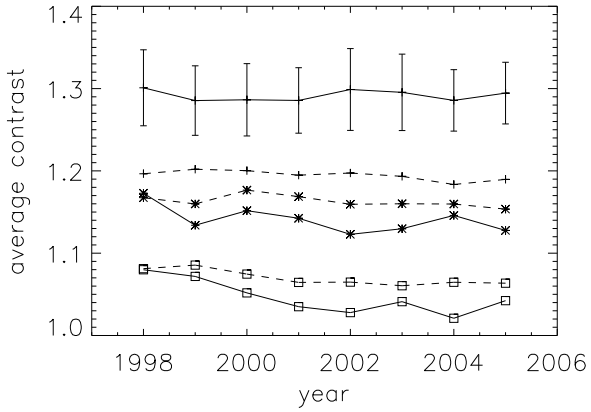

Figure 3.6: Temporal variation of the average contrast of features identified at disk center ($\mu \geq 0.9$) and selected depending on their size: features with area larger (solid line) and smaller (dashed line) than 2000 pixel^2 ($\approx$ 2800 Mm^2). Crosses, stars, and squares show the CaII K, blue, and red measurement results, respectively. For clarity, the deviation in measurements is plotted only for the sample with the highest contrast values.

photometric properties of identified structures do not significantly vary with solar activity cycle, the small variations observed being within the error bars.

3.3.4 Observational limitations

As already explained, results showed in previous paragraphs were obtained with images selected from the OAR PSPT archive. These images were in turn obtained by summing 25 single short exposure frames taken usually within 1 minute, thus increasing the Single to Noise ratio, but reducing the resolution. I will refer to these images as *photometric*. In order to investigate the effects of resolution in the determination of the CLV of facular contrast, we have compared the results obtained with this dataset with results obtained with other two datasets. In particular we analyzed a sample of best quality images from MLSO archive from summer 2005 and the corresponding single frame best image for that day from OAR archive. As already explained, because of the more stable atmospheric conditions of the site, MLSO images are usually characterized by a better resolution and a lower level of scattered light. Single frame images from OAR archive are also characterized by a better resolution than the photometric ones. A statistical analyses (Fazzari et al., 2003) showed that the average resolution of these frames is 3 arcsec, with a large sub sample diffraction limited (2 arcec), compared to about 4 arcsec of photometric images.

Figure 3.7 shows relative differences among the results obtained on OAR photometric images and the other two datasets. On average contrast is higher when measured on higher resolution images, but the differences are very small (within 1%). It is also worth noticing that larger variations are observed at the limb, where other effects like fore shortening are important.

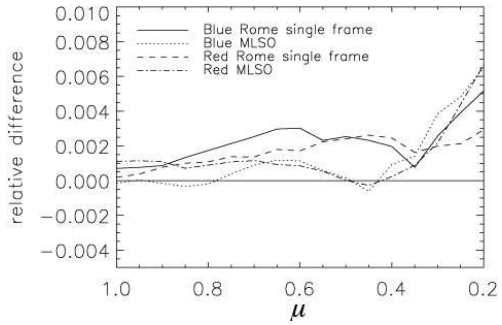

Figure 3.7: CLV of facular contrast relative differences among results shown in previous paragraphs and results obtained with different datasets. Solid and dotted lines: Blue continua from OAR single frame and MLSO respectively. Dashed and dot-dashed: Red continua from OAR single frame and MLSO respectively. For clarity, only results obtained with *Ktr* method are shown.

3.4 Discussion of results and comparison with previous analyses

The literature concerning the study of photometric properties of magnetic regions in the solar atmosphere is very wide and results obtained for facular regions are controversial. Discrepancy among different authors have been ascribed to differences in the data resolution, wavelength, disk position, magnetic filling factor, features size (Solanki, 1993). We also showed that the structures identification method is crucial in the measurements of the CLV of facular contrast and its physical interpretation. A comparison with previous published data with the ones we obtained is therefore very difficult.

In fig 3.8 results obtained by some other recent studies and by our analyses are shown. The data are similar because of resolution and wavelength to the ones we analyzed. In general, our results qualitatively agree with results obtained by authors that employed features identification methods similar to the one described in paragraph 3.2.2, that is methods based on Intensity thresholding. Foukal et al. (2004) and Walton and Preminger (2003b), for instance, also measured in the photosphere a monotonic increase of the contrast toward the limb. Data obtained using the magnetic field intensity to detect structures, like in Ortiz et al. (2006) show instead a maximum toward the limb. Note, however, that results obtained by these latter authors concern the CLV of contrast of pixels whose corresponding flux in contemporary acquired magnetograms exceeds a certain threshold, and different CLVs are obtained for different associated magnetic field intensity. For instance in fig.3.8 CLVs for pixels that have associated a magnetic field of 110 and 450 G are shown. These curves show a negative contrast at disk center and a rapid increase toward the limb for pixels that have associated a more intense magnetic field, and an increasing contrast from a null value at disk center to a maxim value for pixels that have associated a lower magnetic field. The maximum position resulted a function of the associated magnetic field while the point at which the contrast changes sign is always about $\mu = 0.8$. These data are similar, for what concerns the wavelength, to the Red continuum PSPT images, but the agreement of results is not

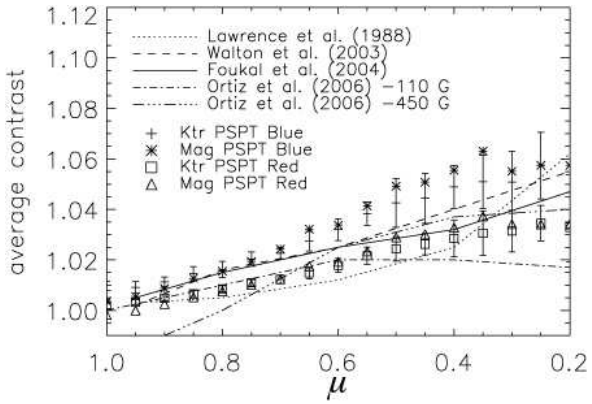

Figure 3.8: Selected facular contrast CLV measurements plotted versus disk position. The symbols with error bars show the results obtained with the *Ktr* method, while those without error bars show the results by the *Mag* method. The different lines show the results of recent measurements of facular contrast presented in the literature.

very good. Particularly, our scatter plots show that very few structures have a negative contrast at disk center, so that the mean value is null or positive. Differences have to be ascribed to the different filters and to the fact that we investigated the mean or the maximum contrast of clusters of pixels, instead of the contrast of single ones. Finally, Berger and Title (2001) showed, by the comparison of high resolution G-band (430.5 ± 1 nm) data and magnetograms, that bright points have associated a high magnetic flux, while to a high magnetic flux concentration not always corresponds a positive contrast region. This result, confirmed recently by Tritschler and Uitenbroek (2006) by MHD simulations, would explain the lower contrast measured in general when solar features are identified on magnetograms.

Other authors have investigated the ratio of contrast of faculae at different wavelengths and at different positions on the solar disk. Chapman and McGuire (1977), by the analyses of solar faculae observed at the very limb in five different wavelengths (namely, in nanometres, 535 ± 78, 525 ± 70, 662 ± 5, 788 ± 5, 1010 ± 125), obtained

$$\frac{\Delta I(\lambda)}{I(\lambda)} \propto \frac{\Delta I(5300\mathring{A})}{I(5300\mathring{A})} \cdot \lambda^{-1} \tag{3.4}$$

independently from disk position in the field of view analyzed. Here $\Delta I(\lambda)/I(\lambda)$ is the ratio measured at each wavelength λ. A small discrepancy from this curve was found for data in the blue filter (435 ± 78 nm). In particular the value of the facular contrast in this filter resulted higher than the value expected by relation 3.4. The authors speculate this result to be caused by an increase of opacity in the blue, consequent to line haze effect ("line haze" are the multitude of weak lines that populate the continuum, thus depressing it), and to an increase in the temperature of faculae in the upper layers of the atmosphere, where the blue light comes from. In general, relation 3.4, that is a decrease of contrast with wavelength, is verified by measurements of facular contrast at the limb

(e.g. de Boer et al., 1997; Wang and Zirin, 1987). Lawrence (1988), by the analyses of facular contrast in three different continua all over the disk, found a good agreement of data with relation 3.3 for faculae at the limb, that is he found that the ratio of contrasts is constant respect to disk position. For faculae at disk center, instead, the ratios of the contrasts at different wavelengths as a function of disk position did not lie on a single straight line, as should be if relation 3.3 was valid all over the disk, but, in agreement with our finding, increased toward the center. Discrepancy from a straight line of ratio of facular contrast was also found by Ahern and Chapman (2000a), who analyzed facular contrast at different disk positions. Our results are thus in agreement with the ones previously shown in the literature. In this thesis I also show that the deviations from relation 3.3 observed, are not due to noise or bad sampling, as suggested by Lawrence (1988), but are an effect of temperature stratification of the atmosphere inside and outside the magnetic structures.

The size dependence of the contrast is also in qualitative agreement with results obtained by previous investigations. In particular Walton and Preminger (2003a) analyzed full disk images in red continuum and CaIIK and investigated the maximum contrast of facular regions in function of their area and position on the disk. Features were identified, in both filters, using a thresholding technique. They found, in agreement with our results, that the maximum contrast is positive and increases with the size of the features in both filters. They also compared these results with the ones obtained identifying structures in red continua with masks in CAIIK images, that is with a method similar to the one we adopted for our analyses. They found that at disk center the 'extreme contrast', that is the contrast whose absolute value is the largest within a structure, has the opposite behaviour, the largest features showing the lower negative contrast and the smallest ones having the higher positive contrast. The mean contrast, instead, was positive at all area ranges. In particular it was smaller at smallest areas, while the same value was found for larger areas. This is not in agreement with our results, since our fig. 3.5 shows that the largest areas have associated a lower mean contrast. This difference might be a consequence of the different area binning.

Ultimately, our finding that photometric properties of faculae do not vary with the solar cycle is in agreement with Ortiz et al. (2006).

3.5 Geometric and Photometric properties of faculae

Figure 3.9 shows the fractal dimension of features identified on Calcium images from different datasets (see chapter 2) and the maximum contrast of faculae measured on Calcium images from year 2000 (these plots have been already shown in fig.2.5 and fig.3.5) as function of the features size. The similarity of the two curves is striking, since they show that both fractal dimension and contrast increase with size and become constant at similar area range, that is at areas larger than about 1000-2000 pixels square. Speculation about a common physical process that might explain the shape of the two curves is thus tempting. Nevertheless, in chapter 2 I showed that fractal dimension estimates are critically affected by pixelization and resolution effects and that the increase of

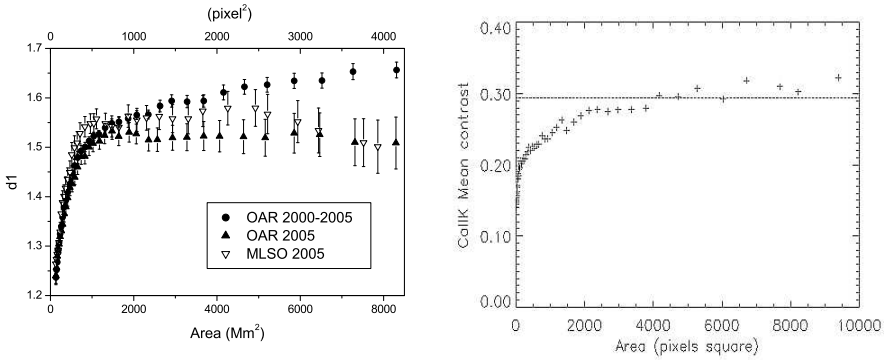

Figure 3.9: Left: Fractal dimension $d1$ versus area of bright features identified on calcium images from different datasets (symbols are the same as in fig.2.5). Right: Mean contrast versus area of bright features identified on PSPT calcium images from summer 2000. Both fractal dimension and contrast rise with features size and reach a plateau at areas larger than 1000 and 2000 pixels squares respectively.

the estimated dimension at smallest areas is most likely an artefact. In previous paragraphs of this chapter I also commented on the fact that the increase of facular contrast at the smallest areas might be a result of the combined effect of filling factor and resolution. Moreover, it is reasonable to assume that regions with higher filling factors, and thus more brilliant, are more compact and thus should have smaller fractal dimension. Measurements by Lawrence (1991) of the fractal dimension of an active region with high resolution data, showed indeed that the periphery of the region is made up of structures of higher fractal dimension, while the bulk resulted more compact and had associated a lower fractal dimension. Plot in fig. 3.9 shows instead the exact opposite, with the highest fractal dimension measured in regions where the the contrast is higher and that are thus expected to be more compact. As already mentioned, this is most likely an effect of pixelization. Nevertheless, the effect could also be enhanced by the fact that structures are selected on images according to brightness criteria. It could thus be that only the most compact part of smallest regions is detected, thus biasing the result. For larger regions, instead, the field is 'more concentrated' even at the periphery of the regions, so that fractal dimension is higher. Unfortunately, it is difficult to verify these last statements with the data employed in the analyses presented in the previous and in this chapter. High resolution observations, as well as the employment of different fractal dimension estimators would allow to investigate the distribution of the magnetic field in active regions.

Chapter 4

The flux tube model

In this chapter I describe the concept of the Magnetic Flux Tube. In the first paragraph I describe the essential scheme of the model, as it was introduced by Spruit (1976) and how it can qualitatively reproduce some observed properties of magnetic structures characteristic of the solar photosphere. A description of the equations that physically describe the problem, that is the Magneto Hydro Dynamic equations, and their static version, the Magneto Hydro Static Equations, is also given. Since their solution is not simple, several simplifications and assumptions have been suggested in the literature. Here I present the two most used: the Thin Flux Tube approximation and the Force-Free tube approximation. A brief review of the 2D and 3D codes nowadays available to investigate magnetic features properties is finally given. When describing the basic concepts of the Flux Tube, I have followed the original works by Spruit (1976) and Spruit and Zwaan (1981). In the composition of the rest of the chapter, the reviews by Solanki (1993) and Steiner (2005b) have been very useful.

4.1 The concept of Flux Tube

The intimate connection between solar activity and presence of magnetic fields is clear since 1908, when Hale (Hale, 1908) conducted the first measurements of magnetic field in sunspots. Since then, observations carried out with more and more sophisticated instruments and techniques, have shown that most of the observed features and events that occur on the sun have a magnetic origin (see also chapter 1). Despite such experimental evidence, the physical processes that govern this connection are not clear and deserve more investigation. Observations in UV and X-ray spectral ranges, have shown that magnetic field in the upper regions of solar atmosphere (corona and chromosphere) manifests in very narrow field aligned features of enhanced emission. In the lowest regions of the atmosphere, the photosphere, high magnetic field concentrations appear as regions of either higher and lower contrast respect to the so called quiet sun, that is regions with null (or better to say 'very low') magnetic field. In particular, high resolution observations (sub arcsec) have shown that photospheric brilliant regions are most probably the result of the aggregation of small elements (some hundred kilometres), that have associated a high magnetic field (1-2 kilogauss). These experimental evidences give credit to the concept of flux tube, the theo-

retical model introduced by Spruit (1976) in order to investigate the properties solar magnetic field and the associated features observed at different layers of the solar atmosphere. The simplest magnetic Flux Tube consists of a region of the space of highly concentrated magnetic fields lines, surrounded by regions in which magnetic field is absent.

The concept of Flux Tube is of course an idealization of magnetic field line organization. The physics that govern these processes are determined by the ratio β of gas to magnetic pressure:

$$\beta = 8\pi \frac{P}{B^2} \tag{4.1}$$

where P is the pressure of external plasma and B is the magnetic field intensity. In the convective zone the gas pressure dominates and consequently $\beta \gg 1$. Near the photosphere $\beta \sim 1$ both in sunspots and small-scale field features. It can be shown that this is not accidental, since fields with $\beta \geq 1$ are subject to instabilities that restore the value of β to unity (Spruit and Zwaan, 1981). In the higher layers of the atmosphere gas pressure decays exponentially with height while magnetic field pressure decays as a power law. Consequently $\beta \ll 1$. Typical values in the lower corona are, for instance, between 10^{-4} to 10^{-1} in areas corresponding to active regions. Under these conditions the flux tube expands to fill the space, so the field lines diverge with height and fill the chromosphere, forming the so called 'magnetic canopy'. A sketch of the magnetic field configuration is given in fig.4.1. In this physical environment gas pressure is subject to large variations from a magnetic field line to an other, since small variations in magnetic field intensity can cause large variations in gas pressure. The flux tube model is used to understand properties of structures that are formed in the three regimes. Because β spans in a large range of values, these structures are governed by different physical processes and are characterized by different properties (like characteristic time scale, energy emission and spatial scale). In the following I will focus only on the $\beta \sim 1$ regime, that is only on structures typical of the photosphere (photospheric faculae, network and sunspots).

At photospheric level, magnetic structure are formed and stabilized by the interaction of the magnetic field with the convective plasma, as shown by numerical simulations (Weiss et al., 1996; Keller et al., 2004; Stein and Nordlund, 2006). Basically, the flux is expelled by the convective motions and pushed toward the boundaries of the overturning cells, where it is accumulated. The tube is held together by the balance between the outward pressure of the field and the inward force caused by a lower gas pressure inside the tube. In next paragraphs I will show that for slender tubes, that is for structures whose section is some hundred kilometres, and if no forces except gravity act on the gas inside the tube, at each height the horizontal pressure equilibrium requires that:

$$P_e(z) - P_i(z) = B^2/8\pi \tag{4.2}$$

where P_e is the pressure of the external un-magnetized plasma, P_i is the gas pressure inside the tube and B is the magnetic field intensity. According to convective collapse model (see paragraph 4.2.2) the gas density inside the tube is reduced and buoyancy makes the tube vertical. A simple sketch of a flux tube is depicted in fig.4.2.

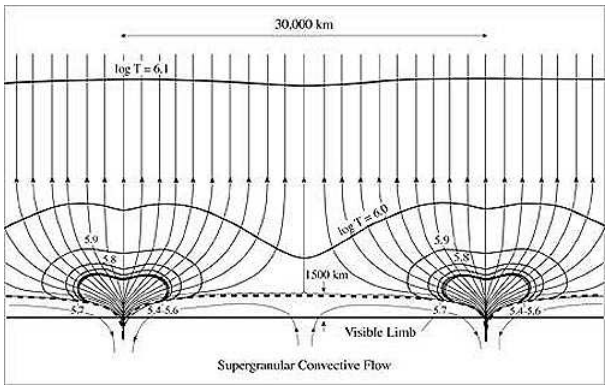

Figure 4.1: Structure of a magnetohydrostatic network model. Field lines are confined in small regions in the photosphere, where $\beta \sim 1$, forming the 'network'. Because gas pressure is highly stratified, at the highest levels of solar atmosphere $\beta \ll 1$ and field lines expand forming the 'canopy'. From Foukal (1990).

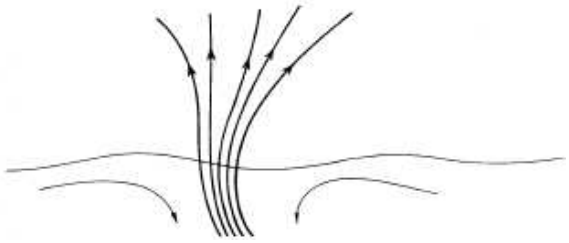

Figure 4.2: Sketch of a magnetic flux tube in the photosphere. Arrows indicate convective motion. In this sketch tube is not exactly vertical, but is inclined because of the interaction with surrounding convective plasma.

The interior and the field free medium are separated by a current sheet. If the tube is un-twisted (the internal field is potential), then its Radius as a function of depth and the field configuration inside are both determined by the magnetic flux and the pressure difference $P_e - P_i$. It can be shown it is impossible to find analytical solutions to this problem and therefore numerical solutions or other assumptions have to be made. Some of these models will be discussed in paragraph 4.2. I will mostly focus on static models, nevertheless it is important to notice that flux tubes are embedded in convective plasma, and are thus subject to motions and interaction with other magnetic structures. In fig.4.2, for instance, convective motion bends the tube that is inclined respect to the vertical direction.

4.1.1 Temperature stratification and photometrical properties

Because of the high magnetic field, convection is suppressed in flux tubes and radiation is the main energy transport mechanism. Consequently in the deeper layers of the photosphere, where convection is still efficient, the internal temperature is lower than external one. Since also the gas density inside the tube is lower than the external one the tube is less opaque than the un-magnetized plasma. The radiation is thus less attenuated inside the tube, that is heated by radiation channelling through the flanks from the hotter environment. This effect is efficient for tubes whose diameter is smaller or comparable with photon mean free path in the photosphere. For larger tubes the radiation that propagates through the flanks can not heat the whole structure which remains colder. The transitions between the two regimes is about 500 km (Knolker and Schussler, 1988; Spruit, 1976) (slightly less than 1 arcsec). Structures whose size is larger than this threshold are representative of micropores, pores and spots, whereas smaller structures reproduce photometrical properties of facular elements and network. In the following I will focus on these latter ones. The temperature profile inside the tube is therefore determined by the intensity of the magnetic field, that determines both pressure and convection efficiency reduction, with a consequent reduction of temperature, and the radiation channelling from the flanks of the tube, that causes an increase of temperature. This last process is dependent on opacity and is thus expected to be more important from few kilometres below the surface and above. In the deeper layers the large increase of opacity makes the channelling less efficient and the temperature inside the tube results lower than the external atmosphere. At higher levels the temperature increases to become eventually higher than the external one. In figure 4.3 the temperature stratification inside and outside a tube is shown. The two atmospheres have the same temperature at height zero, that corresponds, in this model by Fabiani-Bendicho et al. (1992), to the base of the photosphere. Below and above temperatures in the tube are lower and higher respectively.

The radiation intensity emitted depends on the temperature of the gas. It is very common, for instance, to assume black body radiation, so that the intensity is proportional to the 4th power of the temperature. The difference in the temperature stratification between the two atmospheres thus determines the photometrical properties of the structure. Depending on the height at which the $\tau = 1$ surface is located, that is the layers from which the radiation observed is coming, the same structure can have negative, null or positive contrast respect

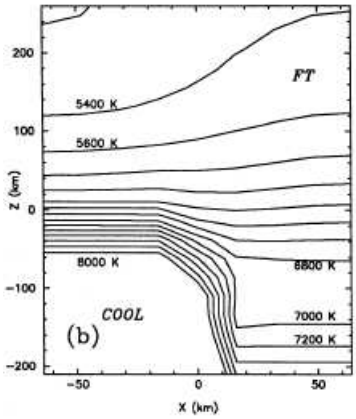

Figure 4.3: Sketch of temperature stratification inside (FT) and outside (COOL) a magnetic flux tube. Since the structure is symmetric only half of the tube is shown. Due to channelling at the same depth the temperature in the tube is lower, equal or higher than the temperature of external un-magnetized atmosphere. The $\tau = 1$ surface (thicker line) is located deeper in the tube. From Fabiani-Bendicho et al. (1992)

to the surrounding atmosphere. Note that the value of τ is determined by the opacity and since the atmospheres inside and outside the tube are different even the $\tau = 1$ surface is located at different heights. In particular, since the gas pressure is lower, in the tube the constant τ surface is located deeper than outside. A schematic example of the resulting shape of the surface is illustrated in fig. 4.4 (left) (this is also the original flux tube model by Spruit (1976)). The portion of the curve inside the tube is also referred to as 'floor' and the flanks as 'walls'. The difference of the heights at which the optical depths outside and inside the tube are equal to one is called *Wilson depression*. The opacity is a function of the wavelength so that the shape of the constant τ surface changes and the same magnetic structures have different contrast when observed with different wavelength filters. The position of the flux tube on the solar disk is an other important parameter in the determination of the magnetic features emissivity. When observed off disk center, in fact, more and more radiation coming from one of the flanks is visible. Because it can radiate almost freely into the vacuum, the temperature of the wall is expected to be relatively cooler respect to the layers located at the same geometric depth but further from the tube. Nevertheless, its intensity center to limb variation is opposite to the center to limb variation of the quiet sun and the contrast is thus enhanced toward the limb, where more 'wall' is visible respect to the 'floor'.

Figure 4.4 (right) shows the center to limb variation of the contrast simulated by Spruit (Spruit, 1976) for different physical and geometric conditions. The contrast value increases from the center to the limb, reaches a maximum at some disk position and decreases again at the limb. Spruit showed in particular that the CLV depends on:

- The CLV of the intensity of the surrounding quiet sun.

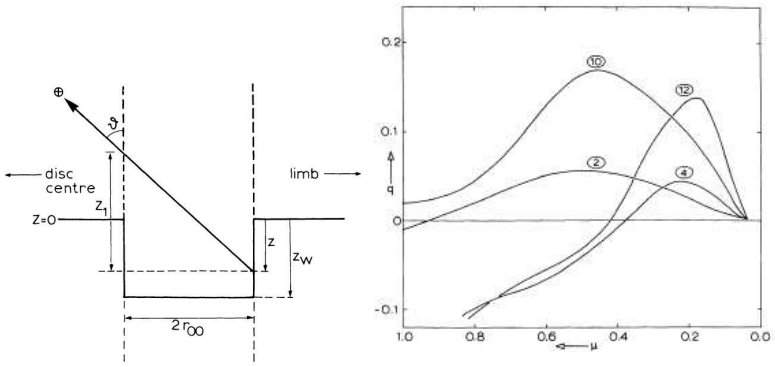

Figure 4.4: Left: Sketch of the Spruit model described in the text. Right: simulated center to limb variation of the contrast observed with a resolution of 0.3" for different models.

- Obscuration of part of the floor at wall from the center side wall
- The CLV of the radiation of the floor.

The observed CLV of the contrast is thus given by a combination of the CLV contrast of the floor:

$$C_f(\mu) = \frac{I_\lambda^f}{I_\lambda^q} - 1 \tag{4.3}$$

and the CLV of the contrast of the wall:

$$C_w(\mu, z) = (\frac{B_\lambda(T_w(z))}{I_\lambda^q} - 1)e^{-\tau(\mu,z)}. \tag{4.4}$$

where superscripts and subscripts q, f and w indicate the quiet sun, the floor and the wall respectively. $T_w(z)$ is the temperature of the wall and B_λ is the Plank function. The last equation 4.4 is valid under the assumption that the wall is emitting as a black body. According to this model, the maximum contribution from the wall to the contrast occurs at a position μ_0, where μ_0 satisfies:

$$\frac{D}{z_w} = \sqrt{1 - \mu_0^2}/\mu_0 \tag{4.5}$$

D is the tube diameter and z_w is the Wilson depression.

As confirmed by 2D and 3D MHD simulations (see 4.2.3), in spite of its simplicity this model picks the most important factors (the ones listed above) that determine the CLV of the observed contrast of bright elements in the solar photosphere.

Finally it is important to notice that this model can reproduce observations of continuum radiation. In the cores of lines the opacity inside the tube is higher and the contribution of the wall is less important. The model is then totally inadequate to explain contrast enhancements observed in the chromosphere (for example CaIIK observations) or in the outer layers of the atmosphere, where other mechanisms like wave propagations and magnetic field reconnection take place.

4.2 The Magneto Hydro Dynamic Equations

Realistic simulations of magnetic features have to solve the Magneto Hydro Dynamic Equations (MHD):

Energy

$$\begin{aligned}\frac{\partial \rho e}{\partial t} + \frac{\partial \rho e u_k}{\partial x_k} &= -p\frac{\partial u_k}{\partial x_k} - \frac{\partial q_k}{\partial x_k} + \frac{\eta}{4\pi}\epsilon_{ijk}\epsilon_{ilm}\frac{\partial B_k}{\partial x_j}\frac{\partial B_m}{\partial x_l} + \\ &+ \mu\left[(\frac{\partial u_i}{\partial x_j} + \frac{\partial u_j}{\partial x_i})\frac{\partial u_j}{\partial x_i} - \frac{2}{3}(\frac{\partial u_k}{\partial x_k})^2\right] \end{aligned} \tag{4.6}$$

Momentum

$$\begin{aligned}\frac{\partial \rho u_j}{\partial t} + \frac{\partial \rho u_j u_k}{\partial x_k} &= -\frac{\partial p}{\partial x_j} - \frac{1}{8\pi}\frac{\partial B_k B_k}{\partial x_j} + \\ &+ \frac{1}{4\pi}B_k\frac{\partial B_j}{\partial x_k} + \rho g_i + \mu(\frac{\partial^2 u_j}{\partial x_k \partial x_k} + \frac{1}{3}\frac{\partial}{\partial x_j}\frac{\partial u_k}{\partial x_k}) \end{aligned} \tag{4.7}$$

Induction

$$\frac{\partial B_j}{\partial t} + \frac{\partial B_j u_k}{\partial x_k} = B_k\frac{\partial u_j}{\partial x_k} + \eta\frac{\partial^2 B_j}{\partial x_k \partial x_k} \tag{4.8}$$

Continuity

$$\frac{\partial \rho}{\partial t} + \frac{\partial \rho u_k}{\partial x_k} = 0 \tag{4.9}$$

Here $\mathbf{u}$ is the velocity of the gas, ρ and p are its density and pressure respectively, B is the magnetic field intensity, $\mathbf{g}$ is the gravitational acceleration vector. $\{j, k, l\}$ specify direction in space, t is the time and q is the total flux. The internal energy e is given by $e = C_V \rho T$, where C_V is the specific heat at constant volume and T is the temperature of the gas. Symbols μ and η are the dynamic viscosity and the magnetic diffusivity respectively. We also have:

$$p = \frac{K_B}{m_e}\rho T \tag{4.10}$$

where K_B is the Boltzmann's constant and m_e is the mean molecular weight. We also need an other relation to close the equations, that is the Gauss Law of Magnetism:

$$\frac{\partial B_k}{\partial x_k} = 0. \tag{4.11}$$

The quantities μ, η, C_V and m_e are gas properties and are functions of the physical conditions (temperature, pressure, density). Their determination in general requires to compute the complete ionization and excitation equilibria of all the atomic and molecular species that compose the gas.

The total flux q is given by the sum of the flux of all the mechanisms that contribute in the transportation of energies. In the convective and photospheric

layers, the major energy transportation mechanism are *Convection* and *Radiation*. The radiative flux is defined by:

$$F_R = \int\int I_\nu \cdot \vec{n} d\Omega d\nu \tag{4.12}$$

where ν is the frequency of the radiation, Ω is the solid angle and $\vec{n}$ is the unit vector that describes the propagation direction of the radiation. In the literature it is very common to evaluate the Radiative Flux using the *diffusion approximation* (see chapter 5):

$$F_R = -K_R \frac{dT}{dx_k} \tag{4.13}$$

where K_R is the radiative diffusion coefficient. As I will show, this approximation is valid in the deeper layers of the sun atmosphere, where the optical depth is larger than unity. In the outer layers this approximation is not valid and a detailed calculation of the radiation field (that is I_ν for each propagation direction and each position in the space) is required. In next chapter I will explain theoretical and numerical approaches to this problem. The convective flux is, in turn, often evaluated by the Mixing Length Theory (Vitense, 1953).

4.2.1 Magneto Hydrostatic Static Equations

Classes of solutions to the problem are obtained in the case of a Static flux tube, whose equations are obtained imposing $\vec{u} = 0$ and $\partial/\partial t = 0$ in previous equations. This new set of equations are known in the literature as the Magneto Hydrostatic (MHS) equations. These are generally solved in a non uniform medium, in which the magnetic field is concentrated in a certain region, i.e. the flux tube, surrounded by a field free medium. For computational purposes the magnetic structures are usually modelled as axially symmetric tubes. Even in this case, the exact solution of the problem can be tricky and other assumptions are generally made in order to simplify the equations. In the following I will discuss the Thin Flux Tube and the Force Free Approximations, since these are the most common approximations used in the literature.

The Thin Flux Tube Approximation

This model assumes that the width of the tube (its diameter) is smaller than the pressure scale height of the gas $H_p = \frac{p}{\rho g}$. The dependent variables are expanded in a power series of the radial coordinate r (evaluated from tube axis):

$$f(r,z) = \sum_{n=0}^{\infty} \frac{r^n}{n!} \left(\frac{\partial^n f}{\partial r^n} \right) \Big|_{r=0} \tag{4.14}$$

where f is a general physical quantity (magnetic field intensity, pressure, density etc.). The case in which only the zero order term is kept corresponds to 'Thin Tube approximation'. Under this assumption all the physical variables are assumed to be averages over the tube cross section and vary only along the tube. The MHS equations then become:

$$\frac{B^2(z)}{8\pi} + p_m(z) = p_s(z) \tag{4.15}$$

$$\frac{dp_{m,s}}{dz} = \rho_{m,s} g \tag{4.16}$$

$$\pi R^2(z) B(z) = \phi = const. \tag{4.17}$$

$$p_{m,s} = \frac{k}{m_e} \rho_{m,s} T_{m,s} \tag{4.18}$$

$$\nabla \cdot (F_C + F_R) = 0 \tag{4.19}$$

Indices m and s describe quantities within and external to the flux tube respectively. R is the radius of the tube and note it is a function of depth z. In this approximation magnetic curvature is neglected and the vertical and horizontal components of the pressure balance decouple from each other. Note also that both convective and radiative flux still have non zero derivatives respect to r only at $r = R$. This approximation is also used very often in dynamical models (Fan, 2004), nevertheless it is interesting to notice that condition 4.15 is satisfied instantaneously, since the time travel of acoustic waves is lower than any other typical dynamic scale of the tube.

Force-Free and Potential Field

Equation 4.7, under static conditions, can be rewritten using a compact form as

$$-\nabla p + \frac{1}{4\pi} (\nabla \times B) \times B + \rho g = 0 \tag{4.20}$$

If the magnetic field is sufficiently strong to dominate the other forces, than the force-free condition :

$$(\nabla \times B) \times B = 0 \tag{4.21}$$

holds. For the interior of a flux tube this condition is valid if $\beta \ll 1$. Small scale magnetic fields are expected to fulfil this requirement in most of the cases. In absence of electric currents $\nabla \times B = 0$, the field is potential and there exists a scalar field φ that satisfies:

$$\nabla \varphi = -B \tag{4.22}$$

The field in a flux tube can be potential if the structure is untwisted and axially symmetric. A potential field surrounded by a thin (from 2 to 10 km, (Steiner, 1994)) current sheet and in pressure equilibrium with the surrounding atmosphere is a good approximation to the magnetic structure of the tube.

A simple Flux Tube model

Under the assumption of a thin flux tube the vertical force balance is expressed by eq.4.16 and the horizontal force balance is given by eq.4.15. Let us assume that at each depth the equality $T_m(z) = T_s(z)$ is satisfied. Then, from the ideal gas law, it follows that

$$\frac{d \ln P_s}{dz} = \frac{d \ln P_m}{dz} \tag{4.23}$$

where the molecular weight is assumed to be the same inside and outside the tube. It follows that the rationP_m/P_s is constant with depth and so is β. Since the tube is thin, the magnetic field does not vary with r and the flux is given by

$$\phi = \pi B R^2 = \pi R^2 \left(\frac{8\pi P}{\beta} \right)^{0.5} \tag{4.24}$$

from which

$$R = \left(\frac{\phi}{\pi}\right)^{0.5} \left(\frac{8\pi P}{\beta}\right)^{-1/4} \tag{4.25}$$

This relation shows that if the magnetic flux is constant then, since the gas pressure decreases with height, R increases that means that the tube expands. Of course the more the tube expands the more the radial component of the magnetic field increases and the more the tube is 'not thin'. As already explained, the approximation is valid as long as $R \leq H_p$. More precisely, if B_r is the radial component of magnetic filed, it follows from previous discussion that:

$$\left|\frac{B_r}{B}\right| = \left|\frac{dR}{dz}\right| = R\left|\frac{d\ln R}{Bdz}\right| = \frac{R}{4H_p} \tag{4.26}$$

The condition of thin approximation is thus valid if $R < 4H_p$.

The models and assumption described above are static. More detailed calculations and observations have shown that magnetic structures are highly dynamic (see for instance 4.2.3). The different kinds of waves that propagate along them (Spruit and Zwaan, 1981), the interaction of the surrounding convectivelly unstable plasma and with other magnetic features cannot be described by previous models.

4.2.2 Formation and Destruction of Intense Magnetic Flux Tubes

Formation

Two main mechanisms have been proposed to explain the formation of intense magnetic flux structures: the flux expulsion and the convective collapse. According to the first mechanism, magnetic field is expelled by upflow convective regions and is advected to downflow regions by granular and supergranular motions. The order of magnitude of the field strength is given by the equipartition field strength, that is the magnetic field is concentrated until the Lorentz force inhibits convection:

$$\frac{B^2}{8\pi} = \frac{\rho}{2}v^2 \tag{4.27}$$

where ρ and v are granular density and velocity respectively. Typical values of these quantities give $B \approx 400G$ and is thus not enough alone to explain concentrations of the order of kG. Nevertheless, let us suppose that at this point an adiabatic downflow occurs in the tube. Than the tube becomes cooler than the surrounding superadiabatic atmosphere and the pressure of the gas decreases. The tube consequently evacuates and contracts until $B \approx (8\pi p_{ext})^{1/2}$. This model is known as the "convective collapse" and was first proposed by Parker (1978). Using this model, Spruit (1979) obtained that an equilibrium of these structures states at $1280 < B < 1650G$, in agreement with observations.

While the first process has been observed and analyzed through 2-D and 3-D numerical simulations (e.g. Nordlund (1983); Hurlburt and Toomre (1988); Vogler et al. (2005)), some aspects of the convective flux process are still unclear. Numerical 3D simulations have in fact shown that if the lower boundary is kept open, the material inside the tube keeps going down and no equilibrium is reached (Solanki, 1993). An oscillatory steady state is reached when

the lower boundary is close (Hasan, 1984, 1985). More recently Cameron and Galloway (2005) have argued that convective collapse on the sun is likely to be effective only for structures of scale of about 10 km. Stein and Nordlund (2006) showed that flux tubes are evacuated at superficial layers (at $\tau = 1$ surface), but that their internal density exceeds the external one at greater depth. They also included flux tube emergence from the deeper layers of the Sun. Finally, Cattaneo (1999); Emonet and Cattaneo (2001); Cattaneo et al. (2003) have suggested that a great part of the magnetic field in the photosphere is generated by Local Dynamo processes associated with granular motions.

Destruction

There are two classes of phenomena that determine the destruction of magnetic structures: processes that remove the magnetic flux and processes that do not. The former types are related to cancellation mechanisms of magnetic flux structures of different polarities. If the cancellation occurs at photospheric level, than the associated energy release may be visible. More recently it has been suggested that magnetic field loops can be pushed down by downflow convective motion thus causing a net magnetic flux reduction (e.g. Stein and Nordlund (2006)). In unipolar regions, fragmentation and coalescence of structures can occur because of the interaction with convective plasma. It has been suggested that small scale magnetic structures can be stable only if surrounded by strong whirl flows (Steiner, 1990; Bunte, 1992). If the whirl ceases, for instance because of the granular motions, than the tube becomes unstable and dissolves in few minutes. This process takes the name of flute instability. If their diameter is below 10km (Solanki, 1993), the fragments so produced are heated by radiative channelling The pressure scale height thus increases and the magnetic field pressure is reduced to the equipartition value given by 4.27. Flux tubes can also be destroyed by strong upflows. These last processes do not involve a net change in magnetic flux through the surface.

4.2.3 Brief review of Numerical Codes of Magnetic Flux Tubes

The models described above were obtained with great simplifications and assumptions about the atmosphere and the magnetic field. More realistic results are obtained by solving the MHS or the MHD equations. Note that however, most of the times, even these simulations are based on some assumption or approximation, like the thin flux tube. In the past numerous authors have solved these equations in order to investigate the physical properties of solar magnetic structures and to interpret the numerous, and often discrepant, observations. Basically two classes of codes have been developed: 2D and 3D.

2D Numerical Codes

There are basically two approaches to the direct solution of the MHS equations: the direct iterative solution and a relaxation approach.

In the first approach MHD equations are solved starting from a prescribed field and plasma configuration, until a stationary or static solution is achieved. The models developed by Deinzer et al. (1984a,b); Knolker and Schussler (1988)

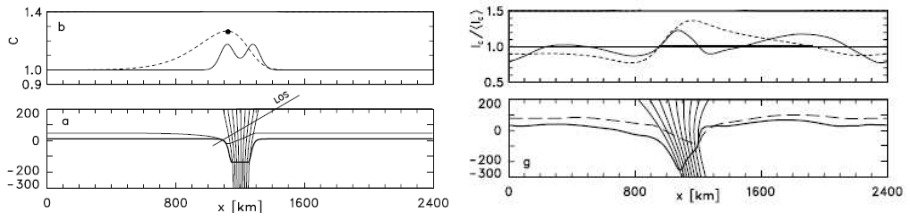

Figure 4.5: Example of static (left) and dynamic (right) 2-D flux tube model, from Steiner (2005a). Left: a) Magnetic flux concentration and $\tau = 1$ surfaces for vertical line of sight (thick line) and as seen with an angle of 60 deg (thin line). b)Continuum contrast corresponding to lines of sight (LOS) of panel a): continuous line corresponds to LOS=0 deg and dashed line to LOS=60 deg. At disk center (vertical line of sight), the contrast shows two bumps in correspondence of the (inclined) tube flanks, that are hotter than the central part of the tube. The contrast is higher when observed at LOS=60 deg, because more wall is visible, as shown by a comparison of the two $\tau = 1$ surfaces. Right: snapshot of a 2-d dynamical simulations. a)Magnetic flux concentration and $\tau = 1$ surfaces for vertical line of sight (continuous line) and as seen with an angle of 60 deg (dashed line). b)corresponding contrast convoluted with a Gaussian in order to mimic a resolution of 0.1". Because of the interaction with the convective plasma, the tube is deformed, and so is the observed contrast at different positions on the disk.

are of this type. The input parameters to these models are: the geometrical dimension of the computational box; the initial density reduction factor inside the tube; the total magnetic flux across the boundaries; the temperature at the bottom boundary; the temperature gradient at the top boundary. The total magnetic flux and matter are assumed constant during the calculations. The energy equation assumes usually gray radiative diffusion and the Mixing Length formalism for radiative and convective processes respectively. Once the stationary state is reached, the radiative properties of the structures are then investigated by a radiative transfer code based on the short characteristic technique (see chapter 5). Models in which radiative diffusion is not assumed and a more realistic radiative intensity field is computed numerically have also been developed (Steiner et al., 1998).

The second approach assumes that the tube is already in Hydrostatic equilibrium and solves the MHS equation using the formalism introduced by Low (1975). Pizzo (1986) developed a numerical technique to solve these equations even in the case in which a thin flux tube is not assumed. In these models the following parameters are specified: the filling factor, that is the square of the ratio of the tube radius to the width of the computational domain; the magnetic field strength; the radius or the total magnetic flux of the tube. The energy equation is replaced by specifying the atmosphere inside and outside the tube. Usually 1-D atmospheric models are assumed and the photometrical properties of structures are investigated by using a radiative transfer code. Radiative transfer was included in these models for instance by Pizzo et al. (1993) and by Steiner (1990). Steiner and Pizzo (1989) have realized a parametric survey of these kind of models. They showed that the radiative heating from

the tube flanks causes an increase of the gas pressure inside the tube, that fans out in order to maintain the pressure balance until it merges with the field of neighbour tubes thus forming the canopy. Thus hotter tubes are expected to expand faster then cooler tubes. They also estimated the height at which the canopy would form and found values consistent with the ones inferred from observations. The radiative heating also increase the opacity inside the tube. The surface at which the optical depth is equal to one is consequently shifted up to cooler regions thereby reducing the contrast.

3D Numerical Codes

3D numerical codes that solve the MHD equations have also been developed. These codes allow usually a more detailed description of convective motions and thus give an insight of the interaction of magnetic field with the surrounding plasma.

Even in this case two kind of approaches exist in the literature. One approach consists in simplifying the equations and exploring the possible solutions at the variation of some parameters. Simulations carried out by Cattaneo et al. (1991); Hurlburt et al. (1996); Brummell et al. (1998); Porter and Woodward (2000); Emonet and Cattaneo (2001); Bushby and Houghton (2005) belong to this first group. A second approach solves instead to more realistic simulations of physics in order to reproduce more realistically the observations. The works by Nordlund (1985); Freytag et al. (1996); Asplund et al. (2000); Keller et al. (2004); Vogler et al. (2005); Stein and Nordlund (2006) are an example of this second approach. Being very time consuming, the MHD equations are solved in boxes that correspond to small portions of the solar atmosphere. They thus usually simulate few square Megametres of the surfaces, extend from some hundreds to some thousand kilometres depth in the atmosphere and have a resolution of few tens of kilometres per pixel.

Such simulations allow to investigate the formation, the dynamic and the destruction mechanism of magnetic flux concentrations. Vogler et al. (2005), for instance, analyzed snapshots obtained initializing the system with uniform vertical magnetic field of different magnetic flux density. They obtained, in agreement with other works (e.g. Stein and Nordlund (2006)), that magnetic field concentrates in the downflow regions forming elongated structures, rather than round and symmetric tubes. Micropores, of sizes of about 1000km, are formed in locations where several downflow regions merge. In other regions, by contrast, the field is weak and randomly oriented, indicating that even the so called Quiet Sun is not field free (see also Khomenko et al. (2005); Socas-Navarro and Sanchez Almeida (2003)). They have also shown that highest magnetic filed concentration regions have maximum brightness comparable (or higher) with the ones of brightest granules, although most of the magnetic structures have associated a lower contrast. They suggest the channelling of radiation to be the main mechanism of emissivity enhancement, thus confirming results obtained with 2D codes. The heating is very small though, since the temperature enhancement induced by the radiative channelling is compensated by the radiative losses in the vertical direction. These simulations have also shown that in regions of high magnetic field concentration the sum of the average gas and magnetic pressure is comparable with the gas pressure of weak-field regions.

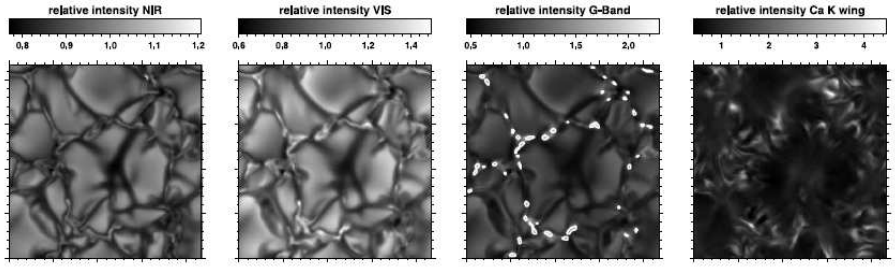

Figure 4.6: Snapshots of a 3D simulations of Magnetoconvection as observed in different wavelengths. From left to right: NIR (continuum band at 1626nm), VIS (continuum band at 575nm), G band (at 430.5nm), wing of the CaIIK line at 393.4nm. From Tritschler and Uitenbroek (2006). The contour lines in the G band image underline very high contrast regions called bright points. The simulations show that magnetic structures appear, at different wavelengths, as filaments and "flower" or "ribbon" like, especially in the CaII K wing image.

Ultimately, 3D sophisticated codes allow to study in more details the interaction of magnetic filed with convection, and have revealed the highly dynamic nature of the magnetic features and can reproduce most of the observations (e.g. DePontieu et al. (2006); Keller et al. (2004)). Nevertheless, they have shown that most of the observed properties are in agreement with the ones predicted by simplified models like the ones based on the hot wall and the thin tube approximation. It is important to notice that these simulations are usually characterized by very high resolution (at least one order of magnitude higher than the one that can be achieved with modern instrumentation) and can reproduce very limited portion of the solar atmosphere. They are thus more representative of very small features, like the network or small faculae. At larger scales other physical processes can take place and determine the formation, evolution and dissipation of magnetic active regions.

Chapter 5

The Radiative Transfer Equation and the Short Characteristic technique

In this chapter I introduce some basic concept about radiative transfer problem in stellar atmospheres. In particular I will describe the radiative transfer equation, focusing on the plane parallel geometry and gray approximation. I will illustrate some analytical and approximate solution to the equation, with particular attention to models I have used for the numerical simulations shown in next chapters. As the radiative transfer equation cannot be solved analytically in most of the cases, in the second part of the chapter I describe the technique I employed to numerically solve it: the Short Characteristic. The end of the chapter is dedicated to the description of two numerical techniques employed to evaluated the mean intensity integral and the total radiative flux: Carlson quadrature scheme and Gauss-Legendre quadrature scheme. Tests and discussions of these numerical techniques are the topics of next chapter.

5.1 The Radiative Transfer Equation

We want to formalize the energy transport mechanism through a medium by radiation. Let us consider the amount of energy dE_ν transported through the area dA at location r, between times t and $t+dt$, at frequency band between ν and $\nu+d\nu$, over the solid angle $d\Omega$:

$$dE_\nu = \ I_\nu(\vec{r},\vec{l},t)(l\cdot n)dAdtd\Omega d\nu \ = I_\nu(x,y,z,\theta,\phi,t)\cos\theta dAdtd\Omega d\nu \qquad (5.1)$$

where n is the normal to dA, $\vec{l}$ is the direction of propagation of radiation, and θ and ϕ are spherical polar coordinates. I_ν is the monochromatic specific intensity, and, for infinitesimal time interval, area, band width and solid angle, it represents the energy carried by photons along a ray. In the following it will be expressed by the units: $erg\cdot s^{-1}\cdot cm^{-2}\cdot Hz^{-1}\cdot ster^{-1}$.
As will be shown in next paragraphs, photons and matter interact by emission and absorption processes, so that energy is removed and added to a beam when radiation passes thorough a medium. We therefore define the *monochromatic*

emissivity j_ν the quantity that describe the intensity contribution from local emission to a beam:

$$dI_\nu(\vec{r},\vec{l},t) = \ j_\nu(\vec{r},\vec{l},t)ds \tag{5.2}$$

and the *monochromatic extinction coefficient* α_ν as the quantity that specifies the energy fraction taken from a beam by absorption processes:

$$dI_\nu(\vec{r},\vec{l},t) = \ -\alpha_\nu(\vec{r},\vec{l},t)I_\nu(\vec{r},\vec{l},t)ds \tag{5.3}$$

where s is the geometrical path length along the beam and is expressed in cm. Units for j_ν are $erg\cdot s^{-1}\cdot cm^{-3}\cdot Hz^{-1}\cdot ster^{-1}$, while units for α_ν are cm^{-1}. α_ν also represents the cross-section per unit volume. The length $l_\nu \equiv 1/\alpha_\nu$ is the mean free path of photons of frequency ν in the material. The local amount of intensity variation of a beam caused by absorption and emission events along the geometrical path ds is therefore:

$$dI_\nu(\vec{r},\vec{l},t) = \ j_\nu(\vec{r},\vec{l},t)ds - \alpha_\nu(\vec{r},\vec{l},t)I_\nu(\vec{r},\vec{l},t)ds \tag{5.4}$$

where

$$dI_\nu(\vec{r},\vec{l},t) = \ I_\nu(\vec{r}+\Delta\vec{r},\vec{l},t+\Delta t) - I_\nu(\vec{r},\vec{l},t) \tag{5.5}$$

and $\Delta t = ds/c$. Moreover

$$I_\nu(\vec{r}+\Delta\vec{r},\vec{l},t+\Delta t) = \ I_\nu(\vec{r},\vec{l},t) + [(1/c)(\partial I/\partial t) + (\partial I/\partial s)]ds \tag{5.6}$$

Substituting this latter relation into eq.5.3 we obtain the **Radiative Transfer Equation** (RTE)

$$[(1/c)(\partial/\partial t) + (\partial/\partial s)]I_\nu(\vec{r},\vec{l},t) = \ j_\nu(\vec{r},\vec{l},t) - \alpha_\nu(\vec{r},\vec{l},t)I_\nu(\vec{r},\vec{l},t) \tag{5.7}$$

In the following I will assume static media and a one-dimensional plane parallel atmosphere, so that eq.5.7 reduces to

$$\mu\cdot\partial I_\nu(z,\mu)/\partial z = \ j_\nu(z,\mu) - \alpha_\nu(z,\mu)I_\nu(z,\mu) \tag{5.8}$$

where μ is the cosine of the angle between the direction of propagation of radiation and the vertical coordinate z, that is $\mu ds = dz$. Previous equation is often written as:

$$\mu\cdot\frac{\partial I_\nu}{\alpha_\nu\partial z} = \ S_\nu - I_\nu \tag{5.9}$$

where $S_\nu = \frac{j_\nu}{\alpha_\nu}$ is the Source Function and has units $erg\cdot s^{-1}\cdot cm^{-2}\cdot Hz^{-1}\cdot ster^{-1}$. When multiple processes contribute to local emission and extinction the total source function is

$$S_\nu^{Tot} = \ \frac{\sum j_\nu}{\sum \alpha_\nu} \tag{5.10}$$

where each pair of j_ν and α_ν describes a different process.

Generally in stellar atmosphere studies eq.5.9, that requires the knowledge of variables (α_ν,S_ν), is preferred to eq.5.8, that requires the knowledge of the variables (α_ν,j_ν). This latter two quantities can vary in fact some orders of magnitude for a line transition, while variations cancel out in their quotient. In eq.5.9 therefore the parameter α_ν describes atomic particles properties, while the source function takes into account of the thermodynamic properties of the medium, which is regarded as an ensemble of particles and photons.

Eq.5.9 is more often written as

$$\frac{\partial I_\nu}{\partial \tau_\nu} = \; S_\nu - I_\nu \tag{5.11}$$

where

$$d\tau_\nu \equiv \; \alpha_\nu ds \tag{5.12}$$

τ_ν is the *monochromatic optical thickness* and for a medium of thickness D is

$$\tau_\nu(D) = \int_0^D \alpha_\nu(s) ds \tag{5.13}$$

τ_ν also describes the probability interaction of photons along their path. A layer is *optically thick* for $\tau_\nu(D) > 1$ and *optically thin* for $\tau_\nu(D) < 1$. In stellar atmosphere radiative transfer literature, instead of the optical thickness, that is measured along the beam in the photon propagation direction, one usually adopts the concept of *optical depth*. Since I am assuming plane parallel atmosphere, and if the z-axis is taken positive toward the direction of the observer, the angle-dependent **optical depth** is

$$d\tau_{\nu,\mu} \equiv \; -\alpha_\nu \frac{dz}{|\mu|} \tag{5.14}$$

where $\mu > 0$ indicates outward directions, that is rays that propagate from some location in the stellar atmosphere to the observer, and $\mu < 0$ inward directions, that is rays that propagate from the observer to the interior of the atmosphere. In many calculations is particularly handy to use the **radial optical depth** τ_ν, defined as:

$$\tau_\nu(z_0) = \int_\infty^{z_0} -\alpha_\nu dz \tag{5.15}$$

With this definition $\tau_\nu = 0$ at $z = \infty$, where the observer's eye is located. Eq.5.11 can then be written as

$$\mu \frac{dI_\nu(\tau_\nu)}{d\tau_\nu} = \; I_\nu(\tau_\nu) - S_\nu(\tau_\nu) \tag{5.16}$$

5.1.1 The exact solution

Let us consider a plane parallel slab bounded by the surfaces τ_1 and τ_2. The analytical solution of eq.5.16 is

$$I_\nu(\tau_{\nu,2}, \mu) = \; I_\nu(\tau_{\nu,1}, \mu) \cdot \exp^{-(\tau_{\nu,2} - \tau_{\nu,1})/\mu} + \frac{1}{\mu} \int_{\tau_{\nu,1}}^{\tau_{\nu,2}} S_\nu(t_\nu) \exp^{-(t_\nu - \tau_{\nu,2})/\mu} \, dt_\nu \tag{5.17}$$

For a semi-infinite slab, the solution for the outgoing radiation is:

$$I_\nu^{out.}(\tau_\nu, \mu) = \; \frac{1}{\mu} \int_{\tau_\nu}^{\infty} S_\nu(t_\nu) \exp^{-(t_\nu - \tau_\nu)/\mu} \, dt_\nu \quad (0 \leq \mu \leq 1) \tag{5.18}$$

where I have imposed that

$$\lim_{\tau_\nu \to \infty} \exp^{-\tau_\nu/\mu} I_\nu(\tau_\nu, \mu) = 0 \tag{5.19}$$

For the incoming radiation

$$I_\nu^{inc.}(\tau_\nu, \mu) = \frac{1}{\mu} \int_0^{\tau_\nu} S_\nu(t_\nu) \exp^{-(\tau_\nu - t_\nu)/\mu} dt_\nu \quad (-1 \leq \mu \leq 0) \tag{5.20}$$

5.1.2 Moments of Intensity

To formally describe the propagation of radiation through an atmosphere, the following three moments of intensity respect to μ are often used:

$$J_\nu(z) \equiv \frac{1}{2} \int_{-1}^{1} I_\nu(z, \mu) d\mu \tag{5.21}$$

$$H_\nu(z) \equiv \frac{1}{2} \int_{-1}^{1} I_\nu(z, \mu) \mu d\mu \tag{5.22}$$

$$K_\nu(z) \equiv \frac{1}{2} \int_{-1}^{1} I_\nu(z, \mu) \mu^2 d\mu \tag{5.23}$$

Each of them has the dimension of intensity. J_ν is the intensity integrated over the solid angle; H_ν is related to the flux F_ν by the relation $H_\nu = F_\nu/4\pi$; K_ν is related to the radiative pressure by $p_\nu = (4\pi/c)K_\nu$. J_ν and H_ν are always positive, while K_ν can be negative. The following relations among these moments provide more radiative transfer equations. The first one is found integrating the radiative transfer equation 5.16 in μ, and supposing isotropic source function,

$$\frac{1}{2} \int_{-1}^{1} \mu \frac{dI_\nu}{d\tau_\nu} d\mu = \frac{1}{2} \int_{-1}^{1} I_\nu d\mu - \frac{1}{2} \int_{-1}^{1} S_\nu d\mu \tag{5.24}$$

$$\frac{dH_\nu}{d\tau_\nu} = J_\nu(\tau_\nu) - S_\nu(\tau_\nu) \tag{5.25}$$

or

$$-\frac{dH_\nu(z))}{dz} = k_\nu \rho (J_\nu(z) - S_\nu(z)) \tag{5.26}$$

which means that the divergence of the radiative flux equals the difference between the angle averaged emitted energy and the angle averaged absorbed energy. The second one is found multiplying the radiative transfer equation eq.5.16 by μ and integrating:

$$\frac{1}{2} \int_{-1}^{1} \mu^2 \frac{dI_\nu}{d\tau_\nu} d\mu = \frac{1}{2} \int_{-1}^{1} \mu I_\nu d\mu - \frac{1}{2} \int_{-1}^{1} \mu S_\nu d\mu \tag{5.27}$$

$$\frac{dK_\nu}{d\tau_\nu} = H_\nu(\tau_\nu) \tag{5.28}$$

differentiating again we obtain the *second order* version of the radiative transfer equation

$$\frac{dK_\nu^2}{d\tau_\nu^2} = J_\nu(\tau_\nu) - S_\nu(\tau_\nu) \tag{5.29}$$

Note that this last equation is equivalent to eq.5.26 and it also represents the divergence of the radiative flux. Similar expressions are obtained for frequency integrated quantities. These expressions are very powerful for solving radiative transfer problems, since they eliminate the angle dependence, thus reducing the dimensionality.

5.1.3 TE and LTE

Since the atmosphere of a star vary its composition and physical properties in space and time, it is necessary to make some assumptions. The simplest assumption is that of *Thermodynamic Equilibrium* (TE). It prevails when matter and radiation are in equilibrium and therefore a single value of temperature T determines particles temperature, atomic states population and the local ratio between emission and absorption. In this state particles have Maxwellian velocity distribution, atomic population levels are described by Saha-Boltzmann equations and radiation field has a black body form given by the Kirchhoff-Plank function. This state is an idealization and is never realized. However stellar atmospheres often satisfy *local thermodynamic equilibrium* (LTE), which occurs when the thermalization length is shorter then the length over which the temperature of the gas changes markedly. When this condition is satisfied, one can assume that the source function is expressed by the Kirchhoff-Plank function:

$$S_\nu = B_\nu(T) \equiv \frac{2h\nu^3}{c^2} \frac{1}{e^{\frac{h\nu}{kT}} - 1} \tag{5.30}$$

where h is the Plank constant and k is the Boltzman constant. LTE can be valid for one particular process or line, while could be wrong for an other. A general rule is that the continuum in the visible and infrared, the wings of most spectral lines and the entire profile of weak lines, are formed in LTE, while the line cores and strong lines are not. Departure from LTE in strong lines or cores of weak lines is due to the non-thermal distribution of atomic levels, while the electrons still maintain Maxwellian distribution. LTE is not a valid assumption in solar corona and wind either. In these regions of the solar atmosphere, in fact, density is low and matter-radiation interactions are too few to establish thermodynamic equilibrium. In the following I will assume always LTE.

5.1.4 Radiation Matter interaction

Radiation interacts with matter through several processes of *absorption*, by which energy removed from the beam is converted into medium thermal energy, and *emission*, by which energy is emitted into the beam at the expenses of material energy. Whether or not a particular process occurs and its contribution to the energy of the beam depends on photon frequency and matter chemical composition and temperature. In addition to these processes, we also have to consider scattering. When a photon interacts with a scattering center it emerges in a different direction, but none (or very little) of its energy goes into

the thermal energy of the gas. As a consequence the beam is attenuated, but its energy is conserved. Radiation-Matter interaction processes determine the opacity, and thus the optical depth τ, and the Source function in eq.5.16. In the typical temperature range of stellar atmospheres ($10^4K \leq T \leq 10^6K$), the following processes are dominant: bound-bound transitions; bound-free transitions; free-free transitions; Thomson scattering. At lower temperatures other physical processes may become important: negative ion absorption; molecular absorption; Rayleigh scattering; Raman scattering; Photo-excitation to autoionizing states. With the exception of Thomson scattering, the cross sections of the processes depend generally on photon energy, particle density, temperature of the medium, populations of atomic levels. Bound-bound transitions occur at fixed wavelength, and contribute mainly to line formation, while the other processes contribute to the continuum spectrum. Other processes, like cyclotron radiation, synchrotron radiation and plasma radiation, may affect the continuum, but only at higher energies, that on the sun occur only during flares and other eruptive events. Cross sections of all these processes are known by laboratory experiments or theoretical calculations, once chemical composition and physical properties of the medium are known.

5.1.5 Rosseland Mean opacity

The Rosseland mean opacity k_R is expressed by the formula:

$$\frac{1}{k_R} \equiv \frac{\int_0^\infty \frac{1}{k_\nu} F_\nu d\nu}{\int_0^\infty F_\nu d\nu} \tag{5.31}$$

where k_ν is the total monochromatic absorption coefficient corrected for electron scattering and induced emission. This the harmonic mean opacity weighted by the Flux F_ν. If we assume LTE and large optical depths, it can be shown (see next paragraph, in *optically thick* section) that

$$\frac{1}{k_R} \equiv \frac{\int_0^\infty \frac{1}{k_\nu} \frac{\partial B_\nu(T)}{\partial T} d\nu}{\int_0^\infty \frac{\partial B_\nu(T)}{\partial T} d\nu} \tag{5.32}$$

This formula gives a useful estimate of the opacity as a function of the chemical composition, the density and the temperature of a stellar atmosphere. In the solar atmosphere, the dominant source of opacity are bound-free, free-free and Thomson scattering. For these processes the opacity is usually approximated by

$$k_R = k_0 \rho^n T^{-s} \tag{5.33}$$

where k_0 is a function of chemical composition, and n and s are parameters. More in general the opacity depends also on the electron density n_e, that reflects the ionization state of matter and is therefore a function itself of ρ and T. Under LTE, n_e is given by the Saha Boltzman equations. The evaluation of stellar opacity requires in general the theoretical knowledge of the cross section of the physical processes that govern the interaction of radiation with matter,

the chemical composition and physical state (ρ and T) of the atmosphere, the population of each atomic level. Because of the big computational effort, in stellar atmospheric models results obtained by big projects like the Los Alamos Opacity Project and the Opal are used. Generally they provide opacity tables as functions of density and temperature. Parameters in eq.5.33 are then estimated by a fit to the tables in the physical ranges of interest. Three cases are of physical relevance:

$n = 1$	$s = 3.5$	Kramer law
$n = 0.75$	$s = 3.5$	Schwarzchild's opacity
$n = 0$	$s = 0$	electron scattering

The Kramer's law is useful when opacity is dominated by free-free absorption, while Schwarzchild approximation yields better results when bound free contributions are important. The case n=0, s=0 corresponds to pure electron scattering.

Upper panel of fig.5.1 shows Rosseland mean opacity estimated by Cox and Giuli (1968) in the case of Population I type chemical composition (Aller mix). Opacity is plotted as a function of the temperature for several density values. The steep initial increase at lower temperatures results mainly by bound free processes, since at these temperatures hydrogen is partially ionized. At higher temperatures, beyond the maximum, hydrogen is totally ionized, free free absorption dominates the opacity, that thus becomes 'Kramer like'. At lower temperatures, indicated in the lower panel, certain types of atoms or molecules can absorb one or more electrons, thus becoming negative ions. This increases the probability of photoionization (bound free) processes. In astrophysics the presence of H^- ion is fundamental. In the case of the sun, and in general of solar like stars, at photospheric level it is responsible of 60% of the continuous opacity.

5.1.6 Approximate solutions to the RTE

The Radiative Transfer Equation has analytical solutions only at large depth, where LTE is valid, i.e. in the optically thick case. In shallower layers analytical solutions exist only under particular assumptions. In the next I will consider the Eddington approximation for optically thin layers, and discuss the diffusion approximation for deep layers.
Approximate solutions are in general found expanding the Source function in power series of optical depth:

$$S_\nu = \sum_{n=0}^{\infty} \frac{(t_\nu - \tau_\nu)^n}{n!} \left| \frac{d^n S_\nu(\tau_\nu)}{dt_\nu^n} \right|_{\tau_\nu} \tag{5.34}$$

Substituting this expression into eq. 5.18 and eq. 5.20, one obtains outgoing and incoming intensity radiation:

$$I_\nu^{out.}(\tau_\nu, \mu) = \sum_{n=0}^{\infty} \mu^n \left| \frac{d^n S_\nu(\tau_\nu)}{dt_\nu^n} \right|_{\tau_\nu} \tag{5.35}$$

$$I_\nu^{inc.}(\tau_\nu, \mu) = \sum_{n=0}^{\infty} \mu^n \left| \frac{d^n S_\nu(\tau_\nu)}{dt_\nu^n} \right|_{\tau_\nu} \left[1 - \frac{e^{-(\frac{\tau_\nu}{|\mu|})}}{n!} \left(\left(\frac{\tau_\nu}{|\mu|} \right)^n + n \left(\frac{\tau_\nu}{|\mu|} \right)^{n-1} + ...n! \right) \right] \tag{5.36}$$

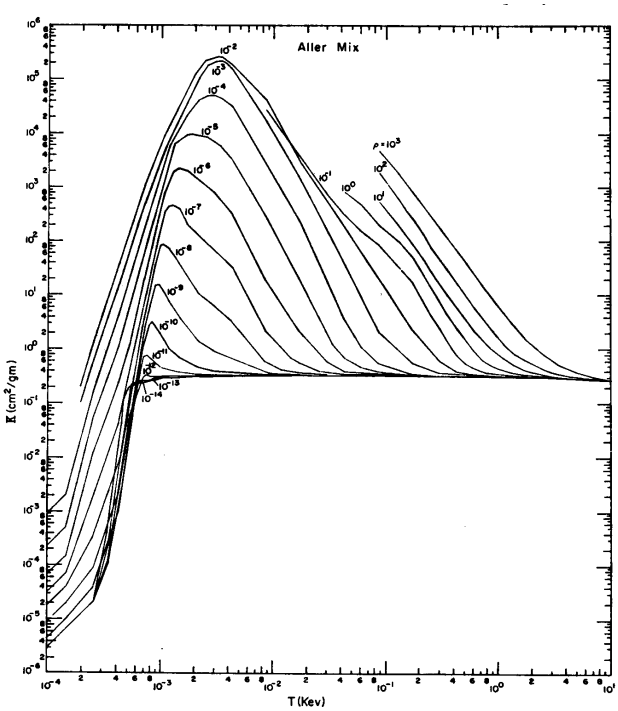

High temperature opacity for an Aller mix (solar composition) star. Opacity is a function of temperature and density. At lower temperature the opacity steeply increases with temperature because of the increase of electron density due to partial hydrogen ionization. At highest temperatures the opacity decreases because the hydrogen is almost fully ionized and the Kramer model is a good approximation. Note that temperatures are given in KeV and 1KeV$\simeq$ 12000 kelvins. From Cox and Giuli (1968).

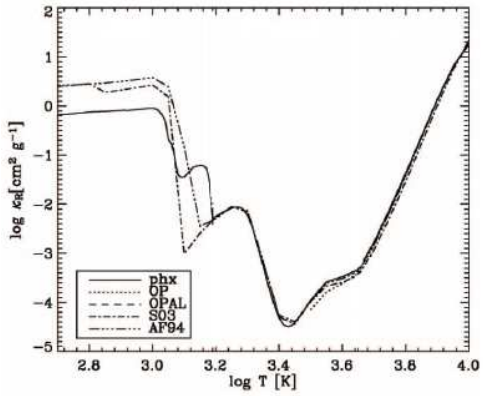

Low temperature opacity for a solar like star evaluated by different projects. The value of gas density is such that $\log \rho/T_6^3 = -3$, where T_6 is the temperature expressed in units of millions of kelvins. Opacity decreases at higher temperature, for values typical of the photosphere. In this regime the H^- is the dominant source of opacity. At higher temperatures it steeply increases because of the presence of molecules. From Ferguson et al. (2005).

Figure 5.1: Opacity values in the interior (upper panel) and in the atmosphere (photosphere and chromosphere) of the Sun.

From these the corresponding moments J_ν, H_ν and K_ν are expressed as power series of optical depth. These series converge for $\tau \to 0$ and $\tau \to \infty$, thus giving a good estimate of the solution of radiative transfer problem at the surface and in the deep of stellar atmospheres.

Optically thin media and the Eddington Barbier approximation

The Eddington-Barbier approximation is based on the assumption that the Source function can be expressed as a linear function of the monochromatic optical radial depth:

$$S_\nu = a + b\tau_\nu \tag{5.37}$$

the outgoing and incoming radiation are then

$$I^{out.}(\tau_\nu, \mu) = a + b\tau_\nu + b\mu, \quad 0 \leq \mu \leq 1 \tag{5.38}$$

$$I_\nu^{inc.}(\tau_\nu, \mu) = a + b\tau_\nu + b\mu - (a + b\mu)e^{\tau_\nu/\mu}, \quad -1 \leq \mu \leq 0 \tag{5.39}$$

and the other moments are

$$J_\nu(\tau_\nu, \mu) = a + b\tau_\nu + \frac{1}{2}[bE_3(\tau_\nu) - aE_2(\tau_\nu)] \tag{5.40}$$

$$H_\nu(\tau_\nu, \mu) = \frac{1}{3}b + \frac{1}{2}[aE_3(\tau_\nu) - bE_4(\tau_\nu)] \tag{5.41}$$

$$K_\nu(\tau_\nu, \mu) = \frac{1}{3}(a + b\tau_\nu) + \frac{1}{2}[bE_5(\tau_\nu) - aE_4(\tau_\nu)] \tag{5.42}$$

where E_n is the exponential integral and is defined has

$$E_n(x) \equiv \int_0^1 \exp^{-x/\mu} \mu^{n-1} \frac{d\mu}{\mu} \tag{5.43}$$

An example of exponential integrands of order $n = 2, 3, 4$ and relative integrand functions is given in fig.5.2

The case in which $\tau = 0$ is particularly instructive. One finds in fact that

$$I_\nu^{out.}(0, \mu) = a + b\mu, \quad 0 \leq \mu \leq 1 \tag{5.44}$$

$$I_\nu^{inc.}(0, \mu) = 0, \quad -1 \leq \mu \leq 0 \tag{5.45}$$

$$J_\nu(0, \mu) = \frac{1}{2}a + \frac{1}{4}b \tag{5.46}$$

that shows that $J_\nu(0) < S_\nu(0)$ if b is small. From eq.5.44 it follows that

$$I_\nu^{out.}(0, \mu) = S_\nu(\tau = \mu) \tag{5.47}$$

This last relation indicates that outgoing intensity radiation seen by an observer 'far' from the star decreases toward the limb of the sun and is maximum at its center. This approximation thus describes the center to limb variation (CLV) of intensity observed on the sun and other stars. Similarly $H_\nu(0) = \frac{1}{4}a + \frac{1}{6}b$ and hence $F_\nu(0) = a + \frac{2}{3}b = S_\nu(\tau_\nu = \frac{2}{3})$.

The case of a homogeneous medium in which $S = a$ is called *Lambert radiator*. Under this hypotheses $I^{out}(0, \mu) = a$ and $I^{inc.}(0, \mu) = 0$ and therefore $F(0) = a$.

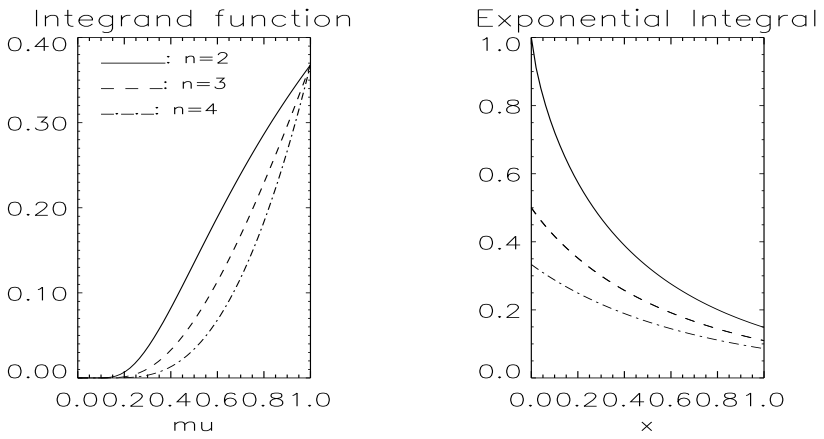

Figure 5.2: Integrand function $\exp^{-x/\mu}\,\mu^{n-1}/\mu$ (left) and Exponential Integrals for orders $n = 2, 3, 4$. Note that the exponential integral of order 1 has a singularity at $x = 0$.

Optically thick media: the Radiative Diffusion approximation

In the limit $\tau \to \infty$, intensity and its moments are given by:

$$I_\nu^{out.}(\mu) = I_\nu^{inc.}(\mu) = S_\nu(\tau_\nu) + \mu\frac{dS_\nu(\tau_\nu)}{d\tau_\nu} + \mu^2\frac{d^2S_\nu(\tau_\nu)}{d(\tau_\nu)^2} + ... \tag{5.48}$$

$$J_\nu(\tau_\nu) = \sum_{k=0}^{\infty}\frac{1}{2k+1}\left[\frac{d^{2k}S_\nu(\tau_\nu)}{d(\tau_\nu)^{2k}}\right]_{\tau_\nu} \tag{5.49}$$

$$F_\nu(\tau_\nu) = \sum_{k=0}^{\infty}\frac{4}{2k+3}\left[\frac{d^{2k+1}S_\nu(\tau_\nu)}{d(\tau_\nu)^{2k+1}}\right]_{\tau_\nu} \tag{5.50}$$

$$K_\nu(\tau_\nu) = \frac{1}{3}\sum_{k=0}^{\infty}\frac{3}{2k+3}\left[\frac{d^{2k}S_\nu(\tau_\nu)}{d(\tau_\nu)^{2k}}\right]_{\tau_\nu} \tag{5.51}$$

It can be shown that series converge at large optical depth (Cox and Giuli, 1968).

5.2 Radiative Equilibrium Gray atmosphere

In this paragraph I consider an atmosphere in which radiation is the only energy transport mechanism. Then the total radiative flux F_{Rad} equals the total energy flux F:

$$F_{Rad}(z) \equiv \int_0^\infty F_\nu(z)d\nu = F \tag{5.52}$$

where

$$F(z) = \frac{L_\odot}{4\pi R_\odot^2} = \sigma T_{eff}^4 \tag{5.53}$$

$L_\odot$ and $R_\odot$ are the solar luminosity and the radius, T_{eff} is the temperature of a black body whose total radiation equals that measured for the sun (or, more in general, for the star). The Radiative equilibrium condition is, using eq.5.25,

$$\frac{dF(z)}{dz} = 4\pi k\rho(J(z) - S(z)) = 0 \tag{5.54}$$

For a non plane parallel atmosphere, previous relation is written

$$\nabla \cdot F = 4\pi k\rho(J - S) = 0 \tag{5.55}$$

follows that, in RE approximation, $S(z) = J(z)$. It can be shown (Mihalas and Weibel-Mihalas, 1999) that previous equation has a solution if

$$J(\tau) = \frac{3}{4\pi} F \cdot (\tau + q(\tau)) \tag{5.56}$$

where $q(\tau)$ is the Hopf function. This means that in RE both J and S are approximately linear functions of optical depth. Applying LTE condition one also finds

$$T(\tau)^4 = \frac{3}{4} T_{eff}^4 \cdot (\tau + q(\tau)) \tag{5.57}$$

The problem of the Gray atmosphere consists in finding $q(\tau)$. A common approximation consists in assuming that this function has constant value $\frac{2}{3}$, so that

$$J(\tau) = \frac{3}{4\pi} F \cdot (\tau + \frac{2}{3}) \tag{5.58}$$

and therefore

$$T(\tau)^4 = \frac{3}{4} T_{eff}^4 \cdot (\tau + \frac{2}{3}). \tag{5.59}$$

This approximation is valid if $J = 3K$. From equations 5.49 and 5.51 this last condition is valid if $\tau \gg 1$ and the Source function varies linearly with τ. In general it is exact for isotropic radiation and for the cases in which the intensity can be expanded as only odd powers of μ. It is also valid in the *two stream* approximation, that is in the case the outgoing and the incoming radiations are two different functions of τ but are independent on the line of sight angle cosine μ. The Lambert radiator case satisfies these requirements. On the other end the assumption is not valid at the surface in the Eddington-Barbier approximation, since $I^{out.}$ varies linearly with μ, but $I^{inc.}$ does not. The assumption of validity of $J = 3K$ in other cases other than these ones is called *Eddington approximation*.

The exact solution to the Gray problem gives $q(0) = 0.577...$ and $q(\infty) = 0.710...$, compared to the assumed value $q = 2/3 = 0.666....$ The error is largest at the surface; it can be shown though that for instance at $\tau = 0$ the approximation leads to an error in the estimation of J of about 15% (Mihalas and Weibel-Mihalas, 1999) and that the source function "yields a reasonably accurate angular distribution of the intensity".

5.3 Numerical solution to the RTE: The Short Characteristic

The formal solution to the Radiative Transfer Equation is given by equation 5.17, that requires the knowledge of optical depth, or density and opacity functions, and source function in the domain. In stellar atmosphere problems usually

these quantities are not expressed as analytical functions, but are tabulated as explained for the opacity in 5.1.5. The intensity radiation field thus has to be estimated numerically. Note that, besides some particular models, in which exist an analytical solution of integrals in eq.5.18 and eq.5.20, intensity radiation is estimated numerically even when the atmosphere is specified by analytical functions of depth or optical depth. In the following I present the numerical technique I adopted to solve this problem.

As already mentioned in chapter 4, the solution of energy equation 4.6 requires the evaluation of radiative flux F. In the flux tube models I developed (see chapter 7) the evaluation of the Intensity mean radiation field J is also required. F and J are the integrals over the solid angle of the first and zero moments of radiation intensity (eq.5.22 and 5.21 respectively). Integrals are usually numerically estimated by a quadrature technique, that is by an opportune linear combination of the integrand function evaluated at some points in the interval of integration. Weights and points (in this case directions) are given by the particular scheme chosen. One therefore needs to estimate at each point of the domain and for each direction the radiative intensity. Spatial domain is discretized by a grid (fig.5.3)at which at the top and the bottom boundary conditions for the intensity field are assumed. Horizontal periodical boundary conditions are also assumed. Intensity radiation at a generic point O of the grid is given solving, for each direction, the equation 5.16, that is by eq.5.17. This problem is solved by the Short characteristic technique (Kunasz and Auer, 1988) that allows to estimate the intensity radiation, given a Source function and the product of the density and the opacity (in the following α function) at each point of the domain. Since the method is numerical, it does not require an analytical form for these functions, but just their values at each point of the domain. By using notation in fig.5.3, and assuming a Gray atmosphere, the radiative transfer equation has solution

$$I_O(\mu) = \; I_M(\mu) \cdot e^{-\Delta\tau_M} + \int_O^{\Delta\tau_M} S(t) e^{-(\Delta\tau_M - t)} dt \tag{5.60}$$

where

$$\Delta\tau = \; \tau_{i-1} - \tau_i = \int_{s_{i-1}}^{s_i} \alpha(s) ds \tag{5.61}$$

here s is the space distance travelled along the direction of propagation by the ray, M is at coordinate $(i-1)$, O at coordinate (i) and P at coordinate (i+1), as shown in fig.5.4. The method basically consists in evaluating integrals in eq.5.60 and eq.5.61 locally by a polynomial expansion of α and source function. In the following I will also consider the case in which opacity and density are given, since this is the case of the simulations I have been running, although the problem can be solved even by knowing the product α of these functions. In the following I will describe integration schemes proposed by Bruls et al. (1999), while in the next chapter other schemes and a comparison among them is described. To solve integral in eq.5.61 let us consider a second order Taylor expansion of the opacity k:

$$k = k_O + k_1 \cdot (s_i - s_{i-1}) + k_2 \cdot (s_i - s_{i-1})^2 \tag{5.62}$$

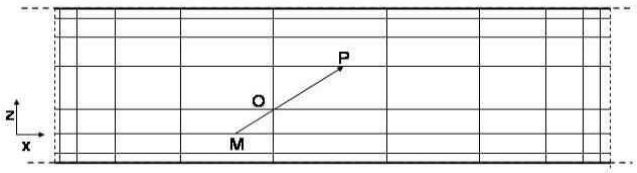

Figure 5.3: The Short Characteristic allows numerical evaluation of intensity at each point of a grid. In this 2D scheme, boundary conditions are imposed at the top and at the bottom (thick horizontal lines), and periodic horizontal conditions are imposed (dashed vertical lines). Intensity at each generic point O of the grid is evaluated by integration techniques, and thus requires to know opacity, density and source function values at points M (upwind) and P (downwind), as well as the intensity value at point M. These points don't belong to the grid, so quantities at this locations are estimated by interpolation.

where k_O is the opacity evaluated at point i, and k_1 and k_2 are given by

$$k_1 = \left.\frac{\partial k}{\partial s}\right|_i = \frac{\frac{k_{i+1}-k_i}{\Delta s_{i+1}} \cdot \Delta s_i - \frac{k_i - k_{i-1}}{\Delta s_i} \cdot \Delta s_{i+1}}{\Delta s_{i+1} + \Delta s_i} \tag{5.63}$$

$$k_2 = \frac{1}{2} \cdot \left.\frac{\partial^2 k}{\partial s^2}\right|_i = \frac{\frac{k_{i+1}-k_i}{\Delta s_{i+1}} - \frac{k_i - k_{i-1}}{\Delta s_i}}{\Delta s_{i+1} + \Delta s_i} \tag{5.64}$$

and $\Delta s_i = s_{i+1} - s_i$. Let us also expand the density at the first order

$$\rho = \rho_O + \rho_{1,j} \cdot (s - s_i) \tag{5.65}$$

where ρ_O is the density evaluated at point i and j=0,1, with

$$\rho_{1,j} = \frac{\rho_{i+1-j} - \rho_{i-j}}{s_{i+1-j} - s_{i-j}} \tag{5.66}$$

The use of different order expansions for opacity and density is legitimated by the fact that usually opacity is a power function of density, as explained in previous paragraphs.

Integral in eq.5.61 is thus approximated by the formula

$$\begin{aligned} \Delta\tau_{i-j+1} &= k_O \rho_O \Delta s_{i-j+1} + \frac{-1^{j+1}}{2}(k_1\rho_0 + k_0\rho_{1,j})\Delta s^2_{i-j+1} + \\ &+ \frac{1}{3}(k_2\rho_0 + k_1\rho_{1,j})\Delta s^3_{i-j+1} + \frac{-1^{j+1}}{4} k_2 \rho_{1,j} \Delta s^4_{i-j+1} \end{aligned} \tag{5.67}$$

In this notation j=1 when the optical depth is estimated integrating between s_{i-1} and s_i, and j=0 when the integration is between s_i and s_{i+1}.
A similar integration scheme is used also to evaluate the integral in eq.5.60. Let us in fact expand the source function at the second order:

$$S(\tau) = S_O + S_1\tau + S_2\tau^2 \tag{5.68}$$

where S_O is the Source function evaluated at point i and

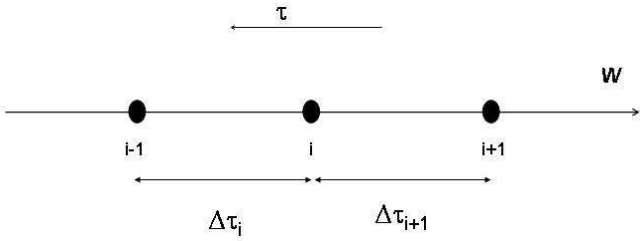

Figure 5.4: A ray is propagating along direction W, that intersects the grid at points $i-1$, i and $i+1$, corresponding to points M, O and P respectively in fig.5.3.

$$S_1 = \left.\frac{\partial S}{\partial \tau}\right|_{\tau_i} = \frac{\frac{S_{i-1}-S_i}{\Delta\tau_{i+1}} \cdot \Delta\tau_{i+1} - \frac{S_i - S_{i+1}}{\Delta\tau_{i+1}} \cdot \Delta\tau_i}{\Delta\tau_{i+1} + \Delta\tau_i} \tag{5.69}$$

$$S_2 = \frac{1}{2} \cdot \left.\frac{\partial^2 S}{\partial \tau^2}\right|_{\tau_i} = \frac{\frac{S_{i-1}-S_i}{\Delta\tau_i} - \frac{S_i - S_{i+1}}{\Delta\tau_{i+1}}}{\Delta\tau_{i+1} + \Delta\tau_i} \tag{5.70}$$

Using a quadrature technique at second order

$$\Delta I = \int_0^{\Delta\tau_i} d\tau S(\tau) e^{-\tau} = \sum_{n=0}^{2} \omega_n(\Delta\tau_n) S_n \tag{5.71}$$

where

$$\begin{aligned} \omega_0 &= 1 - e^{-\Delta\tau_i} \\ \omega_1 &= \omega_0 - \Delta\tau_i e^{-\Delta\tau_i} \\ \omega_2 &= 2\omega_1 - \Delta\tau_i^2 e^{-\Delta\tau_i} \end{aligned}$$

After some algebra it follows that

$$\Delta I = \Omega_{i-1} S_{i-1} + \Omega_i S_i + \Omega_{i+1} S_{i+1} \tag{5.72}$$

where

$$\begin{aligned} \Omega_{i-1} &= \frac{\omega_2 + \omega_1 \cdot \Delta\tau_{i+1}}{\Delta\tau_i(\Delta\tau_i + \Delta\tau_{i+1})} \\ \Omega_i &= \frac{\omega_1(\Delta\tau_i - \Delta\tau_{i+1})}{\Delta\tau_i \cdot \Delta\tau_{i+1}} + \omega_0 \\ \Omega_{i+1} &= \frac{\omega_2 - \omega_1 \cdot \Delta\tau_i}{\Delta\tau_{i+1}(\Delta\tau_i + \Delta\tau_{i+1})} \end{aligned}$$

In previous calculations a second order expansion is used, but higher orders can be implemented depending on the problem to solve. Since generally density and opacity are continuous functions of height, low order expansions yield good accuracy calculations. In the next chapter I discuss and compare results obtained with higher order integration schemes.

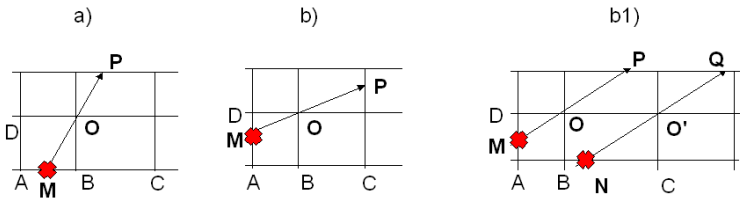

Figure 5.5: Case a): upwind point M lies in between two points of the grid A and B, therefore I_M is estimated through interpolation. Cases b): M lies on a column in between points A and D. If I_D is known, I_M is evaluated by interpolation. If I_D is not known, because for instance O is the first of the row at which intensity has to be evaluated, then interpolation is not possible. In this case, if the grid is irregular, the algorithm looks for the first point on the grid at which M lies on a row, like in case b1). he case in which the grid is regular is illustrated in fig.5.6. Intensity at subsequent points is evaluated sweeping the grid according to the beam direction and applying horizontal periodic conditions.

5.3.1 Propagating the intensity on the grid

Given the boundary intensity conditions, intensity is evaluated at each point of the grid row by row, with the prescription that the intensity is evaluated on the next row only when it has been evaluated on all the points of the previous row. Since periodic conditions are imposed on vertical boundaries, the intensity has the same value on the first and last point of the grid, and the first point processed is the second of the row. From what explained in the previous paragraph, it is clear that to evaluate the intensity on point O of the grid, one must know the intensity in the previous point M and the opacity, the density and the source function on points M, O and P, where M and P do not belong to the grid, so that interpolation is needed. Since S, k and ρ are known on the grid, the evaluation of this quantities by interpolation is always possible, while this is not the case for the intensity. In particular the estimation of the upwind intensity of the first point of the row at which intensity is evaluated can be problematic. In fact let us consider the cases in fig.5.5, where point O is the second of the row (the first on which intensity is evaluated). In cases in which M is in between two points of the previous row, like case a), intensity at point M can be estimated interpolating between them. In case b), M lies on a column and its closest points are A and D. Since intensity at point D is not known, interpolation is not possible and intensity at point M cannot be estimated. If the grid is regular, and case b) is verified at the second point of the grid, than it is verified at each point of the grid. However, if the grid is irregular, than might exist a point of the grid at which case a) is verified, as illustrated in case b1). In this situation the first point of the grid at which intensity is evaluated is the first one of the row that satisfies condition a). Intensity on subsequent points can then be evaluated since now the intensity is known on the previous point (point O' in case b1)) and interpolation is possible. Intensity on remaining points of the row (for instance point O in case b1)) is evaluated imposing horizontal periodic conditions.

If the grid is regular or if in general cases a) are never found, than intensity at point O can be evaluated propagating from the first point of the ray

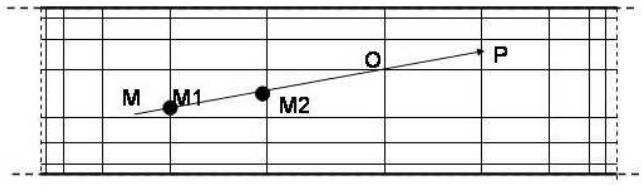

Figure 5.6: For some directions and grid shapes, the closest upwind point M never lies on a row. We then look for further points until the first one that intersects a row. Intensity is then evaluated at other upwind points (M1 and M2 in this case) and finally at point O, using the same integration schemes described in the text. Note that in this case intensity is known by interpolation at point M, by which intensity at point M1, is known. Intensity estimation at M2 and then at O is based on intensity estimation at M1 and M2 respectively.

that intersects the grid on the previous row, as shown in fig.5.6. Intensity on intermediate points is evaluated using the same procedure used for points on the grid. For very shallow angles the ray could never intercept the row and for horizontal directions intensity cannot be estimated by this technique. For this reason it is important to chose a quadrature scheme (necessary to evaluate flux and mean intensity) in which the prescribed directions are not shallow.

The interpolation order used to estimate the various variables on points that are not on the grid is an important aspect of the algorithm. Generally a second order interpolation is employed, since this is the order used to evaluate the integrals. This kind of interpolation requires the knowledge of the quantity to interpolate on at least three points, a request that, as already explained, cannot always be matched. For this reason an asymmetric second order interpolation is generally employed, with the prescription of using first order interpolation for cases b) of the first row of the grid. There are other cases in which a first order interpolation is preferred to a second one and will be discussed in the following chapter.

5.4 Quadrature techniques

Once the intensity field is evaluated, the aim is to evaluate the radiative flux F or the mean intensity J defined in eq.5.21 and eq.5.22. These are integrals over the solid angle and can be numerically evaluated by quadrature techniques. Quadrature techniques are useful tools to estimate the integral of a function by a proper linear combination of the values assumed by the integrand function itself at some points in the integration range. In formula:

$$\int_a^b f(x)dx = \sum_{i=1}^{N} v_i f(x_i), \quad x_i \in [a,b] \tag{5.73}$$

N is the number of points in the interval and is generally referred as the order of quadrature, while v_i are the weights of the quadrature.
Depending on points x_i and weights, many different schemes exist. The most popular is the Gauss Legendre, in which points and weights are found imposing

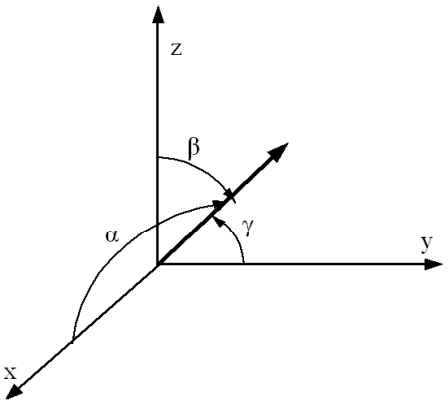

Figure 5.7: The direction of a vector is expressed by its director cosines, that is by the cosines of the angles between the vector and the three axes x,y,z. We thus define $\mu = \cos\alpha$, $\xi = \cos\beta$, $\eta = \cos\gamma$. Because of condition 5.75 a direction is defined by only two of the director cosines.

the integral to be exact for a Legendre polynomial of order N. In the following I will describe two techniques. The first one is the Carlson scheme (Carlson, 1963), the most used in radiative transfer problems, the second one is based on a Gauss Legendre scheme. A comparison of the two techniques is given in the next chapter.

5.4.1 Carlson schemes

In spherical geometry directions are easily represented by direction cosines, i.e., the cosines of the angles between the vector that defines the direction and (x,y,z), as shown in fig.5.7. We define $\mu = \cos\alpha$, $\xi = \cos\beta$, $\eta = \cos\gamma$, where

$$\mu^2 + \xi^2 + \eta^2 = 1 \tag{5.74}$$

The last condition reduces the degrees of freedom, so that just two cosines are necessary to define a direction. Moreover, we impose the directions and weights to be invariant respect to rotation about the particular axis. This means that we impose the projection of the direction on any of the axis, and the relative weights, to be independent from the particular axis. This conditions reduces further the degree of freedom, so that the directions can be described by one cosine, say μ. Each direction is thus described by (μ_l,μ_m,μ_k), or, more easily, by the set (l,m,k). Since μ varies from -1 to 1, our analysis can be restricted to a quadrant. We can therefore use a 1-D scheme and look for the set of $\{\mu_l\}$ level cosines with relative weights $\{w_l\}$. The direction weights $\{v_j\}$ are subsequently retrieved by using, again, symmetry consideration and imposing that the sum of v_j's on a level equals the relative w_l. Figure 5.8 illustrates the points distribution on an octant for different values of N, where numbers in circles are (l,m,k). Here, in counting levels with respect to the x-pole, we start near the side opposite to x and then move toward the pole, and similarly

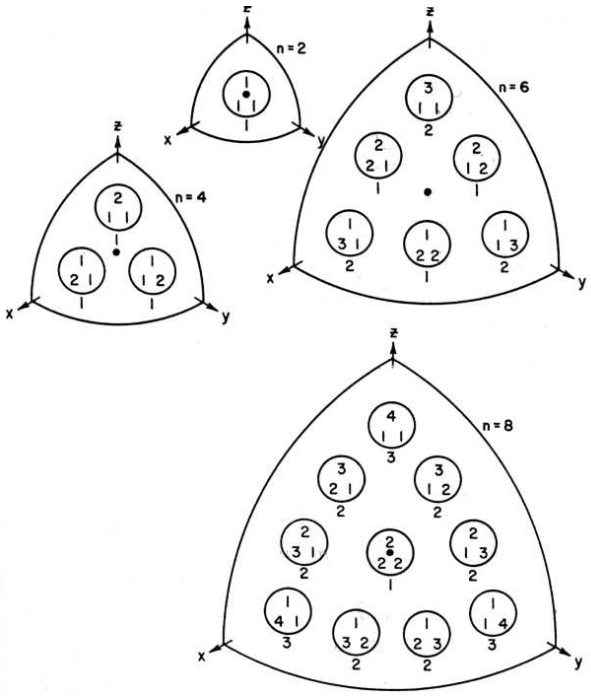

Figure 5.8: Directions and symmetry classes for first N=8 quadrature orders in the Carlson scheme. Numbers in circles indicate the three direction cosines that identify each directions. Numbers under the circle indicate the group of symmetry (and thus the weight). On each l level there are $n_l = N/2 + 1 - l$ points. For instance, if N=8 and l=1 then $n_1 = 4$, if N=6 and l=2 then $n_2 = 2$. From Carlson (1963).

for levels with respect to y and z. There are N(N+2)/8 points per octant in this scheme. An octant exhibits N/2 of the μ levels; a quadrant all N of them. Inspection of fig.5.8 shows that level cosines must satisfy the relation:

$$\mu_l^2 + \mu_m^2 + \mu_{N/2-l-m+2}^2 = 1 \tag{5.75}$$

where l=1,2,3,...N/2; m=1,2,3..N/2-l+1. This condition stems from the symmetry requirements and relation (1). Fig.5.8 also shows that points fall into three types of symmetry class: classes of points with six members (for which $l \neq m \neq k$), classes of points with three (for which $l = m \neq k$, and permutations), classes with one (l=m=k). Symmetry requires that points within a given class have identical weights $\{v_j\}$. In fig.5.8 the j class is indicated under the circles. In analogy with Gaussian quadrature, we also require the following conditions to be satisfied:

$$\sum_l^N w_l = 2 \tag{5.76}$$

$$\sum_l^N w_l \mu_l = 0 \tag{5.77}$$

$$\sum_{l}^{N} w_l \mu_l^2 = \frac{2}{3} \tag{5.78}$$

The first condition 5.76 is the solid angle normalization. In the general case, the sum extends over one, two, or four quadrants, depending on the geometry of the problem (1D, 2D or 3D respectively). The second condition reflects a symmetry about $\mu = 0$. Relation 5.78 guarantees that points of the same class have the same weight. To make clear the last statement, let us rewrite relation 5.76 in terms of $v'_j s$, for instance for the case N=8. For the sake of simplicity let us restrict calculation to one octant:

$$\begin{aligned} w_1 + w_2 + w_3 + w_4 &= v_3 + 2 \cdot v_2 + 2 \cdot v_2 + v_1 + 2 \cdot v_3 + 2 \cdot v_2 = \\ &= 3 \cdot v_3 + 6 \cdot v_2 + v_1 = 1 \end{aligned} \tag{5.79}$$

Relation 5.78, in terms of $v'_j s$, is:

$$\begin{aligned} \sum_{l=1}^{4} w_l \mu_l^2 &= v_3 \cdot \mu_4^2 + 2 \cdot v_2 \cdot \mu_3^2 + 2 \cdot v_2 \cdot \mu_2^2 + \\ &+ v_1 \cdot \mu_2^2 + 2 \cdot v_3 \cdot \mu_1^2 + 2 \cdot v_2 \cdot \mu_1^2 = \\ &= v_3 \cdot (\mu_4^2 + 2 \cdot \mu_1^2) + v_2 \cdot (2 \cdot \mu_3^2 + 2 \cdot \mu_2^2 + 2 \cdot \mu_1^2) + v_1 \cdot \mu_2^2 = \\ &= v_3 + 2 \cdot v_2 + v_1/3 \end{aligned}$$

Where last passage stems from eq.5.75. Finally, by comparison with eq.5.79:

$$\sum_{l=1}^{4} w_l \mu_l^2 = 1/3 \tag{5.80}$$

Because of symmetry we expect the last summation to give the same result when evaluated for the other octant, so that the sum on the whole quadrant is 2/3 and relation 5.79 is proofed.

It is also worth to notice that conditions 5.76, 5.77 and 5.78 are related to the first three intensity moments of a uniform (isotropic) radiation field. The first one is the normalization of mean intensity integral J, the second guarantees flux value is zero, the third one the K-integral to be equal to $diag(J/3)$.

In the following I will restrict the analyses to one octant, results being symmetric, because of relation 5.77, at the other octants. It is also worth to notice that odd N-values give directions along axes. Since intensity along these directions cannot be evaluated by the Short Characteristic technique described in previous paragraphs, discussion will be restricted to even N-values.

Relation 5.80 has a very simple solution derived from the fact that the indices sum to N/2+2, namely

$$\mu_l^2 = \mu_1^2 + (l-1) \cdot \Delta \tag{5.81}$$

where

$$\Delta = 2 \cdot (1 - 3 \cdot \mu_1^2)/(N-2). \tag{5.82}$$

Hence, if μ_1 is given, all other μ's can be calculated, the value of μ_1 defining the spread of the points on the octant. If we now let $W_1 = w_1$, $W_2 = w_1 + w_2$, ...,$W_l = w_1 + w_2 ... + w_l$, we find, making use of 5.81 and 5.78, that

$$\sum_{l=1}^{N/2-1} W_l = (N-2)/3. \tag{5.83}$$

N	ϵ_N
4	0,0
6	0,00416667
8	0,00539164
12	0,00592059
16	0,00583892

Table 5.1: Values of ϵ for some of the first quadrature orders N. At orders higher than the ones shown ϵ goes to zero. Adapted from Carlson (1963).

In Gauss quadrature scheme the μ's are approximately equal to the cosines of a set of angles linear in l, and the weights corresponding to W_l approximately equal the cosines of the equidistant midpoint angles. In our case we have linearity in μ^2 and the transformation is square root rather than cosine. Hence, by analogy,

$$W_l^2 = W_1^2 + (l-1)\cdot\Delta \qquad l = 1, 2, ...N/2 - 1. \tag{5.84}$$

This relation, making use of eq.5.83, has solution

$$\Delta = 2/(N-1), \qquad W_1^2 = (4+\epsilon_N)/3(N-1) \tag{5.85}$$

where ϵ_N is a small quantity whose values for some N's are shown in table 5.1. These values can be evaluated substituting $\Delta = 2/(N-1)$ into eq. 5.84 and then evaluating the summation 5.83. At larger N, ϵ goes to zero. Continuing the analogy we write $\mu_1^2 = W_1^2 - \Delta/2$, that, in combination with eq.5.82, gives:

$$\mu_1^2 = 1/3(N-1) \tag{5.86}$$

The set of level cosines and the relative weights are henceforth derived. The point (or class) weights are then calculated as described above. This method does not allow to evaluate more than N/2 -1 different class weights. There are that many for n=4, 6, 8, 10 and 12. After that the number of classes grows very fast and is not possible to find a unique solution.

As an example in the following I derive weights and levels for the case N=12. Let us divide the evaluation in the following four steps:

W_l 's calculation:

According to 5.85 and table 5.1

$$W_1^2 = (4 + 0.00592049)/33 = 0.12139153, \tag{5.87}$$

and, using 5.84,

$$\begin{aligned} W_2^2 &= W_1^2 + 2/11 = 0.30320971, \\ W_3^2 &= W_1^2 + 4/11 = 0.48502790, \\ W_4^2 &= W_1^2 + 6/11 = 0.66684608, \\ W_5^2 &= W_1^2 + 8/11 = 0.84866426. \end{aligned}$$

Level weights w_l's calculation:

The first N/2-1 level weights are calculated, according to W_l's definition, by inverting the following system of equations:

$$\begin{aligned} W_1 &= w_1, \\ W_2 &= w_1 + w_2, \\ W_3 &= w_1 + w_2 + w_3, \\ W_4 &= w_1 + w_2 + w_3 + w_4, \\ W_5 &= w_1 + w_2 + w_3 + w_4 + w_5. \end{aligned}$$

The last weight is calculated imposing 5.76:

$$w_6 = 1 - w_1 - w_2 - w_3 - w_4 - w_5. \tag{5.88}$$

w_l's values are presented in table 5.2.

Level cosines μl's calculation:

According to eq.5.86

$$\mu_1^2 = 1/33 \tag{5.89}$$

and then, by using relation 5.84:

$$\begin{aligned} \mu_2^2 &= \mu_1^2 + 2/11 = 0.030303030, \\ \mu_3^2 &= \mu_1^2 + 4/11 = 0.21212121, \\ \mu_4^2 &= \mu_1^2 + 6/11 = 0.39393939, \\ \mu_5^2 &= \mu_1^2 + 8/11 = 0.57575758, \\ \mu_6^2 &= \mu_1^2 + 10/11 = 0.93939394. \end{aligned}$$

Points weights v_j's calculation:

According to fig.5.9, classes weights (or points' weights), are evaluated by solving the following system of equations:

$$\begin{aligned} w_6 &= v_1, \\ w_5 &= 2 \cdot v_1, \\ w_4 &= 2 \cdot v_3 + v_5, \\ w_3 &= 2 \cdot v_3 + 2 \cdot v_4, \\ w_2 &= 2 \cdot v_2 + 2 \cdot v_5 + v_4, \\ w_1 &= 2 \cdot v_1 + 2 \cdot v_2 + 2 \cdot v_3. \end{aligned}$$

One equation, let us say the last one, is redundant. Inversion of the first five conditions leads:

$$\begin{aligned} v_1 &= w_6, \\ v_2 &= w_5/2, \\ v_3 &= 0.1 \cdot (4 \cdot w_4 + w_3 - 2 \cdot w_2 + 2 \cdot w_5), \\ v_4 &= (w_2 + 2 \cdot w_3 - 2 \cdot w_4 - w_5)/5, \\ v_5 &= (w_4 - w_3 + 2 \cdot w_2 - 2 \cdot w_5)/5. \end{aligned}$$

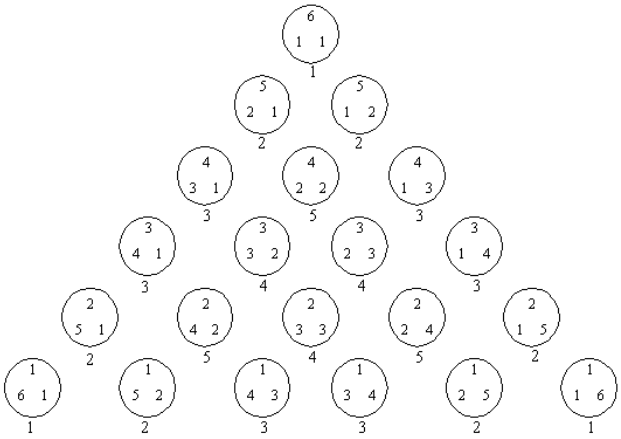

Figure 5.9: Directions and weights for N=12.

$lorj$	w_l	μ_l	μ_l^2	v_j
1	0.34841288	0.17407766	0.030303030	0.078770246
2	0.20223194	0.46056619	0.21212121	0.052311657
3	0.14579462	0.62764591	0.39393939	0.043124537
4	0.12016700	0.75878691	0.57575758	0.029772776
5	0.10462331	0.87038828	0.75757576	0.033917925
6	0.078770246	0.96922337	0.93939394	

Table 5.2: Level l and corresponding level weight, director cosine and its square value, direction weight, for N=12.

5.4.2 Gauss Legendre scheme

In order to increase the number of points an other technique was developed. I will refer to it as the Gauss-Legendre method. We have to solve the double integral:

$$I = \int_0^{2\pi} d\phi \int_0^{\pi} f(\theta, \phi) d\theta \tag{5.90}$$

or, changing variable,

$$I = \int_0^{2\pi} d\phi \int_{-1}^{1} f(\mu, \phi) \cdot \mu d\mu \tag{5.91}$$

The integral in μ is solved by a Gauss-Legendre scheme (e.g. Press et al., 1994). The set $\{\phi\}$ is evaluated imposing that on the n-th μ-level there are n directions equidistant in ϕ. The scheme obtained is similar to the one illustrated in fig.5.8, but symmetry about the three axes (x,y,z) is lost. Weights are estimated imposing that points of a level have the same weight and that their sum is the level weight. Directions in this scheme are represented by the system of variables $[\theta, \phi]$ rather than by director cosines used in the previous case.

Chapter 6

Preliminary Tests

In this chapter I illustrate results obtained by tests I performed to evaluate the errors introduced by numerical techniques employed and described in previous chapter. I particularly investigate error sources in the evaluation of radiation intensity field by short characteristic and errors in mean intensity and radiative flux introduced by the quadrature techniques developed.

For what concerns the intensity radiation field, I analyze the errors obtained with different integration and interpolation schemes at different ray direction and spatial resolution. Spurious effects introduced by interpolation schemes are investigated by the Search Beam technique.

Quadrature technique problems are investigated by the analyses of errors obtained in the evaluation of J and flux for the case of a Lambert radiator atmosphere.

Results presented allowed me to choose, among the different techniques employed, the ones that lead to more reliable results in the problem I am addressing in this thesis: the investigation of radiative properties of magnetic flux tubes.

6.1 Integration techniques

In order to explore dependency of the results on different integration techniques, I have compared results obtained in the evaluation of optical depth τ, that, as already explained, requires the evaluation of:

$$\tau_\nu(D) = \int_0^D \alpha_\nu(s)ds \tag{6.1}$$

where D is the depth of a finite slab, α is the product of density and opacity and s is the optical path. Integration techniques other than the one explained in chapter 5, based on a second order expansion of opacity k, a linear expansion of density ρ and second order expansion of source function S, have been tried. Particularly, I compared results obtained with the following schemes:

- Second Order expansion (***SO*** in the following): the integral is evaluated expanding the opacity at the second order and the density at the first order, as indicated in previous chapter.

- Second Order α expansion (***SO***α in the following): α function, the product of opacity and density, is expanded at the second order, so that τ is evaluated as a third order polynomial.
- Higher Order expansion (***HO*** in the following): both opacity and density are expanded at second order, so that τ is evaluated as a fifth order polynomial.
- Finite Differences (***FD*** in the following): finite difference formula have been used to evaluate both opacity and density at the second order, so that τ is evaluated at fifth order. Using the same notation of previous paragraphs, and letting s be the grid space, and x the ordinary space

$$\begin{aligned} k_1 &= \left.\frac{\partial k}{\partial s}\right|_{x_i} = \frac{\partial k}{\partial x}\frac{\partial x}{\partial s} = \frac{k_{i+1}-k_{i-1}}{s_{i+1}-s_{i-1}} \\ k_2 &= \left.\frac{1}{2}\frac{\partial^2 k}{\partial s^2}\right|_{x_i} \\ &= 2\frac{k_{i+1}-2k_i+k_{i-1}}{(s_{i+1}-s_{i-1})^2} - 2\frac{(s_{i+1}-s_i)-(s_i-s_{i-1})}{(s_{i+1}-s_{i-1})^3}(k_{i+1}-k_{i-1}). \end{aligned}$$

  FD results and *HO* results must coincide on a regular grid (see appendix to this chapter for a more detailed calculation).
- Finite differences for α expansion (***FD***α in the following): previous formulae are used to expand α function at second order, so that τ is evaluated at the third order.

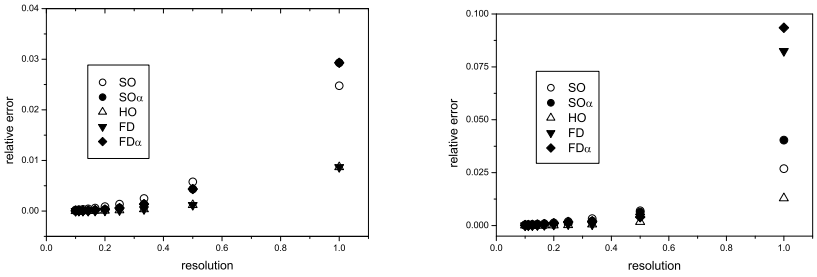

(a) Regular grid (b) Irregular grid

Figure 6.1: Relative error in the evaluation of the optical depth in the case both density and opacity are exponential functions of the depth and for different integration schemes described in the text. In the case of a regular grid, resolution is given by ten times the length of each spatial step (ratio of the total space S along the vertical direction and the number of intervals it is subdivided into). In the case of irregular grids, resolution is the smallest spatial step of the grid multiplied by ten. The error is the relative difference among the analytical solution of the integral and the numerical one at the top of the grid, that is at spatial coordinate S.

In order to compare the different techniques I have evaluated the optical depth in the case of a vertically stratified atmosphere, uniform along the horizontal direction. Results have been compared for different functions of opacity and density and for different resolutions in the case of regular and irregular grids. Regular grids where constructed dividing a fixed spatial interval S in to N equally spaced steps. Irregular ones have been constructed so that the total space S is dived into N not equally spaced steps. In particular the grid is symmetric for a reflection respect to the middle of the vertical direction and the spatial length of n-step is $s(n) = n * S/N$ for $n = (1, ..., N/2)$ and $s(n) = (N - n + 1) * S/N$ for $n = (N/2 + 1, ..., N)$. Plot on the left of fig.6.1 shows for instance absolute relative errors respect to the analytical value of optical depth obtained when opacity and density are exponential decaying functions of space and a regular grid is used for the five integration schemes. As expected, FD and HO expansions coincide, as well as $SO\alpha$ and $FD\alpha$. Plot on the right of fig.6.1 shows results obtained for the same functions, but with an irregular grid. In this latter case the Finite Differences results (FD and $FD\alpha$) are affected by higher errors than the results obtained with HO and $SO\alpha$ schemes, as expected by calculation shown in the appendix to this chapter. Moreover regular grid seems to lead better results for low resolution, while when resolution is increased no differences are evident between the two kind of spacing.

Results shown in fig.6.1 are not surprising. The SO technique produces the worst results because the density is known at the first order, and so the integral of the product of density and opacity. The HO technique produces better results respect to the $SO\alpha$ one because, as demonstrated in appendix to this chapter, the error in the Taylor expansion of a function that is the product of other two functions is different (in this case is less, due to the derivatives of the functions) if the expansion is performed before the product.

6.2 Interpolation effects: Search Beam technique

As explained above, interpolation is a crucial aspect of Short Characteristic. We expect it to be a source of uncertainties, especially in the case of not uniform or discontinuous atmospheres, such as in the presence of flux tubes. Two interpolation schemes have been implemented and tested: first order and second order.

For what concerns the second order, when symmetric second order interpolation is not possible, the following procedures have been adopted to make the algorithm work properly and prevent non-physical results :

- when evaluating intensity on the first row, if the upwind point lies on a column, a fist order interpolation is used, since not enough points are available for a second order.
- right or left second order asymmetric interpolation schemes are used depending on the direction of the beam and the position of the point on the grid.

Additionally in some cases interpolation can create sources or sinks, which can lead to non physical results such as negative intensity. To avoid these problems, a first order interpolation is used if the points used for interpolation

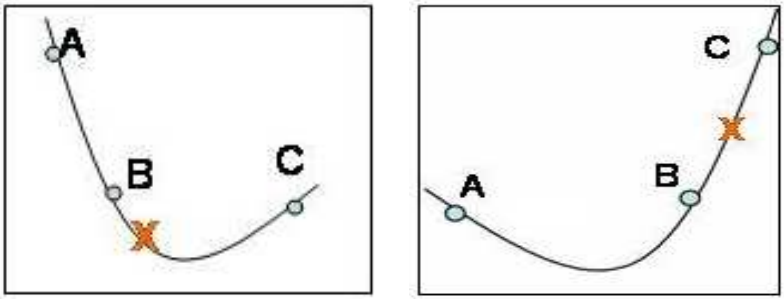

Figure 6.2: Differences between *strict* and *non strict* interpolation. Left: when intensity at interpolation point X is less then intensity at interpoland points (A,B,C), a linear interpolation is used in both schemes. Right: The interpolated intensity value I(X) is in between the intensity values at interpoland points, but the interpoland function (continuous line) assumes lower values. In this case a linear interpolation is used if *strict* monotonicity is imposed, while a second order is used in *non strict* scheme.

do not satisfy monotonicity condition. This issue is illustrated in fig.6.2. We want to estimate intensity at point X, that lies between the grid points B and C. A third point, A, is needed to perform a parabolic interpolation. If the estimated I(X) is greater or lower then the intensity values at interpoland points A,B,C, than I(X) is reevaluated using a first order scheme. It can also happen (right picture in fig.6.2) that the interpolated function assumes values higher or lower than the intensity at interpoland points, but I(X) is still bracketed by I(B) and I(C). In this case we can either keep the intensity value obtained, or reevaluate it with a first order scheme. Both schemes have been investigated. I will refer to the first one as *non strict monotonicity* and to the second one as *strict monotonicity*.

The Search Beam technique consists in the evaluation of intensity of a beam in vacuum, i.e. when density, opacity and Source function are set to zero. In this case, the intensity value evaluated at each point of the grid corresponds to the upwind intensity value (points indicated with X in fig.6.4 and fig.6.6). Since, as shown in previous chapter, in general the upwind point does not lie on the grid, its intensity value has to be determined by interpolation. If no computational error was present, intensity at the top of the grid would be the same as the boundary condition at the bottom. As will be shown this is not the case due to interpolation spurious effects. By the analysis of results obtained with three different boundary conditions, namely a δ function, a step function and a Gaussian function, I have observed indeed that the intensity profile at the top of the grid is:

- Broadened
- Asymmetric
- Peak is attenuated
- Peak is shifted
- Power is not conserved

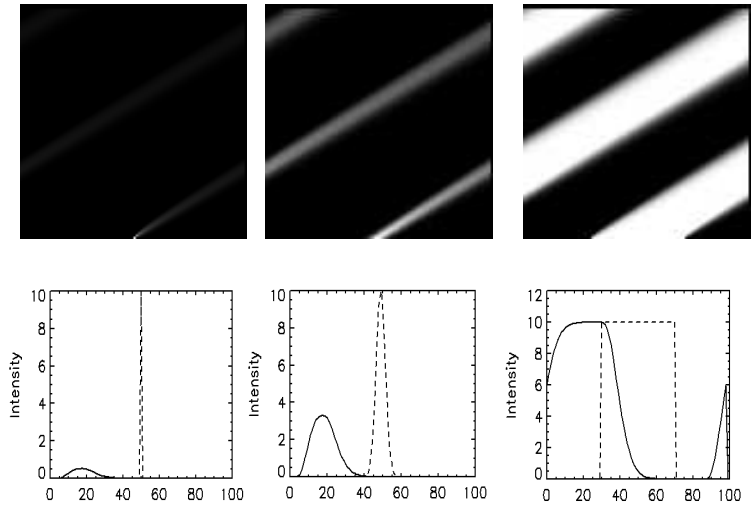

(a) δ function (b) Gaussian function (c) Step function

Figure 6.3: Upper panel: Intensity values on the grid of a beam that propagates in vacuum at an angle of 30° respect to the horizontal direction when three different boundary conditions are imposed at the bottom. The grid size is 100×100 and the *Second Order non strict* interpolation scheme is employed. Lower panel: Intensity profile at the top of the grid for the three cases. Horizontal axis describes the horizontal position (in pixel) on the grid. The three boundary functions have a maximum intensity of 10 (arbitrary units). Both upper and lower panels show that the beam is deformed and attenuated. Note also the effects of the horizontal periodic conditions.

Pictures in fig.6.3 show ray intensity on the grid (upper panel) and the intensity profile at the top of the grid (lower panel) in the case of a beam that propagates on a uniform grid along a direction that forms an angle of 30° respect to the horizontal direction, for the three boundary conditions, and for non strict second order interpolation. Pictures show clearly that the beam is attenuated, broadened and asymmetric. The amount of all these 'aberrations' depends on the interpolation technique adopted, and is more evident for the delta and step functions boundary conditions since these are discontinuous functions.

Broadening is in general more evident for first order interpolation schemes and for shallow angles, since these directions experience a coarser grid and require a higher number of interpolations. Asymmetries are mostly due to the way the grid is swept, and are more evident for second order interpolation schemes and shallow angles. Let us consider, for instance, an angle of 30° respect to the horizontal direction, as in fig.6.4. Open circles represent points of the grid in which intensity is zero or not evaluated by the code. The full black circle is the boundary condition (a Delta function in this case, since only one point of the initial row is not zero) and the gray and shaded circles are points at which the intensity is evaluated by the code. Point A is the first point from the left on the first row (the closest to the boundary) whose intensity is not zero. The upwind point that allows the evaluation of I(A) lies on the previous row far from the beam (full black dot). Intensity at all the other points of the row (B,C,D) is obtained interpolating vertically between points of the previous column, so that the intensity assumes its maximum value in A and smaller and smaller values as we proceed along columns. This produces the peaked intensity profile with the long tail on the right shown in fig.6.5. As we proceed on the rows the curve gets more symmetric due to interpolation, that spreads the signal. The first point on the grid whose value is not zero is always shifted of one position to the right respect to the point at previous row. The corresponding upwind point lies always on the previous row, between two points of which only the one on the right has not null intensity. Its value is thus smaller and smaller as we proceed up on the grid, and the maximum of the intensity profile at each row shifts to the right, to points whose intensity is evaluated interpolating between points whose intensity is not null. Figure 6.5 shows also that asymmetries are more evident for second order interpolation, since the first order is a procedure that intrinsically tends to broad the signal more than the second order.

For directions closer to the vertical axis the broadening on the right is less evident, since, except for points closer to the beam, intensity on interpoland points is always zero, as illustrated in fig.6.6. At the first row, intensity is not zero only at points A0 and A, with the maximum at A. At the second row, intensity is not null at points A0', A' and B' and so on. As we proceed to the top, a small broadening on the right is observed, due to the fact that intensity at points A0, A0', A0" etc. is not zero. A comparison of beam profiles in fig.6.5 and fig.6.7 shows that the beam 'aberrations' are less important for vertical directions.

An other source of asymmetries is the condition of strict monotonicity, since for some angles points close to the beam can be interpolated linearly or at second order depending if they are on the right or on the left of the beam. Fig.6.8 illustrates these aspects: the right sides of the curves coincide for strict and non strict cases, while they differ in the left sides, the strict case using a linear

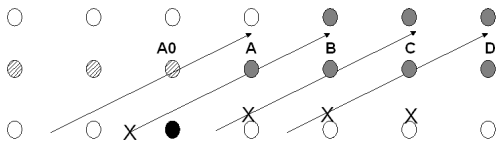

Figure 6.4: Gray circles: points of the grid on which intensity is not zero. Black circle: points at which boundary conditions are imposed. Radiation propagates at an angle of 30° respect horizontal to direction. Shaded circles: points at which intensity is not zero because of periodic condition. Symbol X: upwind point from which the intensity at grid points is evaluated. Sweeping the grid from left to right, on the first row intensity is not zero at points at the right of A, with the maximum in A. On the second, from B' on, with the maximum in B'. On the following rows the first point whose intensity is not null is shifted of one position to the right respect the one on previous row. The maximum is no longer on the first point of the row for the reasons explained in the text.

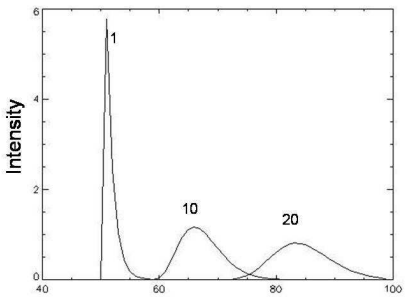

(a) Linear interp.

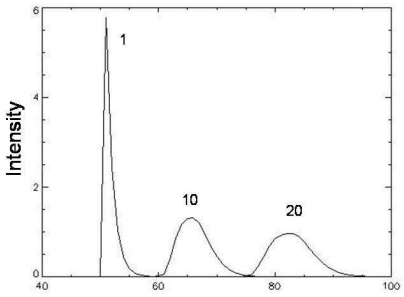

(b) Sec. Ord. strict mon. interp.

Figure 6.5: Intensity profile at rows 1, 10 and 20 of a 100×100 grid in the case of a delta function boundary condition (row 0) and a ray that propagates with an angle of 30°respect to the horizontal direction.(a) Linear Interpolation. (b)Second Order with strict monotonicity interpolation. In both cases, the intensity is not a delta function, but a broad asymmetric curve whose peak is attenuated respect to the initial one. All these effects increase with the height (the row number) and are more evident with a linear interpolation scheme.

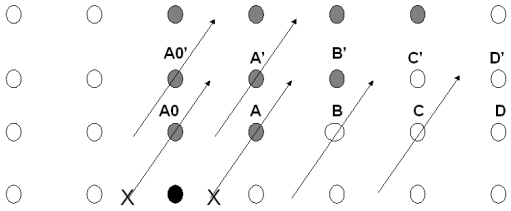

Figure 6.6: Gray circles: points of the grid on which intensity is not zero. Black circle: point at which boundary conditions are imposed. Radiation propagates at an angle of 70° respect horizontal direction. On the first row intensity is not zero only at points A0 and A. On second row not null intensity points are A0', A',B', and so on.

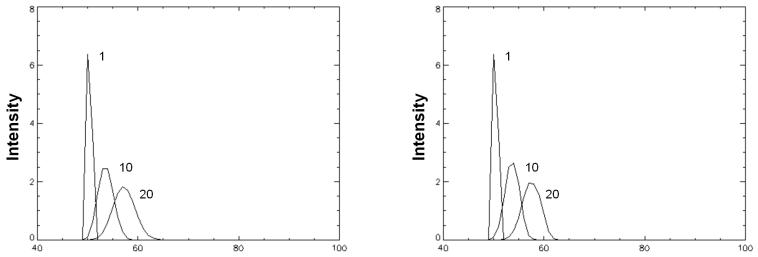

(a) Linear interp. (b) Sec. Ord. strict mon. interp.

Figure 6.7: Intensity profile at rows 1, 10 and 20 of a 100×100 grid in the case of a delta function boundary condition (row 0) and a ray propagates at an angle of 70°respect to the horizontal direction. (a)Linear Interpolation. (b)Second Order with strict monotonicity interpolation. As in fig.6.5 the beam is asymmetric, broadened and attenuated, but these aberration are less important.

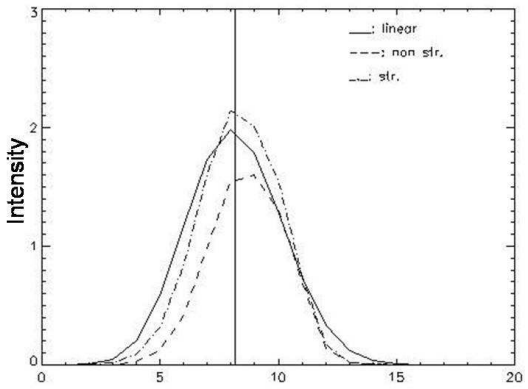

Figure 6.8: Intensity profiles at the top of the grid for a ray that propagates at an angle of 70° respect to the horizontal direction for the three interpolation schemes in the case of a Gaussian function boundary condition. Vertical line indicates the expected position for the maximum. The three curves are asymmetric and the maximum is shifted of some pixels respect to the expected position. *Strict* and *non strict* second order schemes coincide at one side of the curve, where a second order is always possible. On the left side the *strict* scheme is broader since at some points it employs a first order scheme.

interpolation. For comparison linear interpolation case is shown.

Fig.6.8 also shows the attenuation of the peak and its shift, the continuous vertical line being the expected position of the beam for that angle. We also observe that the power of the beam, i.e. the integral of the intensity profile, is conserved if linear interpolation is used but it is not for second order schemes. This is due to the fact that a second order interpolation is not possible everywhere on the grid, as explained above. In general, a power loss of about some few to some tens per cents is observed, the largest values being observed for discontinuous boundary functions. This effect is dependent on the direction of propagation (decreases for vertical directions) in the case of Gaussian functions, while for discontinuous functions is not.

For what concerns the shift, simulations have shown it is more evident for second order schemes.

In general all these effects are reduced when resolution is increased, as shown for instance in fig.6.9. The ray power loss is instead larger for finer grids in the case of discontinuous functions, while a decrease with the increase of grid resolution is observed for Gaussian functions. The same is observed for the peak intensity attenuation: is very large (around 80-90%), almost independent on propagation direction and increases with increasing the resolution, for discontinuous functions; is some tens per cent, with a strong dependency on propagation direction (decreases as the angle increases), grid resolution (decreases with the increase of resolution) and integration scheme (is lower for second order schemes), for Gaussian function.

I finally noticed that, while in general spurious effects become more important as the intensity propagation direction becomes shallower, there must be a direction other than the vertical one, for instance 45° for regular grids, for

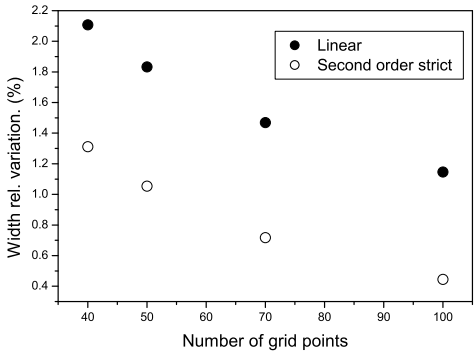

Figure 6.9: Relative variation of the amplitude of the intensity profile (fit with a Gaussian function) at the top of the grid for a Gaussian boundary condition vs number of grid points along the vertical direction. Since the physical space is kept constant, an increase of grid point number corresponds to an increase of resolution. The finer the grid the smaller is the deviation from the original value.

which the upwind points always belong to the grid, so that interpolation is not needed. Therefore for these directions no spurious effects are observed. When analyzing these effects in function of the propagation direction, one thus finds that they are null for 90° (vertical) direction, then increase as the angle increase, go to zero again at 45°, and then increases again for the most shallow directions. Effects are not symmetric respect to the 45° direction, the intensity being evaluated in different ways in the two octants, as explained before.

6.2.1 Conclusions

Spurious effects introduced by interpolation have been investigated. Particularly, I studied the dependence of these effects on propagation direction, resolution and boundary conditions, for three different interpolation schemes. Results are summarized in the following:

- **Broadening** Increases for shallower directions and decreases with increasing the resolution. For the cases analyzed, it is usually of some percent (e.g. fig.6.9). It is more important for first order schemes.
- **Asymmetries** Increases for shallower directions and decreases with increasing the resolution. It is more important for second order schemes.
- **Peak attenuation** Is usually very large (tens per cents) for the cases analyzed, with the largest variations being measured for delta function boundary condition. The effect is more important for shallow angles, and decreases with resolution for Gaussian function. It is larger for first order schemes.
- **Peak shift** Is larger for second order schemes and is usually of few pixels. Increases for shallow angles.

- **Power loss** It is observed for second order interpolation schemes. Power losses are slightly dependent on propagation direction and increase with increasing resolution in the case of discontinuous functions. A strong dependence on propagation angle and resolution is instead observed for Gaussian function.

Rays that propagate at shallower angles are thus more affected by spurious effects. The linear interpolation also leads to larger spurious effects respect to second order schemes. Nevertheless, second order schemes do not conserve the beam energy (while first schemes do) so leading to non physical results. Since most of the effects can be reduced increasing the resolution, I thus conclude that a first order scheme is preferable.

I finally want to stress the fact that the cases analyzed, non uniform or discontinuous boundary conditions, are extreme cases and that in the simulations I'll present in next chapters the expected spurious effects generated by interpolation are less important, as shown by the fact that all the effects analyzed are usually less evident for the Gaussian function boundary condition.

6.3 Combined effects of integration and interpolation

When estimating intensity by the Short Characteristic, results depend both on integration and interpolation schemes adopted. In order to investigate this issue, I have studied the relative error (relative difference of the intensity estimated at the top of the grid respect to the expected theoretical value) in the case in which the source function is null. Again the scaling of the error with grid resolution, for the different schemes and at several beam propagation direction was investigated. For instance, fig.6.10 shows, for different angles, the relative

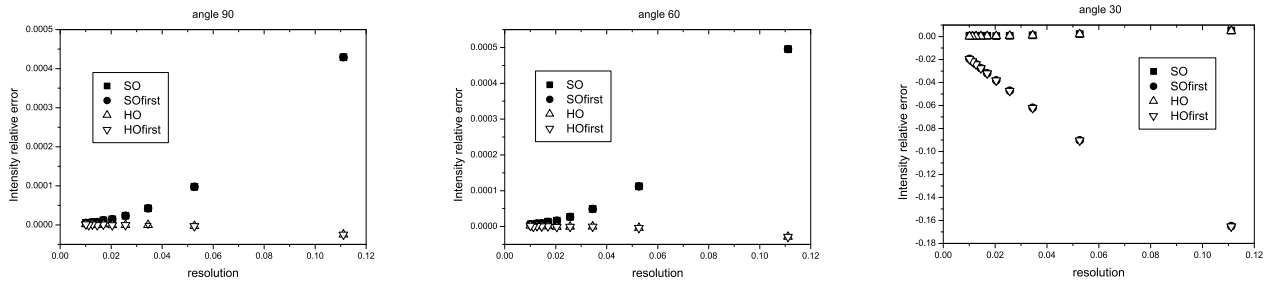

Figure 6.10: Intensity relative error at the top of the grid in the case of a beam that propagates at three different angles on a regular grid. Results obtained for the *Second Order* and *Higher Order* integration schemes (see text) and for first and second order interpolation schemes are shown. At vertical directions (cases a and b) the integration scheme determines the result, while for shallow angles (case c) results are determined by the interpolation scheme.

error of intensity evaluated on a regular grid when opacity and density vary as exponential functions. For this test only results for *SO* and *HO* techniques are

presented, when a second order or a first order interpolation schemes are used. Note that in this case the atmosphere varies with continuity, so that *strict* and *non strict* second order schemes produce identical results. Even in this case higher order integration techniques lead to better results. A comparison between plots in fig.6.10 (left and center) shows that no significant variations occur if the impinging angle is decreased from 90° to 60°. An increase of two or three orders of magnitude in the error for second order interpolation, and about three or four orders for first order interpolation, is observed for radiation that propagates at 30° (right). A comparison of the plots also reveals that for angles greater than 45° the main source of error is the truncation in the series expansion in the integration scheme, while for shallow angles the uncertainties introduced by interpolation are overwhelming. This is due to the fact that for vertical directions the upwind point is on a row of the grid, so that, if the atmosphere (k,ρ, Source function) varies only with height and the boundary conditions are continuous functions (as in the cases here discussed), the interpolation scheme is not important. For shallow angles, instead, the upwind points are on columns of the grid, and the interpolation scheme is crucial to the evaluation of intensity. It is worth to notice that the error for *SO* technique is positive (the measure is an underestimate), while it is negative or oscillates around zero for *HO* technique.

6.4 Eddington Barbier Atmosphere

In order to analyze the combined effects of integration and interpolation, results have been analyze in the case of an Eddington Barbier atmosphere (see 5.1.6), that means in the case in which the source function is:

$$S = a_0 + a_1 \mu \tau \tag{6.2}$$

note that this relation differs from the one in 5.1.6 since here τ is the optical depth and not the radial optical depth (see 5.1). For a finite slab, the solution of RTE is, from eq.5.17

$$\begin{aligned} I_{fin} &= I_{in} e^{-\Delta\tau} + \int_{\tau_{in}}^{\tau_{fin}} (a_0 + a_1 \mu \tau) e^{-(t-\tau_{fin})} dt \\ &= I_{in} e^{-\Delta\tau} + a_0 (1 - e^{-\Delta\tau}) + \\ &+ a_1 \mu \cdot e^{-\Delta\tau} (-\tau_{in} - 1) + a_1 \mu (\tau_{fin} + 1) \end{aligned} \tag{6.3}$$

where I_{in} is the boundary condition (e.g. the intensity at the bottom of the grid) and I_{fin} is the intensity value at a certain height in the atmosphere (e.g. at the top of the grid). For a slab of depth Z, the optical depth is given by

$$\tau = \int_0^D \alpha(s) ds = -\int_Z^0 \alpha(z) \frac{dz}{\mu} \tag{6.4}$$

where s indicates the physical distance travelled by the ray, α is the product of density and opacity and z is the distance along the vertical direction. As already shown in previous chapter, $ds = -\frac{dz}{\mu}$. The minus sign derives from the fact that in the chosen notation z decreases when s increases. For the test the α function was chosen so that

$$\alpha(z) = e^{z-Z} \tag{6.5}$$

Z being an arbitrary constant. Therefore, for a generic height z,

$$\tau(z) = -\frac{1}{\mu}(e^{-z} - e^{(z-Z)}) \tag{6.6}$$

The boundary condition I_{in} is evaluated by

$$I_{in} = \int_{\tau_{in}}^{\infty} (a_0 + a_1\mu t)e^{-(t-\tau)}dt = a_0 + a_1\mu + a_1\mu\tau \tag{6.7}$$

Simulations have been performed at five different angles respected to the horizontal direction: 90°, 70°, 50°, 30°, 20°. Regular and irregular grids of different resolutions have been used, and again results obtained by *strict second order* and *first* order interpolation schemes have been compared. In general relative error decreases of about two orders of magnitude when resolution is increased of one order. No significant difference in results is evident for vertical directions, while the shallower (30°, 20°) give results worse of about one order of magnitude. Fig.6.11 shows the scaling of the relative error, computed respect the real

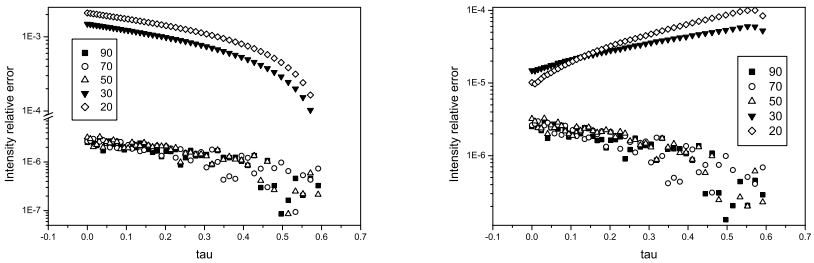

(a) Linear interp. (b) Sec.Ord.interp.

Figure 6.11: Intensity relative error in the case of an Eddington Barbier atmosphere vs optical depth. The integration scheme is the Second Order one, but the interpolation scheme is a) first order and b) second order. Radiation propagates from the bottom (highest optical depth) to the top (lowest optical depth) along different directions. At vertical directions (angles 90, 70 and 50) error is almost independent from interpolation scheme and increases toward the top. At horizontal directions Linear interpolation scheme gives higher errors. Note that the error decreases at horizontal directions for a second order interpolation scheme.

value given by eq.6.3, with the radial optical depth, for different angles and for the two interpolation schemes. In both cases, for directions that form with z axis angles less than 45°, (in this case 90°, 70° and 50°), the error increases when approaching the surface due to the error accumulation, while the amount of error does not vary significantly with angle. Shallower angles present higher error because more interpolations are needed for the evaluation of intensity at the first useful point of the grid (see par.5.3.1 and fig.5.6). When a second order is used, the effect is enhanced by the fact that, for the reasons explained in 6.2, at the first row the intensity is evaluated with a first order scheme. In this case, fig.6.11 (b) shows also that relative error presents a maximum at high τ, corresponding to the first (from the bottom) 2 or 3 rows of the grid. This is caused

Intensity	$N = 6$	$N = 8$	$N = 12$
μ^2	10^{-8}	10^{-8}	10^{-8}
μ^4	10^{-8}	10^{-8}	10^{-8}
μ^6	10^{-8}	10^{-8}	10^{-8}
μ^8	10^{-8}	10^{-8}	10^{-8}
μ^{10}	10^{-8}	10^{-8}	10^{-8}
μ^{12}	$-4.8 \cdot 10^{-3}$	10^{-8}	10^{-8}
μ^{14}	$-2 \cdot 10^{-2}$	10^{-8}	10^{-8}
μ^{16}	$-4 \cdot 10^{-2}$	$4 \cdot 10^{-4}$	10^{-8}

Table 6.1: Mean intensity integral J relative error evaluated with the Gauss-Legendre scheme in the case of an intensity field that is a power function of μ for different orders of quadrature.

by the fact that at the first rows, the effect of linear interpolation is dominant respect to the gain that is obtained by a second order interpolation. When a pure first order is used (fig.6.11,(a)), error always increases as the surface is approached, but the error is about one order of magnitude larger than second order.

6.5 Quadrature techniques

In order to test the quadrature techniques presented in previous chapter and to evaluate their performance and limits, I have analyzed the numerical results obtained with functions whose integral is analytically solvable: the intensity is a power function of μ and a Lambert radiator.

Table 6.1 and table 6.2 report relative errors obtained evaluating mean intensity J in the case Intensity is a power function of μ and does not depend on ϕ. That is

$$J = \frac{1}{2}\int_0^1 \mu^l d\mu + \frac{1}{2}\int_{-1}^0 \mu^l d\mu$$

where l is an even integer. Several values of l for three different order of quadrature and for the Gauss-Legendre and Carlson schemes respectively have been investigated.

Table 6.1 shows that Gauss-Legendre scheme gives results that are exact within the error round off machine, for polynomials of order lower than twice the order of the quadrature, as expected from the theory (e.g. Press et al., 1994). For the Carlson scheme I notice that, for lower order power functions, results get better increasing the order of quadrature, while no significant improvement is obtained when the exponent is higher. As shown in fig.6.12, this is due to the distribution of quadrature points in the integration interval. Higher power functions are sensibly different from zero only at higher values of μ, an interval that is poorly sampled even by the highest order schemes investigated. This shows that, because different orders of quadrature use different quadrature points, increasing the order of quadrature does not always guarantee the increasing of accuracy of results. In atmospheres with flux tubes, whose investigation is the purpose of this thesis, the integrand functions can change abruptly in the in-

Intensity	$N = 6$	$N = 8$	$N = 12$
μ^2	10^{-8}	-0.002	10^{-8}
μ^4	0.0266	0.0144	0.0072
μ^6	0.05	0.03	0.01
μ^8	0.06	0.035	0.02
μ^{10}	0.06	0.04	0.02
μ^{12}	0.05	0.04	0.025
μ^{14}	0.03	0.04	0.03
μ^{16}	0.034	0.04	0.03

Table 6.2: Mean intensity integral J relative error evaluated with the Carlson scheme in the case of an intensity field that is a power function of μ for different orders of quadrature.

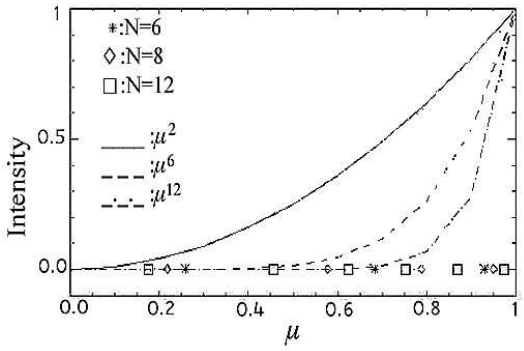

Figure 6.12: Distribution of μ-level points for $0 \leq \mu \leq 1$ in the Carlson scheme. Different symbols indicate the quadrature points positions in the interval for the different orders. The lines show the values of different order polynomials in the interval. High order polynomials are sensibly different from zero only for μ approaching 1. When increasing the quadrature order only some of the points are closer to 1 and since generally the lower order points don't coincide with higher order points, an increase of quadrature order not always implies an increase in accuracy.

terval because of the presence of inhomogeneities introduced by the magnetic field. Results shown in table 6.2 show that in these cases a technique that allows a high number of quadrature points is necessary. In particular 6 levels in an octant (corresponding to N=12) is not sufficient to sample the functions. One would also prefer a technique in which the set of points of a certain order includes the sets of points of lower orders, rather than one, like the Carlson or the Gauss Legendre one, in which the set of points are disjoint. This would allow estimating the best order of quadrature for a problem by studying result variations with increasing the order of quadrature.

Tests with both schemes have been repeated by using a more realistic atmosphere. A Lambert radiator (see 5.1.6), that means an atmospheric model in which the source function is constant with depth and μ ($S = a_0$), was used. Fig.6.13 and 6.14 show the relative error in the computation of J and flux by the two schemes for different orders. In order to discern interpolation uncertainties from quadrature errors, plots show with continuous lines mean intensity and flux relative errors obtained in the case in which intensity is evaluated by an analytical formula. Dashed lines represent errors obtained when numerical intensity values estimated by the short characteristic code developed are used. Both figures show that error is slightly dependent on the intensity field employed (analytical or numerical) and that it is still quite high even at the highest orders for both schemes. This is due to the fact that, while outgoing intensity radiation has the simple expression

$$I^{out} = a_0 \tag{6.8}$$

incoming radiation is the following function of angle and optical depth:

$$I^{inc} = a_0(1 - e^{\frac{-\tau}{|\mu|}}) \tag{6.9}$$

The mean intensity is thus evaluated by solving the integral:

$$J = \frac{1}{2}\int_0^1 a_0 d\mu + \int_{-1}^0 a_0(1 - e^{\frac{-\tau}{|\mu|}})d\mu \tag{6.10}$$

The integral on the left has a trivial solution. By contrast the integral on the right is an exponential integral of order 2. By a change of variable $x = -\frac{1}{\mu}$, we have in fact:

$$\int_{-1}^0 e^{\frac{-\tau}{|\mu|}} d\mu = \int_1^\infty e^{-\tau|x|}/x^2 dx \tag{6.11}$$

Similarly it can be shown that the evaluation of flux requires the evaluation of an exponential integral of order 3. Figure 6.15 shows the errors obtained estimating the 1D integral 6.11 with the Gauss-Legendre scheme at different orders and for different values of optical depth. As the 'true' values, the results obtained by the 'expint' routine of IDL were assumed. Curves present a maximum and a minimum whose absolute value and position diminish with increasing the order of integration. Nevertheless, only at orders greater than 30 the relative error is less than 1%.

The fact that continuous (intensity evaluated analytically) and dashed (intensity evaluated by short characteristic code) lines almost coincide in fig.6.13 and fig.6.14, and a comparison of fig.6.13 with fig.6.15, show that the main source of error in the evaluation of mean intensity and flux for a Lambert radiator atmospheric model is the quadrature scheme and order employed. Note

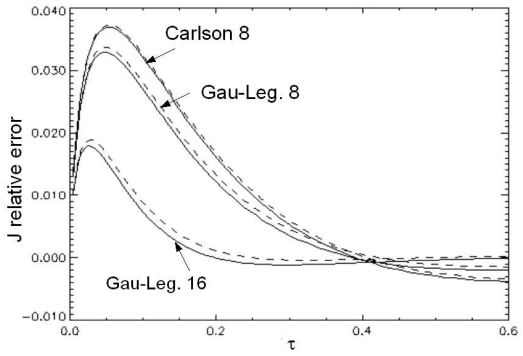

Figure 6.13: Relative error in the evaluation of mean intensity J vs optical depth in the case of a Lambert radiator. Continuous line: results obtained with analytical intensity values. Dashed lines: results obtained with intensity values evaluated by the Short Characteristic code developed. The Carlson and Gauss Legendre scheme give similar results when the same order of quadrature (8 in this case) is employed, but the error is still quite high (about 4%) at some depth. The error is reduced when increasing the quadrature order.

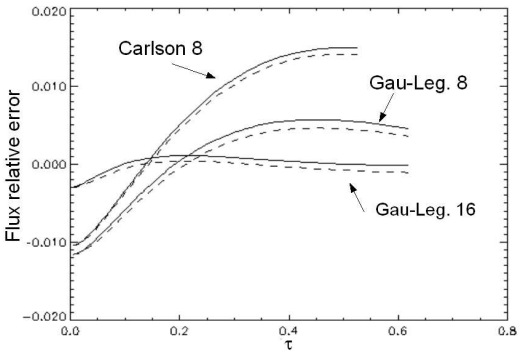

Figure 6.14: Relative error in the evaluation of flux intensity F vs optical depth in the case of a Lambert radiator. Continuous line: results obtained with analytical intensity values. Dashed lines: results obtained with intensity values evaluated by the Short Characteristic code developed. The Gauss Legendre schemes give better results respect to the Carlson scheme even for the same order (N=8). The error is reduced of about one order of magnitude when doubling the quadrature order of the Gauss Legendre scheme (N=8 and N=16).

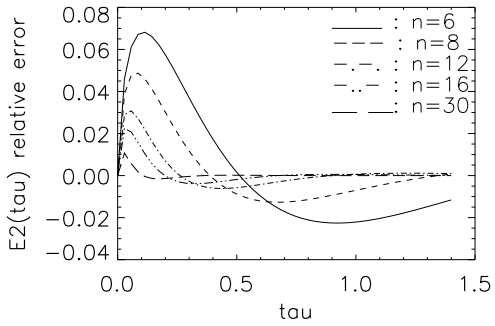

Figure 6.15: Relative error in the evaluation of Exponential integral of order 2 using the Gauss Legendre scheme and different orders of quadrature. Only at orders higher than 30 the values of the function at stationary points are less than 1%.

also that the nature of the error in the evaluation of exponential integrals and power functions of μ is the same, namely the poor sampling of the functions.

6.5.1 Conclusions

In this chapter I have presented the results obtained by some preliminary tests, whose aim was to identify and quantify numerical problems inherent the evaluation of intensity radiation field by the short characteristic code developed, and the estimation of mean intensity and radiative flux through the two quadrature schemes employed. Radiative intensity field can be evaluated with large accuracy in the case of continuous vertically stratified atmospheres, as shown for instance in fig.6.10, especially for vertical direction. Depending on integration and interpolation scheme, the error scales as a power function of the resolution, so that one can adjust the space sampling in order to obtain the desired accuracy. I also observed that results at shallow directions are dominated by interpolation scheme adopted and that errors at vertical directions are determined by the integration scheme. Shallow directions, because of the larger number of interpolation needed, and because they experience a larger total path length, are affected by larger errors. When the atmosphere is not homogeneous, several spurious effects can determine the final horizontal intensity profile. These spurious effects are larger for discontinuous boundary conditions, due to interpolation. Even in this case effects can be reduced increasing the grid resolution. I also observed that second order schemes do not conserve the energy beam all over the domain, so that a first order scheme should be preferred.

Testes concerning the 3-D quadrature scheme have revealed that in order to have a reasonable accuracy high order schemes have to be employed. On the tests carried out, the Gauss-Legendre scheme gave the best results. Note that in the case of Lambert Radiator, the most realistic one among the ones investigated, the error estimated in the evaluation of J is larger then the uncertainties observed for the total radiative flux. In the models I developed (see chapter 7) the radiative equilibrium is imposed by an iterative scheme in which the tem-

perature is updated at each step by the evaluation J, so that an accuracy better then the one observed for instance in fig.6.13 is preferable. This means that an order higher than 12 has to be employed and thus the Gauss Legendre has to be preferred to the Carlson scheme.

Chapter 7

A Flux Tube Model

In this chapter I describe the model I developed to investigate some physical properties of stellar atmospheres and magnetic flux tubes. I firstly describe the geometry of the model and then describe the equations and the numerical techniques employed to solve them. In particular I developed two classes of models. The first one takes into account both convective and radiative processes. In the second one radiation is the only energy transport mechanism but radiative equilibrium is imposed. Differential equations have been normalized in order to explore different scenarios and discern the different physical quantities that determine the final result. Some examples of different atmospheres, obtained changing the free parameters in the models, are given.

7.1 NON magneto NON dynamic Flux Tube Models

In chapter 4 I illustrated the concept of Magnetic flux tube and physical equations to which it obeys, that is the MHD equations. I also illustrated the case of static tubes, that is the MHS equations and some simple models presented in the literature. This chapter describes the model I developed in order to investigate some observed properties of magnetic 'bright' regions.

The general sketch that describes the geometry of the problems I have solved is shown in fig. 7.1. The atmosphere is plane parallel and is built by the infinite repetition of plane $x - z$ along direction y. It is not uniform along x direction (because of the presence of the flux tube) and along z direction (because of the vertical gravitational stratification). It is infinite and uniform along y direction. The space coordinate z is positive and increases with depth.

The presence of the flux tube (shaded area) is simulated imposing lower pressure and lower density in a small region of the domain. Pressure, temperature an density are specified at the bottom. Boundary conditions for intensity are also necessary. At the top the incoming intensity is set to zero, while at the bottom radiative diffusion is assumed. Similarly, the optical depth at the bottom is evaluated assuming radiative diffusion and at the top is set to zero.

Given boundary conditions, temperature, density and pressure inside and outside the tube are evaluated using a set of differential equations that stem from simplifications of MHD equations. In particular, let us assume that the

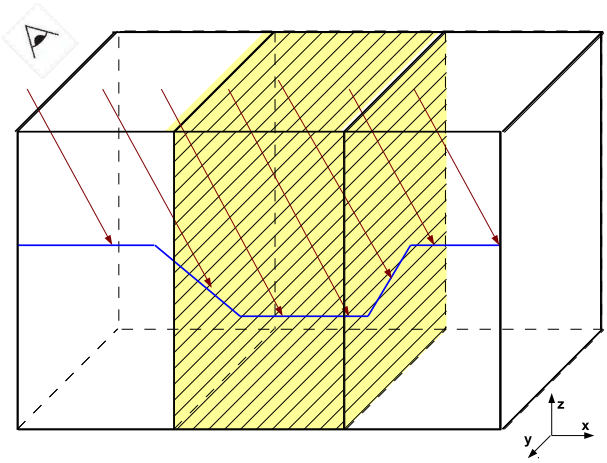

Figure 7.1: Sketch of the geometry of the model. Plane parallel atmosphere, not uniform along x and z directions, and uniform and infinite along y directions. Periodic horizontal conditions are imposed. The presence of the flux tube (shaded area) is simulated imposing lower density and pressure. Boundary conditions are imposed at the bottom (see text). The outgoing intensity for different line of sights (purple arrows) escaping from $\tau = 1$ surface (blue curve) is evaluated.

tube is static, so that derivatives respect to time and the velocities are set to zero. Let us also assume that the magnetic field is constant respect to height inside the tube and its value is given by pressure horizontal balance at the bottom of the tube (eq.4.15). Than the following new set of equations has to be satisfied by the static state:

Energy

$$\frac{\partial q_k}{\partial x_k} = 0 \tag{7.1}$$

Momentum

$$-\frac{\partial p}{\partial x_k} + \rho g = 0 \tag{7.2}$$

Continuity

$$\frac{\partial \rho}{\partial t} = 0 \tag{7.3}$$

where

$$\bar{q} = F_{Radiative} + F_{Convective}$$

Pressure and temperature are related by the perfect gas law and e is the internal energy:

$$e = C_V T.$$

More specifically, previous equations can be rewritten as:

$$\nabla \cdot (\bar{F}_{Radiative} + \bar{F}_{Convective}) = 0 \tag{7.4}$$

$$\frac{dP}{dz} = \rho g \tag{7.5}$$

$$P = \frac{K_B}{m_e}\rho T \tag{7.6}$$

Note that in writing these equations we have omitted the requirement of horizontal pressure balance, therefore the shape of the tube does not change with the height and its flanks remain vertical. This is an oversimplification but it approximates the geometric configuration of magnetic structures in the lowest photospheric levels.

Once an inhomogeneous atmospheric model is obtained, intensity along $\tau = 1$ surface, represented by the blue curve in fig.7.1, and for different view angles (red arrows) is investigated. The intensity field at each angle is evaluated by the short characteristic code developed and described previously.

Several models can be constructed from previous equations. In particular, in this work I have investigated two classes of models. In the first one the two atmospheres are totally independent and therefore in the energy equation 7.4 only variations along vertical directions are different from zero, so that:

$$\frac{dF_{Radiative}}{dz} + \frac{dF_{Convective}}{dz} = 0. \tag{7.7}$$

The convective flux is estimated using the Mixing Length theory (see Appendix to this chapter). In the following I will address models obtained with these schemes as NON Radiative Equilibrium models.

In the second class of models convection is absent and the radiative equilibrium is imposed allowing the radiation to propagate through the medium, so that the energy equation is eq.7.4 with convective flux set to zero. The Radiative flux is estimated by the radiative transfer code and quadrature techniques I developed and that are described in chapter 5. In particular, this quantity is evaluated according to the 3D geometry illustrated in fig.7.1, while the other equations are solved only in plane $x - z$. This is therefore a 2.5-D problem. In the following these are addressed as Radiative Equilibrium models.

The study I present is parametric and no realistic value for each of the quantities is assumed. This allows to investigate several possibilities and to discern the most important physical processes that regulate some observed properties.

In the next paragraphs I describe in more detail the atmospheric models developed to reproduce the physical properties of the quiet and magnetized sun.

7.2 Tubes in NON radiative equilibrium

7.2.1 Radiative Diffusion atmospheres with convection

The case in which both convection and radiation contribute in energy transport have been investigated. In particular, the case transport by a non radiating parcel in the mixing length approximation, described in paragraph C.1.2 of the

Appendix to this chapter, has been considered. The flux conservation (or energy equation), requires that:

$$K_R \nabla + K_C (\nabla - \nabla_a)^{3/2} = F_{Sun} \tag{7.8}$$

where $\nabla = \ln T / \ln P$, $K_R = \frac{16\sigma T^4}{3k\rho H_P}$ and $K_C = \frac{\alpha}{2}\rho c_p T l \sqrt{\frac{g\delta}{8H_P}}$. $\nabla_a = 2/5$ is the adiabatic gradient and H_P is the pressure scale height. The solution of the cubic equation 7.8 gives an estimate of gradient ∇. Nevertheless, convection takes place only in some particular physical conditions, that is only when the *Schwarzschild criterion* is satisfied. This requires $\nabla > \nabla_a$. If this condition is not satisfied, then radiation is the sole energy transport mechanism, and the flux conservation law requires that

$$K_R \nabla = F_{Sun} \tag{7.9}$$

The gradient ∇ is thus evaluated through equations 7.8 or 7.9, depending on whether or not the *Schwarzschild criterion* is satisfied. Temperature $T(z)$ and pressure $P(z)$ are then evaluated solving the set of differential equations:

$$\frac{dT}{dz} = \frac{T}{H_P}\nabla \tag{7.10}$$

$$\frac{dP}{dz} = \frac{g m_e}{K_B}\frac{P}{T} \tag{7.11}$$

where eq.7.11 is derived combining eq.7.5 with relation 7.6. Given the boundary conditions for temperature and pressure, and given an initial condition for the temperature and pressure profiles $T(z)$ and $P(z)$, a solution is found iteratively. The Rosseland mean opacity $k = k_0 \rho^m T^n$, with k_0, n and m as free parameters, is adopted. The mixing length parameter α is left as free.

Different solutions have been obtained changing the values of parameters k_0, n and m and α. Figure 7.2 shows for instance results obtained with α, n and m constant, but for different values of k_0. For the lowest values ($k_0 = 10$ and $k_0 = 15$) only the deeper part of the domain is super adiabatic, while for the highest value ($k_0 = 30$) convection is effective in the whole domain. The amount of relative flux carried by radiation or convection is also a function of depth and k_0, that means that are functions of opacity. Note that ∇ is usually slightly super adiabatic in the regions where convection is efficient, while changes abruptly in the regions where convection is not efficient. The last panel shows finally the relative difference between the temperature profile estimated solving the set of equations 7.10 and 7.11, and the temperature profile expected for an adiabatic gas. Differences are very small in regions were convection is efficient, but increase rapidly in regions where radiation is the only energy transport mechanism. Note also that the higher is the opacity (k_0) the more these differences increase. From eq. 7.8, in fact, if k_0 increases K_R decreases and ∇ increases in order to conserve the total flux.

Finally, variations of parameter α regulate the efficiency of convection. The presence of magnetic field, that inhibits convective motion in flux tubes, has thus been mimicked assuming lower values of mixing length parameter in magnetic regions and higher values in non magnetic regions. Results concerning this point are shown in next chapter.

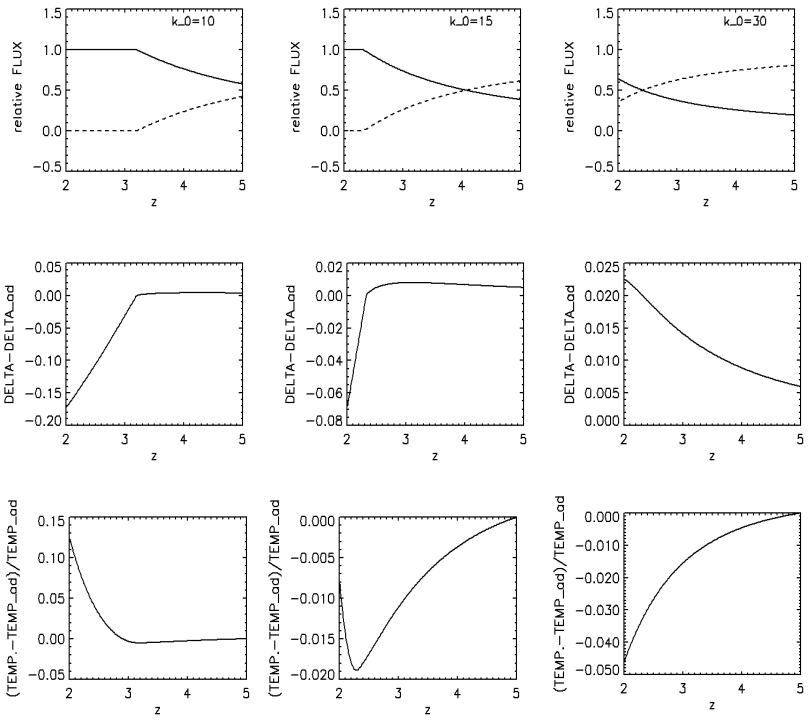

Figure 7.2: Atmospheric models in presence of convection for different values of parameter k_0 and for $m = -0.5$, $n = 3.5$ and $\alpha = 1.5$. First raw: Radiative (continuous line) and Convective (dashed line) relative flux. Second raw: difference between the evaluated gradient and the adiabatic gradient. Third raw: relative differences between the computed temperature profile and the adiabatic temperature profile. As k_0 increases the opacity increases and the regions of the domain in which convection becomes efficient increase. Third raw shows that in regions where convection is efficient, the gas is approximately adiabatic.

7.3 Atmospheres in radiative equilibrium

The case of atmospheres in radiative equilibrium has also been considered. This is achieved via an iterative scheme illustrated in fig.7.3. An initial condition atmosphere is assumed (usually a radiative diffusion atmosphere described in 7.3.1) and the total flux and mean intensity J are then evaluated by the short characteristic code. The new temperature at each point of the domain is evaluated imposing LTE and Radiative Equilibrium, that is $S = J = \sigma T^4$. The new pressure is evaluated solving the differential equation 7.11 and from this the new density (through perfect gas law) and new opacity. In this updated atmosphere the flux and mean intensity J are reevaluated. The iterations are stopped when the total relative difference between the temperature fields of two consecutive iterations is smaller than a certain threshold. In particular the results I will show have been obtained with the threshold value equal to 5×10^{-4}. In the models analyzed, this criterion is satisfied within 10-15 iterations, as illustrated in fig.7.4 (left) for the model *A.A1/3* described in next chapter. Note that, as illustrated by the plot on the right of fig.7.4, the flux converges more slowly than the temperature, so that the flux has not converged yet when temperature, and other physical quantities like pressure and opacity, have. Tests have shown that in order the flux to satisfy the same convergence criterion imposed for the temperature the number of iterations required is from five to ten times larger. For this reason in the models I will show in next chapter flux is not constant respect to height. This is not expected to influence the intensity profiles, the physical quantity I want to investigate, since these are mainly dependent on temperature and opacity (as I will show in detail in next chapter).

For boundary conditions the diffusion approximation is assumed, so that only the temperature at the bottom has to be specified (see also below).

7.3.1 Initial and boundary condition: Radiative Diffusion atmospheres without convection

As initial condition, the radiative diffusion approximation is assumed in most of the models I developed. The Radiative Diffusion approximation and physical conditions under which it is a valid assumption were explained in chapter 5. It is certainly valid in the deeper layers of the atmosphere, at optical depths larger than one. This is thus also a good boundary approximation for the Intensity at the bottom of the domain, provided that the boundary values of the other parameters (temperature and density) are such that the opacity is high and optical depth is large. Let us consider the case in which radiation is the only energy transport mechanism. From eq. 5.59, the temperature and the optical depth are related by the formula:

$$T(\tau) = T_{eff}(\frac{3}{4}\tau + \frac{1}{2})^{\frac{1}{4}} \tag{7.12}$$

where T_{eff} is a function of the total flux F_{Sun}.

Therefore, from LTE condition, $S = \sigma T^4 = \sigma T_{eff}^4(\frac{3}{4}\tau + \frac{1}{2})$. From eq.5.48

$$I^{out.}(\tau, \mu) = \sigma T_{eff}^4(\frac{3}{4}\tau + \frac{1}{2} + \frac{3}{4}\mu) \tag{7.13}$$

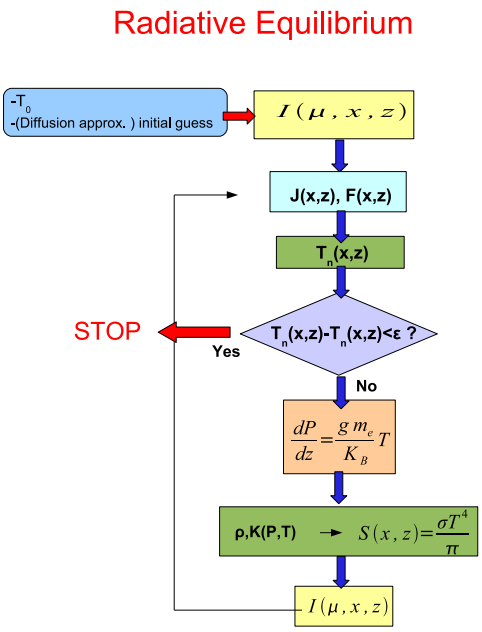

Figure 7.3: Flow chart of the code employed to impose Radiative Equilibrium. The system is initialized with an atmosphere in radiative diffusion approximation and a boundary temperature is imposed at the bottom. The radiative transfer code evaluates the intensity at each point of the domain and for each direction μ of the quadrature scheme adopted to evaluate the mean intensity J and radiative flux F. The value of J allows to evaluate the new T at each point of the domain (RE condition) and the new S (LTE condition). From pressure hydrostatic equilibrium condition the new pressure is evaluated and then the new density and opacity. In this new atmosphere the new values of I, J and F are evaluated. The scheme is iterated until the differences between the temperature values of two consecutive iterations are less than a threshold ϵ.

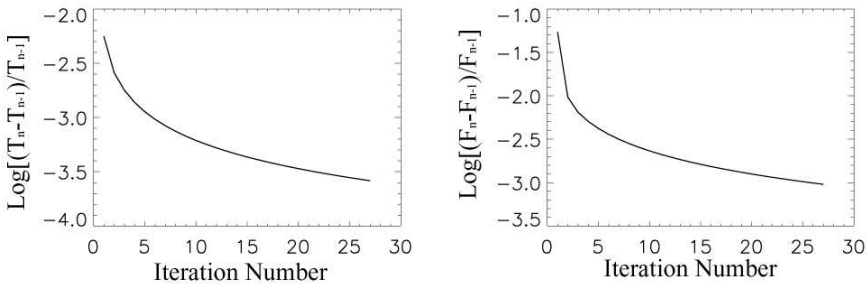

Figure 7.4: Relative difference, in logarithmic scale, between the temperature fields (left) and the total flux (right) of two consecutive iterations n versus the iteration number. These results refer to the model *A.A1/3* described in next chapter.

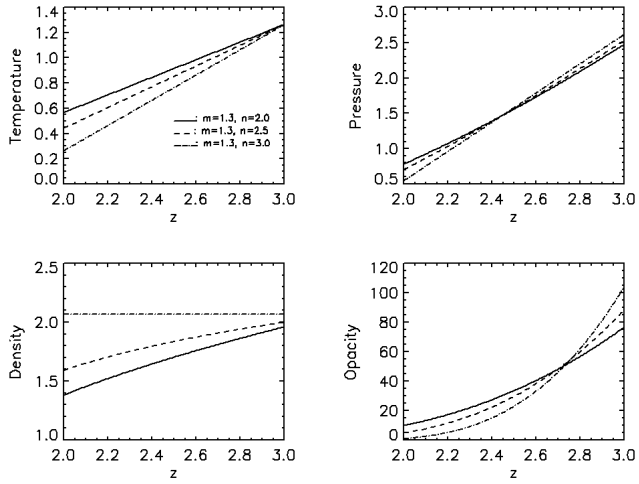

Figure 7.5: Temperature, Pressure, Density and Opacity vertical profiles in the case of pure radiative, radiative diffusion approximation. Different profiles are obtained changing the values of parameters n, m, k_0 and temperature boundary condition. In particular, profiles obtained with three different values of parameter n are shown. These solutions have been obtained by numerically solving the set of differential equations 7.14, 7.5 and 7.6.

From the energy conservation (eq. 5.50):

$$F_{Sun} = \frac{16\sigma T^3}{3k\rho}\frac{dT}{dz} \tag{7.14}$$

where z increases toward the center of the Sun and $k = k_0\rho^m T^n$ is the Rosseland mean opacity. The quantities k_0, n and m are free parameters. In appendix C I show that a solution to equations 7.14, 7.5 and 7.6 is

$$T(z) = \frac{m+1}{m-n+4} gcz + Const. \tag{7.15}$$

$$P(z) = \left[\frac{16\sigma g}{3k_0 F_{Sun}}\left(\frac{K_B}{m_e}\right)^{m+2}\frac{m+1}{m-n+4}T^{m-n+4}\right]^{\frac{1}{m+1}} \tag{7.16}$$

$$\rho(z) = \left[\frac{16\sigma}{3k_0 F_{Sun}}\frac{m+1}{m-n+4}T^{3-n}\right]^{\frac{1}{m+1}} \tag{7.17}$$

with $m \neq -1 \wedge m-n+3 \neq -1$. The solutions in the cases in which parameters n and m do not satisfy these conditions are given in appendix C. Since in a reasonable atmospheric model temperature, pressure and density increase with depth, also the conditions $\frac{m+1}{m-n+4} > 1 \wedge \frac{3-n}{m+1} \geq 1$ have to be satisfied. Moreover, at photospheric level the opacity is strongly dependent on the temperature and slightly dependent on the density so that the conditions $n > m \geq 0$ also hold. Different atmospheric models are constructed by choosing the opportune values of the free parameters and of the boundary conditions. It is important to notice that only the temperature value has to be specified at the bottom, the other

physical quantities being evaluated through relations 7.12 (optical depth), 7.13 (intensity), 7.16 (pressure) and 7.17 (density). Figure 7.5 shows an example of solutions obtained changing the value of parameter n. Note that solutions to this problem are evaluated solving the set of differential equations 7.14, 7.5 and 7.6, and not from analytical solutions 7.15, 7.16 and 7.17. Numerical tests have shown, however, that numerical solutions are in good agreement with analytical ones.

In brief, in most of the models the initial conditions are given by relations 7.15, 7.16 and 7.17. The boundary conditions at the bottom for temperature, pressure and density also satisfy previous relations, while relations 7.13 and 7.12 are used for intensity and optical depth.

7.4 Computational and Numerical Details

The differential equations necessary to describe the atmosphere in the flux tube and its surrounding, described in previous paragraphs, have been solved numerically. At this aim a numerical technique, based on the Relaxation method (Press et al., 1994), has been developed and implemented.

The routines developed for the simulations and for the analyses of the results have been written in the IDL language. The results shown in the next chapter have been obtained sampling the space with a 140×280 points regular grid for models in RE and a 200×400 points regular grid for models with convection. For RE models a smaller grid was chosen in order to optimize the computational time. Most of the simulations have been in fact run on a 3 MHz Sun Work Station. On such a machine the time employed to evaluate the radiative flux with a N=12 per octant quadrature scheme is about 3 hours. The time necessary to satisfy the convergence criterion described in previous paragraph is thus about 2 days. Note that this is also the reason why the quadrature scheme has order 12, in spite of the fact that in chapter 6 I showed that a higher order scheme would be preferable.

The differential equations have been normalized in order, as explained above, to allow a parametric study. Number of grid points and the range of integration of the independent variable ($2 \leq z \leq 3$ and $2 \leq z \leq 5$ for RE and convective models respectively) were chosen in order to prevent numerical instabilities (when integrating close to zero, for instance, convergence is never achieved, while poor resolution leads to non-physical results due to a poor sampling of the transition between super and subadiabaticity).

Chapter 8

Results

In this chapter I show the results obtained by the models described in chapter 7. I firstly show the physical properties of models with convection and models in radiative equilibrium. Then I show results obtained by the investigation of contrast at different values of optical depths and at different disk positions. Finally I compare results obtained with simulations with the ones obtained with PSPT images and shown in chapter 3.

8.1 Physical properties of simulated magnetic flux tubes

8.1.1 Models with Convection: Models *C*

In order to study the effect of the presence of the magnetic field in atmospheres with convection I have investigated two classes of models.

In the first one the presence of the magnetic field is mimicked by reducing the value of the mixing length parameter α, that is equivalent to reduce the distance travelled by a rising convective parcel (see Appendix C). This is in agreement with the fact that, as seen in both observations (Title et al., 1992) and numerical 3-D MHD simulations (Vogler et al., 2005), solar granules appear smaller and less brilliant and are characterized by slower temporal evolution in regions of high concentrations of magnetic field (plages). The reduction of the mixing length causes an increase of the gradient ∇ and therefore a sharper decrease of temperature. In order to investigate the sole effect of α parameter variation, the pressure reduction consequent to the magnetic pressure and horizontal pressure balance are not taken into account.

Different values of α inside and outside the tube have been investigated. Figure 8.1 shows for instance temperature, pressure, density and opacity profiles obtained with $\alpha = 5$ in the quiet atmosphere and $\alpha = 1$ in the magnetic flux tube. The Rosseland mean opacity is $K = \rho T^3$ (that is k_0=1, m=1 and n=3). The boundary conditions at the bottom of the domain are the same inside and outside the tube and their values are assumed to be the ones expected from an

Model $C_{5.1}$

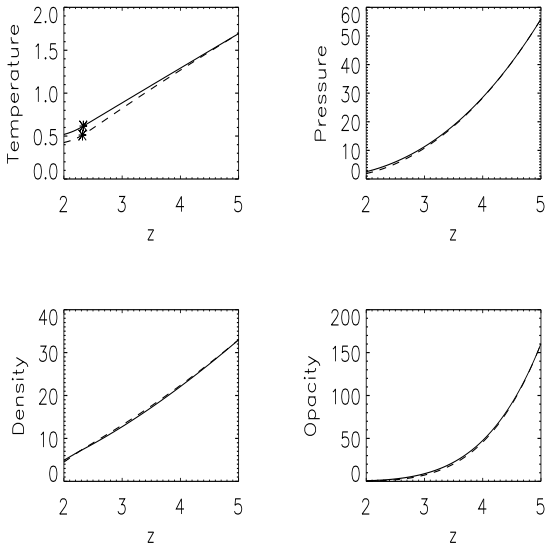

Figure 8.1: Model with convection efficiency reduced inside the tube. Continuous line: $\alpha = 5$ (quiet atmosphere). Dashed line: $\alpha = 1$ (flux tube). The depth z increases toward the interior of the atmosphere. The only quantity to be sensibly affected by variations of α is the temperature. The asterisks indicate the height and temperature at the upper boundary of the convective layer.

adiabatic stratification:

$$T_{bottom} = \nabla_a g \frac{m_e}{K_B} z_{bottom} + Const. \quad (8.1)$$

$$P_{bottom} = z_{bottom}^{1/\nabla_a} \quad (8.2)$$

where z_{bottom} is the spatial coordinate at the bottom of the grid and $Const.$ is an arbitrary constant (in this case its value is -0.3).

Figure 8.1 shows that in general temperature, pressure, density and therefore opacity are slightly sensitive to changes of value of α. The temperature is the quantity that is most effected by the variation. Reduction of mixing length parameter causes indeed reduction of the coefficient K_C in equation 7.8. The gradient ∇ then has to increase in order the total flux to be conserved, and thus the temperature decreases. The gradient of P is inversely proportional to the value of T (eq.7.11) so that a decrease of T corresponds to a decreases of the value of P. As shown in fig.8.1 the relative variation of P is smaller respect to the relative variation of T. From the perfect gas law the density then has to increase. The asterisks on the plot that shows temperature indicate height and the corresponding temperature values at which the gradient becomes from subadiabatic to super adiabatic, that is the upper boundary of convective layer. The position of this boundary is only weekly sensitive to changes in α, being this essentially dependent on the opacity value. This model, in which the parameter

Model $C_{5.1}P1/2$

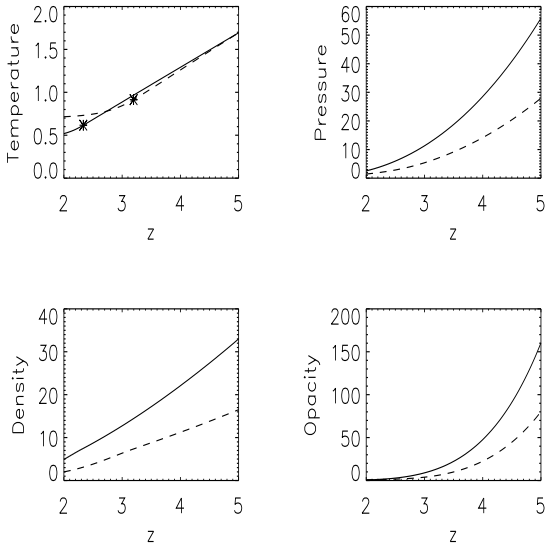

Figure 8.2: Model with convection efficiency and pressure boundary value reduced inside the tube. Continuous line: $\alpha = 5$ (quiet atmosphere). Dashed line: $\alpha = 1$ and pressure boundary value reduced to half (flux tube). The reduction of pressure causes the vertical profiles of all the physical quantities shown to change. In particular reduction of pressure shifts the upper boundary of the convective layer (marked by the asterisks) to the interior.

α is larger in the quiet atmosphere and lower in the magnetic flux tube, is mostly representative of a pore or a sunspot, since the temperature inside the tube is lower than outside. In the following I will refer to this model as model $C_{5.1}$.

The second class of models I investigated is constructed similarly to the first one, that is the mixing length parameter value is smaller inside the tube, but the lower boundary value for the pressure inside the tube is a fraction of the pressure outside the tube. This mimics the gas pressure reduction expected by the horizontal pressure balance. Figure 8.2 shows in particular results obtained imposing the internal boundary pressure value to be half of the external boundary pressure value. In this case pressure, density and opacity stratification are markedly different in the tube. The temperature, instead, is very similar to the one shown in fig.8.1 in the deeper layers, whereas it is higher in the highest layers of the domain. Variations of temperature are essentially consequences of variations of ∇. At the bottom of the domain the reduction of pressure causes coefficient K_R (that is proportional to P^{-2}) to increase and coefficient K_C (that is proportional to P) to decrease in eq. 7.8. Nevertheless the opacity is still too high and the increase in K_R does not compensate for the decrease in K_C. Because of the conservation of flux, then ∇ has to increase, and consequently the temperature decreases. At the top the opacity is lower and the point at which the gradient becomes subadiabatic is shifted deeper respect to the 'quiet'

atmosphere. In the purely radiative regime, at the top of the domain, the opacity is small and thus K_R is high, so that a small value of ∇ is sufficient to carry the flux. Consequently the temperature varies slowly with depth and the atmosphere in the tube is hotter at the top respect to outside. This result is very important since it indicates that heating in the tube can take place even without radiative channelling from the flanks of the tube. It may be objected, though, that this model was obtained without taking into account the radiative exchanges between the tube and the surrounding atmosphere. I will make some comments about this point at the end of paragraph 8.1.2. I will refer to this model as model $C_{5.1}P1/2$.

8.1.2 Radiative Equilibrium models

Two classes of models of flux tubes in radiative equilibrium have been investigated. In the first class of models the boundary value of temperature inside the tube is lower and the pressure and density values are evaluated by relation 7.16. In the second one the temperature at the lower boundary inside and outside the tube is the same and the presence of the magnetic field is mimicked reducing the pressure, and consequently the density (evaluated by the perfect gas law), inside the tube. In the following I will refer to the first kind of models as 'cold' and I will denote them models $B.A$. These models mimic the situation in which the suppression of convection causes a reduction of temperature inside the tube and are representative of small pores or small tubes in downflow regions generated for instance by the 'collapse' phenomenon described in 4.2.1. The second classes of model will be addressed as 'hot' and will refer to them as $A.A$. They physically reproduce the conditions of small tubes in thermal equilibrium with the surrounding atmosphere, as most likely is for small tubes that propagate to the deepest layers of the solar atmosphere. Dependence of results on flux tube size has been investigated.

'Cold' tubes: models B.A

'Cold' flux tube models have been initiated using equations 7.15, 7.16 and 7.17 for temperature, pressure and density initial and boundary conditions. The bottom boundary temperature value inside the tube is equal to the temperature value outside the tube minus an arbitrary constant. Since the temperature scales linearly with height in radiative diffusion models, this is equivalent to use inside the tube a 'collapsed' atmosphere. In particular results shown in this paragraph are obtained with the following boundary values: $T_{bottom} = 1.327, T^{FT}_{bottom} = T_{bottom} - 0.1$. The total flux is 0.05 and the parameters that define the opacity are $K_0 = 20., n = 3$ and $m = 1$. The intensity of incoming radiation at the top of the domain is set to zero, as well as the optical depth value. At the bottom the optical depth value is given by eq.7.12. In order to investigate the sole effect of temperature reduction, the reduction of pressure consequent to the magnetic pressure and horizontal pressure balance are not taken into account.

Figures 8.3-8.7 show results obtained with this model. Figure 8.3 shows in gray scale the temperature intensity in the domain. Isothermal contours are marked in white. The vertical yellow lines show the tube flanks and the blue line shows the $\tau = 1$ surface. The red lines mark the locations were, at each height, the horizontal optical depth (τ_{Horiz} hereafter), evaluated from the axis

Model B.A

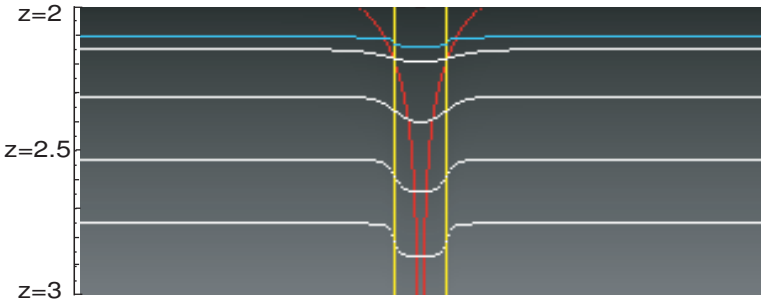

Figure 8.3: Temperature field (gray scale) and temperature isocountours (white lines) of a flux tube in Radiative Equilibrium. The yellow vertical lines represent the tube flanks and the light blue line is the $\tau = 1$ surface. The red lines are the $\tau_{Horiz} = 1$ surface evaluated from the central axis of the tube. This is the border beyond which radiation cannot penetrate inside the tube.

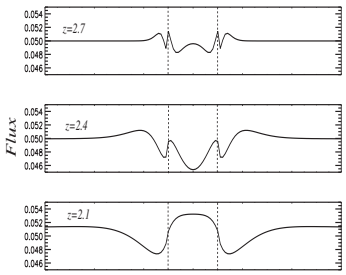

Figure 8.4: Radiative Flux profiles at three different heights. Vertical dashed lines are tube flanks. Only the area around the tube is shown.

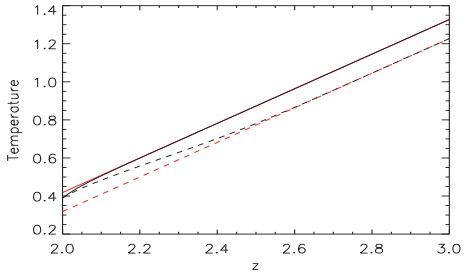

Figure 8.5: Temperature vs height in the quiet atmosphere (solid line) and in the center of the tube (dashed line). The red lines show the corresponding initial conditions temperature profiles.

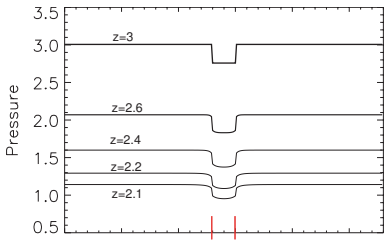

Figure 8.6: Pressure profiles at different heights. Vertical red bars at the bottom indicate flux tube flanks positions.

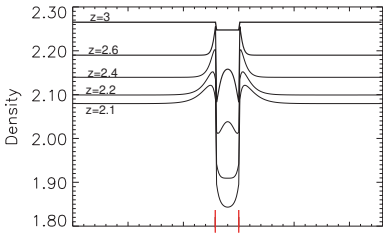

Figure 8.7: Density profiles at different heights. Vertical red bars at the bottom indicate flux tube flanks positions.

of the tube, is equal to one. They are almost vertical straight lines in the deeper layers, where the opacity is very high, but in the outer layers, because of the decrease of opacity, they bend horizontally to eventually expand beyond the tube flanks. In this model this happens at $z \simeq 2.15$. Intensity of radiation originated beyond the red lines is negligible compared to the intensity originating at points within the lines. Therefore, at locations where the red lines are within the tube boundaries (in this model in the lowest layers), the radiative channelling from the flanks is not (or less) effective and no (or little) heating is observed, as shown by fig.8.3 and fig.8.5. Heating starts to be efficient at depths smaller than z=2.4, where the width of the horizontal optical depth surface is roughly half of the width of the tube. In the higher layers the internal temperature increases until it reaches the external temperature.

Channelling is thus more or less effective depending on the ratio of the tube diameter D and the width of the $\tau_{Horiz} = 1$ surface. This last quantity is thus a useful horizontal scale unit (as it is, for instance, the pressure scale height for vertical directions). In the following I will indicated with $d_{\tau H}$ the width of the $\tau_{Horiz} = 1$ surface at the bottom of the domain and will express the tube diameter as multiples of this quantity. For the models in figures 8.3-8.7 $d_{\tau H}$=2 grid points and the diameter of the tube is D=10$d_{\tau H}$. Figure 8.4 shows the flux intensity profiles at three different heights. Along the tube axis the total radiative flux decreases from the boundary bottom value, reaches the minimum at z=2.4, then increases to eventually exceed the external flux value. At the deepest layers the decrease is induced by the increase of temperature in the area around the axis, even though, at least in the deeper layers, these areas are beyond the red lines (fig.8.3). The flux is indeed a measure of the 'difference' between the outgoing and incoming radiation and thus its value is more sensitive to small variations of intensity. On the contrary the mean intensity, being a 'sum' over the different directions, is less affected by small variations. Consequently the temperature value is the same of the initial condition in the deep layers, even though the flux is decreasing. Note that the flux starts to increase again at the same height at which the temperature along the tube starts to increases, that is at $z < 2.4$. In these layers radiation from outside the tube can penetrate and the flux increases toward the surface even though the temperature increases with height. In order to clarify this point let us suppose, for instance, we want to evaluate the flux at $z = 2.3$. The difference among the intensity value of radiation that is generated above and below this point is expected to be small, since the temperature gradient is small, and thus the flux should decrease. Nevertheless, radiation from outside can penetrate. In the quiet atmosphere the temperature gradient is higher and since also the temperature values are higher than in the tube the total flux increases. In the upper layers it finally exceeds the value of the outer atmosphere.

Figure 8.4 shows that even in the quiet atmosphere the flux increases when approaching the surface. This result is not surprising. The radiative diffusion approximation is in fact valid in the deepest layers, where outgoing and incoming radiation have similar values and the Eddington approximation is exact (see paragraph 5.2). In the upper layers, that is at optical depth lower than one, the approximation is not valid and the flux is not balanced until the solution fully relaxes away from its initial condition. In particular the increase is an effect of the upper boundary condition imposed on the incoming radiation. Since this value is set to zero the flux increases. We expect the effect in the tube to be

enhanced by the evacuation that makes the outgoing radiation intensity inside the tube higher than outside. Note that this makes the temperature to decrease at the very top of the domain as shown in fig.8.5. The boundary effect is observed because, as explained in previous chapter, the system has not reached equilibrium yet when iterations are stopped. If the radiative equilibrium was satisfied the flux would have been constant respect to height. It is important to notice that this boundary effect, being smaller than the channelling effect, is not responsible for the excess of flux observed inside the tube respect to the outer atmosphere. An excess of flux is in fact observed even in 'cold' models (not shown) where the temperature at the top is lower and the flux decreases rather than increasing. Moreover, if the boundary effect was the sole responsible of the flux increase, the temperature would decrease inside the tube, as is observed at the very top of the domain for both quiet and flux tube atmospheres, and as observed in models *A.A* (see below). Finally, the 'wrinkles' and spikes that appear in the flux profiles inside and close the tube are also generated by the different gradients of temperature inside and along the tube. In the relaxed solution horizontal variations of the flux will still be there, with wrinkles because of the discontinuity, only the horizontal average flux will be constant with height.

Figure 8.6 shows the pressure intensity profiles at different heights. The small increase of pressure along the tube flanks are caused by the increase of temperature. Note that the changes of temperature with height only slightly affect the pressure gradient, as a consequence eq. 7.11. The density, instead, is more sensitive to temperature variations, as illustrated by fig. 8.7. In the deeper layers inside the tube, for instance, both pressure and temperature are higher in the regions close to the flanks rather than at the axis. Relative variations of pressure are smaller than relative variations of temperature and the density is lower. In the upper layers variations of temperature along the direction perpendicular the axis are small, while variations of pressure are still not negligible, so that the pressure increases along the flanks. In the quiet atmosphere close to the tube the increase of density is caused by the fact that the pressure value is almost the same as the value in areas far from the tube, but the temperature is smaller.

Figures 8.8 and 8.9 show temperature field and temperature versus height for a model in which the physical conditions are the same as the ones in the model shown above but the tube diameter is three times larger (D=$30d_{\tau H}$). In this case the red lines are always located inside the tube except at the very top of the domain and heating is less effective than in the smaller tube. Even in this case the flux (not shown) along the tube axis is lower than the external one, decreases with height to reach a minimum at $z = 2.2$ and then increases again, but never exceeds the outer flux value, this point being roughly located, in previous model, at the level at which the horizontal optical depth lines cross the tube flanks.

'Hot' tubes: models A.A

These classes of models have been obtained imposing the same bottom boundary value of the temperature inside and outside the tube. The presence of the magnetic field is mimicked by imposing the internal pressure to be a certain fraction of the external pressure. The initial conditions in the quiet atmosphere are given by relations 7.15, 7.16 and 7.17. In the tube the temperature is the

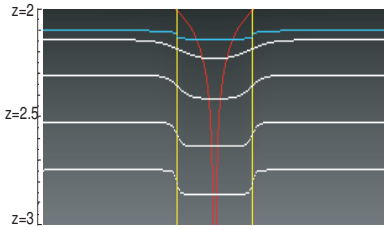

Figure 8.8: Temperature field (gray scale) and temperature isocountours (white lines) of a 'cold' flux tube in Radiative Equilibrium whose diameter is three times larger than in model shown in fig.8.3.

Figure 8.9: Temperature vs height in a 'cold' model where the diameter is three times larger than in the models shown in figures 8.3-8.6. Solid black line: quiet atmosphere. Dashed black line: temperature along the tube axis. Dash dot red line: temperature along the tube in the smaller tube model shown in fig.8.5.

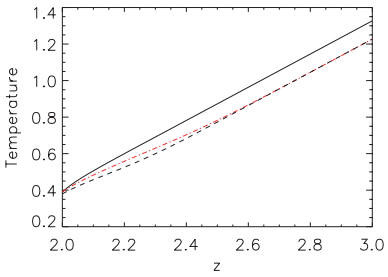

same as outside, while the pressure profile is imposed to be a smaller fraction of the external one. The density inside is evaluated by the perfect gas law. These same conditions are kept at the bottom boundaries. Both the intensity of radiation at the bottom and the value of optical depth are evaluated, as for the previous models, by relations 7.13 and 7.12 and thus they have the same value inside and outside the tube.

These models allow to investigate the sole effect induced by the reduction of opacity consequent to the reduction of pressure and density inside the tube.

In the following I will illustrate results obtained reducing pressure boundary value inside the tube to one third and two thirds of the external one. I will refer to these models as *A.A1/3* and *A.A2/3* respectively.

Figures 8.10-8.13 show results obtained with models *A.A1/3* for tubes of two sizes: D=1.4$d_{\tau H}$ and D=4.3$d_{\tau H}$ (corresponding to 20 and 60 grid points respectively). Figure 8.10 shows the temperature fields, the isothermal contours, and the surfaces at which vertical and horizontal optical depth are equal to one. Unlike the previous 'cold' models, the tube and the surrounding atmosphere are hotter than the quiet atmosphere and the heating is larger for the larger tube, as also illustrated in fig.8.11. Since the initial condition for temperature are the same inside and outside the tube (and thus the source term), in these models the heating is consequence of the reduction of opacity (that is of the attenuation term), induced by the reduction of pressure and therefore of density, inside the tube. Thus, the larger the tube, the longer the lengths of sections of ray path that cross the tube and the higher is the intensity. Large heating is observed from the very first iteration. This also makes the opacity to increase, so that temperature variations are smaller and smaller in subsequent iterations, until the convergence criterion is satisfied. The dependence of temperature increase on the ratio of tube diameter and photon mean free path (that is, in a more pictured way, the relative position of tube flanks and $\tau_{Horiz} = 1$ surface) is the opposite of the one observed in 'cold' models. In 'hot' models the heating is

Model A.A1/3

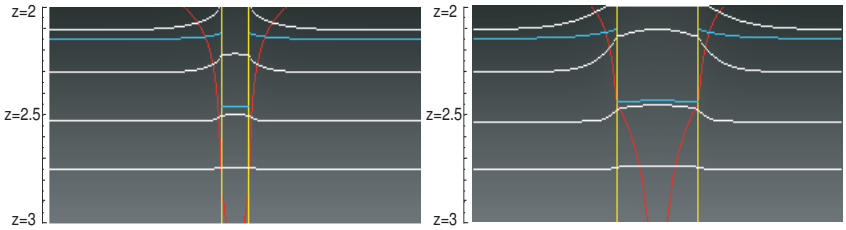

Figure 8.10: Temperature field, isothermal contours, $\tau = 1$ and $\tau_{Horiz} = 1$ surfaces for 'hot' tubes models A.A1/3 in radiative equilibrium. Left: D=$1.4 d_{\tau H}$ (20 grid points). Right: D=$4.3 d_{\tau H}$ (60 grid points).

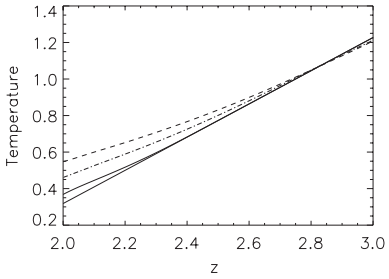

Figure 8.11: Temperature vs height. Solid line: quiet atmosphere at radiative equilibrium. Dot dashed line: temperature along the tube axis for a structure of D=20 grid points. Dashed line: temperature along the tube axis for a structure of D=60 grid points. Solid thick line: temperature initial condition.

Figure 8.12: Flux in the radiative equilibrium quiet atmosphere (continuous line) and along the tube axis for a tube of D=20(dot dashed line) and a tube of D=60 (dashed line) grid points.

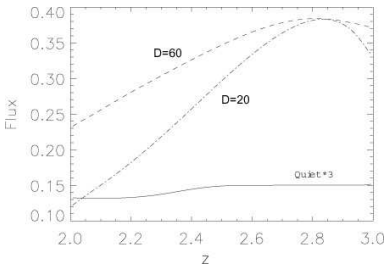

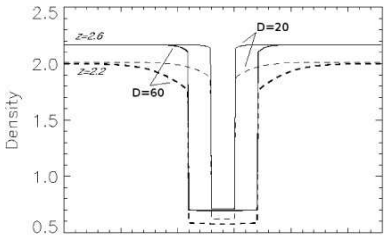

Figure 8.13: Density profiles at two different heights for tube of D=20 (continuous lines) and D=60 (dashed lines) grid points.

larger in tubes whose diameter is larger than the mean free path and smaller for models in which the diameter is lower than the mean free path. The large difference of opacity also causes the discontinuity of the $\tau_{Horiz} = 1$ surface when this crosses the tube flanks. In particular, the red lines 'fan' more rapidly with height when they are located inside the tube rather than when they are outside. Note also than in these models the tube is heating the surrounding, so that the more the red lines expand from the tube flanks into the quiet atmosphere the more this latter is heated, as shown by the isothermal contours.

In brief, the reduction of opacity inside the tube is the cause of temperature increase in both cold and hot models. In cold models because of the channelling of radiation from hotter surrounding atmosphere through tube flanks, in hot models because the attenuation is smaller inside the tube. Therefore when increasing the tube size heating is smaller in cold models and is higher in hot models.

Figure 8.11 shows the temperature in function of height for the quiet atmosphere in radiative equilibrium and along the axis of the two size tubes investigated. The temperature initial condition is also shown. It is worth to notice that, close to the surface, the temperature of the quiet atmosphere in radiative equilibrium is higher than the initial condition, i.e. is higher than the value prescribed by the radiative diffusion approximation model. As for the 'cold' models, this is an effect of the boundary conditions. In particular, the initial condition temperature profile is such that the ratio outgoing/incoming intensity radiation is very low, so that the flux decreases and the temperature increases. In the tube the flux is higher than the surrounding atmosphere. This is consequence of the fact that both the initial and boundary conditions for temperature and pressure do not satisfy the diffusion approximation equations. In particular the atmosphere inside the tube is more transparent to radiation so that, being the boundary temperature values the same for the quiet and the 'magnetic' atmospheres, the flux in the tube is higher. It increases from the bottom to the top to reach a maximum at $z \simeq 2.8$. This increase is consequence of the underestimation of the intensity radiation at the bottom of the tube. This, in turn, is caused by the overestimation of the optical depth that is imposed to have the same value as the external atmosphere, and not lower as should be because of the reduction of opacity inside the tube. The effect is enhanced in smaller tubes because of the (lower intensity) radiation that channels through the flanks from the quiet atmosphere. After reaching the maximum, the flux decreases. The decrease in this region is entirely due to the channelling from the external regions, as also indicated by the fact that it is more important for smaller tubes.

Finally, fig.8.13 shows the density horizontal profiles at two different heights for the two models. The density is of course lower than the surrounding atmosphere in the tube, but also in the regions adjacent because of the increase of temperature.

Figures 8.14-8.16 show results obtained for models in which the pressure value at the bottom of the tube is two thirds of the pressure value outside. The opacity inside the tube is thus increased respect to previous models and the distance of the $\tau_{Horiz} = 1$ surfaces at each depth is smaller. In particular also $d_{\tau H}$ is smaller and, in spite of the fact that the diameters of the tubes analyzed are the same in grid points units (20 and 60 respectively), these tubes are "physically" larger (namely, D=$5d_{\tau H}$ and D=$15d_{\tau H}$). Consequently the

Model A.A2/3

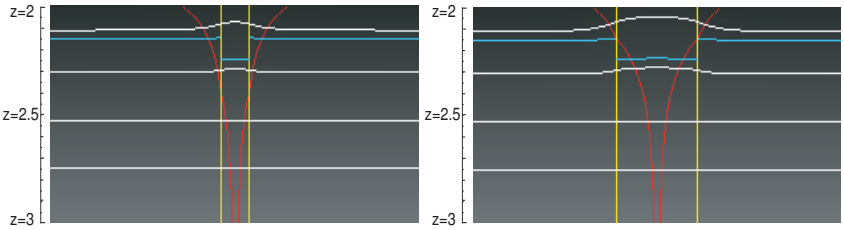

Figure 8.14: Temperature field, isothermal contours, $\tau = 1$ and $\tau_{Horiz} = 1$ surfaces for 'hot' tubes models *A.A2/3* in radiative equilibrium. Left: D=$5d_{\tau H}$ (20 grid points). Right: D=$15d_{\tau H}$ (60 grid points).

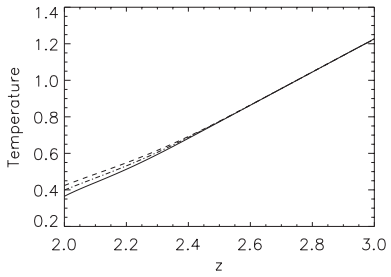

Figure 8.15: Temperature vs height. Solid line: quiet atmosphere at radiative equilibrium. Dot dashed line: temperature along the tube axis for a structure of D=20 grid points. Dashed line: temperature along the tube axis for a structure of D=60 grid points. Solid thick line: temperature initial condition.

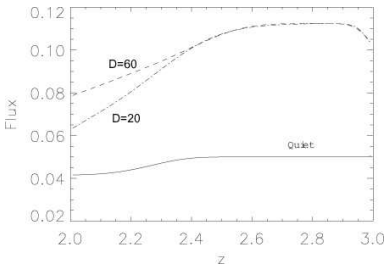

Figure 8.16: Flux in the radiative equilibrium quiet atmosphere (continuous line) and along the tube axis for a tube of D=20(dot dashed line) and a tube of D=60 (dashed line) grid points.

decrease of flux at the bottom is less evident respect to previous models and is independent on tube size. For the same reason the flux is constant in the tube in a larger range. The decrease of flux toward the top of the domain is more important for the smaller tube as for the model *A.A1/3*. The temperature and flux increase at the top of the domain inside the tube is lower respect to previous models.

Models *A.A1/3* and *A.A2/3* show that when the tube is in thermal equilibrium with the surrounding atmosphere at the lower boundary, the temperature inside the tube increases. It is thus reasonable to expect that the same would happen in models $C_{5.1}P1/2$, where the reduction of mixing length parameter value and gas pressure inside the tube causes an increase of temperature inside the tube in the subadiabatic layers and a small decrease of temperature in the superadiabatic ones, if the radiative equilibrium with surrounding atmosphere was imposed.

8.2 Intensity profiles at constant optical depth

8.2.1 An illustrative example

Intensity profiles at constant optical depth of discontinuous atmospheres show features that depend on the atmospheric models employed and geometric properties of the tube. In order to have a general understanding of the different profiles obtained with the simulations I describe here some results obtained with a very simple model.

Let us consider for illustration the case of two atmospheres that are not stratified, that is in which density, opacity and temperature are constant with height. The values of these constants is lower in the tube rather than in the not magnetized atmosphere. In particular let us suppose that in the tube the temperature is null, thus imposing that the Source function is null as well. Note that the opacity in the tube is not set to zero, so that this model represents an highly idealized situation in which the flux tube is more transparent and evacuated respect the surrounding atmosphere, but is not emitting radiation. The intensity profile at the bottom is the same inside and outside the tube and has an arbitrary value. Optical depth at the top of the domain is set to zero. Figure 8.17 shows results obtained for four different lines of sight. In particular, images on the right show the intensity values on the entire spatial domain. The vertical lines indicate the tube flanks and the curve mainly made up of segments is the $\tau = 1$ surface. The corresponding intensity profiles are shown in plots on the left.

It is interesting to notice how the $\tau = 1$ surface changes with the sight angle. For vertical directions the $\tau = 1$ surface is located much deeper in the tube with respect to the non magnetized atmosphere (*Wilson depression*), but the difference in depth becomes smaller and smaller as the angle diminishes (shallower directions). Moreover, at vertical directions the shape of the surface resembles the one of the tube, while at shallower directions it is wider and shallower. The shape can be easily understood considering that to variations of angle of sight correspond variations of the length of the section of path that crosses the tube. Being the tube more transparent, paths that cross more tube are longer and paths that cross less tube are shorter. More details are given in

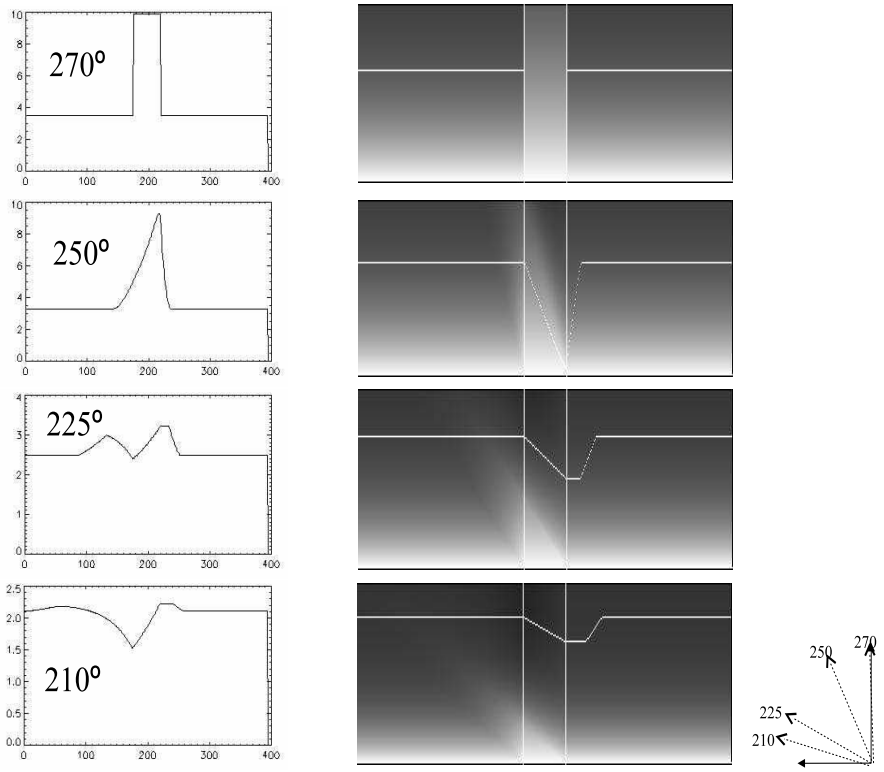

Figure 8.17: Right: Intensity field in the 2D spatial domain for four different view angles. Vertical white lines represent the flux tube flanks. Discontinuous line is the $\tau = 1$ surface. Left: Intensity profiles observed at $\tau = 1$. Intensity profiles present typical features that are strongly dependent on the sight angle. Moreover, not zero contrast area extends around and asymmetrically around the tube.

the appendix to this chapter. It is also important to notice that the shallower the angle, the more 'non magnetized' atmosphere is observed, the $\tau = 1$ surface extending more and more in the area close to the tube, but not inside of it. The corresponding intensity profiles present very peculiar shapes. At vertical directions the intensity in the tube is higher, since the intensity at the bottom is constant and the tube is more transparent. At disk center (270°) the positive contrast area corresponds to the flux tube locations. As the angle diminishes (off disk positions) the intensity peak diminishes and the profiles is deformed. In particular a 'tail' toward disk center (left, in the picture) is observed. In 250° case, for instance, this corresponds to the diagonal line of the τ=1 surface inside the tube and by some points at its left. These last points correspond to rays that generated inside the tube but that cross a lower and lower section of it, so that the intensity slowly approaches the 'quiet sun' one. With decreasing the angle a typical 'two bumps' structure appears. The bump on the right is generated at points that correspond to the diagonal and horizontal lines in the quiet sun on the right (away from the observer) of the τ=1 surface. The intensity is higher

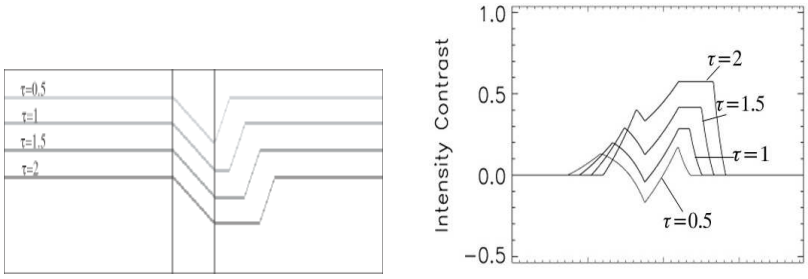

Figure 8.18: Left: Optical depth iso-contours for the model illustrated in fig.8.17 at angle 225°. Right: corresponding intensity contrast.

because the source function is not null outside the tube, than it decreases inside the tube (the straight diagonal line $\tau = 1$ surface inside the tube corresponds to the positive curvature line in the intensity profile), where the source function is zero. The second bump on the left is formed by rays that partially cross the tube. For shallower directions the bumps attenuate more and more. The bumps on the right because the $\tau = 1$ surface becomes shallower, the bump on the left because the portion of path that crosses the tube is smaller and smaller respect to the portion of the path that does not cross it.

Profiles here shown are just an example. Different shapes appear for different atmospheric models and boundary conditions. These features can be understood considering that different paths cross different portions of the tube, or do not cross it at all, but generate at different depths, as shown in the example above. In general positive or negative contrast area increase at shallower angles, thus making the structure to appear larger at positions off disk center. The position of the peak coincides with the center of the tube only at disk center. Off disk the peak is shifted toward the limb and at shallower angles more than one peak can appear. The observation of these features requires very high resolution (less than 0.1 arcsec), and have been observed only recently (Lites et al., 2004). They rise some observational issues. In particular, the not exact spatial coincidence of the tube and the not zero contrast area should be taken into account when comparing magnetogram and filtergram images, especially when dealing with high resolution data. Magnetic field intensity measurements themselves, based on Zeemaan splitting of some spectral lines, might be affected. Moreover, as shown by fig.8.18, the intensity (in the figure the contrast) changes at different optical depths and shows different features. This situation resembles observations carried out at different wavelengths, so that the same considerations made for magnetograms apply to filtergrams.

In chapter 3 I illustrated measurements of contrast of facular regions obtained identifying magnetic structures through comparison of images obtained at different wavelengths. In particular, structures whose intensity contrast exceeded a certain threshold in CAIIK images were identified as magnetic. Other techniques to detect magnetic structures exist, but most of them are based on comparison with contemporary acquired magnetograms or on intensity contrast measurement of images acquired in some 'magnetic sensitive' lines or bands (Ermolli et al., 2007; Tritschler and Uitenbroek, 2006). Analyses based on these kind of identification techniques, especially the ones carried out on high reso-

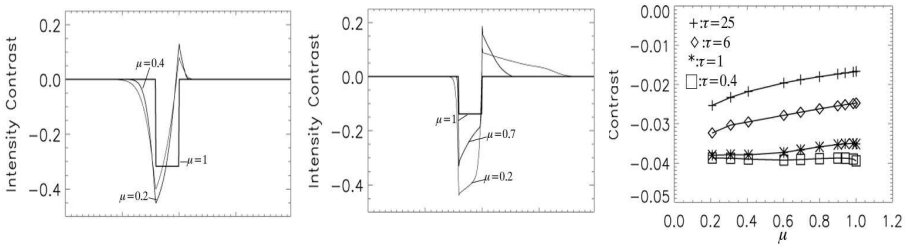

Figure 8.19: **Model $C_{5.1}$**. Left: Intensity profiles along $\tau = 1$ surface. Center: Intensity profiles along $\tau = 25$ surface. Right: Average intensity contrast at different isotau surfaces and different disk positions.

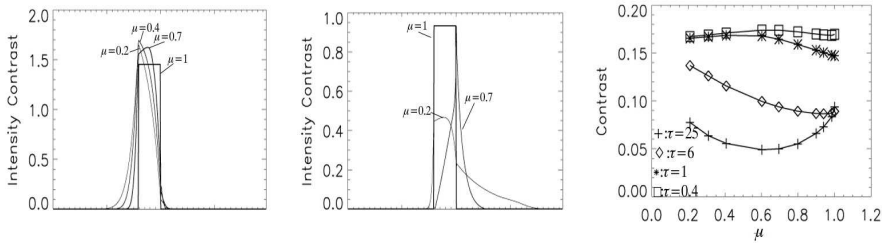

Figure 8.20: **Model $C_{5.1}P1/2$**. Left: Intensity profiles along $\tau = 1$ surface. Center: Intensity profiles along $\tau = 25$ surface. Right: Average intensity contrast at different isotau surfaces and different disk positions.

lution data, might in particular be affected by the fact that non zero contrast area do not always coincide with flux tube location and that intensity profile features differ at different wavelengths.

8.2.2 Developed Models

In the following paragraph I present the results obtained by the analysis of the photometric properties of the flux tube models described in previous section. In particular I investigated the intensity contrast (not the intensity profiles as in previous paragraph) along isotau surfaces at different sight angles. The different optical depth values have been chosen in order to sample different layers of the simulated atmospheres, thus mimicking observations at different wavelengths. In particular, because of the H^- opacity wavelength dependence, low values of τ mimic observation at the shorter wavelengths (blue), while higher values of τ mimic observations at higher wavelengths (red). The contrast is defined as the ratio of the intensity along the isotau surface and the intensity in the quiet atmosphere minus one. As intensity of the quiet atmosphere the intensity in a point of the isotau surface 'far' from the tube is chosen. In order to connect the results to observations presented in chapter 3, the mean contrast over the entire isotau surface as a function of the value of τ and the cosine of the sight angle μ was also investigated.

Figure 8.19 shows results obtained for model $C_{5.1}$ described above. The contrast profiles at the two isotau shown (τ=1 and τ=25 respectively) are quite different. The contrast at locations that correspond to the tube are negative

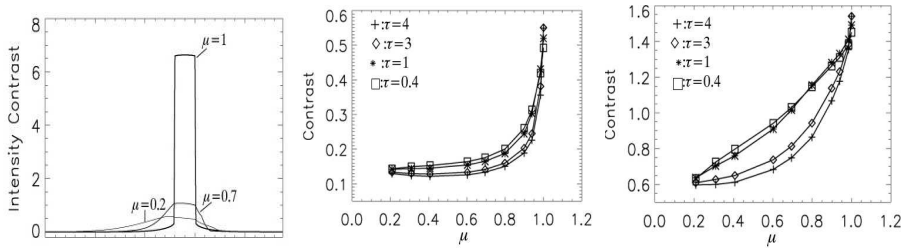

Figure 8.21: **Model A.A1/3**. Left: Intensity profiles along $\tau = 1$ surface for D=20. Center: Average intensity contrast at different isotau surfaces and different disk positions for D=20 grid points. Right: Average intensity contrast at different isotau surfaces and different disk positions for D=60 grid points.

in both cases but the contrast is lower at $\tau = 1$ rather than at $\tau = 25$, that is the contrast is lower if we 'look' at shallow layers rather than at deep ones. This is consequence of the fact that the opacity inside the tube is only slightly lower than the opacity outside the tube (fig.8.1), so that the Wilson depression is small and the isotau surfaces inside and around the tube occur almost at the same height at which they occur in the quiet atmosphere. Since the difference among the temperature inside and outside the tube increases going toward the surface (fig.8.1) the contrast becomes more negative. For the same reason the contrast inside the tube diminishes at shallow angles (the isotau surface shifts in fact toward the top). Variations are larger at larger optical depth, where the isotau surface locations vary largely with sight angle, and smaller at smaller values of τ, for which the isotau surface locations are less dependent on sight angle. These, in turn, depend on the variation of opacity with depth. Figure 8.1 shows in fact that in this model the opacity varies slowly with depth at the top of the domain and faster toward the bottom.

The positive contrast wings on the right of the tube are the 'hot wall' effect, that is the enhancement of the intensity generated by the fact that off disk center part of the observed intensity comes from the quiet (and hotter) atmosphere adjacent to the tube. The enhancement is at the side of the tube that is closer to the limb and further from the observer. The wing on the right is larger at higher τ values, since at low τ values the isotau surfaces are almost flat at shallow angles. The resulting contrast is thus very close to zero. The contrast at the left of the tube (toward the observer) diminishes at shallower angles and is more important at low vales of τ. At this side of the tube the observed intensity is generated by rays that crossed the tube and that therefore have 'experienced' a lower source function. At higher τ the effect is thus smaller, since the temperature inside and outside the tube are closer. The effect is also more important at shallower angles, for which the portion of a ray path length that crosses the tube is larger.

Inspection of the plot of average contrast versus μ reveals that the mean contrast is largely dominated by the contrast of the locations inside the tube. At larger optical depth, in fact, the decrease of contrast toward the limb is larger than at smaller optical depth and the value of average contrast is smaller at high values of τ, as shown for contrast profiles inside the tube.

Figure 8.20 shows results obtained for model $C_{5.1}P1/2$. As for the previous

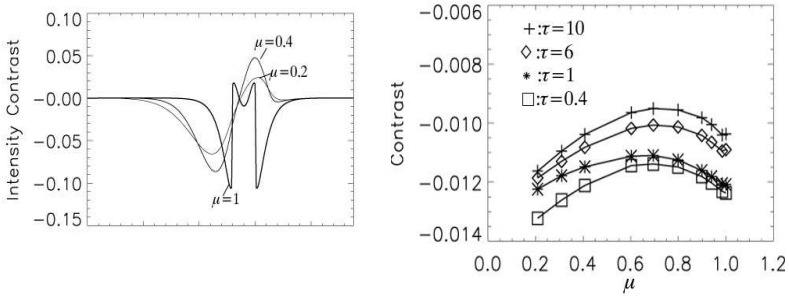

Figure 8.22: **Model B.A**. Left: Contrast profiles along $\tau = 1$ surface for D=20. Right: Average intensity contrast at different isotau surfaces and different disk positions for D=20 grid points.

case the contrast profiles and average contrasts largely depend on temperature stratification. In general the isotau surfaces investigated are located, with the exception of the $\tau = 25$ one, at depth for which the temperature inside the tube is higher than outside, that is, from fig.8.2, at z<2.8, so that the contrast is positive and increases when the optical depth decreases (toward th top of the domain). At τ=6, as observed on PSPT data, the contrast increases toward the limb because the isotau surfaces shift toward the top of the domain, where the differences of temperature among the tube and the quiet atmosphere are larger (in this case close to the surface the tube is hotter than the quiet atmosphere and the contrast is positive). At τ=0.4 the average contrast diminishes from the center to the limb because, while isotau surfaces locations slightly shift toward the top of the domain, the optical path travelled by outgoing rays increases. The τ=1 case is in between the τ=0.4 and τ=6 ones. As also shown by the contrast profile (fig.8.21, left), at μ <0.6 the contrast increases when μ decreases because of the increase of temperature difference explained for τ=6. At μ >0.6 the contrast decreases when μ decreases for the same reasons explained for τ=0.4. The contrast profile and the average contrast at τ=25 are very peculiar, since they show a minimum at about μ=0.6. At disk center, in fact, the isotau surface inside the tube is located much deeper than outside (that is the Wilson depression is large) because the opacity is lower (see fig.8.2). The contrast is thus positive even though the temperature inside the tube is lower than outside at the same height. Off disk center the location of isotau surface outside the tube shift less than inside (the Wilson depression diminishes) and the contrast diminishes. The contrast diminishes until the isotau surface crosses the point above which the internal temperature is higher than the external temperature (from fig.8.2 at z=2.8). A minimum is thus observed at μ=0.6. At smaller μ's the contrast increases toward the limb (the shallower the angle the higher is the difference of temperature inside and outside), as shown also by contrast profiles. The excess of temperature inside the tube respect to outside also explains the features of average contrast of model *A.A1/3* shown in fig.8.21 (center: D=20, right: D=60 grid points). The contrast is positive and decreases from disk center toward the limb even though the temperature differences get larger and larger toward the surface (and therefore toward the limb). This is due to the fact that when moving from disk center to the limb the isotau surfaces shift

upward more inside the tube rather than outside (that is the Wilson depression decreases) and the difference of temperature decreases rather than increase. The decrease of contrast toward the limb is lower for lower values of τ since the Wilson depressions decrease is lower and the isotau surfaces are located toward the top of the domain (see fig.8.11) where the tube is hotter and hotter than the quiet atmosphere. Figure 8.21 (left) also shows that the contrast is dominated by radiation coming from locations within the tube at disk center (μ=1), while the more μ decreases the more the radiation coming from area surrounding the tube becomes important. For this reason at μ=1 the contrast increases with τ while the opposite is observed at μ <1. Finally all these effects are enhanced when increasing the tube diameter (fig.8.21, right).

Figure 8.22 shows finally contrast profile and average contrast for model *B.A*. The contrast profiles show features that were absent in previous profiles and that are generated by the temperature stratification. The two 'horns' observed at disk center are generated by the increase of temperature when moving from the tube axis toward outside (see fig.8.5). Because of the Wilson depression, the contrast is null or positive inside the tube. Instead, along the isotau surface in the quiet atmosphere close to the tube, the temperature is lower respect to the temperature on the same isotau but far from the tube (the quiet atmosphere by definition) so that the contrast drops down (is negative) and than slowly increases to zero. When moving toward the limb a deep is observed toward the observer sight. This is also an effect of the decrease of temperature close to the tube. At the area corresponding to the tube location and to the area toward the limb, the contrast is positive and higher than at disk center, since the isotau surface is shifted upward, where the temperature value inside (and around the tube) is closer to the value of temperature in the quiet atmosphere. The decrease at the lowest μ's is due to the increase of optical path length, as explained for previous models. The average contrast plot reveals that the contrast is negative and slightly dependent on disk position and optical depth.

8.3 Ratio of contrasts

In chapter 3 I showed that the ratio of contrasts measured on PSPT images at two different wavelengths is not constant with respect to disk position, as instead expected by the black body approximation (Allen, 2000). In order to interpret these results, in this paragraph I show results obtained with simulations. Since the models developed are gray, I have investigated the ratio of intensity contrasts measured at different optical depths. This approximation is justified by the fact that, as already explained, different wavelengths sample different layers of the atmosphere. Figure 8.23 shows the ratio of contrast measured at different values of τ in function of disk position for two of the models developed, namely the $C_{5.1}$ and the *A.A1/3*. In particular the plots show the ratio of the contrast measured at the lowest value and the other three values of τ analyzed for the models (in chapter 3 I investigated the ratio of blue contrast respect to red contrast, where the blue samples a higher layer of the atmosphere). Both plots show that the ratio is not constant, but of course reflect the variations observed for the average contrast with μ. It is worth to notice that while for model $C_{5.1}$ the ratio decreases monotonically toward the limb, for model *A.A1/3* a monotonic decrease is observed at μ <0.9, while a deep minimum is observed

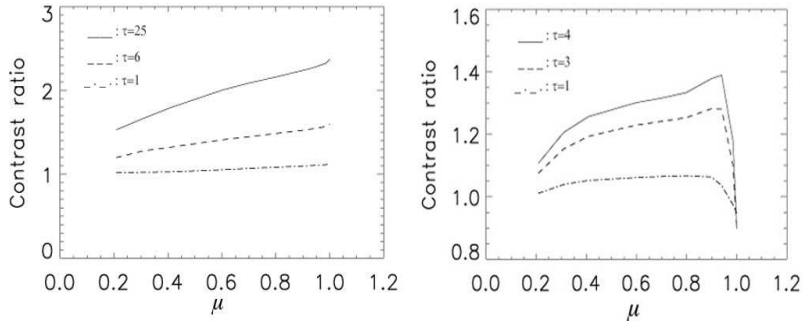

Figure 8.23: Ratio of average contrasts for model $C_{5.1}$ (left) and model *A.A1/3* (right).

at μ=1. This difference is ascribed to the fact that, as already explained in previous paragraph, for model $C_{5.1}$ the average contrast is always dominated by radiation that comes from the tube, while for model *A.A1/3* from the center to the limb the average contrast is more and more dominated by radiation coming from the area surrounding the tube.

None of the simulated flux tubes reproduces the experimental curve in fig.3.4. Nevertheless, the fact that the simulated profiles show that the ratio of contrast is not constant respect to μ, that in some cases largest variations are observed at disk center, and that from the Eddington model a slight dependence on μ is expected (see the Appendix to this chapter), suggest that the measured contrast is dominated by the intensity that comes from the tube at disk center, and from the 'walls' off disk center.

The fact that the ratio of contrasts measured at different wavelengths cannot be constant respect to disk positions and that the largest variations are expected at disk center can also be qualitatively explained even by using the Black Body approximation. Formula 3.2, according to which the ratio of contrast is inversely proportional to the ratio of the wavelengths, comes from the Wien approximation to the Plank function:

$$B(\lambda) \simeq \frac{2hc^2}{\lambda^5} e^{-\frac{hc}{\lambda KT}} \tag{8.3}$$

deriving the formula respect to T

$$\frac{dB}{dT} = \frac{2hc^2}{\lambda^5} \frac{hc}{k\lambda T^2} e^{-\frac{hc}{\lambda KT}} \tag{8.4}$$

from which

$$\frac{dB}{B} = \frac{hc}{k\lambda T^2} dT \tag{8.5}$$

If we suppose that the atmospheres in the quiet sun (that I will indicate with subscript q) and the tube (subscript f) emit as black bodies at two different temperatures, T_q and T_f respectively, we have

$$\frac{I_f(\lambda, T_f) - I_q(\lambda, T_q)}{I_q(\lambda, T_q)} = \frac{\Delta I(\lambda)}{I(\lambda)} = \frac{\Delta B}{B} = \frac{hc}{k\lambda T^2} \Delta T \tag{8.6}$$

$$\frac{I_f(\lambda, T_f) - I_q(\lambda, T_q)}{I_q(\lambda, T_q)} = \frac{hc}{k\lambda T_q^2}(T_f - T_q) \tag{8.7}$$

and the ratio of the contrast measured at two wavelengths is

$$\frac{\Delta I(\lambda_1)}{I(\lambda_1)} \frac{I(\lambda_2)}{\Delta I(\lambda_2)} = \frac{\Delta T_1}{\Delta T_2} \frac{T_2^2}{T_1^2} \frac{\lambda_2}{\lambda_1}. \tag{8.8}$$

If $\Delta T_1 = \Delta T_2 = T_f - T_q$ and $T_1 = T_2 = T_q$, or, more in general if $\frac{\Delta T_1}{\Delta T_2} \frac{T_2^2}{T_1^2} = 1$ at each disk position, than the ratio of the contrasts is equal to the inverse of the ratio of the wavelengths. Since the atmospheres in the magnetic structure and in the 'quiet sun' are differently stratified, and since observations at different disk positions sample different layers of the atmosphere, these equalities are not in general satisfied and the ratio of the contrast is not constant with μ.

8.4 Comparison with Observations and Conclusions

The different models investigated have produced very different results. The contrast profiles have typical features that mainly reflect the temperature stratification. The mean contrast can increase, decrease or have maxima or minima depending on the model and on the isotau surface value we look at (that means the observation wavelength). Among the models analyzed, the $C_{5.1}P1/2$ one, in which both convection and pressure reduction were taken into account, is the one that qualitatively reproduces the observed CLV of the contrast in blue and red bands. The average contrast at τ=6 is positive and increases from the center to the limb, like results obtained with PSPT data shown in chapter 3, while increases up to a certain value of μ to decrease at the very limb at smaller values of τ, as observed by other authors (e.g. Ortiz et al., 2002). Models $C_{5.1}P1/2$ thus show clearly that discrepancies of results presented by different authors must be imputed not only to resolution or image analyses techniques employed (as shown in chapter 3), but also to the wavelengths and filter widths employed during the observations.

As already explained, the relation between contrast and disk position depends on the temperature stratification inside the tube with respect to the stratification outside and the opacity function, that determines the position and shape of the isotau surface. The importance of both physical quantities is shown by the fact that in both models $A.A$ and $C_{5.1}P1/2$ the temperature is higher in the tube respect to outside, but the Wilson depression is lower in models $C_{5.1}P1/2$, so that the contrast is lower in these latter models rather than in models $A.A$.

The small contrast observed in PSPT images thus suggests that the temperature difference at locations where observed intensity comes from is quite small.

On the contrary, none of the models analyzed reproduces the CLV of the ratio of contrasts. Most likely this is due to the fact that in most of the models the contrast is dominated by the intensity that comes from the tube, while, as explained in previous paragraph and in the Appendix, plot in fig.3.4 suggests the contrast to be dominated by the intensity that comes from the tube at disk

center and the one that comes from the surrounding quiet atmosphere (the wall) toward the limb.

Simulations have also shown that the same model can produce different CLV profiles depending on the depth of the constant tau surface and that in order to infer physical properties of magnetic structures measurements at different wavelengths are fundamental.

Chapter 9

Conclusions and Future Work

In this thesis I have investigated photometric and geometric properties of magnetic bright features on the solar lower atmosphere. The investigation has concerned both theoretical and experimental aspects and has been carried out using image analysis and numerical simulations.

In the first part of the thesis I show results obtained by the analysis of medium resolution full disk images. In particular results obtained by the analyses of Rome-PSPT images, acquired in blue and red continua and CaII K during summers 1998-2005 have been shown.

Geometric properties have been investigated by the study of the fractal dimension of the identified features. Among the multitude of fractal dimension estimators presented in the literature, two estimators, based on the perimeter-area relation, have been employed. The perimeter-area relation was chosen because it allows to easily evaluate the fractal dimension of a large amount of features and because it was employed by other authors that analyzed data similar (for resolution and observation wavelength) to the PSPT ones. In order to compare results with previous works, that looked at magnetograms and CaIIK images, geometric properties of features identified on CaIIK data were investigated.

Results obtained agree very well with the ones presented in the literature. In particular I have shown that the fractal dimension increases with feature size at areas smaller than about 2000 Mm^2. At areas larger than this threshold the fractal dimension has the constant value 1.6. Theoretical explanations, based on the fact that 1000-2000 Mm^2 corresponds to the scale of supergranulation, have been proposed in previous works. Nevertheless, fractal dimension estimation of features defined on digital images is indirect and requires several stages, each of which introduces a certain degree of arbitrariness. The effects of image segmentation, pixelization, perimeter algorithm estimation and resolution have thus been investigated. The analyses, carried out on both fractals whose dimension is known by the theory and PSPT images, have shown that all these aspects influence the estimation of fractal dimension. In particular the increase of fractal dimension with feature size is due to pixelization, that is to the impossibility to represent on a square grid (i.e. a CCD) curves and not grid allined

lines. The minimum area threshold above which pixelization effect is negligible is, for the estimators employed, between 500 and 1000 pixels squares, that correspond to about 2000 Mm^2 on PSPT images (and also on images employed in previous analyses). The occurrence of the threshold at supergranular scales is thus accidental and conclusions drawn in previous works should be revisited.

The dependence of fractal dimension on solar activity cycle has also been investigated. Variations have been observed at areas larger than about 2000 Mm^2 for the different years analyzed. Nevertheless these variations are not clearly correlated with solar cycle and can be included in the deviations of measurements. More details about these results can be found in Criscuoli, Rast et al., 2007.

Photometric properties of faculae have been investigated by the analyses of their contrast measured in blue, red and calcium images. Magnetic features have been identified on calcium images by a threshold technique. In CaIIK images, that sample chromospheric layers, the average contrast of faculae is high (about 30%) and is almost independent from disk position. In blue and red observations, that sample photospheric heights, the average contrast is much lower than in chromosphere (around 5%) and increases with disk position. These results agree with the ones obtained by other authors by the analysis of data taken at similar wavelengths and resolution and that employed thresholding techniques similar to the one we adopted to select features on images. Authors that employed magnetograms to select structures, usually obtained negative contrast at disk center and a maximum positive contrast at about μ=0.4. The dependence of maximum average contrast on features area has also been investigated. I have shown that in the three wavelengths maximum contrast increases with feature size at areas smaller than about 2000 Mm^2 and that above this threshold a constant contrast is observed. That is maximum contrast varies like the fractal dimension with respect to features area. By contrast, a similar trend is observed for average contrast measured in Calcium, while a decrease with feature size at areas smaller than 2000 Mm^2 and a constant average contrast above this threshold, is observed in blue and red continua. The different scaling of maximum and average contrast with respect to area was interpreted as a signature of the fact that faculae are collections of smaller magnetic elements of different sizes. The increase of average contrast with area is instead most likely a filling factor effect. Results thus indicate that in smaller features the number of magnetic flux tubes in a single pixel is lower than in larger ones. The similarity of plots of contrast and fractal dimension versus area is therefore generated by different effects. The ratio of contrasts measured in blue and red at different disk positions has also been investigated. This ratio is not constant with the heliocentric angle μ, as one might expect by the black body approximation, and larger variations are observed at disk center. A complete description of results obtained is given in Ermolli, Criscuoli et al., 2007.

In order to interpret the experimental results and validate some of the conclusions drawn, theoretical models and numerical codes to simulate flux tubes and their photometric properties have been developed. To date these models assume LTE and gray atmosphere. In particular a code that solves the radiative transfer equation for different directions in a non uniform plane parallel atmosphere by the technique of short characteristic has been developed and tested. As explained in chapter 5, this technique requires the evaluation of several integrals and interpolations between adjacent points of the grid that samples the

space. Different integration and interpolation techniques have been thus implemented and compared in order to evaluate numerical effects on the final result. Tests have shown that spurious effects are more important for shallow angles, the number of interpolations being larger and the effective spatial resolution (the grid space) being poorer for these directions. Two quadrature techniques to evaluate the radiative flux and mean intensity have also been developed and evaluated. In particular I have shown that the Carlson scheme, the one usually employed in radiative transfer problems, might not give results accurate enough, the maximum order allowed per octant being too low to sample the radiation field.

Several static flux tube models have been developed for numerical simulations. In particular two classes of models have been investigated. In the first one the energy transport mechanisms considered are convection, modelled by the Mixing length theory, and radiation, under the assumption of radiative diffusion. In the second class only radiative processes have been considered, but radiative diffusion approximation is dropped and radiative equilibrium has been imposed by an iterative scheme. In both cases pressure equilibrium was not imposed and the presence of magnetic field was mimicked imposing at the bottom boundary layer the gas pressure inside the tube to be lower than outside. The equations solved to build the models (energy, pressure and state) have been normalized thus allowing a parametric investigation. Boundary and initial conditions have been chosen in order to mimic two situations. In the first one the temperature and pressure are lower at the bottom boundary layer, thus reproducing flux tubes formed by collapse mechanisms, in the second one the temperature at the bottom of the tube is the same as outside, thus reproducing the situation of a thermalized structures that rise, because of buoyancy, from the deepest layers of the atmosphere. In models with convection the presence of magnetic field was also mimicked imposing a lower value of mixing length parameter inside the tube. I have shown that in these latter models the reduction of mixing length efficiency causes a decrease of temperature inside the tube respect to outside in the lowest layers, while an increase is observed at the upper layers. This shows that it is possible to have heating inside the tube without invoking radiative channelling through the tube flanks.

This latter effect is instead observed in 'cold' models in radiative equilibrium, that is models in which as initial and boundary conditions the temperature inside the tube is lower than outside (models $B.A$). In particular simulations have shown that heating is due to the channelling of 'hotter' radiation from outside into the (more transparent) tube and is thus observed for structures whose radius is smaller than twice the horizontal optical depth. For 'hot' models, that is models in which as initial and boundary conditions the temperature inside the tube is the same as outside (models $A.A$), heating is observed as well, but in this case the increase of temperature is consequence of the reduction of opacity (attenuation) inside the tube, so that the larger the tube the higher is the increase of temperature. The analysis of the flux also reveals that the radiative equilibrium is not reached yet in any of the models. Radiative equilibrium is in fact imposed, as in some previous works, by an iterative algorithm, that is stopped when the difference of temperatures among two consecutive iterations is lower than a certain threshold. This method, also employed by other authors, allows to reach convergence in few iterations and to obtain temperature, pressure and density fields very close to the radiative equilibrium ones. Nevertheless, the

flux converges more slowly, so that radiative flux is not uniform all over the field even though the other physical quantities have reached the convergence. Some boundary problems have also been discussed. Finally an increase of density and a decrease of temperature is observed around the tube in 'cold' models. This result is very important since it shows that the presence of magnetic flux tubes can drive convection and that they 'cool' the atmosphere.

The analyses of the intensity contrast of radiation across the tubes have revealed that, depending on the different models, several features, whose contrast can be either positive or negative, are present. An area larger or smaller than the tube itself can thus appear darker or brighter than the non magnetic atmosphere depending on both the thermal structure of the tubes and the angle at which it is viewed. Because the same magnetic flux tube can generate areas of different contrast around it, more than one feature can be detected by thresholding techniques. As shown for instance by Lites et al. (2004), these features have typical spatial scales smaller than the tube size (some hundred of kilometers), so that they are very difficult to observe and thus we expect them to be detected only in very high resolution observations (better than 0.1 arcsec/pixel). These features reflect both temperature and opacity stratification differences inside and outside the tube and are generated not only from radiation that comes from within the tube, but also from the surrounding area. The mean contrast at different optical depths has also been investigated. Results have shown that even for the same model, the variation of contrast with disk position can be very different when looking at different optical depths, a monotonic increase, a maximum or a minimum being for instance observed for models with convection (models C) at different values of τ. This shows that when comparing observational results obtained by different authors is very important to take into account the wavelength and the filter width of observation, since these determine the layers from which radiation comes from. Discrepancies observed in the literature concerning the center to limb variation of contrast of faculae are thus partially explained. Among the models developed, the one that best reproduces PSPT results is the model in which both convection and pressure reduction have been taken into account, since this is the only model that has produced a monotonic positive increase of contrast from the center to the limb. This suggests that the temperature in the tube is lower than outside in the deepest layers and that is higher in the highest layers. On the contrary, none of the models reproduces the center to limb variation of ratio of contrast observed in PSPT images. I have showed that the observed variation of ratio of contrasts suggest that the contrast is dominated by the 'non magnetic' atmosphere (observed at deeper layers because of the presence of the flux tube) toward the limb, and by the radiation that comes from within the tube at disk center. In the models developed, instead, the contrast is mostly dominated by radiation that comes from the tube (with the exception of 'hot' models). This can be probably ascribed to the fact that the structures simulated are not in horizontal pressure equilibrium so that the fanning, expected in the highest layers of the domain because of the gravitational vertical stratification of the atmosphere, is not present and the flanks of the tube are vertical. If fanning was taken into account the isotau surface would extend for a larger area in the non magnetic atmosphere thus increasing its contribution to the contrast of the structure.

In order to validate the conclusions here drawn, it is thus important to improve the models developed. In particular it is important to include horizontal

pressure equilibrium. Models with convection need also to be in radiative equilibrium, since radiative effects can sensibly change the temperature and opacity stratifications inside the tube. Finally, properties of one structure have always been investigated. In full disk medium resolution images, more than one element fills each pixel of the detector so that, in order to interpret these kinds of data, it is important to study contrast and physical properties of clusters of tubes. This will help not only in the investigation of center to limb variation of contrast, but will also help in the understanding of its variation with object size and in the investigation of correspondence of high magnetic field concentrations and bright features. These aspects will be investigated in near future works.

A further validation will come from the analysis of high resolution data. In fact, results obtained by the simulations also indicate that in order to evaluate the temperature stratification inside magnetic structures it is important to observe them at different wavelengths with high resolution data. To address this topic two observing campaigns have been already carried out in 2005 and 2006 at the Dunn Solar Telescope, at National Solar Observatory (New Mexico), in collaboration with the Solar Group at Rome 'Tor Vergata' University. This telescope allows to obtain 0.25 arcsec/pixel images and, when operating with IBIS monochromator, it also allows to obtain high spectral resolution frames (the resolving power is about 250000). In particular images were taken in two photospheric lines (FeI 7090 $\AA$ and FeII 7224 Å), a chromospheric line (CaII 8542 Å), white light and G-band. Results obtained by these campaigns are now under analysis. The comparison with developed models will give a good improvement in our understanding of physics of small magnetic elements. A third campaign has been recently carried out at the New Swedish Solar Tower at La Palma (Spain), in collaboration with Solar Group at Osservatorio Astronomico di Roma, IAC and University of Valencia. This telescope allows to obtain 0.1 arcsec/pixel images. Observations have been carried out in the G-band, which sample the photosphere. Since in this wavelength magnetic structures have high contrast (about 30%), we hope to make use of these data to improve our understanding of their geometric properties. A comparison with contemporary acquired magnetograms will also allow to investigate the correspondence of magnetic features and bright elements.

Bibliography

Abbett, W. P., Beaver, M., Davids, B., Georgobiani, D., Rathbun, P., and Stein, R. F. (1997). *The Astrophysical Journal*, (480):395A.

Abramenko, V. (2005). *Solar Physics*, (228):29.

Abramenko, V. I. and Longcope, V. (2005). *The Astrophysical Journal*, (619):1160.

Ahern, S. and Chapman, G. (2000a). *Solar Physics*, (191):71.

Ahern, S. and Chapman, G. (2000b). *Solar Physics*, (191):71.

Albregtsen, F., Joras, P. B., and Maltby, P. (1984). *Solar Physics*, (90):17.

Allen, C. (2000). *Allen's astrophysical quantities, The new edition 2000*. AIR Press (Springler-Verlag), NY.

Asplund, M., Nordlund, A., Trampedach, R., and Stein, R. (2000). *Astronomy and Astrophysics*, (359):743.

Auffret, H. and Muller, R. (1991). *Astronomy and Astrophysics*, (246):264.

Balke, A., Schrijver, C., Zwaan, C., and Tarbell, T. (1993). *Solar Physics*, (143):215.

Balmforth, N. J., Gough, D. O., and Merryfield, W. J. (1996). *Monthly Notices of the Royal Astronomical Society*, (278):437.

Baveye, P., Boast, C.W., Ogawa, S., Parlange, J., and Steenhuis, T. (1998). *Water Resources Research*, (34):2783.

Bensch, F., Stutzki, J., and Ossenkopf, V. (2001). *Astronomy and Astrophysics*, (366):636.

Bensch, F.and Ossenkopf, V., Zielinsky, M., and Stutzki, J. (1998). *Astronomical Gesellschaft Abstract Service*, (14):129.

Berger, T. E. and Title, A. M. (2001). *The Astrophysical Journal*, (553):449.

Bruls, J., Vollmoller, P., and Schussler, M. (1999). *Astronomy and Astrophysicss*, (348):233.

Brummell, N., Hurlburt, N., and Toomre, J. (1998). *The Astrophysical Journal*, (493):955.

Bunte, M. Steiner, O. P. V. (1992). *Astronomy and Astrophysics*, (268):736.

Bushby, P. J. and Houghton, S. M. (2005). *MNRAS*, (362):313.

Caccin, B., ermolli, I., Fofi, M., and Sambuco, A. (1997). *Memorie della Societa' astronomica Italiana*, 68:459.

Cameron, R. and Galloway, D. (2005). *Monthly Notices of the Royal Astronomical Society*, (358):1025.

Carbonneau, P. (2005). Dynamo models of the solar cycle. *Living Rev. Solar Phys.*, (5):2. http://www.livingreviews.org/lrsp-2005-2.

Carlson, B. G. (1963). volume 1, page 1. Methods in Computational Physics.

Cattaneo, F. (1999). *The asptrophysical Journal*, (515):L39.

Cattaneo, F., Emonet, T., and Weiss, N. (2003). *The Astrophysical Journal*, (588):1183.

Cattaneo, F., Hulburt, N., and Toomre, J. (1991). *The astrophysical Journal*, (349):L63.

Chapman, G., Cookson, A., and Dobias, J. (1996). *J.Geophys. res.*, (101):13541.

Chapman, G. and McGuire, T. (1977). *The Astrophysical Journal*, (217):657.

Coughlin, K. and Tung, K. K. (2004). *Journal of Geophysical Research*, (109).

Cox, J. and Giuli, R. (1968). *Principles of Stellar Structure*, volume 1. Gordon and Breach, Science Publishers.

Criscuoli, S., Rast, M., Ermolli, I., and Centrone, M. (2007). *Astronomy and Astrophysics*, (461):331C.

Crommelynck, D., Fichot, A., Lee, R. B., I., and Romero, J. (1995). *Advances in Space Research*, 16(8):(8) 17.

de Boer, C., Stellmacher, G., and Wiehr, E. (1997). *Astronomy and Astrophysics*, (324):1179.

Deinzer, W., Hensler, G., Schussler, M., and Weisshaar, E. (1984a). *Astronomy and Astrophysics*, (139):426.

Deinzer, W., Hensler, G., Schussler, M., and Weisshaar, E. (1984b). *Astronomy and Astrophysics*, (139):435.

DePontieu, B., Carlsson, M., Rouppe van der Noorte, L., Lofdhal, M., van Noort, M., Nordlund, A., and Scharmer, G. (2006). *The Astrophysical Journal*, (646):1405.

Dikpati, M. and Gillman, P. A. (2006). *The Astrophisical Journal*, (649):498.

Durrant, C. (1988). *The Atmopshere of the Sun*. Adam Hilger Bristol and Philadelphia.

Emonet, T. and Cattaneo, F. (2001). *The Astrophysical Journal*, (560):L197.

Ermolli, I., Berrilli, F., and Florio, A. (2003). *Astronomy and Astrophysics*, (412):857.

Ermolli, I., Criscuoli, S., Centrone, M., and Giorgi, F. (2007). *Astronomy and Astrophysics*. in press.

Fabiani-Bendicho, P., F., K., and J., T. B. (1992). *Astronomy and Astrophysics*, (264):229.

Fan, Y. (2004). Magnetic fiields in the solar convective zone. *Living. Rev. Solar Phys.*, (1):1.

Fazzari, C., Ermolli, I., Centrone, M., Criscuoli, S., and Giorgi, F. (2003). *Memorie della societa Astronomica Italiana*, 74:667.

Ferguson, J. W., Alexander, D. R., Allard, F., Barman, T., Bodnarik, J. G., Hauschildt, P. H., Heffner-Wong, A., and Tamanai, A. (2005). *Astrophysical Journal*, (623):585F.

Fligge, M. and Solanki, M. (2000). *Journal of Astrophysics and Astronomy*, 21:275.

Fontenla, J. and Harder, J. (2005). In *Memorie dela Societa' Astronomica Italiana*, number 76, page 826F.

Fontenla, J., Harder, J., Rottman, G., Woods, T.N. andLawrence, G., and Davis, S. (2004). *The Astrophysical Journal*, (605):L85.

Fontenla, J., White, O., P.A., F., E.H., A., and R.L., K. (1999). *The Astrophysical Journal*, (518):480.

Foukal, P. (1990). *Solar Astrophysics*. Wiley-Interscience Publication, NY.

Foukal, P., Bernasconi, P., Eaton, H., and Rust, D. (2004). *The Astrophysical Journal*, (611):L57.

Foukal, P., Frhlich, C., Spruit, H., and Wigley, T. M. L. (2006). *Nature*, (443):161F.

Foukal, P. and Lean, J. (1988). *The Astrophysical Journal*, (328):347.

Frazier, A. (1971). *Solar Physics*, (21):42.

Freytag, B., Ludwig, H.-G., and Steffen, M. (1996). *Astronomy and Astrophysics*, (313):497.

Frohlich, C. (2000). *Space Science Reviews*, (94):15.

Frohlich, C. and Lean, J. (2004). *Astronomy and Astrophysics Review*, 12(4):273F.

Frohlich, C., Romero, J., Roth, H., Wehrli, C., and Andersen, B. N. e. a. (1995). *Solar Physics*, (162):101.

Garcia de La Rosa, J. I. (1987). In Schrter, H., Vzquez, M., and Wyller, A., editors, *The Role of Fine-Scale Magnetic Fields on the Structure of the Solar Atmosphere, Proceedings of the Inaugural workshop and round table discussion for the D-E-S Telescope installations on the Canary Islands, La Laguna, Tenerife, Spain, 6-12 October 1986*, page 140. Cambridge Press.

Gergoulis, M. (2005). *Solar Physics*, (228):5.

Gonzalez, R. and Woods, P. (2002). *Digital Image Processing*. Prentice Hall, London.

Hale, G. (1908). *The Astrophysical Journal*, (28):315.

Hansen, J., Sato, M., and Nazarenko, M. e. a. (2002). *Journal of Geophysical Research*, 107(D18):4347.

Hasan, S. (1984). *The aSprophysical Journal*, (285):851.

Hasan, S. (1985). *Astronomy and Astrophysics*, (143):39.

Hickey, J. R., Alton, B., K.H., H. L., and Hoyt, D. (1988). *Solar Physics*, 48(3-4):321.

Hudson, H. S., Silva, S., Woodard, M., and Willson, R. C. (1982). *Solar Physics*, (76):211.

Hurlburt, N., Matthews, P., and Proctor, M. (1996). *The Astrophysical Journal*, (457):933.

Hurlburt, N. and Toomre, Y. (1988). *The Astrophysical Journal*, (327):920.

Jansen, K., Vogler, A., and Kneer, F. (2003). *Astronomy and Astrophysics*, (409):1127.

Keller, C., Schussler, M., Vogler, A., and Zakharov, V. (2004). *The Astrophysical Journal*, (607):L59.

Khomenko, V., Shelyag, S., Solanki, S., and Voegler, A. (2005). (442):1059.

Knolker, M. and Schussler, M. (1988). *Astronomy and Astrophysics*, (202):275.

Krivova, N. A., Solanki, S. K.and Fligge, M., and Unruh, Y. C. (2003). *Astronomy and Astrophysics*, (399):L1.

Kuhn, J. R., Libbrecht, K. G., and Dicke, R. H. (1988). *Science*, (242):908k.

Kunasz, P. and Auer, L. (1988). *Journal of Quantum Spectroscopic Radiative Transfer*, 39(1):67.

Labitzke, K. (2004). *Journal of atmospheric and Solar-Terrestrial Physics*, (66):1151.

Lawrence, J. (1988). *solar Physics*, (116):17.

Lawrence, J. (1991). *Solar Physics*, (135):249.

Lawrence, J., Cadavid, A., and Ruzmaikin, A. (1996). *Astronomy and Astrophysics*, (465):425.

Lawrence, J. and Chapman, G. (1988). *The Astrophysical Journal*, (335):996.

Lawrence, J. and Schrijver, C. (1993). *The Astrophysical Journal*, (411):402.

Lean, J., Cook, J., Marquette, W., and Johannesson, A. (1998). *The Astrophysical Journal*, (492):390.

Lean, J., Rottman, G., Harder, J., and Kopp, G. (2005). *Solar Physics*, (230):27.

Leighton, R. B. (1969). *The Astrophysical Journal*, 156:1.

Li, L. H. and Sofia, S. (2001). *Astrophysical Journal*, (549):1204L.

Lin, H. (1995). *Astrophysical Journal*, (446):421.

Lites, B. W., Scharmer, G. B., Berger, T. E., and Title, A. M. (2004). *Solar Physics*, (221):65L.

Low, B. (1975). *The Astrophysical Journal*, (198):211.

Maltby, P., Avrett, E. H., Carlsson, M., Kjeldseth-Moe, O., Kurucz, R. L., and Loeser, R. (1986). *The Astrophysical Journal*, (306):284.

Mandelbrot, B. (1967). *Science*, (156):636.

Mandelbrot, B. (1975a). *Journal of Fluid Mechanics*, 72(2):401.

Mandelbrot, B. (1975b). *Les objets fractals: forme, hasard, et dimension*. Flammarion, Paris.

Mandelbrot, B. (1982). *The Fractal Geometry of Nature*. W.H.Freeman and company, N.Y.

McAteer, R., Gallagher, P., and Ireland, J. (2005). *The Astrophysical Journal*, (631):628.

Meisner, R. and Rast, M. (2002). In *200th AS Meeting, Bulletin of American Astronomical Society*, number 34 in 55.13, page 734. American Astronomical Society.

Meneguzzi, M. and Pouquet, A. (1989). *Journal of fluid Mechanic*, (205):297.

Meunier, N. (1999). *The Astrophysical Journal*, (515):801.

Meunier, N. (2004). *Astronomy and Astrophysics*, (420):333.

Mihalas, D. and Weibel-Mihalas, B. (1999). *Foundations of Radiation Hydrodynamics*. Dover Publications, INC.

Miville-Deschênes, M., Levrier, F., and Falgarone, E. (2003). *The Astrophysical Journal*, (593):831.

Nesmes-Ribes, E., Meunier, N., and Collin, B. (1996). *Astronomy and Astrophysics*, (308):2213.

Nordlund, A. (1983). In Stenflo, J., editor, *Solar and Stellar Magnetic Fields: Origins and Coronal Effects*, number 102, page 79. IAU Symposium, Dordrecht.

Nordlund, A. (1985). *Solar Physics*, (100):209.

Ortiz, A., Domingo, V., and Sanahuja, B. (2006). *Astronomy and Astrophysics*, (452):311.

Ortiz, A., Solanki, S., Domingo, V., Fligge, M., and Sanahuja, B. (2002). *Astronomy and Astrophysics*, (388):1036.

Ossenkopf, V., Bensch, F., Mac Low, M., and Stutzki, J. (1999). In V., O., J., S., and G., W., editors, *The Physics and Chemistry of the Interstellar Medium, Proceedings of the 3rd Cologne-Zermatt Symposium*, ISBN 3-928973-95-9.

Parker, E. (1978). *The aStrophysical Journal*, (221):368.

Parker, E. (1992). *The Astrophysical Journal*, (390):290.

Peitgen, H. O. and Jurgen, D. (1992). *Fractals for the classroom*, volume I: Introduction to fractals and chaos. Springer-Verlag, New-York.

Penza, V., Caccin, B., Ermolli, I., and Centrone, M. (2004). *Astronomy and astrophysics*, (413):1115.

Penza, V., Caccin, B., Ermolli, I., Centrone, M., and Gomez, M. (2003). ESA SP535, page 299.

Pierce, A. K. and Slaughter, C. D. (1977). *Solar Physics*, 51:25.

Pizzo, V. (1986). *The Astrophysical Journal*, (302):785.

Pizzo, V., MacGregor, K. B., and Kunasz, P. B. (1993). *The Astrophysical Journal*, (404):788.

Porter, D. and Woodward, P. (2000). *The astrophysical Journal Supplement*, (127):159.

Press, W., Teukolsky, S., Veterling, W., and Flannery, B. (1994). *Numerical Recipes in Fortran*. Cambridge University Press.

Radick, R. R., Lockwood, G. W., Skiff, B. A., and Baliunas, S. L. (1998). *The Astrophysical Journal Supplement Series*, (118):239.

Rottman, G. J., Woods, T. N., and Sparn, T. (1981). *Journal of Geophysical Research*, (98):10.

Roudier, T. and Muller, R. (1987). *Solar Physics*, (107):11.

Rozelot, J., S., L., Pireaux, S., and Ajabshirizadeh, A. (2004). *Solar Physics*, (224):229.

Sànchez, N., Alfaro, E., and Perez, E. (2005). *The Astrophysical Journal*, (625):849.

Scherrer, P. H., e. a. (1995). *Solar Physics*, (162):129.

Schrijver, C., Zwaan, C., Balke, A., Tarbell, T., and Lawrence, J. (1992). *Astronomy and Astrophysics*, (253/L1).

Skumanich, A., Lean, J. L., Livingston, W. C., and White, O. R. (1984). *The Astrophysical Journal*, (282):776.

Socas-Navarro, H. and Sanchez Almeida, J. (2003). *The Astrophysical Journal*, (593):581.

Sofia, S. (1998). *Solar Physics*, (177):413.

Solanki, S. (1993). Smallscale solar magnetic fields - an overview. *Space Science Reviews*, 1(63):1.

Solanki, S. (2003). *Astronomy and Astrophysics Review*, (11):153.

Spruit, H. (1976). *Solar Physics*, (50):269.

Spruit, H. (1979). *Solar Physics*, (61):363S.

Spruit, H. (1982). *Astronomy and astrophysics*, (108):348.

Spruit, H. and Zwaan, C. (1981). *Solar Physics*, (70):207.

Stein, R. and Nordlund, A. (2006). *The Astrophysical Journal*, (642):1246.

Steinegger, M., Vazquez, M., Bonet, J. A., and Brandt, P. N. (1996). *The Astrophysical Journal*, (461):478.

Steiner, O. (1990). *Astronomy and Astrophysics*, (231):278.

Steiner, O. (1994). Theoretical models of magnetic flux tubes: Structure and dynamics. In D. M. Rabin, J. T. J. and Lindsey, C., editors, *Infrared solar physics: proceedings of the 154th Symposium of the International Astronomical Union; held in Tucson; Arizona; U.S.A.; March 2-6,1992*, number 154, page 407. IAUS, Kluwer Academic Publishers.

Steiner, O. (2005a). *Astronomy and Astrophysics*, (430):691.

Steiner, O. (2005b). In *Proceedings of the 11th European Solar Physics Meeting-The Dynamic Sun: Challenges for Theory and Observations, 11-16 September 2005*, number 596. ESA-SP.

Steiner, O., Grossmann-Doerth, U. Knolker, M., and Schussler, M. (1998). *The Astrophysical Journal*, (495):468.

Steiner, O. and Pizzo, V. (1989). *Astronomy and Astrophysics*, (211):447.

Stenflo, J. and Holzreuter, R. (2002). In A.A., P. and H., H. U., editors, *Current Theoretical Models and Future High Resolution Solar Observations: Preparing for ATST*, 286, page 169. ASP Conference Serie.

Stix, M. (2002). *The Sun : An Introduction*. Springer, astronomy and astrophysics library edition.

Stutzki, J.and Bensh, F., Heithaunsen, A., Ossenkopf, V., and Zielinski, M. (1998). *Astronomy and Astrophysics*, (336):697.

Taylor, S., Varsik, J., Woodward, M., and Libbrecht, K. (1998). *Solar Physics*, (178):1.

Title, A., Topka, K., TArbell, T., Schmidt, W., Balke, C., and Scharmer, G. (1992). *The Astrophysical Journal*, (393):782.

Tritschler, A. and Uitenbroek, H. (2006). *The Astrophysical Journal*, (648):741.

Trujillo Bueno, J., Shchukina, N., and Ramos, A. A. (2004). A substantial amount of hidden magnetic energy in the quiet sun. *Nature*, (430):326.

Turner, M., Blackledge, J., and Andrews, P. (1998). *Fractal Geometry in Digital Imaging*. Academic Press, London.

Unruh, Y., Solanki, S., and Fligge, M. (2000). *Space Science Reviews*, 90(1/2):145.

Vasconcelos, G. (2004). *Brazilian Journal of Physics*, (34):1039.

Vernazza, J. E., Avrett, E. H., and Loeser, R. (1981). *The Astrophysical Journal Supplement Series*, (45):635.

Vitense, E. (1953). *Zeitschrift fr Astrophysik*, (32):135.

Vogelaar, M. and Wakker, B. (1994). *Astronomy and Astrophysics*, (291):557.

Vogler, A., Sheylag, S., Schussler, M., Cattaneo, F., Emonet, T., and Linde, T. (2005). *Astronomy and Astrophysics*, (429):335.

Walton, S. (2005). In *Memorie della Soieta' Astronomica Italiana*, volume 76, page 819.

Walton, S. and Preminger, D. a. G. (2003a). *Solar Physics*, 213(2):301.

Walton, S. and Preminger, D. a. G. (2003b). *The Astrophysical Journal*, (590):1088.

Wang, H., Spirock, T., Goode, P., Lee, C., Zirin, H., and Kosonocky, W. (1998). *The Astrophysical Journal*, (495):957.

Wang, H. and Zirin, H. (1987). *Solar Physics*, (110):281.

Weiss, N. O., Brownjohn, D. P., Matthews, P. C., and Proctor, M. R. E. (1996). *Montly Notices of the Royal Astronomical Society*, (283):1153.

Wenzler, T., Solanki, S., Fluri, D., Frutiger, G., Fligge, M., and Ortiz, A. (2002). In Wilson, A., editor, *Proceedings of the SOHO 11 Symposium on From Solar Min to Max: Half a Solar Cycle with SOHO, 11-15 March 2002, Davos, Switzerland*, ISBN 92-9092-818-2, page 231. ESA Publications Division.

Wenzler, T., Solanki, S., and Krivova, N. (2005). *Astronomy and Astrophysics*, (432):1057.

White, W. B., Dettinger, M. D., and Cayan, D. R. (2003). *Journal of Geophysical Research*, (108):4W.

Willson, R. C. (1981). *Solar Physics*, (74):217.

Zwaan, C. (1985). *Solar Physics*, (100):397.

Zwaan, C. (1987). *Annual review of Astronomy and Astrophysics*, (25):83z.

Appendix A

Appendix to Chapter 2

A.1 Fractal dimension measurement of Non-fractal objects

Figure A.1 plots $d1$ (first row) and D (second row), evaluated using the different perimeter finding algorithms explained in chapter 2, as a function of object size for three non-fractal objects: squares, right triangles, circles. The fractal dimension $d1$ is evaluated as explained in paragraph 2.4, while D is evaluated as a function of object size by fitting the perimeter-area relation only above a minimum threshold size. Since the *Sides* and the *Roberts* techniques yield almost to identical results, plot shows those obtained with the *Sides* and *8-cont* methods only. Note that the correct fractal dimension, 1, is obtained independent of object size only for the square and only when applying the *Sides/Roberts* algorithms. In all the other cases *d1* and D are functions of the object size and tend to 1 only as the area increases. In the case of the *Sides/Roberts* methods, this results directly from image pixelization, from errors introduced by the impossibility of reproducing on a rectangular grid curves or non–grid-aligned lines. For example, the right triangles I examined were constructed to have two of the sides grid-aligned. The hypotenuse length was thus always over estimated because of image pixelization. This leads to relative errors in the *Sides/Roberts* perimeter measures which are independent of object size, $\frac{2-\sqrt{2}}{2+\sqrt{2}} \approx 0.17$ and an error in the area measure which scales as $\frac{1}{l}$, where l is the length of the triangle's side. The relative error in the *8-cont* perimeter measure, on the other hand, is not independent of object size. Consider grid aligned squares. They have areas of $\{1, 4, 9, 16\ldots\}$ with no pixelization error, but *8-cont* perimeters of $\{1, 4, 8, 12\ldots\}$ instead of $\{4, 8, 12, 16\ldots\}$, so that the relative error in the perimeter decreases for squares greater than one pixel in area, as $1/l$, where l is the length of the side of the square. The fractal dimension is thus over estimated when employing the *8-cont* perimeter measure, with the error decreasing with increasing object size. For circular objects, pixelization causes an underestimation of fractal dimension when the *Sides/Roberts* perimeter measures are used, while the *8-cont* perimeter measure continues to produce an over estimation. With the exception of grid aligned squares, the errors in fractal dimension for small area objects are non-negligible, and substantial errors persist to objects of significant size. Table A.1 indicates, for each method and geometric figure, the

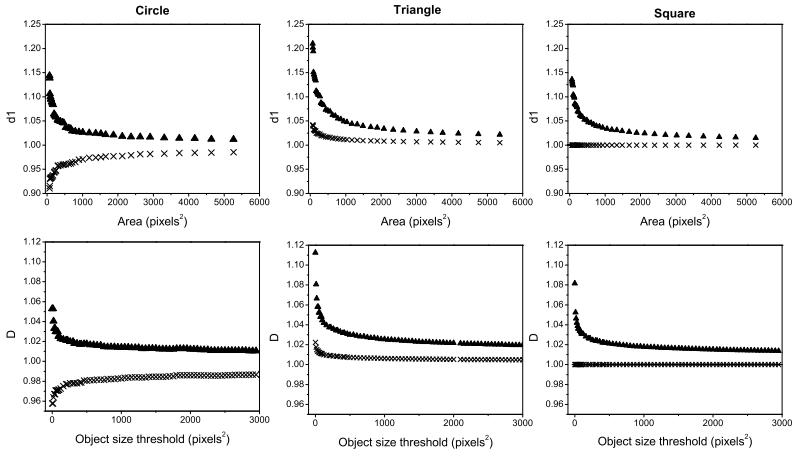

Figure A.1: Fractal dimension d1 (first row) and D (second row) of a square, a triangle and a circle as a functions of area and minimum area threshold respectively (see text) obtained using two different perimeter estimation algorithms. Crosses: external sides. Triangles: 8-contiguous points. Because of perimeter definition and pixelization effects (see text) the fractal dimension is a function of the object size. The error is larger for smaller objects, and an overestimation or underestimation may occur.

minimum area above which the error in *d1* is less than 5% or 1%. For circular objects the error never drops below 1%, independent of the perimeter measure employed, even for areas exceeding 5000 square pixels, although, for all shapes studied, errors of less than 5% are achievable for object sizes greater than 1000 square pixels.

A.2 von Koch snowflake

von Koch snowflake images of different sizes were produced following the iterative scheme of Peitgen and Jurgen (1992). After each iteration, or level, the snowflake is more structured, with an increase in both perimeter and area. In the limit of infinite iterations, the perimeter tends toward infinity and the area approaches a finite value. Here I investigate structures constructed with up to 6 levels. The fractal dimension of the von Koch snowflake is $\log 4/\log 3 \approx 1.26$.

In fig. A.2(left), the perimeter-area relationships for snowflakes of levels 2, 4, and 6 are plotted with logarithmic scaling. For each level, the relationship traces a curve made up of segments whose slope is 1/2 connected by segments of slope greater than 1/2. At largest areas all the points lay on parallel lines of slope one-half. At those scales the snowflakes of all the represented levels are fully resolved on the grid employed. As the dimensions of the objects are reduced, fewer details at any fixed construction level are resolved, the measured perimeter decreases at a rate faster than $A^{1/2}$, and the perimeter-area curve steepens. The slope flattens to a value of one-half again each time the grid

	Figure	*Sides/Roberts*	$8-cont$
Error $\prec 5\%$			
	Square	Always	500
	Triangle	Always	950
	Circle	270	350
Error $\prec 1\%$			
	Square	Always	Never
	Triangle	1450	Never
	Circle	Never	Never

Table A.1: Minimum area above which the error in *d1* estimation is less than 5% and 1%, for each method and geometric figure analysed.

resolution is sufficient to capture the details of the next lower level. Finally, at smallest areas most geometric detail is lost and all the objects, independent of their initial construction level, appear non-fractal.

The scaling of *d1* better illustrates the changing of slopes with objects size. As an example in right panel of fig.A.2 I show results obtained for level 6. Here full and open dots represent respectively *d1* obtained with a window of $\Delta \log A = 1.5$ and a window of $\Delta \log A = 0.5$. With the largest window only the slope change that occurs at largest areas is visible. The others occur on scales smaller than the window so that they are not 'detected' and a plateau is observed. At smallest areas *d1* drops because of the resolution effects explained before. When a smaller window is used 6 peaks are visible, corresponding to the 6 slope-changing visible in the perimeter area scatter plot. In this case there is an area range in which fractal dimension oscillates around a constant value. At smallest areas larger amplitude oscillations are observed, with a net signal increase with object size.

Both curves show clearly three regimes. The object scales as a fractal in the range $3 < \log(\text{Area}) < 4.5$. At smaller and larger area pixelization effects dominate the measurements. At smaller areas because resolution is not enough to detect structures details, at larger areas because the objects are fully resolved. In order to correctly estimate the fractal dimension, perimeter-area fit had to be performed in this area range. Fits performed over larger or different ranges, lead to an underestimate of fractality. Plot also shows that small area-range measure 'local' slope changes and give wrong estimate of fractal dimension as well. The choice of the area range and width over which the fit is performed is thus critical.

In this case, the largest window $\Delta \log A = 1.5$ leads to the most correct results. In order to measure the lower bound of the range over which the snowflake is fractal and the plateau value of $d1$, I fit the function $d1 = a + b \cdot \exp(-k \cdot \log A)$, for $k > 0$, to the $d1$ versus A data over the full area range extending to $\log A < 4.5$, that being the value beyond which the level six snowflake is fully resolved. Parameter a then gives an estimate of the fractal dimension of the von Koch snowflake, while the area A at which the relative difference between the two terms becomes less than 1% is an estimate of the minimum size at which the discrete grid is still able to capture the snowflake fractality. I obtained $a = 1.34$ and $\log A \simeq 3$. Direct fits to all points in the perimeter-area plot above and below $\log A = 3$ yield $D = 1.21 \pm 0.03$ and $D = 1.31 \pm 0.007$ respectively. I no-

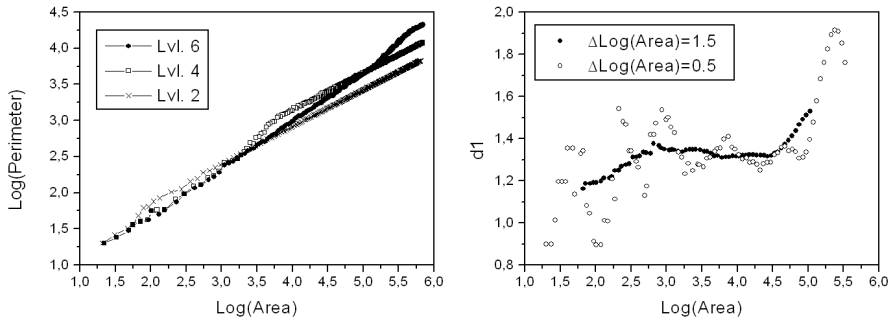

Figure A.2: Left: Perimeter versus area in logarithmic scale of snowflakes of levels 2,4 and 6. Because of pixelization, these structures scale as fractals only at certain area range, bounds depending on the level. Right: $d1$ versus area evaluated with different window sizes for snowflake of level 6. Peaks obtained with the small window (open circles) are due to the steep variations visible in plot on the left. Peaks are not detected with a larger window (full circles). The area range in which $d1$ is almost constant is the range in which simulated images are fractals.

tice that these values for both *d1* and D at highest areas exceed those expected theoretically. This reflects the overestimation of snowflake perimeter inherent in the perimeter measure algorithm employed, as discussed previously for simple non fractal triangles. Here, the largest area snowflakes have the most well resolved triangular boarder structure yielding an increase in perimeter error with size combined with a slower growth in area error.

Figure A.3 shows $d1$ estimates obtained on vonKoch snowflakes images convolved with Gaussian functions of widths 2,4,6 and 8 pixels. The more the image is degraded the more the fractal dimension is underestimated, with a larger effect at smallest areas.

A.3 Fractal dimension measurement of Fractional Brownian motion patterns

Images obtained by fractional Brownian motion have been widely used for simulation of interstellar clouds and terrestrial atmospheric clouds (Vogelaar and Wakker, 1994; Stutzki et al., 1998; Ossenkopf et al., 1999; Bensch et al., 2001; Miville-Deschênes et al., 2003). They are particularly well suited for use in algorithmic tests because they allow the construction of images containing structures of arbitrary but known fractal dimension. The images are constructed in Fourier space to have random phase and a power-law power-spectrum P:

$$P(f) \propto f^{-\beta},$$

where f is the spatial frequency. For a two-dimensional image the power-law index β is related to the box counting dimension D_B as

$$\beta = 8 - 2D_B$$

(Turner et al., 1998). Moreover, the perimeter-area fractal dimension D of the

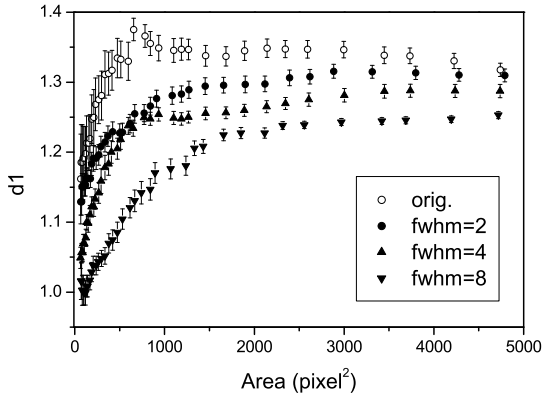

Figure A.3: $d1$ evaluated on vonKoch snowflakes images convolved with gaussian of different widths. As the image degradation increases the fractal dimension estimates decrease. The effect is more relevant at smallest areas.

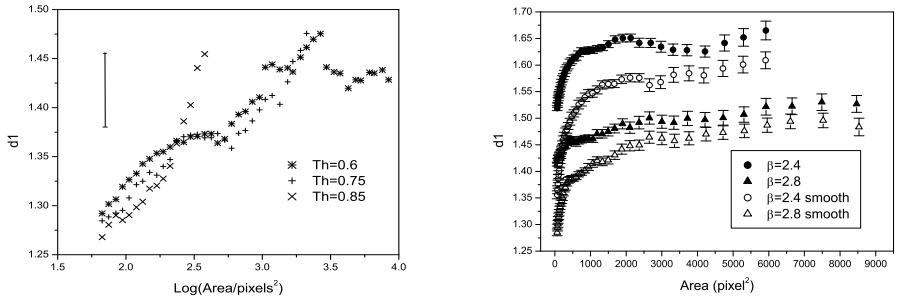

(a) (b)

Figure A.4: (a) fbm $\beta = 2.8$. $d1$ evaluated for three different threshold values. (b) fbm $\beta = 2.8$ and $\beta = 2.4$. $d1$ evaluated on original (full symbols) and degraded images (open symbols). Each curve is obtained combining perimeters and areas obtained with 7 different thresholds.

contour levels of a two-dimensional image (its *zero sets*) is related to the box counting dimension as $D = D_B - 1$. Vogelaar and Wakker (1994) confirmed this relationship using fBms of fractal dimension 1.2 and 1.6. Bensch et al. (1998), however, found a systematic discrepancy at highest and lowest β fBms tested. For this study I have generated two sets of 150 independent fBm images, one with spectral index $\beta = 2.8$ and one with spectral index 2.4, corresponding to a fractal dimension D equal to 1.6 and 1.8 respectively. To each set of images seven different intensity thresholds were applied. The perimeters and areas of the structures within each set were then measured. Figure A.4 (left) presents the results obtained with threshold values, 0.6, 0.75, and 0.85, on normalized fBms images produced with $\beta = 2.8$. All the curves show that, as was the case for both the non-fractal objects and the von Koch snowflakes, because of pixelization the fractal dimension is a function of the size of the object. Moreover, increasing the threshold causes an increase in the fractal dimension deduced for larger structures and a decrease in the measure for smaller structures. The same is observed for the set $\beta = 2.4$. This is partially due to the fact that the same object have different area when selected with different thresholds. Moreover, biggest structures appear more discontinuous and more voids are created when increasing the threshold, thus increasing the perimeter and reducing the area, and therefore increasing the fractal dimension. Variations are small though, generally within the error bars, especially at smaller areas, and are significant only at highest thresholds. The value of D is 1.52, 1.51 and 1.499 respectively. The small decrease obtained increasing the threshold is due to the decrease of big structures and the consequent larger weight of smaller structures in the fitting.

Figure A.4 (right) shows results obtained combining data from the seven *zero sets* for the two sets of fBms generated. Both cases show that fractal dimension increases at smallest areas, to become constant at larger areas, as observed for vonKoch snowflakes. The value assumed by $d1$ at the plateau gives an underestimate of fractal dimension in both cases, whereas an overestimate was measured for snowflakes.

Figure A.4 (right) also shows results obtained combining data from the seven *zero sets* for the two sets of fBms images convolved with a Gaussian function of amplitude 2 pixels. As for vonKoch snowflakes, image degradation causes an underestimate of fractal dimension at all scales and the effect is larger at smallest scales.

Appendix B

Appendix to Chapter 6

I want to show that the scheme adopted in the Short Characteristic technique to evaluate optical depth and source term (that is relations 5.62,5.63,5.64 and 5.69,5.70) are schemes at the second order and allow to obtain more accurate results than a Finite Difference scheme (see paragraph 6.1).

Let us consider the first derivative:

$$k_1 = \left.\frac{\partial k}{\partial s}\right|_i = \frac{\frac{k_{i+1}-k_i}{\Delta s_{i+1}} \cdot \Delta s_i - \frac{k_i - k_{i-1}}{\Delta s_i} \cdot \Delta s_{i+1}}{\Delta s_{i+1} + \Delta s_i} \tag{B.1}$$

Let us expand K_{i-1} and K_{i+1} in Taylor series of K_i:

$$k_{i-1} = k_i - \frac{\partial k}{\partial x}\Delta x_{i-1} + \frac{\partial^2 k}{\partial x^2}\frac{\Delta(x_{i-1})^2}{2} - \frac{\partial^3 k}{\partial x^3}\frac{\Delta(x_{i-1})^3}{6} \tag{B.2}$$

$$k_{i+1} = k_i + \frac{\partial k}{\partial x}\Delta x_{i+1} + \frac{\partial^2 k}{\partial x^2}\frac{\Delta(x_{i+1})^2}{2} + \frac{\partial^3 k}{\partial x^3}\frac{\Delta(x_{i+1})^3}{6} \tag{B.3}$$

In the following I will assume $\Delta x_{i-1} = \Delta x_{i+1} = \Delta x$, so that

$$\Delta s_i = s_{i+1} - s_i = \frac{\partial s}{\partial x}\Delta x + \frac{\partial^2 s}{\partial x^2}\frac{\Delta(x)^2}{2} - \frac{\partial^3 s}{\partial x^3}\frac{\Delta(x)^3}{6} \tag{B.4}$$

$$\Delta s_{i-1} = s_i - s_{i-1} = \frac{\partial s}{\partial x}\Delta x - \frac{\partial^2 s}{\partial x^2}\frac{\Delta(x)^2}{2} - \frac{\partial^3 s}{\partial x^3}\frac{\Delta(x)^3}{6} \tag{B.5}$$

where s denoted the grid space and x the regular space.
Substituting B.2-B.5 into B.1, and after some algebra, we find:

$$k_1 \simeq \frac{\partial k}{\partial s} + \frac{(\Delta x)^2}{6}\frac{\partial^3 k}{\partial s^3}\left(\frac{\partial s}{\partial x}\right)^2 \tag{B.6}$$

For a Finite Difference scheme, instead, the first derivative is given by

$$k_{1FD} = \left.\frac{\partial k}{\partial s}\right|_{x_i} = \frac{\partial k}{\partial x}\frac{\partial x}{\partial s} = \frac{k_{i+1} - k_{i-1}}{s_{i+1} - s_{i-1}} \tag{B.7}$$

Substituting refAk2-B.5 into this last expression we have

$$k_{1FD} \simeq \frac{\partial k}{\partial s} + \frac{(\Delta x)^2}{6}\left[\frac{\partial^3 k}{\partial s^3}\left(\frac{\partial s}{\partial x}\right)^2 + 3\frac{\partial^2 s}{\partial x^2}\frac{\partial^2 k}{\partial s^2}\right] \tag{B.8}$$

Comparison of relations B.6 with B.8 shows that in the Finite Differences scheme the error is larger, since the diffusion term $3\frac{\partial^2 s}{\partial x^2}\frac{\partial^2 k}{\partial s^2}$ is present.

Similar calculations lead to the same considerations for the second order coefficient k_2.

In agreement with these calculations, tests presented in chapter 6 show that results obtained by Finite Differences and the scheme described in chapter 5 coincide on regular grids, while better results are obtained by the second scheme on irregular grids.

I want to show that if a function χ is the product of two functions ρ and k, and we want to approximate χ using the scheme described in 5, than the error is smaller if χ is estimated by the product of the approximations of ρ and k rather than expanding χ.

By definition we have $\chi = k\rho$. If we expand k and ρ at second order, we have

$$\chi = (k_0 + k_1\Delta s + k_2(\Delta s)^2)(\rho_0 + \rho_1\Delta s + \rho_2(\Delta s)^2) = \rho_0 k_0 + (\rho_0 k_1 + \rho_1 k_0)\Delta s + ... \tag{B.9}$$

A shown above,

$$k_1 \simeq \frac{\partial k}{\partial s} + \frac{(\Delta x)^2}{6}\frac{\partial^3 k}{\partial s^3}\left(\frac{\partial s}{\partial x}\right)^2 \tag{B.10}$$

and also

$$\rho_1 \simeq \frac{\partial \rho}{\partial s} + \frac{(\Delta x)^2}{6}\frac{\partial^3 \rho}{\partial s^3}\left(\frac{\partial s}{\partial x}\right)^2 \tag{B.11}$$

so that the first order term in the Taylor expansion B.9 is

$$\rho_0 k_1 + \rho_1 k_0 \simeq \rho_0\frac{\partial k}{\partial s} + k_0\frac{\partial \rho}{\partial s} + \frac{(\Delta x)^2}{6}\left(\frac{\partial s}{\partial x}\right)^2\left[\rho_0\frac{\partial^3 k}{\partial s^3} + k_0\frac{\partial^3 \rho}{\partial s^3}\right] \tag{B.12}$$

If instead we expand χ to the second order

$$\chi = \chi_0 + \chi_1\Delta s + \chi_2(\Delta s)^2 \tag{B.13}$$

where

$$\chi_1 \simeq \frac{\partial \chi}{\partial s} + \frac{(\Delta x)^2}{6}\frac{\partial^3 \chi}{\partial s^3}\left(\frac{\partial s}{\partial x}\right)^2 \tag{B.14}$$

and

$$\frac{\partial^3 \chi}{\partial s^3} = k_0\frac{\partial^3 \rho}{\partial s^3} + \rho_0\frac{\partial^3 k}{\partial s^3} + 3\frac{\partial^2 k}{\partial s^2}\frac{\partial \rho}{\partial s} + 3\frac{\partial^2 \rho}{\partial s^2}\frac{\partial k}{\partial s} \tag{B.15}$$

Comparison of relations B.14 and B.15 with B.12 shows that the error in the evaluation of the first coefficient of Taylor expansion is larger if the expansion is performed directly on χ rather than on ρ and k separately.

Appendix C

Appendix to Chapter 7

C.1 Mixing Length models

There are three main mechanisms that regulate energy flow through a star: Conduction, Radiation and Convection. The three mechanisms are more or less efficient depending on the physical conditions and chemical composition. Since these can considerably vary in different layers of a star, some mechanism can dominate on the others at some locations. In the Sun, for instance, Conduction is efficient only in the very deeper layers, close and inside the core. In the outer layers Convection and Radiation dominate, but not in the same way. In particular, convection sets in only when the *Schwarzschild criterion* is satisfied:

$$\frac{dT}{dr} > \left(\frac{dT}{dr}\right)_a \tag{C.1}$$

that is when the temperature gradient is steeper than the adiabatic gradient. Previous condition is also often expressed as

$$\nabla > \nabla_a \tag{C.2}$$

where $\nabla = \ln T / \ln P$. If the *Schwarzschild criterion* is satisfied, than motions of increasing amplitudes occur. If the fluid is viscous, then the motions can form regular cell patterns and become stationary. But in stellar plasma the viscosity is usually too low and the fluid is turbulent. The problem of quantitative description of turbulence is essentially not solvable and numerical simulations are necessary. The Mixing Length is a model that, under some simplifications, allows to estimate some physical quantities, like the energy flux carried by convective motion, the vertical and horizontal velocities of the plasma and its temperature. The theory was first developed by G.I. Taylor, W. Schmidt and L. Prandtl, between 1915 and 1930, but the most used in the literature concerning stellar physics is the one developed by Vitense (1953). This theory is based on the assumption that the parcels, or 'eddies', in a convective fluid all travel the same distance l (the Mixing Length) before blending with the surrounding fluid. Th length l is assumed to be proportional to the pressure scale height of the fluid H_P

$$l = \alpha H_P \tag{C.3}$$

where α is a constant. Its value for stars is usually between 1.5 and 2 (see for instance Abbett et al. (1997)). Description of this theory can be find in several books. I will therefore just give the outline of the derivation, following the scheme of Stix (2002).

The aim is to calculate the mean temperature gradient dT/dr of the medium in the presence of convection and radiation. The conservation of the flux requires that the sum of the radiative and convective flux equals the total energy flux F_S:

$$F_R + F_C = F_S \tag{C.4}$$

where $F_S = L_S/4\pi r^2$ and L_S is the total solar Luminosity. For the radiative flux it is custom to use the radiative diffusion approximation:

$$F_R = \frac{16\sigma T^4}{3k\rho H_P}\nabla \tag{C.5}$$

and for the convective flux

$$F_C = \frac{\alpha}{2}\rho c_p T l\sqrt{\frac{g\delta}{8H_P}}(\nabla - \nabla')^{\frac{3}{2}} \tag{C.6}$$

where the factor δ takes into account possible variations of the mean molecular weight μ and c_p is the specific heat at constant pressure. ∇' is the gradient of the parcel during its rise. This quantity is in principle different from the adiabatic gradient, since the parcel loses energy through radiative processes. Using previous expression, after some algebra flux conservation can be expressed as

$$\nabla - \nabla_R + \frac{9}{8U}(\nabla - \nabla')^{\frac{3}{2}} = 0 \tag{C.7}$$

where

$$U = \frac{24\sqrt{2}\sigma T^3 P^{1/2}}{c_p k g l^2 \delta^{1/2}\rho^{5/2}} \tag{C.8}$$

and

$$\nabla_R = \frac{3k\rho H_P L_S}{64\pi r^2 \sigma T^4} \tag{C.9}$$

Equation C.7 contains two unknowns, ∇, the quantity we want to estimate, and ∇'. We thus need an other condition. This comes from supposing that the radiative losses of the parcel during its rise can be described by radiative diffusion approximation and from making some assumptions about the geometry of the parcel. If we suppose that the parcel is a sphere (see Stix (2002) for details) we have the second condition:

$$\nabla' - \nabla_a = 2U(\nabla - \nabla')^{1/2} \tag{C.10}$$

This last expression can be rewritten as a second order equation in ∇'. If we solve it we find

$$\nabla - \nabla' = (x - U)^2 \tag{C.11}$$

where

$$x^2 \equiv \nabla - \nabla_a + U^2. \tag{C.12}$$

Substituting relation C.11 into eq. C.7 we find the *Cubic equation* of the Mixing Length:

$$\frac{9}{8U}(x-U)^3 + x^2 - U^2 - \nabla_R + \nabla_a = 0 \tag{C.13}$$

By an analyses of the discriminant of this equation, it can be shown it always admits one Real and two Imaginary solutions. The equation in the variable x is analytically solved and thus ∇ can be estimated.

C.1.1 Generalization of Mixing Length Formulation

I now discuss the case in which the Radiative Flux is not estimated by the radiative diffusion approximation. Since the code developed to solve the radiative transfer equation allows also to evaluate the Radiative Flux, in the following this quantity is just referred as F_R. Then, from flux conservation,

$$\frac{9}{8U}(\nabla - \nabla')^{3/2} = (F_S - F_R)\frac{3k\rho H_P}{16\sigma T^4} \tag{C.14}$$

If we still suppose that the radiative losses of the parcel can be approximated by the radiative diffusion, than, with x expressed by relation C.12, and the relation C.11 still holding, we have

$$\frac{9}{8U}(x-U)^3 = \mathcal{F} \tag{C.15}$$

where $\mathcal{F} = (F_S - F_R)\frac{3k\rho H_P}{16\sigma T^4}$. For a given atmosphere, a total flux F_S, and if F_R is known, than eq. C.15 gives ∇.

C.1.2 Not radiating parcel

I now consider the case in which the parcel is not losing energy by radiation, that is $\nabla' = \nabla_a$, but still assume radiative diffusion. Flux conservation can be written, using a notation different from eq. C.7, as:

$$K_R\nabla + K_C(\nabla - \nabla_a)^{3/2} = F_S \tag{C.16}$$

where K_R and K_C are radiative and convective diffusion coefficients respectively, and by a comparison with equations C.5 and C.6, are given by: $K_R = \frac{16\sigma T^4}{3k\rho H_P}$ and $K_C = \frac{\alpha}{2}\rho c_p T l\sqrt{\frac{g\delta}{8H_P}}$. I define $\nabla_R = F_S/K_R$ (note that this is equivalent to relation C.9, but the notation is different). Then previous equation is rewritten as

$$\nabla + \frac{K_C}{K_R}(\nabla - \nabla_a)^{3/2} - \nabla_R = 0 \tag{C.17}$$

From this equation ∇ can be evaluated without any additional condition. I want to discuss the cases in which the equation admits real solutions. A cubic admits one Real solution and two Imaginary if its discriminant is greater than zero. For simplicity let us rewrite previous equation introducing the new variable $y = \nabla - \nabla_a$:

$$\left(\frac{K_C}{K_R}\right)^2 y^3 - y^2 + 2y(\nabla_R - \nabla_a) - (\nabla_R - \nabla_a)^2 = 0 \tag{C.18}$$

After some algebra we find that the the discriminant $\triangle$ of the equation is

$$\triangle = (\nabla_R - \nabla_a)^3 \left(\frac{K_C}{K_R}\right)^2 \left[-4 + 27(\nabla_R - \nabla_a)\left(\frac{K_C}{K_R}\right)^2\right] > 0 \qquad \text{(C.19)}$$

From the left term:

$$(\nabla_R - \nabla_a)^3 > 0 \Longrightarrow \nabla_R > \nabla_a \qquad \text{(C.20)}$$

From the right term:

$$(\nabla_R - \nabla_a) > \frac{4}{27}\left(\frac{K_C}{K_R}\right)^2 \Longrightarrow \nabla_R > \nabla_a + \frac{4}{27}\left(\frac{K_C}{K_R}\right)^2 \qquad \text{(C.21)}$$

Combining the two conditions we have that the discriminant is greater than zero if

$$\nabla_R < \nabla_a; \qquad \nabla_R > \nabla_a + \frac{4}{27}\left(\frac{K_C}{K_R}\right)^2 \qquad \text{(C.22)}$$

Note that in a convective unstable layer the conditions $\nabla_a < \nabla < \nabla_R$ must hold, so that the inequality on the left is never satisfied. Note also that the case $\nabla_a < \nabla_R < \nabla_a + \frac{4}{27}\left(\frac{K_C}{K_R}\right)^2$ is still physically possible, but in this case the discriminant of the equation is negative and three real distinct solutions exist.

Not radiating parcel: Generalization

I now discuss the case in which, as above, the particle is not radiating, so that $\nabla' = \nabla_a$, but the radiative diffusion is not valid. The conservation of flux is:

$$F_R + K_C(\nabla - \nabla_a)^{3/2} = F_S \qquad \text{(C.23)}$$

from which

$$\nabla = \nabla_a + \left(\frac{F_S - F_R}{K_C}\right) \qquad \text{(C.24)}$$

This case is thus simple to solve once the Radiative Flux is estimated.

C.2 Radiative Diffusion models

In the case in which radiative diffusion is a good approximation and supposing radiation is the sole energy transport mechanism, the energy equation is:

$$F_{Sun} = \frac{16\sigma T^3}{3k\rho}\frac{dT}{dz}. \qquad \text{(C.25)}$$

This equation, together with the momentum equation:

$$\frac{dP}{dz} = \rho g \qquad \text{(C.26)}$$

and the perfect gas law $P = \frac{K_B}{m_e}\rho T$ allow to simulate simple atmospheric model. In particular, analytical solutions can be derived in the case in which the opacity is given by the Rosseland mean and is parametrized through $k =$

$k_0\rho^m T^n$. Here I show, in particular, that the solutions are given by relations 7.15, 7.16 and 7.17.

For simplicity, let us define $c = K_B/m_e$. Let us rewrite the energy and momentum equation in the following way:

$$dz = \frac{16\sigma T^3}{3k\rho F_{Sun}} dT \tag{C.27}$$

$$\frac{dP}{P} = \frac{gc}{T} dz \tag{C.28}$$

Substituting eq. C.27 into C.28, we have

$$\frac{dP}{P} = \frac{16\sigma gc}{3kF_{Sun}} \frac{T^2}{\rho} dT \tag{C.29}$$

using the perfect gas law

$$\frac{dP}{P} = \frac{16\sigma gc^2}{3kF_{Sun}} \frac{T^3}{P} dT \tag{C.30}$$

The opacity can also be rewritten as $k = k_0 \frac{P^m T^{n-m}}{c^m}$. Substituting in previous expression, we have

$$\frac{dP}{P} = \frac{16\sigma gc^{m+2}}{3k_0 F_{Sun}} \frac{T^{m+3-n}}{P^{m+1}} dT \tag{C.31}$$

If $P \neq 0$ we can write

$$P^m dP = \frac{16\sigma gc^{m+2}}{3k_0 F_{Sun}} T^{m+3-n} dT \tag{C.32}$$

This equation, if $m \neq -1 \wedge m - n + 3 \neq -1$, has solution:

$$P(z) = \left[\frac{16\sigma gc^{m+2}}{3k_0 F_{Sun}} \frac{m+1}{m-n+4} T^{m-n+4} \right]^{\frac{1}{m+1}} \tag{C.33}$$

Using the perfect gas law and expliciting the opacity as a function of P and T, the energy equation can be rewritten as:

$$\frac{dT}{dz} = \frac{3k_0 F_{Sun}}{16\sigma c^{m+1}} P^{m+1} T^{-(m-n+4)} \tag{C.34}$$

Substituting the solution C.32 into previous expression we obtain:

$$\frac{dT}{dz} = gc \frac{m+1}{m-n+4} \tag{C.35}$$

that has solution

$$T(z) = \frac{m+1}{m-n+4} gcz + Const. \tag{C.36}$$

The density $\rho(z)$ is derived by the perfect gas law:

$$\rho(z) = \left[\frac{16\sigma}{3k_0 F_{Sun}} \frac{m+1}{m-n+4} T^{3-n} \right]^{\frac{1}{m+1}} \tag{C.37}$$

Note that the gradient is constant respect to depth and is given by

$$\nabla = \frac{d\ln T}{d\ln P} = \frac{m+1}{m-n+4} \tag{C.38}$$

This quantity has to be greater than 0.4 for *Schwarzschild criterion* to be satisfied.

Let us consider now the solutions generated when conditions $m \neq -1 \wedge m - n + 3 \neq -1$ are not satisfied.

If $m = -1$ and $m - n + 3 = -1$, than $n = 3$. Than the gas is a polytrope and P and T are related by:

$$P = T^{\frac{16\sigma g}{3k_0 F_{Sun}}} \tag{C.39}$$

The quantity $\frac{16\sigma T^3}{3k\rho}$ is a constant so that

$$T(z) = \frac{3k_0}{16\sigma} F_{Sun} z + Const. \tag{C.40}$$

If $m = -1$ but $m - n + 3 \neq -1$, that is $n \neq 3$, than P and T are related by:

$$\ln P = \frac{16\sigma g c^{m+2}}{3k_0 F_{Sun}} \frac{T^{3-n}}{3-n} \tag{C.41}$$

Finally, if $m \neq -1$ and $m - n + 3 = -1$, that is $n = m + 4$, than

$$P = \frac{16\sigma g c^{m+2}}{3k_0 F_{Sun}} \frac{\ln T}{m+1} \tag{C.42}$$

Appendix D

Appendix to Chapter 8

D.1 About the iso-optical depth surfaces and the intensity profile

In this paragraph I show in detail how iso-optical depth surfaces form in 2D plane parallel atmospheres in presence of flux tubes. This is also useful to the understanding of the shape of intensity profile relative to the optical depth considered. In order to point out the most relevant effects, I will discuss some very simple examples. Intensity profiles and iso-optical depth surface can be inferred using the same considerations here presented.

Let us consider the case in which density and opacity do not depend on depth and let us assume that the values of these quantities in the tube are lower than outside. Source function is null inside and outside the tube so that temperature is not specified. Uniform intensity at the bottom of the domain is imposed. At the top the optical depth is uniform as well and set to zero. I want to show that the iso-optical depth surfaces have the shape illustrated in fig.D.1 and D.2 and that the intensity profile observed is the one shown. Let us consider first fig.D.1. Optical paths that come from positions x, with $x < x_D$ or $x > x_A$, reach the value $\tau = 1$ without intersecting the tube. If χ_0 is the product of opacity and density in the quiet atmosphere, than the optical path length s and τ are related by $\tau = s \cdot \chi_0$, so that if $\tau = 1$ than $s = 1/\chi_0$. If α is the angle formed by the rays and the horizontal direction, than $s = z/\sin\alpha$, where z is the height in a coordinate system in which the zero is at the top of the domain. It follows that the position at which $\tau = 1$ is $z = \sin\alpha/\chi_0$. The value x_D beyond which the rays intersect the tube is found considering that

$$\frac{z}{x_B - x_D} = \tan\alpha \tag{D.1}$$

from which $x_D = x_B - \frac{\cos\alpha}{\chi_0}$. Rays that come from positions $x_D < x < x_C$ reach the $\tau = 1$ value inside the tube. These paths thus partially cross the tube. Since τ is by definition an integral, for the additive property we have $\tau = \tau_1 + \tau_2$ where the subscript denote optical depth evaluated outside and inside the tube. It is easy to show that in this case the position z at which $\tau = 1$ is

$$z = \frac{\sin\alpha}{\chi_1} + (x_B)\tan\alpha(\frac{\chi_0}{\chi_1} - 1) \tag{D.2}$$

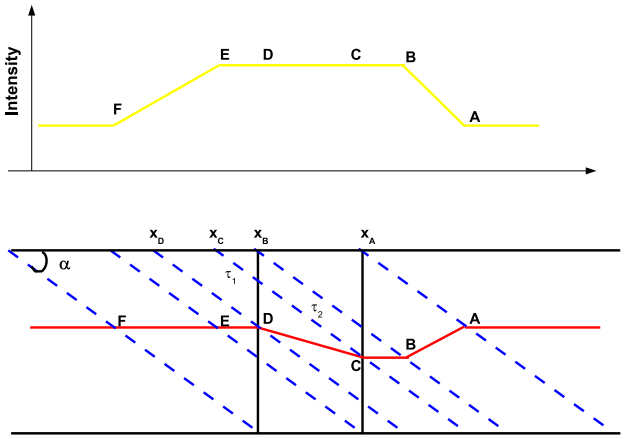

Figure D.1: Sketch of τ=1 surface (red line in bottom panel) and intensity profile (top panel) for a model in which the source function is set to zero and opacity and density are constant with height and have a lower value in the tube. Intensity boundary condition at the bottom is the same inside and outside the tube. τ=1 surface and intensity profile shapes are determined by the lengths of optical paths portions that cross the tube.

where χ_1 is the product of opacity and density in the tube. Previous relation shows that the shape of the curve of the $\tau = 1$ surface of rays that propagate at position $x_D < x < x_C$ is a line of slope $\tan\alpha(\chi_0/\chi_1 - 1)$, as shown in fig.D.1. Note also that since $\chi_0 > \chi_1$ the slope of the line is positive. If $\chi_0 < \chi_1$ than the slope is negative. Moreover, the angle that this line forms with the horizontal direction is smaller than the angle α if $\chi_0 < 2\chi_1$.

If $x_C < x < x_B$ than the path starts in the quiet atmosphere, crosses the tube and crosses the quiet atmosphere again. It is easy to see that the length of the segment that crosses the tube is always the same, while the sum of the two segments that cross the quiet atmosphere is constant for directions that originate at $x_C < x < x_B$. The corresponding $\tau = 1$ surface is thus a horizontal line.

The case $x_B < x < x_A$ is similar to the case $x_D < x < x_C$ so that the iso-optical depth surface is a line whose slope has opposite sign respect to the $\overline{DC}$ line.

Figure D.2 illustrates the case in which the angle formed by the tube flanks and the line of sight is smaller, that is the structure is closer to disk center. In this case the $\tau = 1$ surface is flat inside the tube, and corresponds to paths that originate and travel totally inside the tube, that is for paths that originate at positions $x_C < x < x_B$. Paths that originate at locations $x_D < x < x_C$ and $x_B < x < x_A$ form lines inside and outside the tube respectively as already explained.

The intensity profiles observed at the $\tau = 1$ surfaces are shown in the upper panels of fig.D.1 and fig.D.2. They can be easily understood considering that the intensity at the bottom is constant and that there is no source function,

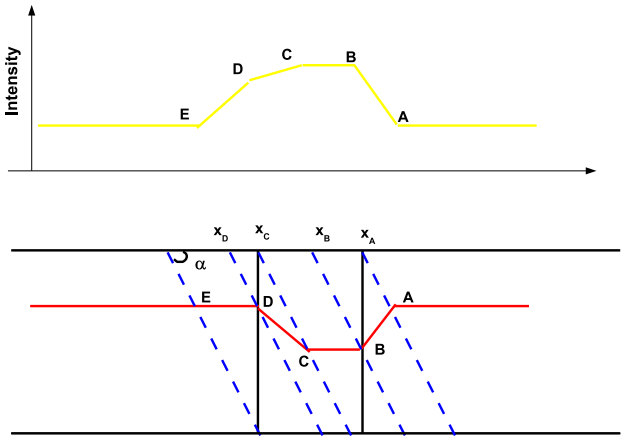

Figure D.2: τ=1 surface (red line in bottom panel) and intensity profile (top panel) for the model in fig. D.1 but for a different view angle.

so that the intensity at each point depends only on the amount of attenuation. For instance, for the case in fig.D.1, the intensity corresponding to segment $\overline{AB}$ of $\tau = 1$ surface, increases from A to B, since the lower the location of $\tau = 1$ the lower is the attenuation. Intensity corresponding to segment $\overline{BC}$ is obviously constant. Intensity corresponding to segments $\overline{CD}$ and $\overline{DE}$ is constant as well, since the segments of optical paths from the bottom to the $\tau = 1$ line cross the tube and the non magnetic atmosphere in proportions that make attenuation constant. Intensity decreases along segment $\overline{EF}$ since more and more non magnetic atmosphere is crossed respect to the tube.

Intensity in fig.D.2 is very similar to intensity shown in fig.D.1, but here the intensity corresponding to segment $\overline{CD}$ decreases from C to D. The corresponding rays, in fact, originate inside and cross only the tube, so that the attenuation is larger in D rather than in C, where the path is shorter. Intensity decreases again from D to E since more and more non magnetic atmosphere is crossed.

Note that in both cases the intensity profile is asymmetric and broader than the tube width. In particular a large asymmetry toward the observer (disk center) is formed.

D.2 Ratio of contrasts in quiet atmosphere

I want to show that the ratio of contrast measured at different wavelengths for a 'quiet' atmosphere is slightly dependent on disk position, thus explaining to the observed ratio of contrast of disk center. According to the Spruit flux tube model, a magnetic element shows the wall behind it when observed at the limb, being it more transparent than the surrounding 'quiet' atmosphere. This means that one is looking (through the tube) at the 'same' atmosphere but at a deeper region with respect to where one is looking far from the tube. The structure thus appears more brilliant, the temperature being higher in the deeper layers.

If we assume that the observed quiet atmosphere far from the tube comes from the τ_1=1 surface, in the regions around the tube it comes from τ_2 >1. Let us suppose that the Source function is a second order function of τ. The intensity is thus:

$$I(\lambda,\tau) = a_\lambda + b_\lambda\tau + c_\lambda\tau^2 + \mu(b_\lambda + 2c_\lambda\tau) + c\mu^2 \tag{D.3}$$

and the contrast is

$$C(\lambda) = \frac{a_\lambda + b_\lambda\tau_2 + c_\lambda\tau_2^2 + \mu(b_\lambda + 2c_\lambda\tau_2) + c\mu^2)}{a_\lambda + b_\lambda\tau_1 + c_\lambda\tau_1^2 + \mu(b_\lambda + 2c_\lambda\tau_1) + c\mu^2)} - 1 \tag{D.4}$$

Pierce and Slaughter (1977) fitted the CLV variation of the quiet sun observed in several wavelengths with second order polynomial in μ, that is:

$$I(\lambda,\tau) = \alpha_\lambda + \beta_\lambda\mu + \gamma_\lambda\mu^2 \tag{D.5}$$

If we suppose that these coefficients were estimated at τ=1, a comparison of previous two formulas gives

$$\begin{aligned} \alpha_\lambda &= a_\lambda - b_\lambda + c_\lambda \\ \beta_\lambda &= b_\lambda - 2c_\lambda \\ \gamma_\lambda &= c_\lambda \end{aligned} \tag{D.6}$$

Among the wavelengths investigated by Pierce and Slaughter (1977), the closest to the PSPT ones are 6109.7 and 4069.4 Å. They found a_R=0.3463, b_R= 0.92988, c_R=-0.27635 and a_B=0.1386, b_B= 0.99664, c_B=-0.13524, where subscripts R and B denote the red and blue wavelengths respectively. Substituting into D.6 we find α_R=-0.85993, β_R= 1.48258, γ_R=-0.27635 and α_B=-0.99328, β_B= 1.26712, γ_B=-0.1524. Figure D.3 shows the ratio of contrast in the two

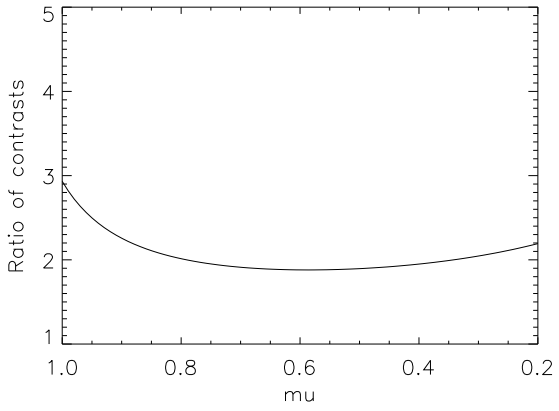

Figure D.3: Ratio of contrasts at two different wavelengths evaluated according to D.4, where the coefficients are evaluated from the ones estimated by Pierce and Slaughter (1977), τ_1=1 and τ_2=2.

wavelengths evaluated by substituting for each wavelength these values in formula D.4 and supposing τ_1=1 and τ_2=2. This function is almost constant in

the range $0.2 < \mu < 0.8$ and increases toward the center, as observed with real data. Nevertheless both the value of the function in the range $0.2 < \mu < 0.8$ and the peak value do not correspond to the observed values. Discrepancies are due to the fact that the wavelengths at which coefficients are evaluated are not the same as observations, to the uncertainties in the value of τ_2 and of course to the fact that the presence of the flux tube is not taken into account.